



HAL
open science

Development of diagnostics for the experimental studies of ignition in sprays

Tapish Agarwal

► **To cite this version:**

Tapish Agarwal. Development of diagnostics for the experimental studies of ignition in sprays. Other. Ecole Centrale Paris, 2013. English. NNT : 2013ECAP0026 . tel-00969174

HAL Id: tel-00969174

<https://theses.hal.science/tel-00969174>

Submitted on 2 Apr 2014

HAL is a multi-disciplinary open access archive for the deposit and dissemination of scientific research documents, whether they are published or not. The documents may come from teaching and research institutions in France or abroad, or from public or private research centers.

L'archive ouverte pluridisciplinaire **HAL**, est destinée au dépôt et à la diffusion de documents scientifiques de niveau recherche, publiés ou non, émanant des établissements d'enseignement et de recherche français ou étrangers, des laboratoires publics ou privés.

THÈSE

présentée par

Tapish AGARWAL

pour l'obtention du

GRADE de DOCTEUR

Formation doctorale : Énergétique

Laboratoire d'accueil : Laboratoire d'Énergétique Moléculaire
et Macroscopique, Combustion (EM2C)
du CNRS et de l'ECP

Development of diagnostics for the experimental studies of ignition in sprays.

Soutenue le 27 Février 2013

Jury : Mme Cuenot B. Rapporteur
MM Darabiha N. Directeur de thèse
Gajan P. Examineur
Lederlin T. Encadrant Turbomeca
Lemoine F. Examineur
Renou B. Rapporteur
Zimmer L. Co-Directeur

Remerciements

There is a long list of people who I am grateful to for their support and help during the three years of my Ph.D. First and foremost, I would like to thank my supervisor, Dr. Laurent ZIMMER for his continued interest and perseverance in the project. His knowledge of the subject and the techniques helped greatly at each stage of the work. I would also like to thank Dr. Nasser DARABIHA, the director of my thesis, for his continued motivation and support. Technical inputs and discussions with Dr. Thomas LEDERLIN of Turbomeca almost every week helped improve the quality and planning of the research. I would also like to thank Dr. Sebastien CANDEL, whose presence and visibility in the laboratory motivates one towards better research output. I would also like to thank Dr. Sebastien Ducruix for introducing me to EM2C Laboratory.

I would like to express my gratitude to all my colleagues at EM2C, Ecole Centrale Paris, who created a pleasant atmosphere and helped me during those three years of PhD. In particular, I thank Theodore PROVIDAKIS, for helping with ignition experiments in two phase flow burner. The burner developed by him proved to be very useful for the ignition experiments. The time spent by him in helping me understand the setup is highly appreciated. I would also like to thank the colleagues with whom I got to share the office especially Fred, Paul, Aless, Theodore, Benedetta, Raphael, Antoine, Wenzie, Peb, Ayane and many others with whom I had the opportunity to discuss work as well as other issues.

I would also like to thank the technical staff at EM2C, whose expertise in designing experimental setups was a great help. Many thanks to the administrative support staff at EM2C, especially Anne-Cecile, whose kind help made it easy to go through administrative stuff while settling down in a foreign country. My final thanks goes to Akanksha, who has been here as my girlfriend and my wife and has kept me going through thick and thin.

Abstract

The need to ignite within a very short time the aircraft engines led to many studies. However, the ignition process is not yet fully understood. Many experimental studies are based on obtaining ignition probability at different points and in different average flow conditions but few have focused on the study of a single ignition event. The reason for the lack of full understanding is transient nature of the the ignition process, which depends on many physical parameters, before, during and after the deposition of spark energy.

The purpose of this study is to develop the tools necessary to understand unique events by simultaneously measuring multiple parameters that affect the ignition process. A new technique of measurement, two-dimensional laser-induced plasma spectroscopy (2D-LIPS) was developed for the spatially resolved concentration gradients of species and energy in a laser-induced plasma. This technique is based on the use of two cameras, each provided with an interference filter centered on a transition atomic emission. This technique provides the initial size of plasma containing the minimum fuel concentration, thereby justifying the success/failure of an event. It was first validated in a mixing layer of air/nitrogen mixture to determine and resolve the spatial uncertainty of the technique. It was then applied to an aviation fuel injection system. The flow of air, preheated to 200°C, was set at 10 g/s and drops of dodecane having a Sauter mean diameter between 30 and 40 μm were inserted. This injector has a aerodynamic instability type precessing vortex core around 550 Hz, measured by 2D-PIV on the droplets at 20 kHz. Simultaneous measurements 2D-LIPS and 2D-PIV at 20 kHz have established a scenario of ignition. A minimum concentration of dodecane and a minimum size of plasma are necessary but not sufficient for a successful ignition. The strength of PVC also appears to play a role in the fate of the initial nucleus. The study proposes to establish conditional probabilities of ignition using measurements by 2D LIPS. It is shown that for ignition tests having an unconditioned probability of 33% show a conditional probability of 88% through the 2D-LIPS measurements.

Résumé

Le besoin d'allumer avec un temps très court les moteurs aéronautiques a conduit à de nombreuses études. Cependant, le processus d'allumage n'est pas encore parfaitement compris. Beaucoup d'études expérimentales sont basées sur l'obtention de probabilité d'allumage en différents points et sous différentes conditions moyennes de l'écoulement mais peu se sont concentrées sur l'étude d'un évènement unique. La raison pour le peu de compréhension totale est la nature transiente de l'allumage, qui dépend de nombreux paramètres physiques, avant, pendant et après le dépôt de l'énergie.

Le but de cette étude est de développer les outils nécessaires à la compréhension d'évènements uniques en mesurant simultanément plusieurs paramètres affectant le processus d'allumage. Une nouvelle technique de mesure; la spectroscopie en deux dimensions de plasma induit par laser (2D-LIPS) a été mise au point pour obtenir les gradients de concentration d'espèces et d'énergie dans un plasma induit par laser. Cette technique se base sur l'utilisation de deux caméras, chacune munies d'un filtre interférentiel centré sur une transition atomique. Cette technique permet d'obtenir la taille initiale du plasma contenant une concentration minimale en combustible, ce qui permet de justifier le succès/l'échec d'un évènement. Elle a d'abord été validée dans une couche de mélange air/oxygène afin d'en déterminer les incertitudes et la résolution spatiale.

Elle a ensuite été appliquée à un système d'injection aéronautique. Le débit d'air, préchauffé à 200°C, a été fixé à 10 g/s et les gouttes de dodécane avaient un diamètre moyen de Sauter entre 30 et 40 μm . Cet injecteur présente une instabilité aérodynamique de type Precessing Vortex Core aux alentours de 550 Hz, mesurée par 2D-PIV sur les gouttes à 20 kHz. Les mesures simultanées de 2D-LIPS et 2D-PIV à 20 kHz ont permis d'établir un scénario d'allumage. Une concentration minimum de dodécane ainsi qu'une taille minimum de plasma sont nécessaires mais non suffisants à un allumage réussi. La force du PVC semble aussi jouer un rôle dans le destin du noyau initial. L'étude propose d'établir des probabilités conditionnées d'allumage en utilisant les mesures de 2D-LIPS. Il est ainsi montré que des essais d'allumage menant à une probabilité non conditionnée de 33% peuvent mener, grâce à la 2D-LIPS, à une probabilité conditionnée de 88%.

Contents

List of Tables	xi
List of Figures	xiii
1 Introduction	1
1.1 Background	1
1.2 Process of ignition	1
1.3 Laser-Induced Plasmas	4
1.4 Minimum Ignition Energy (MIE)	5
1.5 Ignition studies	6
1.6 Experimental measurement of fuel concentration	9
1.7 Objectives	10
1.8 Outline of the Manuscript	11
2 Diagnostic Techniques	13
2.1 Laser diffraction technique	13
2.2 Phase Doppler Anemometry(PDA)	13
2.3 Particle Image Velocimetry (PIV)	16
2.4 Spark energy measurements	19
2.5 Laser-Induced Plasma Spectroscopy (LIPS)	19
2.6 Chemiluminescence	22
3 Experimental Setups	25
3.1 Laminar gaseous burner	25
3.2 Turbulent two-phase burner	29
4 Post-Processing Techniques	39
4.1 Inverse Abel Transform	39
4.2 Discrete Fourier Transform	40
4.3 Wavelet Transform	42
4.4 Dynamic Mode Decomposition	44
5 Flow characteristics inside burner	45
5.1 Aerodynamic flow measurements	45

5.2	Droplets' size measurements	50
5.3	Droplets' flow measurements	54
5.4	Difference between droplets' and aerodynamic velocity fields . .	63
6	Ignition at fixed location	67
6.1	Spark Measurements	68
6.2	Spectral analysis	70
6.3	Flow measurements	71
6.4	Dynamics of flame propagation	77
7	Development of Two Dimensional Laser-Induced Plasma Spec-	
	troscopy (2DLIPS)	85
7.1	Objective of 2D-LIPS Technique	85
7.2	Energy Measurements	88
7.3	Spectral Measurements - LIPS	93
7.4	Image acquisition	99
8	Application and validation of 2D-LIPS	109
8.1	Validation in non-reacting conditions	109
8.2	Ignition studies in a laminar stratified burner	118
9	Ignition experiments in two-phase burner	125
9.1	Spark Locations	125
9.2	Experimental Conditions	126
9.3	Results and Discussions	127
10	Conclusions and Perspectives	153
A	Potential of polarization-resolved laser-induced plasma spec-	
	troscopy for ignition studies	157
B	Transmission properties of band-pass filters used for 2D-LIPS	
	measurements	161
C	Estimation of initial flame kernel size	163
D	Results of 2D-LIPS experiments.	173
D.1	Location a	173
D.2	Location b	177
D.3	Location c	180
D.4	Location d	185
D.5	Location e	188
D.6	Location f	188
D.7	Location g	199
	References	214

List of Tables

2.1	Wavelength (λ), Oscillator strength or the strength of transition (A_{ki}), energy levels at states i and k (E_i and E_k), and the states between which the transition occurs (g_i and g_k), corresponding to some of the atomic emissions as obtained from NIST database (Kramida et al. (2012)).	21
9.1	Summary of ignition experiments at location b inside the burner. Yes represents successful prediction of fate of ignition attempt and No represents failure in prediction of fate of ignition attempt by the given technique. NA represents cases when single shot ignited and therefore velocity fields' comparison could not be performed.	141

List of Figures

2.1	Position of the He-Ne laser with respect to spray in the combustion chamber.	14
2.2	Typical signal of a Doppler burst.	15
2.3	Typical setup for PIV measurements.	17
2.4	Typical setup and principle of LIBS/LIPS measurements.	22
3.1	Schematic view of the co-flow nozzle used for calibration and validation of the 2D-LIPS technique.	26
3.2	Experimental setup for simultaneous 2D-LIPS and PIV measurements	27
3.3	Chronology of the PIV measurements simultaneously with spectral and 2D-LIPS measurements	28
3.4	Schematic and image of the injector.	29
3.5	Schematic of Pilot stage of injector system	30
3.6	Schematic and image of the chamber.	31
3.7	Experimental setup for ignition experiments in two-phase, turbulent conditions.	32
3.8	Schematic of HSPIV setup.	33
3.9	Chronograph showing acquisition times of the various techniques.	37
4.1	A discrete signal as a function of time.	40
4.2	Typical mother wavelet for Frequency-B Spline (a), Complex Morlet 1-1.5 (b), Complex Morlet 50-0.5 (c) and Complex Morlet 25-7 (d).	43
4.3	Results of Continuous Wavelet Transform (CWT) analysis of a synthetic signal.	43
4.4	Decomposing a matrix D containing all data into three matrices representing respectively the modes, the amplitudes and temporal evolution.	44
5.1	Mean and fluctuations of Mie-scattering intensity in an axial plane, averaged over 1 s, <i>i.e.</i> 10000 image frames.	46
5.5	Mean and fluctuations (over 0.5 s) of Mie-scattering intensity in a transverse plane at an axial distance of 25 mm.	49

5.6	Mean U (axial) and V (vertical) components in transverse planes at an axial distance of 25 mm, Mean calculated over 10000 velocity fields (0.5 s).	50
5.7	Radial velocity fields for different axial locations inside the burner.	51
5.8	Azimuthal velocity fields for different axial locations inside the burner.	52
5.10	Histogram of horizontal velocity component at $y = 0$ mm and $z = 12$ mm for a transverse plane at an axial distance of 25 mm.	53
5.11	Histogram of droplet diameters (μm), at axial locations of (a) 5 mm, (b) 20 mm, (c) 40 mm, and (d) 60 mm. At each axial location, histograms are plotted at few vertical locations z	55
5.12	Sauter Mean diameter of droplets coming out of injector at various axial locations as a function of radial location, Aerodynamic and spray recirculation zone also simultaneously plotted.	56
5.13	Mean and fluctuations of Mie-scattering intensity in an axial plane, averaged over 1 s.	57
5.14	Mean axial (U) and vertical (V) components of droplets velocity fields, calculated over 1 s	57
5.15	Mean and fluctuations (over 1 s) of Mie-scattering from fuel droplets in a transverse plane at an axial distance of 23 mm.	58
5.16	Radial velocity fields (m/s) for droplet flow at different axial locations inside the burner.	59
5.17	Azimuthal velocity fields for droplet flow at different axial locations inside the burner.	60
5.19	Histogram of vertical velocity component (m/s) at $y = -20$ mm and $z = 20$ mm for a transverse plane at an axial distance of 13 mm.	61
5.20	Histogram of vertical velocity component (displacement in pixels) at $y = 0$ mm and $z = 48$ mm for a transverse plane at an axial distance of 13 mm.	62
5.23	Dominant frequencies inside the burner calculated using FFT of vertical velocity components in the axial plane	64
5.25	Difference between aerodynamic and droplets' velocity fields in an axial plane.	65
6.1	Variation of incident laser energy with shot number; Circles correspond to successful ignition and + correspond to unsuccessful ignition attempts.	68
6.2	Images of spark as captured by the ICCD camera.	69
6.3	From top to bottom: Integrated spark intensity, Area of the laser induced spark, Mean intensity of the laser induced spark, Maximum intensity of the laser induced spark; Circles correspond to successful ignition and stars correspond to unsuccessful ignition attempts.	69

6.4	(a) Typical Spectral measurements from a laser induced spark; and, (b) Hydrogen to oxygen spectral ratio; Circles correspond to successful ignition and stars correspond to unsuccessful ignition attempts.	70
6.5	(a) Fast fourier transform of the helium neon laser transmitted energy measurements.; and, (b) Variation of phase of PVC at the times of spark, obtained from Helium Neon measurements; Circles correspond to successful ignition and stars correspond to unsuccessful ignition attempts.	72
6.6	Temporal variation of PVC frequency (blue-bottom) and variation of He-Ne transmitted energy signal (black-top); red lines indicate locations of sparks, last spark corresponding to igniting spark.	73
6.7	Fast fourier transform of the Mie scattering intensity at the exit of the injector.	74
6.8	Expansion of the precessing vortex core (PVC).	74
6.9	Frequency spectrum at the location of the spark.	75
6.10	Phase of the mie scattering signal at the exit of the injector resolved at the frequency of the corresponding PVC at the time of the spark; Circles correspond to successful ignition and stars correspond to unsuccessful ignition attempts.	75
6.11	Mean (over 100 ms) and instantaneous axial velocity fields calculated using the Mie-scattering images of the droplets	76
6.12	Mean (over 40 velocity fields $\bar{1}$ PVC cycle) of vertical velocity components at the axial location of the spark before spark energy deposition; \times corresponds to non-igniting sparks and \bullet corresponds to successfully igniting spark; from left to right: test 1-5.	77
6.13	Mean (over 40 velocity fields $\bar{1}$ PVC cycle) of vertical velocity components at the axial location of the spark after spark energy deposition; \times corresponds to non-igniting sparks and \bullet corresponds to successfully igniting spark; from left to right: test 1-5.	78
6.14	Typical magnitude of the eigenvalues corresponding to the PVC mode as obtained from DMD.	79
6.15	Time-resolved DMD before igniting spark, Test 1: images 1-12 show results using velocity fields, respectively, over (130-to-110 ms), (120-to-100 ms),, (30-10 ms), (20-0 ms) before the igniting spark	80
6.16	Time-resolved DMD after igniting spark, Test 1: images 1-12 show results using velocity fields, respectively, over (0-to-20 ms), (10-to-30 ms),, (30-10 ms), (20-0 ms) after the igniting spark	81
6.17	Chemiluminescence images acquired at 10 kHz, at respectively 60, 62, and 64 ms after the igniting spark.	82
6.18	Time-resolved DMD after igniting spark, Test 1: images 1-8 show results using velocity fields, respectively, over (54.75-to-64.75 ms), (55.00-to-65.00 ms),, (56.5-66.5 ms), after the igniting spark	83

7.1	Laser Energy Measurements	88
7.2	Probability of breakdown as a function of incident laser energy. .	90
7.3	Laser Energy Measurements: (a) Spark Energy as a function of incident energy, and (b) absorption percentage of the laser beam energy as a function of incident energy.	91
7.4	Effect of laser pulse frequency on breakdown:(a) Incident vs Transmitted Energy for different laser pulse frequency; and, (b) Breakdown probability as a function of incident laser energy.	92
7.5	Incident Vs Transmitted energy for different seeding droplet densities.	93
7.6	Typical images of laser-induced plasmas generated in presence of droplets. Images acquired through oxygen filter ($\lambda = 780 \pm 10$ nm), 1500 ns after the deposition of spark energy with a 90 ns exposure.	94
7.7	Example of single shot spectral emission obtained in methane-air mixture with an equivalence ratio of 0.6, for an integration time of 90 ns at a delay of 1 500 ns from plasma formation.	96
7.8	Mean spectra and various values used in calculating alpha	97
7.9	Effects of delay after plasma formation on, from top to bottom: (1) volume of the plasma, (2) aspect ratio of the plasma, (3) area of the plasma image, (3) normalized intensity for different atomic emission and (4) α for the same atomic emissions, as a function of time after the initial occurrence of plasma; plasma created in premixed air-methane mixture with an equivalence ratio of 0.6. .	98
7.10	Mean Images of laser-induced plasmas in air, acquired with oxygen filter for different delays with respect to the initial occurrence of plasma; Spark energy = 30 mJ	99
7.11	Image Correlation Procedure.	101
7.12	Intensity ratio of images obtained after image correlation using PIV measurements; Images acquired with nitrogen filters on both cameras, laser-induced spark of energy 94.8 mJ created in a constant flow of air.	102
7.13	Typical image of the grid used for initial image calibration. . . .	102
7.14	Typical intensity ratio (O/N) obtained using image correlation through a grid image and image processing with Flow Manager; Images acquired with oxygen and nitrogen filters on ICCD cameras, laser-induced spark of energy 117 mJ created in a constant flow of air.	103
7.15	Typical intensity ratio (O/H) obtained using bounding box approach; Images acquired with oxygen and hydrogen filters on ICCD cameras, laser-induced spark of energy 110.4 mJ created in a constant flow of methane-air mixture with equivalence ratio of 0.9. .	104

7.16	Steps of intensity ratio calculation for a laser-induced plasma of spark energy 110.4 mJ, generated in an air-methane mixture of equivalence ratio 0.9. From bottom to top: (a) Image from camera 1 corresponding to hydrogen emission. (b) Image from camera 2 corresponding to oxygen emissions. (c) Intensity ratio obtained after division of images (O/H) (fluctuations 8.19 %). (d) Intensity ratio obtained after applying an average filter of size 4×4 pixels, therefore resulting in a spatial resolution of 200 μm instead of actual resolution of 50 μm (fluctuations 5.73 %). (e) Intensity ratio obtained after removal of edges using a disk of size 2 (fluctuations 4.37 %).	106
7.17	Variation of standard deviation in calculations of intensity ratio and the number of points/pixels where intensity ratio information is available for different levels of intensity ratio threshold.	107
7.18	Variation of standard deviation in calculations of intensity ratio and the number of points/pixels where information is available with size of digital FIR filters or resulting resolution of measurements.	107
7.19	Variation of standard deviation in calculations of intensity ratio and the number of points/pixels where information is available with size of erosion disk for a fixed filter size of 4 and an intensity threshold of 33%.	108
8.1	Typical intensity ratio calculations using the bounding box approach in the region of concentration gradient.	110
8.2	Evolution of the image intensity ratio of oxygen over nitrogen emissions as a function of the oxygen concentration.	111
8.3	Comparison of 0D-LIPS and 2D-LIPS technique: Mean and fluctuations of 2D-LIPS and 0D-LIPS measurements as a function of oxygen concentration.	112
8.4	Variation of oxygen-by-nitrogen intensity ratio as a function of axial distance from the center of the burner.	113
8.5	Analysis of the spectral data in premixed conditions. From bottom to top: (a) Oxygen/Nitrogen ratio as calculated from spectral measurements as a function of input oxygen concentration (b) uncertainty in the measurements of oxygen concentration for given input oxygen concentration.	114
8.6	Analysis of the spectral data across the mixing layer. From bottom to top: (a) error bar showing calculated Oxygen concentration and corresponding fluctuations. (b) Uncertainty in the calculation of oxygen concentration. (c) Difference in the uncertainty in oxygen concentration as compared to the uncertainty corresponding to the same mean oxygen concentration in the premixed measurements.	115
8.7	Velocity field measurement above the burner using PIV.	117

8.8	Velocity Measurements and fluctuations at vertical location of the plasma as a function of horizontal location.	117
8.9	Absolute uncertainty in (a) velocity and (b) concentration measurements.	119
8.10	Variation of Hydrogen-Oxygen ratio obtained by LIPS as a function of equivalence ratio.	120
8.11	Variation of Hydrogen-Oxygen ratio obtained by 2D-LIPS as a function of equivalence ratio.	120
8.12	Difference between the mean H/O ratio calculated by 2D-LIPS for two different spark energies of 73 mJ and 113 mJ.	121
8.13	(a) Mean intensity of oxygen images as a function of equivalence ratio; and, (b) Correction factor for oxygen image intensity as a function of local equivalence ratio in order to obtain local spark energy.	122
8.14	Raw ICCD image corresponding to oxygen emissions and Abel transformed image to look at spatial variation.	123
9.1	(a) Ignition probability (percentage) at few locations inside the chamber, (b) Locations of the laser-induced spark chosen for ignition experiments together with typical ignition delay.	126
9.2	Location of laser-induced spark for location b (small black rectangle) shown in mean velocity fields.	128
9.3	(a) Location b; Test#1, Analysis of 2D-LIPS experiments for Spark#1 which failed to ignite, (b) Location b; Test#1, Analysis of 2D-LIPS experiments for Spark#2 which successfully ignited.	129
9.4	(a) Location b; Test#3, Analysis of 2D-LIPS experiments for Spark#1 which failed to ignite, (b) Location b; Test#3, Analysis of 2D-LIPS experiments for Spark#2 which failed to ignite, (c) Location b; Test#3, Analysis of 2D-LIPS experiments for Spark#3 which failed to ignite, (d) Location b; Test#3, Analysis of 2D-LIPS experiments for Spark#4 which successfully ignited.	131
9.5	Location b; Test#7, Analysis of 2D-LIPS experiment where single shot ignition occurred.	132
9.6	(a) Location b; Test#2, Analysis of 2D-LIPS experiments for Spark#1 which failed to ignite, (b) Location b; Test#2, Analysis of 2D-LIPS experiments for Spark#2 which failed to ignite, (c) Location b; Test#2, Analysis of 2D-LIPS experiments for Spark#3 which successfully ignited.	133
9.7	Location b; Test#1, Calculation of initial flame kernel size for (a) unsuccessful and (b) successful sparks, From left to right: Oxygen intensity and H/O ratio as obtained by 2D-LIPS, regions above thresholds separately applied to H/O and oxygen image intensity, and regions above both the thresholds.	134

9.8	Size of the initial flame kernel as a function of mean H/O inside the kernel. Filled markers represent successful sparks and blank markers represent unsuccessful sparks.	135
9.9	Radial profiles of mean Mie-scattering intensity (over 10 ms, before sparks) at axial location of the sparks created at location 'b'; Seven successful and one unsuccessful sparks compared.	136
9.10	Location b; Test#1, Analysis of PIV measurements for 2 consecutive sparks. Spark#1 failed to ignited while Spark#2 successfully ignited. Velocity profiles at the location of spark have been plotted as a function of radial distance (Z-axis); spark located at 8-13 mm. Profiles plotted using mean velocity fields (over 100 instantaneous fields equivalent to 10 ms) before the deposition of spark energy.	137
9.11	Location b; Test#3, Analysis of PIV measurements for four consecutive sparks. Spark#1, Spark#2 and Spark#3 failed to ignited while Spark#4 successfully ignited. Velocity profiles at the location of spark have been plotted as a function of radial distance; spark located at 8-13 mm. Profiles plotted using mean velocity fields (over 100 instantaneous fields equivalent to 10 ms) before the deposition of spark energy.	138
9.12	Location b; Test#2, Analysis of PIV measurements for 3 consecutive sparks. Spark#1 and #2 failed to ignited while Spark#3 successfully ignited. Velocity profiles at the location of spark have been plotted as a function of radial distance; spark located at 8-13 mm. Profiles plotted using mean velocity fields (over 100 instantaneous fields equivalent to 10 ms) before the deposition of spark energy.	139
9.13	Variation of PVC strength before sparks for 7 igniting and 1 failed sparks.	140
9.14	Strength of the PVC 10 ms before the spark as a function of decrease in the strength of PVC, for sparks created at location 'b'	141
9.15	Size of the initial flame kernel as a function of mean H/O inside the kernel for sparks created at location 'a'. Filled markers represent successful sparks and blank markers represent unsuccessful sparks.	142
9.16	Location a; Test#3, Analysis of PIV measurements for 2 sparks. Spark#1 failed to ignite while Spark#2 successfully ignited. Velocity profiles at the location of spark have been plotted as a function of radial distance; spark located at 8-13 mm. Profiles plotted using mean velocity fields (over 100 instantaneous fields equivalent to 10 ms) before the deposition of spark energy.	143
9.17	Radial profiles of mean Mie-scattering intensity (over 10 ms, before sparks) at axial location of the sparks created at location 'a'; Five successful and two unsuccessful sparks compared.	143
9.18	Strength of the PVC 10 ms before the spark as a function of decrease in the strength of PVC, for sparks created at location 'a'	144

9.19	Size of the initial flame kernel as a function of mean H/O inside the kernel for sparks created at location ‘c’. Filled markers represent successful sparks and blank markers represent unsuccessful sparks.	144
9.20	Radial profiles of mean Mie-scattering intensity (over 10 ms, before sparks) at axial location of the sparks created at location ‘c’; Five successful and one unsuccessful sparks compared.	145
9.21	Strength of the PVC 10 ms before the spark as a function of decrease in the strength of PVC, for sparks created at location ‘c’	145
9.22	Size of the initial flame kernel as a function of mean H/O inside the kernel for sparks created at location ‘d’. Filled markers represent successful sparks and blank markers represent unsuccessful sparks.	146
9.23	Radial profiles of mean Mie-scattering intensity (over 10 ms, before sparks) at axial location of the sparks created at location ‘d’; Three successful and two unsuccessful sparks compared.	147
9.24	Strength of the PVC 10 ms before the spark as a function of decrease in the strength of PVC, for sparks created at location ‘d’	147
9.25	Size of the initial flame kernel as a function of mean H/O inside the kernel for sparks created at location ‘e’. Filled markers represent successful sparks and blank markers represent unsuccessful sparks.	148
9.26	Strength of the PVC 10 ms before the spark as a function of decrease in the strength of PVC, for sparks created at location ‘e’	148
9.27	Size of the initial flame kernel as a function of mean H/O inside the kernel for sparks created at location ‘f’. Filled markers represent successful sparks and blank markers represent unsuccessful sparks.	149
9.28	Radial profiles of mean Mie-scattering intensity (over 10 ms, before sparks) at axial location of the sparks created at location ‘f’; Two successful and two unsuccessful sparks compared.	150
9.29	Strength of the PVC 10 ms before the spark as a function of decrease in the strength of PVC, for sparks created at location ‘f’	150
9.30	Size of the initial flame kernel as a function of mean H/O inside the kernel for sparks created at location ‘g’. Filled markers represent successful sparks and blank markers represent unsuccessful sparks.	151
9.31	Radial profiles of mean Mie-scattering intensity (over 10 ms, before sparks) at axial location of the sparks created during Test#6 at location ‘g’; Two unsuccessful and one successful sparks compared.	151
9.32	Strength of the PVC 10 ms before the spark as a function of decrease in the strength of PVC, for sparks created at location ‘g’	152
A.1	Spectral emission of a plasma created in air	158
A.2	Spectra with synthetically reduced continuum level.	158
B.1	Transmission percentage as a function of wavelength for FB750-10	161
B.2	Transmission percentage as a function of wavelength for FB780-10	162

B.3	Transmission percentage as a function of wavelength for FB660-10	162
C.1	Ignition delay, τ_i (ms) as a function of initial temperature, T_o ($^{\circ}\text{C}$) for methane-air mixture.	164
C.2	Rate of generation of combustion energy and rate of convection and radiation losses as a function of initial spherical kernel diameter, for sparks created in premixed methane-air mixture with an equivalence ratio of 0.7.	167
C.3	Rate of generation of combustion energy and rate of convection and radiation losses as a function of initial spherical kernel diameter for dodecane.	169
C.4	Size of critical initial flame kernel as a function of equivalence ratio at the location of the spark.	169
D.1	Location a; Test#1, Analysis of 2D-LIPS experiments for (a) Spark#1, (b) Spark#2, and (c) Spark#3 which failed to ignite, and (d) Spark#4 which successfully ignited.	174
D.2	Location a; Test#2, Analysis of 2D-LIPS experiments for (a) Spark#1 which failed to ignite, and (b) Spark#2 which successfully ignited.	175
D.3	Location a; Test#3, Analysis of 2D-LIPS experiments for (a) Spark#1 which failed to ignite, and (b) Spark#2 which successfully ignited.	175
D.4	Location a; Test#4, Analysis of 2D-LIPS experiments for (a) Spark#1 which successfully ignited.	176
D.5	Location a; Test#5, Analysis of 2D-LIPS experiments for (a) Spark#1 which successfully ignited.	176
D.6	Location b; Test#4, Analysis of 2D-LIPS experiments for (a) Spark#1, and (b) Spark#2 which failed to ignite, and (c) Spark#3 which successfully ignited.	177
D.7	Location b; Test#5, Analysis of 2D-LIPS experiments for (a) Spark#1, (b) Spark#2, and (c) Spark#3 which failed to ignite, and (d) Spark#4 which successfully ignited.	178
D.8	Location b; Test#6, Analysis of 2D-LIPS experiments for (a) Spark#1, (b) Spark#2, and (c) Spark#3 which failed to ignite, and (d) Spark#4 which successfully ignited.	179
D.9	Location c; Test#1, Analysis of 2D-LIPS experiments for (a) Spark#1, (b) Spark#2, and (c) Spark#3 which failed to ignite, and (d) Spark#4 which successfully ignited.	180
D.10	Location c; Test#2, Analysis of 2D-LIPS experiments for (a) Spark#1, (b) Spark#2, and (c) Spark#3 which failed to ignite, and (d) Spark#4 which successfully ignited.	181

D.11	Location c; Test#3, Analysis of 2D-LIPS experiments for (a) Spark#1, and (b) Spark#2 which failed to ignite, and (c) Spark#3 which successfully ignited.	182
D.12	Location c; Test#4, Analysis of 2D-LIPS experiments for (a) Spark#1, and (b) Spark#2 which failed to ignite, and (c) Spark#3 which successfully ignited.	183
D.13	Location c; Test#5, Analysis of 2D-LIPS experiments for (a) Spark#1, (b) Spark#2, and (c) Spark#3 which failed to ignite, and (d) Spark#4 which successfully ignited.	184
D.14	Location d; Test#1, Analysis of 2D-LIPS experiments for (a) Spark#1 which successfully ignited.	185
D.15	Location d; Test#2, Analysis of 2D-LIPS experiments for (a) Spark#1, (b) Spark#2, and (c) Spark#3 which failed to ignite, and (d) Spark#4 which successfully ignited.	186
D.16	Location d; Test#3, Analysis of 2D-LIPS experiments for (a) Spark#1 which successfully ignited.	187
D.17	Location d; Test#4, Analysis of 2D-LIPS experiments for (a) Spark#1 which successfully ignited.	187
D.18	Location e; Test#1, Analysis of 2D-LIPS experiments for (a) Spark#1, (b) Spark#2, and (c) Spark#3 which failed to ignite, and (d) Spark#4 which successfully ignited.	188
D.19	Location e; Test#2, Analysis of 2D-LIPS experiments for (a) Spark#1, (b) Spark#2, and (c) Spark#3 which failed to ignite, and (d) Spark#4 which successfully ignited.	189
D.20	Location e; Test#3, Analysis of 2D-LIPS experiments for (a) Spark#1, (b) Spark#2, and (c) Spark#3 which failed to ignite, and (d) Spark#4 which successfully ignited.	190
D.21	Location e; Test#4, Analysis of 2D-LIPS experiments for (a) Spark#1, and (b) Spark#2 which failed to ignite, and (c) Spark#3 which successfully ignited.	191
D.22	Location e; Test#5, Analysis of 2D-LIPS experiments for (a) Spark#1, (b) Spark#2, and (c) Spark#3 which failed to ignite, and (d) Spark#4 which successfully ignited.	192
D.23	Location e; Test#6, Analysis of 2D-LIPS experiments for (a) Spark#1, (b) Spark#2, and (c) Spark#3 which failed to ignite, and (d) Spark#4 which successfully ignited.	193
D.24	Location e; Test#7, Analysis of 2D-LIPS experiments for (a) Spark#1, (b) Spark#2, and (c) Spark#3 which failed to ignite, and (d) Spark#4 which successfully ignited.	194
D.25	Location e; Test#8, Analysis of 2D-LIPS experiments for (a) Spark#1, (b) Spark#2, and (c) Spark#3 which failed to ignite, and (d) Spark#4 which successfully ignited.	195

D.26	Location e; Test#9, Analysis of 2D-LIPS experiments for (a) Spark#1, (b) Spark#2, and (c) Spark#3 which failed to ignite, and (d) Spark#4 which successfully ignited.	196
D.27	Location f; Test#1, Analysis of 2D-LIPS experiments for (a) Spark#1, (b) Spark#2, and (c) Spark#3 which failed to ignite, and (d) Spark#4 which successfully ignited.	197
D.28	Location f; Test#2, Analysis of 2D-LIPS experiments for (a) Spark#1, (b) Spark#2, and (c) Spark#3 which failed to ignite, and (d) Spark#4 which successfully ignited.	198
D.29	Location g; Test#1, Analysis of 2D-LIPS experiments for (a) Spark#1, (b) Spark#2, and (c) Spark#3 which failed to ignite, and (d) Spark#4 which successfully ignited.	199
D.30	Location g; Test#2, Analysis of 2D-LIPS experiments for (a) Spark#1, (b) Spark#2, and (c) Spark#3 which failed to ignite, and (d) Spark#4 which successfully ignited.	200
D.31	Location g; Test#3, Analysis of 2D-LIPS experiments for (a) Spark#1, (b) Spark#2, and (c) Spark#3 which failed to ignite, and (d) Spark#4 which successfully ignited.	201
D.32	Location g; Test#4, Analysis of 2D-LIPS experiments for (a) Spark#1, (b) Spark#2, and (c) Spark#3 which failed to ignite, and (d) Spark#4 which successfully ignited.	202
D.33	Location g; Test#5, Analysis of 2D-LIPS experiments for (a) Spark#1, (b) Spark#2, and (c) Spark#3 which failed to ignite, and (d) Spark#4 which successfully ignited.	203
D.34	Location g; Test#6, Analysis of 2D-LIPS experiments for (a) Spark#1, and (b) Spark#2 which failed to ignite, and (c) Spark#3 which successfully ignited.	204
D.35	Location g; Test#7, Analysis of 2D-LIPS experiments for (a) Spark#1 which failed to ignite, and (b) Spark#2 which successfully ignited.	205

Chapter 1

Introduction

This section justifies the need for ignition studies in the context of aeronautical combustion chambers and injection systems. An understanding of the ignition process in gas turbine engines, including a literature survey of experimental and numerical ignition and relevant combustion studies has been presented.

1.1 Background

Combustion of fuel provides energy (or power) for the functioning of most of the machines of everyday use. Moreover, operation of almost all the modes of transport, airplanes, automobiles, etc. depend mainly on the process of combustion. This makes initiation of combustion or *ignition* vital to the functioning of various machines and, therefore, it has been widely studied. The methods used for ignition have also come a long way from the use of friction to the use of highly advanced electrical spark plug systems. The need to have very economic, clean combustion has led to great advancements in the technology and studies of combustion as well as ignition. It is also anticipated that gas reciprocating engines of the future will operate at higher compression ratio, faster compression rates, and much leaner fuel-to-air ratios. Laser-induced spark could be a viable solution to create sparks in such engines, where temperatures as high as 4000 K and pressures as high as 50 MPa would be seen.

1.2 Process of ignition

Aircraft gas turbine engines need to have rapid and reliable ignition systems on the ground and sometimes there is a need to relight after a flameout during flight. There is a need to achieve successful ignition in adverse conditions, *e.g.* in presence of high amount of water during takeoff in rainy season, turbulent heterogeneous mixtures flowing with velocities up to 25 m/s. Previous studies have shown (Lefebvre and Ballal (2010)) that ignition is easier by increase in pressure, temperature, and spark energy and increasingly difficult with increase

in velocity, turbulent intensity and fuel drop size.

The process of ignition is composed of few phases, where failure of any one of the phase results in failure of an ignition attempt. Phase 1 is considered to be the generation of a flame kernel of sufficient size and temperature to be capable of combustion. For homogeneous mixtures, phase 1 depends on Minimum Ignition Energy (MIE). For inhomogeneous mixtures, it depends additionally on mixture fraction gradients. For spray combustion, it also depends on Sauter Mean Diameter (SMD) of spray droplets. Phase I also depends on turbulence in the flow at the spark location. Phase 2 of ignition is the flame growth when the initial flame kernel increases in size and moves towards the injector. Phase 3 can be defined as the condition when combustion occurs in whole burner.

Decrease in air temperature has an adverse effect on ignition. At lower temperatures, a higher amount of energy is required to increase the temperature of the fuel-oxidizer mixture to reaction temperature. As shown by [Ballal and Lefebvre \(1978\)](#), MIE for a stoichiometric flow can change from 2 mJ to 20 mJ when air temperature was changed from 350 K to 228 K. Increase in air velocity leads to higher convection losses from the initial kernel and can be detrimental to the development of successful flame. A high turbulence intensity is also detrimental to ignition as shown by [Ballal and Lefebvre \(1975\)](#), where MIE for propane-air mixtures increase with increase in turbulence intensity for all equivalence ratios. Type of fuel and fuel air ratio obviously define the MIE. Therefore, in spray combustion, for ignition to be successful, the spatial distribution is also important. A higher energy will be required for successful ignition if local equivalence ratio at the spark location is lesser or higher than optimum equivalence ratio for the fuel.

A basic difference between the ignition process in homogeneous mixture and ignition of fuel spray is that in homogeneous mixtures ignition is dominated by chemical reaction rates while in spray ignition ignition process is dominated by time required to create enough fuel vapor. Because chemical reaction is generally very short as compared to the time required to produce an adequate amount of fuel vapor in the ignition zone.

1.2.1 Altitude relight problem

On June 21, 1972, Jean Boulet of France piloted an Aerospatiale Lama helicopter to an absolute altitude record of 12,442 meters. At the extreme altitude the engine flamed out and the helicopter had to be landed via the longest-ever auto rotation in history. High altitude relight is a complex problem. High altitude flame extinction inside a gas turbine can be caused by transient disturbances of the air flow through the engine, or by severe ingestion of ice, water and dust. The altitude and speed of an aircraft determines the physical conditions inside a gas turbine combustor in event of a flame-out. These conditions can vary drastically even on the ground depending on the place and season. Although pressure does not change very much on the ground, but temperature

can change from -60°C to as high as 56°C .

When the engine is extinguished, the temperature and pressure in the combustor are low, causing a significant decrease in vapor pressure of fuel and the decreased air flow rate may lead to poor atomization, both of which imply the need for large amounts of spark energy to initiate a flame kernel. As most of the modern gas turbine combustors employ air blast atomizers, a drop in temperature, pressure and flow velocities significantly degrades the atomization quality of the air blast atomizers.

1.2.2 Ignition Systems

1.2.3 Conventional spark system

Étienne Lenoir, a belgian engineer, used an electric spark plug in his first successful internal combustion engine and is generally credited with the invention of the spark plug. The design and principle of electrical spark plugs have evolved over the years. Almost all petrol engines today use an electric spark for ignition. Electrical ignition systems are being used in aircraft engines as well since 1930. Widespread uses of electric spark for ignition have lead to numerous studies for making the spark ignition system more efficient.

1.2.4 Laser-induced spark system

An alternate method to create that vital spark for ignition has been the use of a laser-induced spark. Laser ignition is an advancement in ignition systems which has the potential to solve various problems such as the issue of high altitude relight, and can be a much more reliable source of ignition than the conventional spark plugs. The potential advantages of laser ignition have motivated many researchers and engineers to develop these ignition system. The development in laser technology and the availability of small lasers has made it a real possibility. In the very first attempts to use laser-induced spark for ignition, [Weinberg and Wilson \(1971\)](#) used laser-induced breakdown for the measurement of minimum ignition energy of gases. A review of laser ignition application for internal combustion engines applications is also provided in [Morsy \(2012\)](#). It was concluded that the laser-ignition could provide significant enhancement to the combustion process through multi-point ignition. It was also concluded that open beam delivery systems were impractical and laser beam delivery can possibly be achieved by only two methods, namely laser mounted directly on a cylinder or the use of optical fibre for laser beam delivery. Moreover, the research going on the use of optical fibres for transferring laser beam to the combustion chamber ([Mullett et al. \(2009\)](#)) could make it more feasible to apply laser ignition to actual engines.

Comparison of laser ignition with conventional spark plug ignition

- Laser ignition can be used in engines that will be required to operate under much higher compression ratios, faster compression rates, and much leaner fuel to air ratios than gas engines today (Phuoc (2005)).
- Greater control over timing and location of ignition.
- The absence of electrodes and the possibility of igniting the mixture at the center of the combustion chamber reduces the heat losses toward the walls and promote the transition of the flame kernel to a steady propagating flame (Phuoc (2005)).
- Ignition in multiple locations is a viable possibility, which in turn will decrease the time needed for combustion (Phuoc (2000)).
- Laser ignition system has a zero percent misfire rate, as long as the mixture is within flammability limits and the energy of laser is sufficient, while the spark plug often requires multiple firings before the mixture is successfully ignited.
- Laser ignition is less effective for igniting mixtures close to the lean limit. This is due to the high rate of stretch at the plasma boundary resulted from the spark expansion. If the stretch rate is not so high as to prevent ignition, however, the increased surface area arising from the gasdynamic third lobe enhances the rate of flame propagation. This effect is advantageous in lean burn automotive combustion provided the operation regime is not too close to the lean limit.

1.3 Laser-Induced Plasmas

Morgan (1978) presented a review of various studies aimed at understanding the laser-induced breakdown of gases. He presented breakdown thresholds for various gases as a function of pressure for a few laser beam wavelengths. A reduction in breakdown threshold with increase in pressure was observed for all the wavelengths of laser beams used to create sparks in different gases. He also pointed out that some gases exhibit departure from this p^{-1} at high pressures (higher than 7-8 atm). It was also shown that breakdown threshold decreases with size of particles, if sparks are created in gases containing even small particles of sizes less than 1 μm . Phuoc (2004) performed experiments and simulations to understand the evolution of the laser-induced sparks. They measured temperature of the plasma using two-line ratio technique, where they measured emissions at two O(I) lines (748.07 nm and 777.54 nm) to estimate the temperature of the laser-induced spark. They used beam deflection technique to understand the evolution of the laser-induced plasma. They used a He-Ne laser in proximity of the laser-induced spark, which upon interaction with shock front, deflects at a particular angle. With the value of this angle and change in PMT signal, they identified the time of shock arrival, the shock location, and the shock strength. They showed that the shock expansion spends

about 70% of the spark energy, and about 22% losses occur due to radiation. Therefore, about 7 to 8% of spark energy is left after shock front has propagated. [Aragon and Aguilera \(2008\)](#) presented a review of experimental methods to understand laser-induced plasmas by optical emission spectroscopy. [Ershov-pavlov et al. \(2008\)](#) presented time-space distribution of laser-induced plasma parameters and variation of emission spectra with time and space for various atomic emissions. A summary of laser-induced breakdown and spark evolution processes is presented in [Phuoc \(2010\)](#). Different approaches to explain process of ignition after the deposition of spark energy were also presented.

1.4 Minimum Ignition Energy (MIE)

In order to optimize the ignition process, minimum energy required to successfully ignite a reactive mixture, also known as Minimum Ignition Energy (MIE), was first measured by [Lewis and von Elbe \(1987\)](#). They measured MIE using electrical sparks for different gaseous mixtures at various physical conditions. Similarly various studies for the measurement of MIE have been performed using a laser-induced spark. MIE for methane-air mixtures using laser-induced sparks from nanosecond and picosecond laser pulses was measured by [Lim et al. \(1996\)](#). They observed a consistent MIE at the lean and rich fuel limits compared to the values reported by Lewis and Von Elbe ([Lewis and von Elbe \(1987\)](#)). However, the values they obtained for conditions near stoichiometry were higher. They also observed a higher MIE for picosecond pulses compared to nanosecond pulses. [Lim et al. \(1996\)](#) attributed these differences to the influence of the gas dynamic shock losses.

1.4.1 MIE using Laser-induced plasmas

[Phuoc and White \(1999\)](#) investigated the laser spark ignition of CH₄-air mixtures and calculated the minimum ignition energy to be about one order of magnitude higher as compared to electrical spark ignition. They also concluded that although laser-induced spark ignition works poorly at fuel-lean conditions, it favors fuel-rich conditions. In another study, [Beduneau et al. \(2003\)](#) performed a parametrical study to characterize the effects of flow velocity, equivalence ratio and converging lens focal length on the minimum ignition energy required for laser ignition. They showed through Schlieren images that critical radius reached by blast wave was the determining factor for successful or failed ignition. This radius was found to be independent of equivalence ratio but was proportional to spark energy. [Syage et al. \(1988\)](#) proved that pulse durations below 15 ns and wavelength of the laser light does not affect the ignition process and the minimum ignition energy. [El-Rabii et al. \(2005\)](#) performed experiments for the measurements of minimum ignition energy using a laser-induced spark for two-phase reactive mixtures. MIE was measured for n-heptane and JP4 fuels. They measured MIE values between 16 and 30 mJ for

the two fuels. They also experienced high uncertainties in the measurements due to limited number of realizations possible in a close-to-actual gas turbine combustion chamber. The reason for high uncertainties in MIE measurements was attributed to high dispersions in transmitted energy measurements.

1.4.2 Theoretical MIE calculations

[Kondo et al. \(2003\)](#) calculated minimum ignition energy of premixed gases. For this calculation they considered two approaches, one accounting the amount of energy that the minimal flame should have, and the other approach accounting losses from the surface of the minimal flamelet. They found better correlation with experiments using the second approach and thereby concluded heat loss from the surface of the kernel is better criterion to calculate minimum ignition energy.

1.5 Ignition studies

[Phuoc et al. \(2001\)](#) investigated the laser ignition for a jet diffusion flame. They performed experiments to measure ignition probability at different locations inside the jet. [Bradley et al. \(2004\)](#) did breakdown study for air and ignition studies for some rich air-fuel mixtures. They used high speed schlieren for visualization of the laser-induced plasma and flame kernel. It was found that breakdown energy increases with increase in pressure, decrease in temperature. The review paper by [Phuoc \(2005\)](#) presents the theory of laser ignition, the different process of breakdown and ignition. A review of the available theoretical models for replicating the stages of laser ignition was also presented. The review paper also presents a good overview of the advantages of laser ignition and the studies required to reach to the application level of laser ignition in real engines. The studies of laser ignition generally require much sophisticated instruments and measurement techniques as there is a need to resolve very small scales. Schlieren images have often been used to study the shape of the plasma and the flame kernel ([Beduneau et al. \(2003\)](#)).

[Kiefer et al. \(2011\)](#) also used laser-induced plasmas for simultaneous ignition and combustion diagnostics. During these measurements in methane and dimethyl ether, they utilized small size of plasma to measure quantitative equivalence ratios at different locations. They also performed few experiments in turbulent cases where they measured equivalence ratio fluctuations at a fixed location using LIBS measurements. [Phuoc \(2006c\)](#) again presented the use of laser-induced spark for ignition and equivalence ratio measurements. They performed measurements in methane-air and hydrogen-air mixtures to show the potential of laser-induced plasmas for ignition and simultaneously providing quantitative information of the local equivalence ratio. [Phuoc \(2004\)](#) presented a numerical model for the study of laser ignition and its comparison with experimental investigations.

1.5.1 Ignition studies of gaseous fuels

Achieving successful ignition in a turbulent, non-premixed, and multi-phase flow is a complex process. Various studies have been performed to understand the process of ignition in simple as well as complex flows. A review of ignition of turbulent non-premixed gaseous fuels has been presented in detail by [Mastorakos \(2009\)](#). It was concluded that in homogenous stagnant mixtures successful ignition occurs when an initial flame kernel is generated with size above a critical radius, which is proportional to laminar flame thickness. On the other hand, ignition has a stochastic nature in turbulent flows, as successful generation of flame kernel does not always result in successful ignition. Ignition of flame depends on convection of the flame kernel as well as turbulent diffusion. [Ahmed and Mastorakos \(2006\)](#) presented ignition experiments in turbulence methane-air flame. They observed an increase in ignition probability with increase in spark energy. They also found that failed sparks were statistically associated with high local velocities. They also performed simultaneous OH-PLIF measurements to understand the growth of the flame kernel. Using these measurements a turbulent flame speed was estimated to be 3-6 times of the corresponding laminar flame speed. [Ahmed et al. \(2007\)](#) also performed ignition experiments in another turbulent non-premixed burner. They used a small inductive ignition system to place the spark at different locations inside the burner. The disturbance of the flow by the presence of the spark system was neglected. An important observation from these experiments was that the initial movement of kernel depended more on location of the spark as compared to the flow conditions. To simulate these experiments, an LES study was performed by [Subramanian et al. \(2010\)](#). They performed LES of forced ignition using flamelet fully detailed tabulated chemistry combined with pdfs of mixture fractions and velocity at few locations. They analyzed various scenarios of flame kernel development and correlated them to the experimental observations by [Ahmed et al. \(2007\)](#). [Juddoo and Masri \(2011\)](#) acquired high speed OH-PLIF images to look at extinction and re-ignition phenomenon in non-premixed gaseous flames. Such measurements proved to be very useful in identifying reasons for extinction or re-ignition of flames. Quantitative measurements of flame kernel sizes and their temporal variations could also be performed. Laser-induced spark ignition was also performed in a combustion bomb for lean hydrogen-air mixture ([Srivastava et al. \(2009\)](#)) and natural gas-air mixture ([Srivastava et al. \(2011\)](#)). Laser-ignition has also been used for Homogenous charge compression ignition (HCCI) by [Srivastava et al. \(2009\)](#). [Lacaze et al. \(2009\)](#) presented LES calculations of laser-induced spark ignition of gaseous hydrogen and oxygen in a rocket like combustor. They included the treatment of shock wave produced by laser-induced spark in the calculations of ignition process. They showed that the initial flame kernel expands as a pre-mixed turbulent spherical flame. LES of spark ignition in a turbulent methane jet was also performed by [Lacaze et al. \(2009\)](#). They analyzed the flame ker-

nel formation, propagation, and stabilization mechanisms and compared them to experimental results. The process of ignition was studied in terms of four phases of ignition: (1) kernel initiation, (2) quasi-spherical expansion, (3), rapid upstream propagation, and (4) stabilization.

1.5.2 Ignition studies of liquid fuels

[Aggarwal \(1998\)](#) provided a review of theoretical and computational studies of spray ignition studies at the time. It was concluded that ignitability limits are wider for liquid-air mixtures as compared to gaseous-air mixtures. The review presented the statistical nature of ignition studies, and the need for more detailed investigations in such cases. [Marchione et al. \(2009\)](#) examined ignition process in a liquid-fuelled burner. They measured ignition probabilities at various locations inside the burner using single or multiple electrical sparks. They also captured high-speed images of the sparks and flame inside the burner, and concluded that multiple sparks increase the probability of ignition as preceding sparks create favorable conditions for successive sparks. They emphasized the need for instantaneous measurements as mean quantities did not suffice. They also suggested use of LIPS technique for equivalence ratio measurements in partially vaporized spray.

[Linassier et al. \(2011\)](#) performed visualization of early propagation of ignition kernel using tomographic imaging. They showed how a strong precessing vortex core leads to strong fluctuations in concentration inside the burner. They also calculated ignition probability map inside the burner using RANS simulations and ignition map showed good agreement with the few experimental results.

[Boileau et al. \(2008\)](#) performed LES of an ignition sequence in a multi burner gas turbine engine. They used parallel computing to successfully simulate the ignition process. They attempted the ignition process in the three phases: spark energy deposition, flame ignition, and propagation of kernel. They showed flame propagation process to be strongly influenced by large turbulent structures in the flow.

An alternate approach to simulate the ignition process was developed by [Dahms et al. \(2011a\)](#) and [Dahms et al. \(2011b\)](#). They used the ignition model to analyze ignition phenomenon in a spray-guided spark-ignition in direct-injection gasoline engine. They validated RANS simulations against experimental results of high-speed CN chemiluminescence imaging. Their model tried to take into account large variations in turbulence intensity and local equivalence ratios and showed the necessity of apply such complexities in order to understand the ignition phenomenon.

[Eyssartier et al. \(2013\)](#) used LES to predict ignition probability in turbulent two-phase flows. The model I-Crit-LES divides the process of ignition in six phases: (1) Injection of fuel, described by LES of a cold, two-phase flow. It provides local equivalence ratio and velocity fields at the moment of ignition, (2) Spark or laser discharge which leads to generation of a small hot gas ker-

nel, (3) Growth and convection of the initial hot gas kernel. If conditions are helpful, the hot gas kernel becomes a flame kernel and its size increases, (4) Transition of flame kernel to turbulent flame, (5) Propagation of turbulent flame towards the injection system, (6) Flame stabilization. In helicopter engines, an additional phase was included which verified the transition of flame from one burner to all other burners. At each phase of ignition, the model checks for the possibility of achieving next phase and if all six conditions are satisfied then a successful ignition is predicted. This model was successful in prediction of zones of high and low ignition probabilities. [Neophytou et al. \(2012\)](#) also present another model to predict ignition probability for ignition of turbulent recirculating non-premixed gas and spray flames. In this study, focus was specially on development of a Monte-carlo method to estimate propagation and expansion of initial flame kernel to complete flame inside the combustor. [Neophytou et al. \(2012\)](#) also presents 3D DNS calculations to compute spark ignition in uniformly-dispersed droplets. They showed different ignition modes depending on the density of the droplets.

1.6 Experimental measurement of fuel concentration

[Ahmed and Mastorakos \(2010\)](#) measured emissions from the sparks created by a inductive ignition system to measure local fuel concentration. They used this value to correlate to the probability of ignition above an annular jet flow burner. For the measurement of concentration ratios another technique, Laser induced Plasma (or Breakdown) Spectroscopy (LIPS/LIBS) has often been used. This is very useful in the case of laser ignition as the same spark which is created for ignition can be used for the measurement of equivalence ratios. [Fansler et al. \(2002\)](#) used CN emissions at 388 nm to measure fuel concentration inside an internal combustion engine. [Ferioli and Buckley \(2006\)](#) also used LIBS for the measurement of concentration in combustible mixtures. They performed measurements in methane-air and propane-air mixtures. They also showed the potential of LIBS to measure concentration in products of combustion. [Shudo and Oba \(2009\)](#) used LIPS to measure mixture fraction distribution in direct injection stratified charge of hydrogen. [Itoh et al. \(2001\)](#) also used spatially resolved LIPS for elemental analysis in a hydrogen-air diffusion flame. They showed that LIPS could be used for elemental analysis in gaseous flames as well.

[Phuoc and White \(2002a\)](#), [Stavropoulos et al. \(2005\)](#), [Zimmer and Tachibana \(2007b\)](#) have used laser induced-plasma spectroscopy for the measurement of fuel to air ratio. Simultaneous use of the same laser-induced spark for ignition and equivalence ratio measurement has also been performed by [Phuoc \(2006c\)](#), and [Zimmer et al. \(2007\)](#). This technique of laser-induced plasma spectroscopy has seen much application in the measurement of concentration of solids. Thus, there have also been attempts of spatial characterization of the spectroscopy

performed for solids, *e.g.* [Aguilera and Aragon \(2004\)](#).

To measure spatially resolved concentration in the region of energy deposition, there is a need to develop some new technique. As the existing techniques are either very difficult to perform simultaneously with other techniques *e.g.* Acetone-LIF([Trost et al. \(2010\)](#), [Shringi et al. \(2009\)](#)), or do not provide the required spatial resolution, *e.g.* Laser Induced Plasma spectroscopy (LIPS) ([Phuoc and White \(2002a\)](#), [Zimmer et al. \(2005\)](#), [Stavropoulos et al. \(2005\)](#), [Phuoc \(2006a\)](#), [Zimmer et al. \(2007\)](#), [Zimmer and Tachibana \(2007b\)](#), [Zimmer and Yoshida \(2008\)](#), [Zimmer and Yoshida \(2011\)](#), [Zimmer et al. \(2010\)](#)).

[Letty et al. \(2010\)](#) compared concentration measurements using emissions from laser-induced sparks and electrical sparks. They performed measurements in methane-air mixtures and concluded that LIBS is more accurate technique for measurement of concentration in hydrocarbons as compared to SIBS(spark-induced breakdown spectroscopy).

For the measurement of spatially resolved concentration/ equivalence ratio, a new diagnostic technique namely two-dimensional laser-induced plasma spectroscopy (2D-LIPS) is developed ([Agarwal et al. \(2010\)](#)).

1.7 Objectives

Objective of this research was to study ignition in two-phase flows. It was envisioned to measure simultaneously various physical parameters with high spatial and temporal resolution before and after the deposition of spark energy, and then to correlate the information of physical parameters with the success or failure of an ignition attempt. This should provide an insight into the physics of the ignition process and a database of physical conditions which lead to a successful/failed ignition, which can also be used for computations of ignition. The aim of this study was to find the reason for the failure or success of single laser ignition attempts.

In order to completely understand the physics of laser ignition, simultaneous measurement of various physical properties is necessary. Thus the aim of this thesis is to perform highly resolved experiments to measure various parameters at the same time.

The physical parameters to be measured were energy deposited in the spark, velocity field before and after the deposition of energy, and around the spark; concentration ratio in the region of energy deposition; size and velocity of droplets; and the identification of flame region. The energy deposited in the spark was measured by measuring the incident and transmitted energy of the laser beam. Velocity field of the droplets was to be measured using Particle Image Velocimetry (PIV), where the PIV cameras were coupled with a liquid crystal to protect the PIV cameras from intense spark. Laser-induced plasma spectroscopy (LIPS) was performed to measure local equivalence ratio at the location of the spark. An extension of this spectroscopy technique was devel-

oped to reveal spatially resolved concentration information at the location of the spark.

These diagnostics were simultaneously performed to understand the physical process leading to success/failure of ignition. The diagnostics were developed first on laminar-gaseous burner while keeping in mind the application to turbulent-two phase flow burners. As the main aim of the thesis is to apply these techniques in turbulent two-phase ignition and find the conditions that lead to successful ignition in this near practical configuration.

1.8 Outline of the Manuscript

This manuscript is presented in 10 chapters.

- Chapter 1 presents review of various experimental and numerical studies in the field of ignition. A brief review of ignition systems, especially the laser ignition system is also presented.
- Chapter 2 presents the two experimental setups used for the experiments, respectively in gaseous laminar and two-phase turbulent conditions.
- Chapter 3 presents brief information of the experimental techniques used for the physical measurements during this thesis.
- Chapter 4 presents the analytical methods used for the analysis of measurements in the course of this thesis.
- Chapter 5 presents the characterization of the two-phase burner used during the ignition experiments. Both aerodynamic and droplets' flow inside the burner has been quantified. Velocity fields in both transverse and axial planes is presented. The size of droplets at various locations inside the burner is also presented. Frequency domain analysis is also presented to understand the dominant frequencies present in the combustor.
- Chapter 6 presents the first ignition experiments inside the turbulent burner. Objective of these experiments was to define important physical parameters, whose measurement is necessary to understand the process of ignition.
- Chapter 7 presents development of a new two-dimensional laser-induced plasma spectroscopy (2D-LIPS) technique to measure spatially resolved equivalence ratios in the region of the laser-induced plasma. The development of this technique from scratch is presented along with methods to improve the accuracy of the measurements.
- Chapter 8 presents application of 2D-LIPS technique for the measurement of mixing layer in a nitrogen-air co-flow. Further application of the technique in reactive conditions is presented with measurements in methane-air mixing layer.
- Chapter 9 presents application of 2D-LIPS along with other simultaneous diagnostics in turbulent two-phase flow burner.
- Chapter 10 presents conclusions of the research work and recommendation

for future work.

Chapter 2

Diagnostic Techniques

This chapter presents the principle of various measurement techniques. Special emphasis has been put on the elements of these techniques which are most important while using them in ignition experiments of a two-phase turbulent combustor. At first, techniques also used for the characterization of non-reacting flows are discussed.

2.1 Laser diffraction technique

In order to have an estimation of the flux of droplets along a specific region of the combustor, a diffraction based technique can be used. For that purpose, a small He-Ne laser (632 nm, 20 mW) was placed at one side of the combustor and its intensity was recorded at the other side by using a Photomultiplier Tube (PMT, *Hamamatsu*) equipped with a bandpass filter centered on the laser's wavelength. When passing through the combustor, the beam is scattered by the droplets of dodecane. The multiple scattering phenomena tends to attenuate the energy of the beam as it travels along the combustor. Hence, it is expected that variation in either diameter and/or density of droplets may result in differences in the measured signal. To enhance this behavior, the laser was placed off-axis in order to be sensitive to any non-symmetry of the spray, as depicted in Figure 2.1. For practical considerations, the signal was acquired at a frequency of 16 kHz. It was verified that the laser intensity was stable in time so that any variation recorded should come from a change in the spray itself.

2.2 Phase Doppler Anemometry(PDA)

In order to get detailed measurements of droplets velocities and size, a phase Doppler Anemometer (PDA) is used. This system consists of two different techniques; one measuring the velocity of droplets (like in a Laser Doppler Velocimeter or LDV) and the other one their mean diameters. At first, the principle of LDV is recalled and typical limitations are discussed.

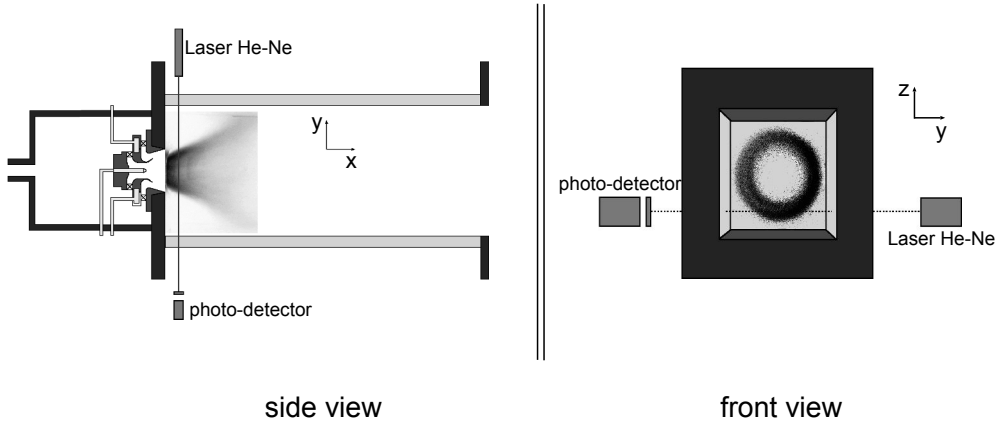


Figure 2.1: Position of the He-Ne laser with respect to spray in the combustion chamber.

Even though the name LDV tends to show that one measures a Doppler shift, in practical applications, one uses different properties of laser. Typical frequencies of laser emitting in the visible range are of the order of 10^{14} Hz. Typical velocities involved in combustion studies would lead to a Doppler shift of at most 10 MHz, which would be difficult to distinguish from the original signal. In order to measure actually such small differences, interference based approaches are used. For that purpose, an initial laser beam is first split into two different beams, keeping the coherence between them. The two beams pass through a converging lens and are focussed at the same point. At their intersection, they create interference fringes whose spacing is a function of the initial angle formed by the two beams and the wavelength of the laser. The distance between two fringes Δx can be written as function of the optical parameter of the system

$$\Delta x = \frac{\lambda_b}{2\sin(\Theta/2)} \quad (2.1)$$

with λ_b the wavelength of the laser beam and Θ the angle between the two incoming laser beams. The probe volume hence formed is composed of alternate bright and dark band. When a particle or a droplet crosses this region, it will scatter alternatively light. Therefore, a typical signal recorded by the PMT may look like the one displayed in figure 2.2. This type of signal is often called a Doppler burst. One can see that the intensity of the fringes is usually maximum in the center of the probe due to the Gaussian shape of the initial beams.

To convert this signal into velocity, one measures first the frequency content with a Fourier transform. In practical cases, one gives typical ranges for the frequencies of concern and electronic band-pass filters are implemented to reject noise. One of the main drawbacks with this simple approach is that it would be impossible to distinguish between positive and negative velocities; both giving

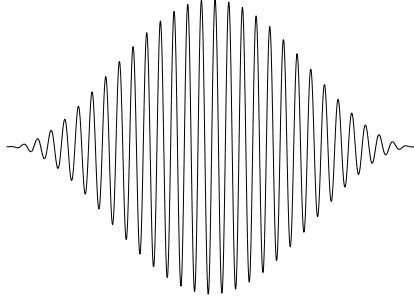


Figure 2.2: *Typical signal of a Doppler burst.*

the same frequency of scattering. To circumvent such limitations, one can introduce a frequency shift between the two signals. Hence, with a zero velocity one would measure a positive frequency. To such a purpose, an opto-acoustic device, called a Bragg cell is used. This cell transforms acoustic changes in optical variations, through its optical index. Varying optical index will modify the path of one of the laser, hence changing the fringe pattern with time. The location of the intersection of the two beams remains constant. In the present manuscript, two different particles have been considered for the measurement. The first one, to characterize the airflow are ZrO_2 particles with a nominal diameter of few micrometers. Such particles are required as air is preheated at $200\text{ }^\circ\text{C}$ and oil droplets may not sustain such temperatures. The particles are injected in the device through a cyclone type of injection, with a controlled airmass flow. An important parameter to check when introducing particles is the extent up to which they can follow the flow. This may be addressed using the Stokes number, which is the dimensionless number of the ratio between a typical timescale of the particle and a typical timescale of the flow. The Stokes number has to be small compared to one for particles to follow perfectly the flow. The first timescale is usually obtained considering the time required for a particle initially injected to a fluid at rest to achieve $1/e$ of its initial velocity. Physically, it can be expressed by considering the density ρ_p and diameter d_p of the particle and the viscosity of the fluid μ_f .

$$\tau_p = \frac{\rho_p d_p^2}{18\mu_f} \quad (2.2)$$

In the present situation, this timescale is of the order of 1ms. The timescale of the flow can not be expressed universally and one has to check at each measurement point the validity of the assumption that particles do follow the flow. The other particles measured by the system are the droplets of dodecane themselves. In this case, it is obvious that the velocity retrieved correspond to the

droplet's velocity. An important aspect of the LDV system is that it provides information only when particles are crossing the probe volume. Therefore, the temporal sampling varies strongly. Another aspect to take into account is that small particles crossing the probe volume at the edges will scatter a low intensity as compared to bigger one. To avoid noise, a typical threshold is put on the detector and only signals higher than this threshold are treated. Therefore, the actual size of the probe volume is not unique and one may take this into account when considering statistical quantities. To overcome this problem, it is usual to take the time of flight of each signal into account. This time of flight corresponds to the time for which the particle was in the interferometric fringes. This allows an estimation of the position of the droplets within the probe volume and correct any bias by using a weight inversely proportional to the probe length.

The second aspect of PDA measurement is to retrieve the sizes of the droplets. For that purpose, three different PMT are used. The three different detectors are placed at different position so that the difference in the time of arrival of the scattered light is linked to the actual size of the scattering droplet. The phase can only be determined modulo 2π and therefore three detectors are used. The phase shift between the two close detectors is very sensitive but reaches 2π for small diameters. The distance between the first and the third detector is such that it is less sensitive but achieves a 2π phase for big diameters. In practice, the two shifts are taken into account to compute the diameter and rejection criteria based on coherence are used. Whereas the measurement of velocity was not sensitive to neither the optical index of the particle, nor the scattering angle used, to determine the sizes, those two parameters are very important. A calibration procedure is first carried out to subtract an intrinsic phase shift dependent on the optical apparatus. This calibration procedure consists in measuring the phase shift from the light emitted by a diode situated in the receiving head. The calibration is performed before each set of PDA measurements. In the present manuscript, all measurements have been performed based on forward scattering taken at 30° relative to laser beams direction.

2.3 Particle Image Velocimetry (PIV)

Particle Image Velocimetry (or PIV) is a technique for the measurement of the velocity field. In most measurements, tracer particles (that should follow all eddies of the flow) have to be added. A plane within the flow is illuminated by means of a laser. Two laser sheets are created with a small time delay, this delay depends on the mean flow velocity and the resolution of the images. The light scattered by the particles is then acquired in a sequence of images. The displacement of particles between subsequent images is then calculated through correlation of images. Fig. 2.3 shows typical experimental arrangement for PIV experiments. As it is assumed that tracer particles follow the local flow, the

movement of the tracer particles between two laser sheets is equal to the true displacement of the flow. Knowing the time between the two images, the two components of the velocity of the tracer particles (the flow) can be calculated in the plane of the laser sheet.

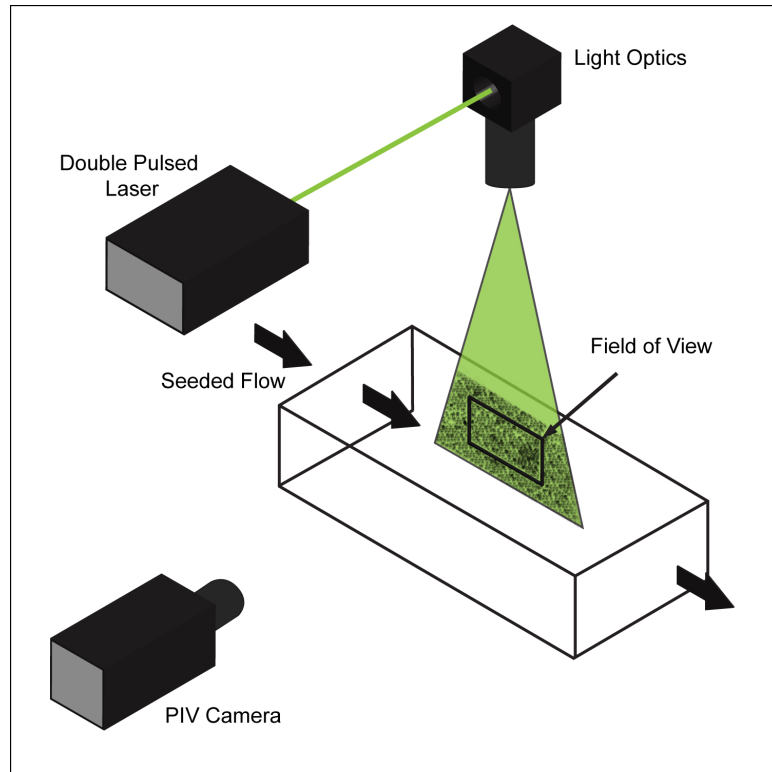


Figure 2.3: *Typical setup for PIV measurements.*

For velocity calculations, the images are divided into small sub-areas called "interrogation windows". The minimum size of these areas depends on the number of tracer particles contained in the interrogation area. In order to calculate velocity field, it is assumed that all particles in an interrogation area have moved homogeneously between the two illuminations and for having a good estimation of the displacement, the typical number of particles should be higher than eight. The displacement between two interrogation areas of two illuminations is calculated using statistical methods (cross-correlation). Correlations are performed for each interrogation area in the image planes and a quantitative measure of the velocity field is obtained in the whole plane. To have a wide range of velocities, current algorithms use a multi-pass approach. In this approach, the initial images are first divided into windows of relatively large sizes. A first estimation of the mean displacement is performed on those big areas. This initial measurement is then used as a predictor when dealing with smaller windows. Several iterations may be used to achieve the best spa-

tial resolution while keeping a good accuracy in the measurement. More recent algorithms are no more limited to rectangular windows but adapt the shape of the windows to the local gradients and local density of particles (Theunissen et al. (2010)). This latest approach is not used here and only multi-pass algorithms on squared windows are performed.

Albeit numerous applications and advantages, PIV has some limitations which must be remembered when performing experiments. The density of seeding particles in all parts of the laser sheet can not be very low or very high. A moderate density of tracers has to be maintained. A very low density requires the use of another approach based on individual trajectories (PTV : Particle tracking velocimetry; Cowen and Monismith (1997)) while a very high density needs optical flow type of approach (Horn and Schunck (1981)) as it is difficult to distinguish between individual particles. The size and density of particles has to be chosen so that they follow the flow perfectly. The intensity of the laser beam, the time between the laser pulses, the duration of the laser pulses have to be chosen with regards to the application. Furthermore, the measurements can be fairly accurate in two-dimensional flows but measurements of two-dimensional velocity fields in three dimensional flows is subjected to some debate. The third component of velocity field (out of the plane) can make it difficult to track the same tracer particles in sequence of images. *e.g.* swirled flows present in the burner shown in Fig. 3.6, where a high swirl and a strong PVC results in high azimuthal component of velocities. These high azimuthal components require PIV to be performed at rates high enough to not allow out of the plane movements of tracer particles or fuel droplets during axial field measurements. Some corrections for taking into account the third component exist but require the use of simultaneously two field of views (Prasad (2000)). In the present context no such approach was used and only two components have been measured with a small delay to limit the 3D effects.

One of the particularity of the PIV applied to sprays is that no seeding particles are introduced. Droplets are themselves the scattering media and one has to determine the exact nature of the measurements. Detailed comparisons between Mie-scattering based correlations and fluorescence based images have shown that Mie-scattering images represent a mean velocity with a weighting function based on the square of the droplets' diameters, where LIF based are weighted by the cubic power of the diameter (Zimmer et al. (2003)). This effect is even stronger when dealing with evaporation as droplets' diameter may change drastically from neighboring regions. Therefore, the final size of the interrogation grid has to be properly adjusted so as to avoid any bias towards bigger droplets.

With the recent advances in both cameras and lasers, it is possible now to use high repetition rate hardware to have the information of the velocity fields at few kHz (Barbosa et al. (2009)).

2.4 Spark energy measurements

The energy of the laser-induced sparks was measured using a two energy meters configuration. A part of the incident laser beam before converging was reflected using a beam splitter on to an energy meter. The laser beam intensity transmitted after the creation of spark was converged on to a second energy meter.

Spark energy is usually defined as the amount of energy deposited in a laser-induced spark. In practical considerations, the energy deposited is partially lost in the shock wave and in radiation losses, leaving only a part of actual energy to locally heat the gases (Phuoc and White (2002b)). In the present manuscript, spark energy was defined as being the difference between incident and transmitted energy of the laser beam used for creating the spark. Readings of the second energy meter provide the transmitted laser beam energy whereas readings of the first energy meter provided a fraction of the incident laser beam energy. Multiplying this meter value by a constant coefficient enabled the conversion from the readings of the energy meter to actual incident laser beam energy. A calibration step was performed to calculate this required constant coefficient. For the calibration step, laser pulses of energy less than breakdown threshold energy for the given experimental parameters were used. As no spark was created, the transmitted beam energy was equal to the incident beam energy minus the optical losses. The readings of the two energy meters were divided to obtain the required coefficient for incident energy calculations. The value of the coefficient remained constant for all the laser beam energies below breakdown threshold and it was assumed that the value of this coefficient remained constant even for higher energies.

2.5 Laser-Induced Plasma Spectroscopy (LIPS)

Laser-induced plasma spectroscopy (LIPS) also known as Laser-induced breakdown spectroscopy (LIBS) is a type of optical emission spectroscopy. In this technique a highly energetic laser pulse is focused to create a plasma plume with temperatures in excess of 100,000 K. At the high temperatures during the early plasma, the sample dissociates (breaks down) into excited ionic and atomic species. During this time, the plasma emits a continuum of radiation which does not contain any useful information about the species present, but within a very small time frame the plasma expands behind a shock wave and cools. After local thermodynamic equilibrium is established, plasma temperatures typically range from 5,000~20,000 K. At this point the characteristic atomic emission lines of the elements can be observed. The delay between the emission of continuum radiation and characteristic radiation is in the order of 1 μ s. This detected emission is spectrally resolved by the spectrometer. Each chemical element has a unique spectral signature having several lines which can be discriminated from the obtained spectra. As a result, the multi-elemental

composition of the sample can be determined.

LIPS is considered one of the most convenient and efficient analytical techniques for trace elemental analysis in gases, solids, and liquids. One of the main advantages of LIPS is that it can provide real-time measurements. It is a non-intrusive technique and measurements can be done from a large distance in hostile environments. This technique is non-intrusive in the sense that it does not affect the flow before measurements but can affect the flow after spectral measurement. Virtually any chemical element can be analyzed using LIPS technique. For combustion applications, this technique can be used for the analysis of various gaseous fuels and liquid fuels. This technique is also applicable when fuel is present as a mixtures of liquid and vapor states.

For combustion applications, LIPS of hydrocarbons requires measurement of atomic emissions from the following atoms: oxygen, nitrogen, carbon, and hydrogen. The wavelengths corresponding to these atomic emissions can be seen in Table. 2.1 obtained from [Kramida et al. \(2012\)](#). Each atom can emit at several wavelengths depending on possible electron transitions. The values shown in Table. 2.1 correspond to emissions with relatively high emission intensity. In practice, one has to deal with the quantum efficiency (QE) of the detector for the specific wavelength and a typical emission for a transition between k and i may be modeled as

$$I_{ki} = n_a A_{ki} g_k \frac{h\omega_{ki}}{8\pi^2} \exp\left(\frac{-E_{ki}}{k_b T}\right) \exp\left[-\frac{(\lambda - \lambda_{ki})}{2 \times slit}\right] \times QE \quad (2.3)$$

It is also interesting to note that some molecular emissions, like CN^* may also be measured but they appear for later delays under atmospheric conditions.

In combustion applications, the objective is to simultaneously measure the emissions from various atomic emissions. Thus the objective is to have higher wavelength range and the resolution is not that important. It is also to be kept in mind that the emissions from different atoms should not overlap. As these line emissions exhibit some broadening, it is not always possible to distinguish peaks very close to each other.

For the experiments performed during this thesis, simultaneous measurements of hydrogen, oxygen and nitrogen emissions is performed. Simultaneous measurement required a wavelength range of approximately 160 nm, from 640 nm to 800 nm. Available spectrometer provided a spectral resolution of approximately 0.31 nm for this wavelength range. As resolution is not very high it is not always possible to distinguish between different peaks. *E.g.*, it is not easy to distinguish three peaks corresponding to oxygen emissions at wavelengths 777.194 nm, 777.417 nm, and 777.539 nm because the spectral resolution is not good enough to distinguish between these close peaks. On the other hand, the three peaks of nitrogen emission at wavelengths 742.364 nm, 744.229 nm, and 746.831 nm can be relatively easily distinguished. An example of these measurements can be seen in Fig. 7.7. The emissions corresponding to oxygen

Elemental species	λ (nm)	A_{ki} (s^{-1})	E_i (cm^{-1})	E_k (cm^{-1})	$\frac{g_i}{g_k}$
H(I)	486.133	2.06e+07	82259.2865	102823.9114	4-6
H(I)	656.272	2.25e+07	82258.9559	97492.3214	2-4
H(I)	656.285	6.47e+07	82259.2865	97492.3574	4-6
N(I)	742.364	5.95e+06	83284.070	96750.840	2-4
N(I)	744.229	1.24e+07	83317.830	96750.840	4-4
N(I)	746.831	1.93e+07	83364.620	97750.840	6-4
O(I)	777.194	3.69e+07	73768.200	86631.454	5-7
O(I)	777.417	3.69e+07	73768.200	86627.778	5-5
O(I)	777.539	3.69e+07	73768.200	86625.757	5-3
O(I)	844.625	3.22e+07	76794.978	88631.303	3-1
N(I)	862.924	2.66e+07	86220.510	97805.840	4-4
N(I)	868.028	2.46e+07	83364.620	94881.820	6-8

Table 2.1: Wavelength (λ), Oscillator strength or the strength of transition (A_{ki}), energy levels at states i and k (E_i and E_k), and the states between which the transition occurs (g_i and g_k), corresponding to some of the atomic emissions as obtained from NIST database ([Kramida et al. \(2012\)](#)).

atom appear as single peak, while three different peaks are seen for nitrogen emissions. Different atomic emissions have different relative emissions intensity. While performing simultaneous measurements it is important to have all emissions with sufficient signal-to-noise ratio but below saturation level of the ICCD used with the spectrometer.

For the analysis of spectral emissions, the area of the peaks are used as the measurement of element concentration. The continuum emission is subtracted from area of the peaks for a true measure of atomic concentration. In measurement of relative concentration, the ratio of areas of different peaks provides ratio of corresponding atomic concentrations.

Principle and typical experimental setup for LIPS experiments can be seen in Fig. 2.4.

During the course of this thesis, variation of plasma emissions as a function of time was performed (Presented in Fig. 7.9), to determine the time of acquisition. A time of acquisition 1000-1500 ns after the start of laser-induced plasma was selected for the measurements. The exposure time of the measurements (90 ns) was decided on the basis of other simultaneous measurements and signal-to-noise ratio of LIPS measurements. The area of the peaks were used as a representation of the atomic emission to continuum ratio. Signal to noise ratio for oxygen, hydrogen and nitrogen peaks was approximately 7.6, 7.0, and 4.2, respectively.

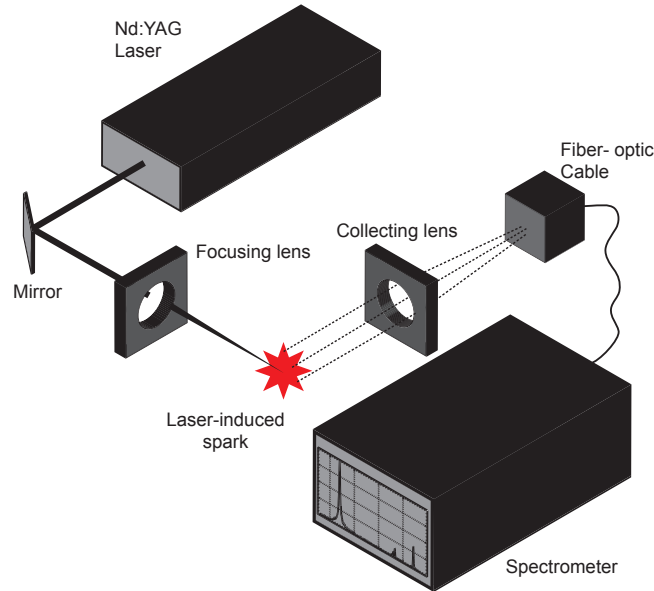


Figure 2.4: *Typical setup and principle of LIBS/LIPS measurements.*

2.6 Chemiluminescence

Chemiluminescence is the emission of light as result of an exothermic chemical reaction. Two chemicals react to form an excited (high-energy) intermediate, which breaks down releasing some of its energy as photons of light to reach its ground state. To the advantage of combustion diagnostics, the light is emitted at different wavelengths depending on the radicals formed in intermediate stages of chemical reactions. OH^* and CH^* emissions have often been used in combustion diagnostics as a quantitative measure of heat release rates. Broadband emissions of light can also be measured to derive some information about the flame. Chemiluminescence has been more used for a measurement of fluctuations in heat-release rates. Chemiluminescence measurements can be performed with the use of a photomultiplier (PMT) which provides integrated measurement of emissions from the flame. In this setup, the light from the flame is collected by a converging lens on to PMT. The advantage of a PMT is high acquisition rates, and good signal-to-noise ratio due to integrated intensity measurements. PMTs can be equipped with a band-pass filter to acquire only the emissions from OH^* and CH^* to provide more quantitative information on heat release rates.

Images of chemiluminescence images can also be acquired on the CCD cameras for spatially resolved measurements. The issues with chemiluminescence images is the low intensity of the flame. Use of band-pass filters can further deterio-

rate the intensity and the signal to noise ratio. Longer exposure times defeat the purpose of spatially resolved measurements as temporal resolution is lost. An alternate to spatial chemiluminescence measurements is the development of Planar Laser-Induced Fluorescence (PLIF). In current experiments, chemiluminescence images were acquired without any band-pass filters in the same plane as PIV measurements. Integrated chemiluminescence measurements with OH* filter have also been simultaneously performed. Integrated chemiluminescence measurements also helped in the determination of time of laser-induced sparks and the ignition delay.

Chapter 3

Experimental Setups

This chapter presents details of experimental setup and the conditions in which experiments were performed. Technical specifications of the equipments used during the experiments are also presented.

3.1 Laminar gaseous burner

Laser-induced plasma was created by converging the fundamental emission of an Nd:YAG 1064 nm laser (*Continuum Surelite II*) with the combination of a double convex lens of focal length 150 mm (BICX-50.8-153.4-C, *Melles Griot*) and a plano-concave lens of focal length -50 mm. The concave lens was installed 11 mm before the converging lens and the resulting spark was created approximately 20 mm ahead of the converging lens.

Plasma was created above a co-flow nozzle, with an inner section diameter of 20 mm with a lip of 1.5 mm thickness and an external section diameter of 39 mm, as shown in Fig. 3.1. This open jet burner configuration was used as it provides the optical access required to perform such experiments. The gaseous flow through the center and annular region of the burner was controlled using four digital mass flow controllers (EL-Flow, *Bronkhorst High-Tech*) having an accuracy of 1% of full scale. For the development of the 2D-LIPS technique, plasma was created in a flow of air and nitrogen. In both central and annular regions of the burner, mixtures of nitrogen and air could be injected depending on the requirements. For the application of 2D-LIPS technique during ignition, plasma was created in methane-air mixtures and the equivalence ratios in both center and annular regions were independently controlled using the four flow controllers.

Laser-Induced Plasma Spectroscopy (LIPS) was performed by acquiring plasma emission with an optical fiber (Single-Leg Fibre, *Roper Scientific*) and a spectrometer (SpectraPro 500i, *Acton Research*). The spectrometer was set at a grating of 150 lines/mm, a slit width of 10 μm and used an ICCD camera (512 \times 512 pixels, PI-MAX, *Princeton Instruments*). The center wavelength of the spectrometer was set at 720 nm which enabled measurement of emissions

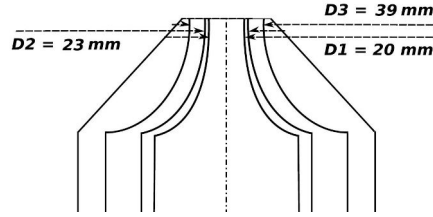


Figure 3.1: Schematic view of the co-flow nozzle used for calibration and validation of the 2D-LIPS technique.

at wavelengths between 640 nm to 800 nm. Intensity emitted by the plasma was recorded along the line of the laser beam after reflection from a dichroic mirror (DMLP900, *Thorlabs*), which reflects 99 % of the light intensity in the wavelength range 400-880 nm. The dichroic mirror allowed the fundamental laser beam wavelength to pass through and thus facilitated the measurement of transmitted laser beam energy.

Energy of the laser pulse before and after the plasma was obtained using two energy meters (PE25-SH, *Ophir Electronics*). The incident energy of the laser beam was recorded by splitting the laser beam with a 10 % beam splitter (BS1-532-10-2506M-45-P, *Melles Griot*), as shown in Fig. 3.2. The transmitted energy of the laser beam was measured by collecting the residual laser beam after the spark through a converging lens of focal length 150 mm (KBX160, *Newport corporation*) on to a second energy meter.

Images of the plasma were simultaneously recorded with two Intensified Charge Coupled Device (ICCD) cameras (PI-MAX, *Princeton Instruments*) having same objectives, *UV-NIKKOR* 105 mm. Various band pass filters with FWHM (Full Width Half Maximum) of 10 nm and center wavelengths 780 nm (FB780-10, *Thorlabs*), 750 nm (FB750-10, *Thorlabs*), 660 nm (FB660-10, *Thorlabs*), and 760 nm (FB760-10, *Thorlabs*), were installed in front of the cameras. The filters were mounted in a cage filter wheel so that they could be easily changed without disturbing the setup. The ICCD cameras used for imaging had a resolution of 512×512 pixels and were focussed at a typical field of view of 25×25 mm, thus giving a magnification of approximately 20 pixels/mm. The two ICCD cameras were installed at an angle of 90° to each other. A pellicle beam splitter (PBS-2C, *Newport corporation*), which provides 50-50 reflection transmission, was installed at 45° to both the cameras in order to obtain plasma images in both cameras from the same side of the burner. The ICCD cameras were operated in gated mode to allow very small (up to 2 ns) and precise integration times.

The time delay between the formation of the spark and the measurements is a key parameter. The time delays for all the measurements were individually identified with respect to the laser Q-switch delays with an accuracy of 2 ns. The timings and the delays of all the instruments were controlled by a multi-channel Digital delay/pulse generator (BNC 555, *Berkeley Nucleonics*).

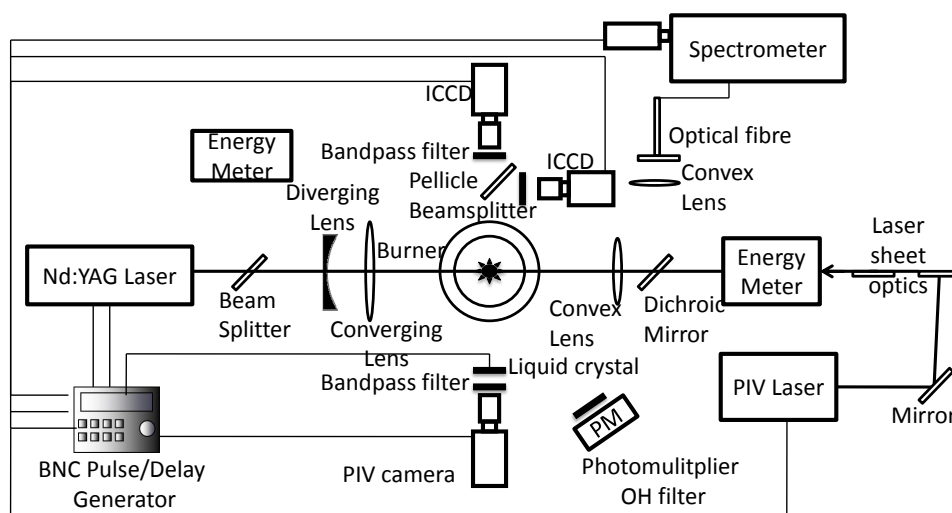


Figure 3.2: *Experimental setup for simultaneous 2D-LIPS and PIV measurements*

PIV (Particle Image Velocimetry) technique was used to measure velocity field just before the creation of the spark. In the current setup, PIV technique was performed by using images of small oil droplets illuminated by a laser sheet. Small oil droplets of Edward Oil No. 12 were used for seeding in both the center and annular flow. The laser sheet was created at the top of the burner by using a 10 Hz double pulsed Nd:YAG laser (*Continuum Inlite*), emitting at a wavelength of 532 nm. The plane of the laser sheet coincided with the laser beam which generates plasmas. The laser sheet was perpendicular to the line of sight of the ICCD cameras. The time delay between the two pulses was kept at 120 μs . The two PIV image frames were acquired 200 and 80 μs before the spark using the camera (M2/E, 8 bit, *FlowSENSE Dantec Dynamics*) equipped with an objective (*Nikkor*) of focal length 60 mm. The effect of the densities of seeding droplets on the laser induced plasma were also studied and a quantification of the effects of droplet densities on the laser-induced plasmas is presented in Section 7.2.5. As a consequence of droplet effects, a very high density of droplets could not be used for PIV technique.

Performing PIV in the presence of laser induced plasma was complex because of the high intensity of laser-induced plasmas, which could damage the PIV camera. Therefore, a liquid crystal shutter (Model No. LV4500P-OEM, *Micron Technology*) was used in front of the PIV camera to cut off the intensity of the plasma. The timing of the liquid crystal was adjusted so as to be open only for about 120 μs and it opened 200 μs before the plasma formation. Along with liquid crystal a band pass filter centered at 532 nm is also used in front of PIV camera to save the camera from infrared emissions of the plasma.

A photomultiplier (*Hamamatsu*) was attached to the setup to measure the duration of the flame kernel for cases where an initial kernel was generated

but the flame was not stabilized. The photomultiplier was coupled with an OH filter ($\lambda = 310 \pm 10$ nm) to measure hydroxyl emissions from the flame. Data was acquired from the photomultiplier at rates of 16384 samples per second through a data acquisition card (NI 2090, *National Instruments*). The measurements of the photomultiplier were separately controlled as it was easy to find the location of the sparks in the measurements.

The chronology of the measurements is presented in Fig. 3.3. It shows that the liquid crystal was switched on for small duration only to allow the measurement of velocity fields. Afterwards, the liquid crystal was switched off to save the PIV cameras from the intense laser-induced spark. The laser beam of pulse duration 6-7 ns created a spark with duration of the order of 10 μ s. The spark images and spectral measurements were acquired during the lifetime of the spark. The incident and transmitted energy of the laser beam was also measured but is not shown in the chronograph. Laser-induced sparks were created at 1 Hz and measurements were performed for each spark.

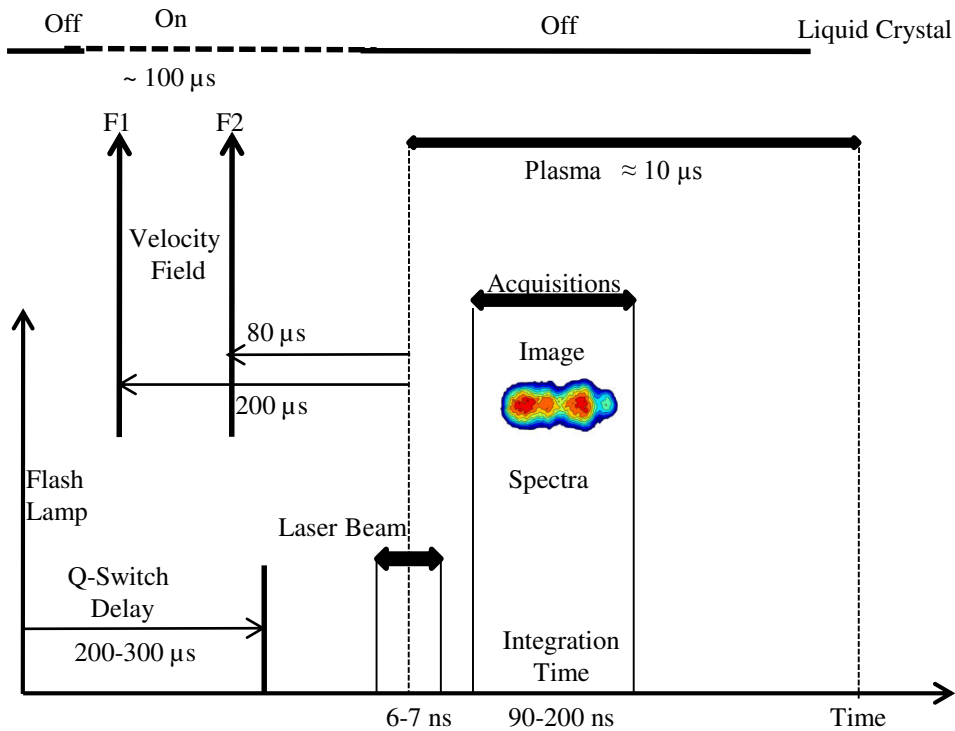


Figure 3.3: Chronology of the PIV measurements simultaneously with spectral and 2D-LIPS measurements

3.2 Turbulent two-phase burner

In order to understand ignition process, an existing two-phase, turbulent flow burner was used. The experimental burner was designed to keep high similarities with an industrial burner. In order to get closer to two-phase flow physics, experiments were performed in a multi-injection, two stage, system using liquid fuel (dodecane). Dodecane was chosen because of its thermodynamic and chemical properties being close to that of kerosene; the fuel generally used in aeronautical combustion chambers.

The experimental injector was composed of two stages: the Pilot stage and the Takeoff stage. In each stage, air was injected through a swirl to provide a rotational movement to the flow and to ensure a better mixing. A schematic view and a picture of the injection system is shown in Fig. 3.4.

A schematic view of the Pilot stage is shown in Fig. 3.5. Dodecane was introduced in the Pilot stage via a pressurized nozzle (IJ 6390-0-03, *Micro Mecanique Pyreneenne*) having a flow number, $F_n = 1.41 \text{ l.h}^{-1} \cdot \text{bar}^{-1/2}$. The position of the nozzle was chosen to limit droplet impact on the conical lip at the exit of the Pilot stage. The maximum angle of the nozzle did not exceed 50° . Air was injected through a swirler composed of 18 equally spaced vanes, 6 mm wide each and inclined at an angle of 42° . The inner and outer diameters of the swirl were respectively 30 mm and 45 mm and its geometry ensured the injection of 13 % of the global air flow rate through this Pilot stage. The rest of the air, *i.e.* 87 %, was injected through the Takeoff stage. It should be noted that the distribution of air among Pilot and Takeoff stages could not be externally controlled, and was decided during the design stage of the injector.

In the Takeoff stage, air was injected through a swirler composed of 20 equally spaced vanes, 10 mm wide and inclined at an angle of 34° . The inner and outer diameters of the swirl were respectively 55 mm and 75 mm.

The injection system was placed in a rectangular combustion chamber with

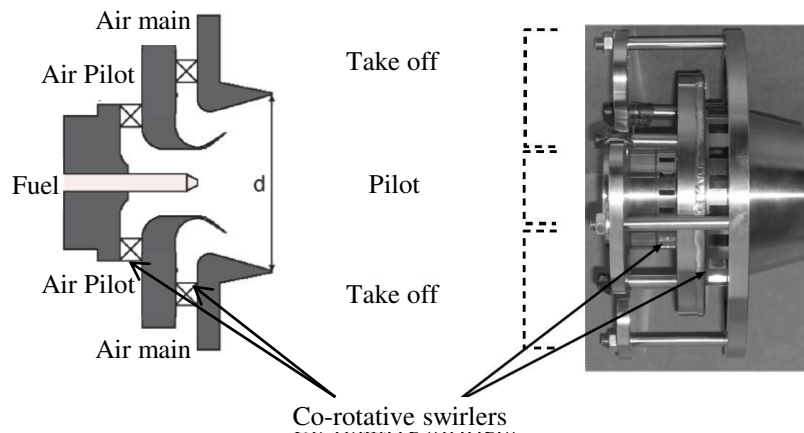


Figure 3.4: Schematic and image of the injector.

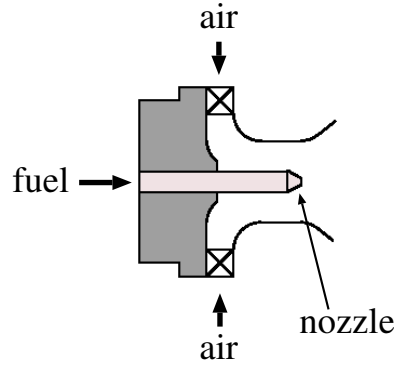


Figure 3.5: Schematic of Pilot stage of injector system

square cross section *i.e.* $500 \times 150 \times 150$ mm. It was composed of two silica walls for optical access and two water cooled walls. A schematic view and a photograph of the injection device coupled to the chamber is given in Figure 3.6. The metallic walls also had a small rectangular silica window to allow entrance and exit of laser sheet and beam.

The air flow rate was controlled using an electronic mass flow meter coupled to a controller (F-206-BI-FAD-00-V, *Bronkhorst High tech*), precision of ± 1 of the full range ($300 \text{ nm}^3 \cdot \text{h}^{-1}$). A manual control system (LM326, *Bronkhorst High tech*) was used to fix the flow rates. Before entering the plenum, the air was heated to 473 K using a preheater (*OSRAM Sylvania, Sureheat*, Max control 18 kW). For the Pilot stage, high pressure was needed to achieve high fuel flow rates. Thus, fuel was stored in a tank pressurized at 2.5 MPa with Helium as pressure source. Fuel flow rate was controlled by an electronic mass flow meter (M14-AAD-33-0, *cori-flow, Bronkhorst High tech*, full range 20 kg/hr of kerosene) coupled to the controller. Fuel flow rate was fixed manually using the same manual controller as air.

For current experiments, constant air flow of 10 g/s and fuel flow rate of 0.46 g/s were used, resulting in a constant global equivalence ratio of 0.7. These flow conditions resulted in a burner power of about 20 kW. As the fuel supply was cut off soon after ignition, the cooling of burner and injector walls was not required.

Burner and injector system were fixed to the ground. The spark creation system, other laser systems and measurement techniques were fixed on a table (TPP 1/2, *AXMO precision*) which allowed independent movement along three perpendicular axes. This allowed changing the location of the spark inside the burner while performing simultaneous measurements. This also facilitated non-reactive flow measurements at various locations inside the burner.

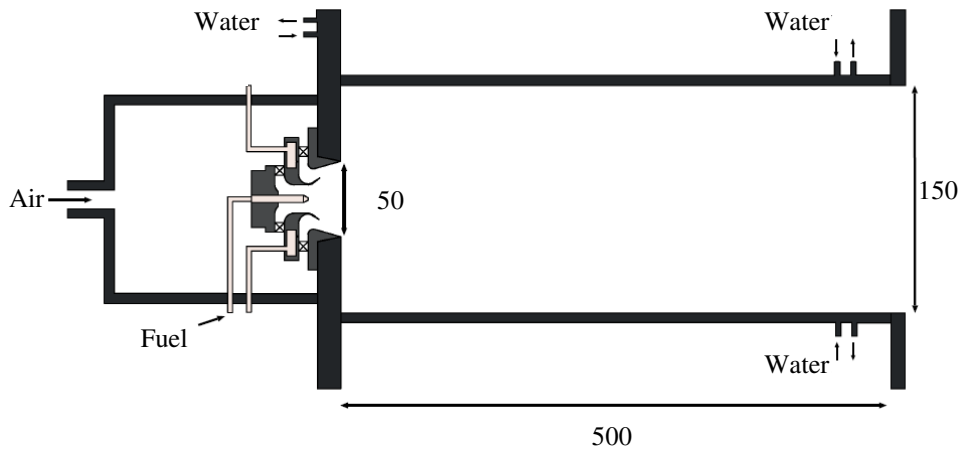


Figure 3.6: *Schematic and image of the chamber.*

3.2.1 Measurement techniques

Measurement of various physical parameters was performed inside the burner. Some of the measurements were performed for characterization of the burner, e.g. droplets' size measurements, velocity fields measurements in axial and transverse planes. There were many other measurements which were simultaneously performed during ignition experiments, e.g. axial PIV measurements, He-Ne laser diffraction intensity measurements, LIPS, 2D-LIPS, and chemiluminescence as shown in Fig. 3.7.

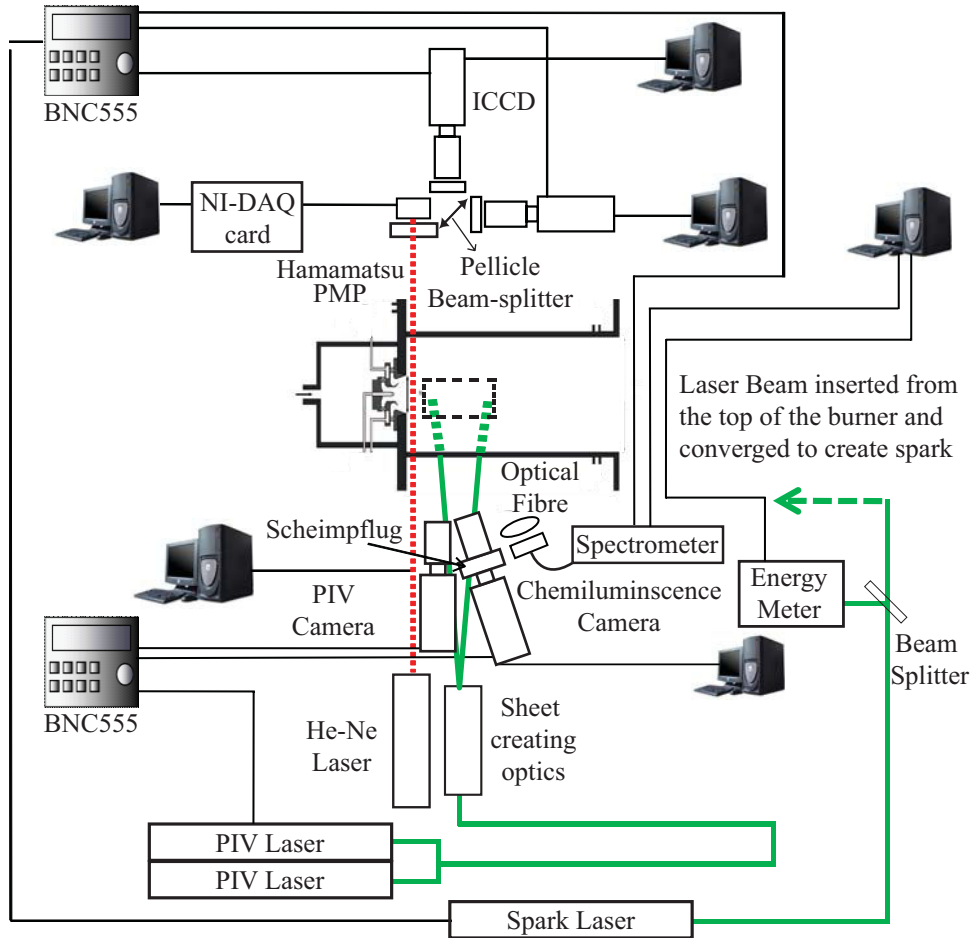


Figure 3.7: *Experimental setup for ignition experiments in two-phase, turbulent conditions.*

3.2.1.1 Droplet size measurements

The measurement of droplet size in the current setup had already been performed and the results have been presented in [Providakis \(2013\)](#) and [Providakis et al. \(2012\)](#). In this study, a *Dantec* dual-beam PDA system was installed to measure the local distribution of droplet diameters and two velocity components. The system was composed of a 5 W Ar⁺ laser with two lines respectively at 488 nm and 514 nm combined with a 40 MHz Bragg cell for frequency shift. In order to measure the size of the particles, three photo detectors were used and positioned at different distances from the probe volume. This resulted in a phase shift between the three collected signals from which the size of individual droplets was calculated.

3.2.1.2 Mie-scattering and Velocity field measurements

In the experimental setup for axial High Speed Particle Image Velocimetry (HSPIV) measurements, the laser sheet was generated by a system consisting of two Nd:YAG lasers (*Condor PIV, Quantronix*). Both lasers emitted pulses at a wavelength of 532 nm with a pulse energy of 5 mJ, a temporal width of 120 ns and at a frequency of 10 kHz. An optical system (Custom made by *Melles Griot*) was used to convert the laser beam into a planar light sheet 100 mm wide and 1 mm thick. The laser sheet was inserted from the bottom of the combustion chamber after reflection from a mirror. For the axial measurements, two small rectangular quartz (100 mm long and 15 mm wide) were designed and placed in the upper and lower walls of the combustion chamber allowing the laser sheet to cross the chamber in its axial center direction. A schematic of the PIV setup is shown in Figure 3.8.

No seeding particles were required for the measurement of velocity fields in this study of ignition. The fuel droplets could directly be used as tracers. A camera collected the Mie-scattering signal from individual droplets lying in the laser sheet. It was assumed that, at the exit of the injection system as droplets were not too large, droplet flow could be used as a close representative of the aerodynamic flow.

A fast speed camera (*Photron Fastcam*, 1024×1024 pixels at a rate of 6000 frames per second) equipped with a 105 mm, F/2.8 *Nikon Nikkor* objective was used to acquire the resulting images. The two lasers worked at half of

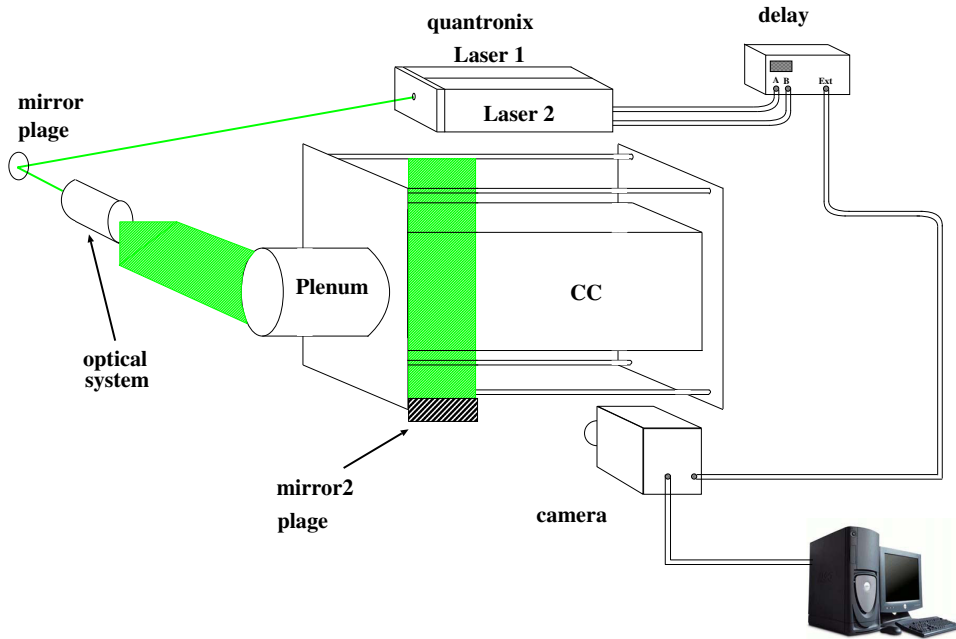


Figure 3.8: Schematic of HSPIV setup.

the camera's acquisition frequency, and were synchronized by a pulse delay generator (BNC 555 pulse/delay Generator, *Berkeley Nucleonics*). Images of 448×776 pixels were acquired at a rate of 20 kHz, corresponding to an actual field of view of about 68×118 mm. Thus the resolution of the images was about $150 \mu\text{m}$ per pixel. In each run 32,932 images were acquired comprising a duration of 1.6466 seconds.

The acquisition by the camera was controlled by the use of a BNC Pulse/Delay generator. The camera was continuously capturing the images but it stored images when the command to stop the acquisition was given. If the command to stop the acquisition was given at t_f , then the images corresponding to the time duration $[t_f - 1.6466: t_f]$ could be stored.

PIV measurements were also performed in non-reactive conditions using ZrO_2 as seeding particles. The size of the particles was of the order to 2-3 μm . Measurements were performed in both axial and few transverse planes to characterize the aerodynamic flow inside the burner. Transverse plane measurements were also similarly performed by capturing Mie-scattering from fuel droplets. For transverse plane measurements light sheet was inserted from the side of the burner, and its axial location was changed from 5 mm to 60 mm in steps of 5 mm using the translation table. The images of the scattered light were acquired after reflection from a mirror installed at the exit of the burner. This provided a quantification of droplet and aerodynamic flow in transverse planes as well.

3.2.1.3 Chemiluminescence

High speed chemiluminescence images were also acquired using a high speed camera (*Photron Fastcam*, 1024×1024 pixels at a rate of 10000 frames per second), equipped with an objective (*Nikkor*, 105 mm) with an aperture of 2.8. The chemiluminescence images were acquired with the high speed camera at an acquisition rate of 10 kHz and an exposure time of 100 μs . The high-speed camera was equipped with a Scheimpflug to acquire chemiluminescence images. The focal plane of the camera lied in the axial plane at the center of the burner. Integrated chemiluminescence measurements were also performed with a *Hamamatsu* photomultiplier equipped with an OH* filter ($\lambda = 310 \pm 10$ nm) at an acquisition rate of 16384 Hz. Measurements were recorded with a data acquisition card (NI BNC 2090, *National Instruments*).

3.2.1.4 Laser diffraction technique

The measurement of the frequency of the Precessing Vortex Core (PVC) was performed with the use of a small Helium-Neon laser (*Siemens* LGK 7627, 15 mW max power). The laser beam was inserted in the radial direction at the center of the burner, just at the exit of the injector (See Fig. 3.7). The transmitted beam was measured using a photomultiplier (H5784-04, *Hama-*

matsu) equipped with a band pass filter of wavelength 630 ± 10 nm (FB630-10, *Thorlabs*). The transmitted laser beam intensity was measured using the data acquisition card (NI BNC 2090, *National Instruments*). As the incident intensity of the laser beam remains constant, the transmitted intensity changes as a function of the amount of laser intensity diffracted by the fuel droplets along the path of the laser beam. This provided an integrated value of the surface of droplets, with increasing values in transmitted energy for decreasing overall surface area. Frequency domain analysis of the transmitted beam provided frequencies present in the droplet flow coming out of the injector.

3.2.2 Spark creation and measurements

Laser-induced spark was created by converging the second harmonic emission, i.e. 532 nm of an Nd:YAG laser (*Continuum Surelite*). The Q-switch settings of the laser were kept constant so as to have constant incident energy of the laser beam creating the spark. For laser ignition experiments at a fixed location, two plano convex lenses of focal lengths 150 mm and 100 mm were used to converge the laser beam at a distance of 40 mm from the top of the burner and 25 mm from the exit of the injector in the axial direction and in the center of the burner in the transverse direction. For laser ignition experiments at various locations inside the burner, the spark was created using a converging lens of focal length 150 mm. The lens was kept on a vertical rail to change the vertical location of the spark. Axial location of the spark was also changed by moving the table on which experimental setup was installed. The laser was controlled with another BNC 555 pulse and delay generator. The flash lamp was triggered at 10 Hz and the Q-switch was triggered at 3.33 Hz, creating sparks at 3.33 Hz.

3.2.2.1 Incident energy measurements

The incidence energy of the laser beam creating sparks was measured by reflecting a part of the incident laser beam using a 1 – 10 % beam sampler (BSF10, *Thorlabs*) on to a laser energy meter (PE25-SH, *Ophir Optronics*). The transmitted energy of the laser beam could not be measured due to optical access limitations.

3.2.2.2 Spectral measurements

Laser induced plasma spectroscopy (LIPS) was first performed using a compact Charge-Coupled Device (CCD) spectrometer (CCS-200, *Thorlabs*), having a spectral range of 200-1000 nm and a Full Width at Half Maximum (FWHM) spectral resolution of 2 nm. The optical fibre from *Thorlabs* (High OH, 0.22 numerical aperture, 200 μ m Core diameter) was placed at an angle of about 45° from the direction of the laser beam, and intensity from the laser-induced spark was converged onto the fibre using a convex lens of focal length 75 mm. This

compact spectrometer was used to measure spectral emissions from each laser induced spark. Measurements integrated over the whole duration of spark are acquired. In final experiments this spectrometer was replaced by spectrometer presented in Section 3.1 as it allowed time resolved measurements.

3.2.2.3 2D-LIPS measurements

Images of the plasma were simultaneously recorded with two Intensified Charge Coupled Device (ICCD) cameras (PI-MAX, *Princeton Instruments*) having same objectives, *UV-NIKKOR* 105 mm. Various band pass filters with FWHM (Full Width Half Maximum) of 10 nm and center wavelengths 780 nm (FB780-10, *Thorlabs*), 750 nm (FB750-10, *Thorlabs*), 660 nm (FB660-10, *Thorlabs*), and 760 nm (FB760-10, *Thorlabs*), were installed in front of the cameras. The filters were installed in a cage filter wheel so that they could be easily changed without disturbing the setup. The ICCD cameras used for imaging had a resolution of 512×512 pixels and were focussed at a typical field of view of 25×25 mm, thus giving a magnification of approximately 20 pixels/mm. The two ICCD cameras were installed at an angle of 90° to each other. A pellicle beam splitter (PBS-2C, *Newport corporation*), which provides 50-50 reflection transmission, was installed at 45° to both the cameras (See Fig. 3.7) in order to obtain plasma images in both the cameras. The ICCD cameras were operated in gated mode to allow very small (up to 2 ns) and precise integration times.

3.2.3 Data acquisition

Three delay generators were used to control the acquisition of measurements. The air flow was turned on along with the pre-heater and the preheater power was adjusted so as to reach a constant preheating temperature of 200°C . The flow of fuel inside the burner was started, and flow rates used to take about 30 seconds to stabilize. The flash lamp of the ignition laser was run at 10 Hz. The PIV laser was also turned on at the same time and PIV camera was also started in end mode at the same time. After a few seconds (in order to have constant laser incident energy), the Q-switch of the spark laser was also turned on, which started generation of sparks in the combustion chamber. As soon as successful ignition was achieved the PIV camera and Q-switch of the spark laser were stopped. The OH^* chemiluminescence and He-Ne transmitted energy measurements were also stopped.

The chronograph of data acquisition is shown in Figure 3.9. It shows the durations and rates of acquisition of different measurement techniques. Synchronization 1 corresponds to measurement of chemiluminescence images, which were acquired until successful ignition was achieved. Synchronization 2 corresponds to measurement of OH^* and He-Ne transmitted energy measurements which were independently acquired through the data acquisition card. Synchronization 3 shows PIV laser and PIV camera operation. Synchronization 4 gen-

eration of laser-induced plasma and LIPS and 2D-LIPS measurements. These four synchronizations were independently calibrated but all measurements were simultaneously performed.

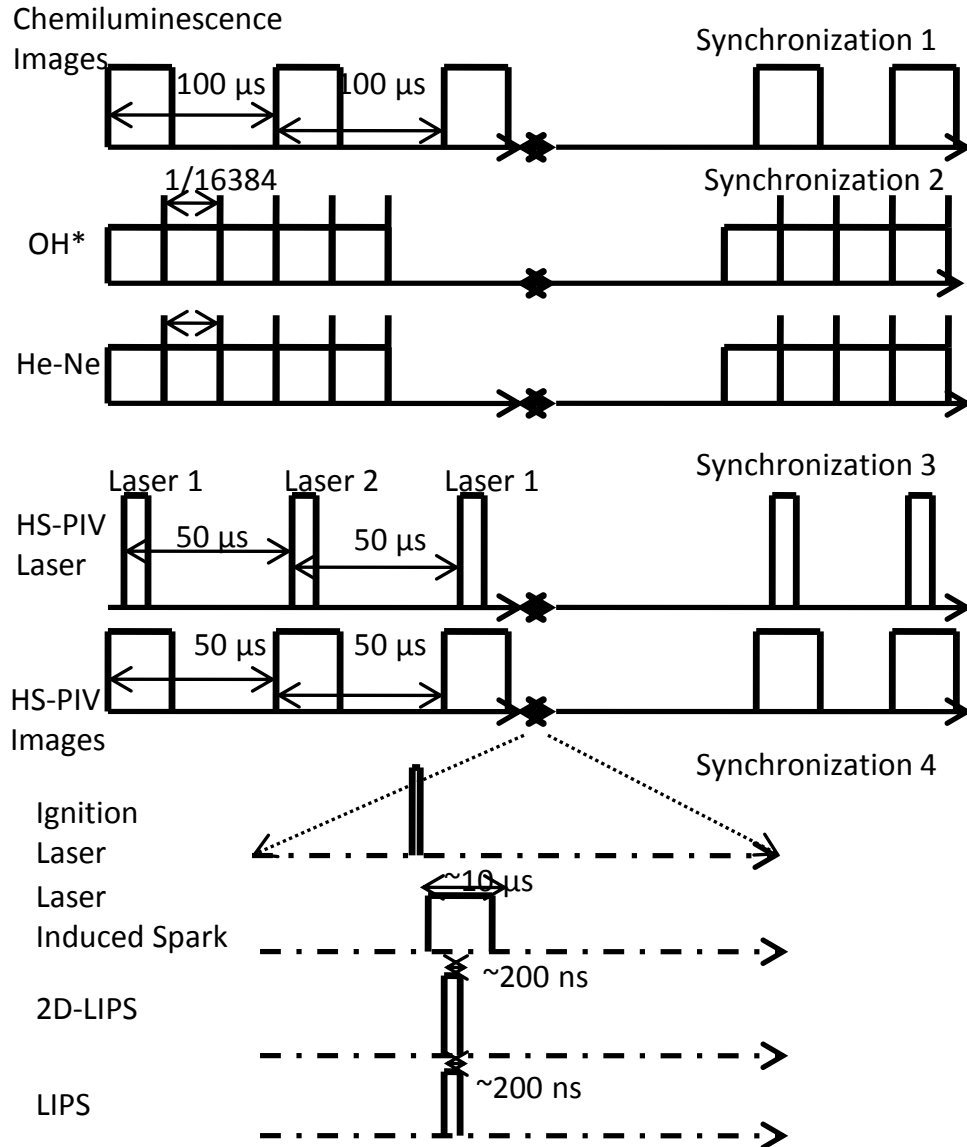


Figure 3.9: Chronograph showing acquisition times of the various techniques.

Chapter 4

Post-Processing Techniques

In this chapter, a brief summary of analytical methods used during the analysis of measurements is presented. Special attention is however put on the Dynamic Mode Decomposition, which is a new tool for treating time resolved data and for which many open questions are left.

4.1 Inverse Abel Transform

Abel transform is an integral transform often used in the analysis of spherically/axially symmetric functions. In image analysis, the reverse Abel transform is used to calculate the emission function given a projection (i.e. a scan or a photograph) of that emission function.

Inverse Abel transform of a projection F can be written as,

$$f(r) = -\frac{1}{\pi} \int_r^\infty \frac{dF}{dy} \frac{dy}{\sqrt{y^2 - r^2}} \quad (4.1)$$

The 2D-LIPS experiments performed during this thesis required acquisition of images, which were the projections of laser-induced plasmas on to the CCD. Abel transformation technique was used to obtain two-dimensional information from the image projection. This assumption is valid as long as the focal length of the objective is high enough to ensure that parallax is negligible. The errors for a focal length of 105 mm is relatively low (Zimmer and Tachibana (2007a)) and therefore an onion-peeling type of algorithm can be used (Dasch (1992)). Abel transformation was performed at each row of the image shown in Fig. 8.14. Each row was divided in to left and right parts by finding the local center for the chosen row. Abel transformation of left and right parts were separately performed using the formulation shown in Eqn. 4.1. Therefore, two dimensional intensity values were calculated in a plane.

4.2 Discrete Fourier Transform

Fourier transform is a unique way of describing any kind of signal as the sum of simple sinusoids of different frequencies. The principle of Fourier is that each temporal function $h(t)$ can be written in a generalized form as:

$$H(f) = \int_{m=-\infty}^{\infty} h(t) \exp(-j2\pi ft) dt \quad (4.2)$$

Inverse Fourier transform, which enables to retrieve real signals from functions in the Fourier space $H(f)$, can also be similarly written as:

$$h(t) = \int_{m=-\infty}^{\infty} H(f) \exp(j2\pi ft) df \quad (4.3)$$

where, j is the complex number, $j^2 = -1$.

In practical applications, the signals are not obtained on a continuous base but rather on a discrete one and for a limited duration of time, similar to the example shown in Fig. 4.1. Therefore, specific discrete Fourier transform techniques need to be applied to the measured data. The Discrete Fourier Transform (DFT) is a specific kind of discrete transform, used in Fourier analysis. The DFT requires an input function that is discrete as seen in Fig. 4.1. T is the sampling time, *i.e.* time difference between two consecutive measurements. Sampling frequency of measurements can also be written as $1/T$. In

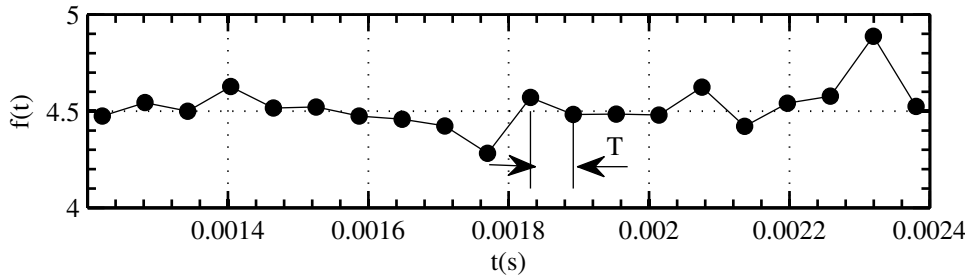


Figure 4.1: A discrete signal as a function of time.

case of periodic functions with a time period of N , discrete Fourier transform can be written as:

$$H(n) = \sum_{k=0}^{N-1} h(k) \exp(-j2\pi \frac{nk}{N}) \quad (4.4)$$

In order to correctly measure the frequency 'f' contained in a signal, the sampling frequency should be at least '2f'. Inversely it can also be said that with a sampling frequency 'F', frequencies that can be resolved from the signal are less than 'F/2'.

Fast Fourier transform (FFT) is a specific algorithm to compute the discrete Fourier transform (DFT) and its inverse for a number of samples equal to a power of two. There are many algorithms to calculate FFT, from simple complex-number arithmetic to group theory and number theory. During the course of this manuscript, FFT was calculated using MATLAB[®], which uses FFTW library developed at MIT by [Frigo and Johnson \(2005\)](#).

Power spectral density (PSD) is an alternate way of viewing frequency content of a signal. PSD is a positive real function of a frequency variable associated with a stationary stochastic process, or a deterministic function of time. It provides power carried by a wave as a function of frequency. DFT/FFT can be used to calculate PSD, in which case it is the square of the Fourier transform. A commonly used method to calculate PSD of a discrete function is Welch's technique. Welch's method splits the data into overlapping segments, computes modified periodograms of the overlapping segments, and averages the resulting periodograms to produce the power spectral density estimate. This is required for reducing the effects of noise and integration limits. In practice, a windowing function (like a Hanning type) is used so that each sample is actually taken one time.

DFT is widely employed in signal processing and related fields to analyze the frequencies contained in a sampled signal. During current experiments, DFT was extensively used to extract frequency information from the flow measurements. Analysis of pressure measurements provided dominant frequencies present in the combustor and variation in these frequencies with ignition or combustion. Analysis of He-Ne measurements provided frequencies of the precessing vortex core which were dominantly present in flow of droplets. Temporal evolution of these PVC frequencies could also be obtained by further analysis. Mie-scattering images obtained by droplets as well as tracer particles were also analyzed to provide frequency information at different locations in the image plane. Velocity fields calculated using Mie-scattering images were also subjected to frequency domain analysis.

It is known however that to properly evaluate the energy contained in a signal, an average estimate is performed on several realizations. This comes from the fact that the discrete Fourier based approach, to be perfectly correct, requires that the last sample and the first one have identical values. Furthermore, it is known that the frequency resolution (δ_f) is a direct consequence of the sampling frequency (F_s) and the number of points used (N_s). Those quantities are linked through the following relation

$$\delta_f = \frac{F_s}{N_s} \quad (4.5)$$

Thus, even for short term analysis, the accuracy in the frequency is limited by this constraint. Therefore, for a signal sampled at 10 kHz and if one wants to treat only 100 samples, the accuracy in frequency would be at most 100 Hz

without any overlapping and averaging. Hence, any DFT based approach for very short term analysis would not provide a quantitative information on the temporal evolution of the system.

4.3 Wavelet Transform

A continuous wavelet transform (CWT) is used to divide a continuous-time function into wavelets. Unlike Fourier transform, the continuous wavelet transform possesses the ability to construct a time-frequency representation of a signal that offers very good time and frequency localization. In mathematics, the continuous wavelet transform of a continuous, square-integrable function $f(t)$ at a scale $a > 0$ and translational value $b \in \mathbb{R}$ is expressed by the following integral,

$$X_w(a, b) = \frac{1}{\sqrt{|a|}} \int_{-\infty}^{\infty} f(t) \Psi^*\left(\frac{t-b}{a}\right) dt \quad (4.6)$$

where $\Psi(t)$ is a continuous function in both the time domain and the frequency domain called the mother wavelet and $*$ represents operation of complex conjugate. The main purpose of the mother wavelet is to provide a source function to generate the daughter wavelets which are simply the translated and scaled versions of the mother wavelet. The wavelet function $\Psi(t)$ and the scaling function $\varphi(t)$ define a wavelet. The scaling function is primarily responsible for improving the coverage of the wavelet spectrum. This could be difficult since time is inversely proportional to frequency. In other words, if we want to double the spectrum coverage of the wavelet in the time domain, we would have to sacrifice half of the bandwidth in the frequency domain.

First part of CWT analysis requires identification of a mother wavelet. Choice of mother wavelet depends on the frequency values and frequency resolution required. For the identification of mother wavelet, a synthetic signal was created with frequencies closer to those present in the signal to be analyzed. On the basis of previous experiments and DFT of signals in current experiments, a PVC frequency in the range of 500-500 Hz was observed. Therefore the synthetic signal was formed using sinusoids with different frequencies in this range. The amplitude of sinusoids for different frequencies was also changed. Different wavelets available in the Wavelet ToolboxTM of *MATLAB*[®] were used and compared for their capability to resolve changes in frequency in the synthetic signal. The typical mother function of those wavelets is displayed in Figure 4.2. The frequency in the synthetic signal was changed from one value to another in the following sequence: 500-540-520-495-510-535 Hz. Different mother wavelets were attempted to analyze the synthetic signal. Results from four of the mother wavelets are shown in Fig. 4.3. It was observed that for the given frequency range and sampling frequency, Complex Morlet wavelets provide more accurate

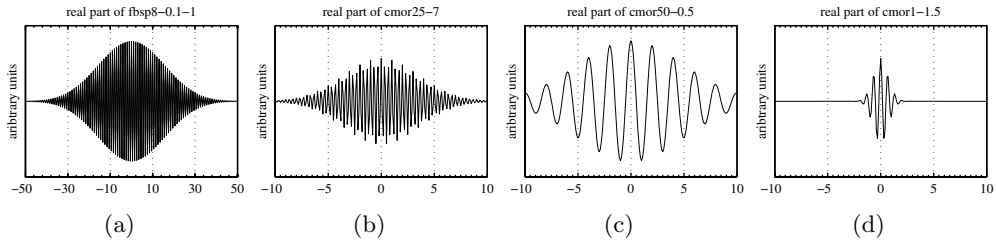


Figure 4.2: Typical mother wavelet for Frequency-B Spline (a), Complex Morlet 1-1.5 (b), Complex Morlet 50-0.5 (c) and Complex Morlet 25-7 (d).

results. Wavelets are generally defined by two parameters; a positive bandwidth parameter and a center frequency parameter. *e.g.* cmor25-7 represents a complex morlet wavelet with a bandwidth of 25 and a center frequency of 7 Hz. Fig. 4.3 shows results from one Frequency B-Spline (fbsp) Complex wavelet and three morlet wavelets.

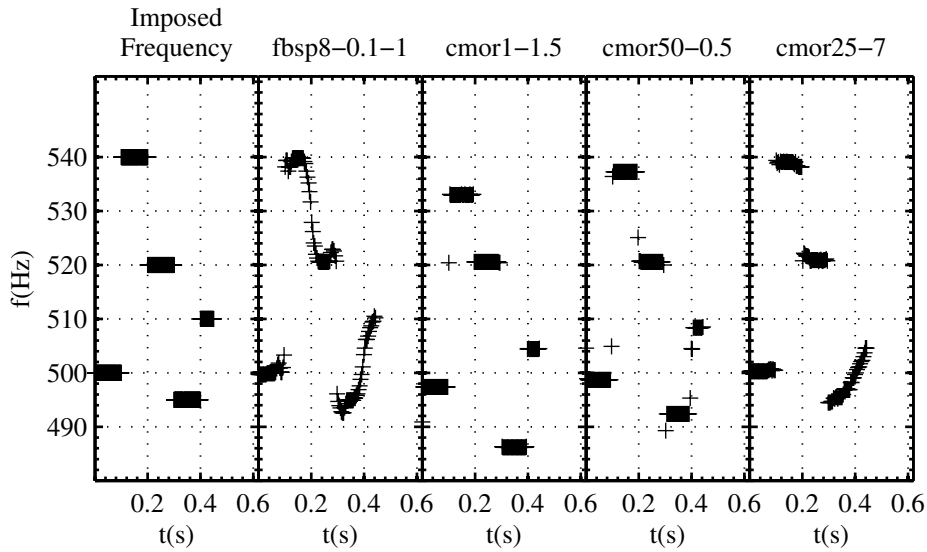


Figure 4.3: Results of Continuous Wavelet Transform (CWT) analysis of a synthetic signal.

It can be seen that the fbsp wavelet does not respond very well to abrupt frequency change. All morlet wavelets respond well to frequency change. But the predicted frequency values are not correct for wavelet with bandwidth of 1 and central frequency of 1.5Hz (cmor1-1.5). Both cmor50-0.5 and cmor25-7 calculate correct frequency values. cmor25-7 was chosen for the analysis of He-Ne transmission intensity measurements.

4.4 Dynamic Mode Decomposition

Whereas in both Fourier transform and Wavelet decomposition, the base on which the data are projected is defined, the dynamic mode decomposition (DMD) is a mathematical method to extract the relevant modes from time-resolved data without imposing the projection base. This is similar to the Proper Orthogonal Decomposition (POD, see [Berkooz et al. \(1993\)](#)) but with a major difference that is now addressed. Both decomposition tools are based on the concept of decomposing a matrix containing all the realizations into three matrices representing respectively the modes, the amplitudes and temporal evolution (see [Fig. 4.4](#)).

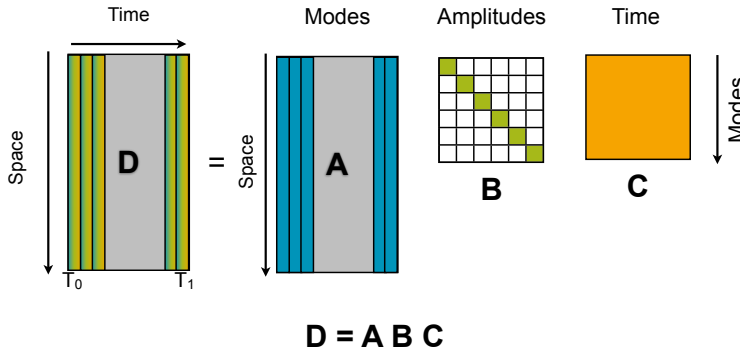


Figure 4.4: *Decomposing a matrix D containing all data into three matrices representing respectively the modes, the amplitudes and temporal evolution.*

To obtain a POD representation of the data, the constraint is put on the modes that have to be uncorrelated (orthogonal to each others). Amplitudes can then also be linked to an energy and if time-resolved data are used, a Fourier transform can be applied to the data to extract the dynamics. It is however known that this approach leads to a multiple frequency content for each mode and that typical structures such as Precessing Vortex Core (PVC) require two POD modes to be correctly represented ([Stöhr et al. \(2012\)](#)).

DMD was performed using a QR decomposition algorithm [Schmid \(2010\)](#). During current experiments, DMD was used to extract the PVC mode from Mie-scattering images and velocity vectors. Temporal as well as spatial evolution of the PVC was studied. One advantage of DMD versus a Fourier based approach is that there is no periodicity required and that the frequency base is not pre-fixed. Indeed, even though the mean frequency resolution has similar constraints as the DFT based approach (see [equation 4.5](#)), the local resolution may change and adapt itself to the real dynamics of the system if one studies the signal without subtracting the mean. More details about this processing technique and the way to apply to combustion diagnostics may be found in [Richecoeur et al. \(2012\)](#)

Chapter 5

Flow characteristics inside burner

This chapter presents the characterization of the two-phase flow burner used for ignition experiments. In order to discuss the process of ignition, it is necessary to understand the flow inside the chamber. Therefore flow field measurements were performed in both axial and transverse planes inside the chamber. For all the measurements as well as ignition experiments, the overall flow rates of air and dodecane inside the burner were kept constant at an air flow rate of 10 g/s and a global equivalence ratio of 0.7. For aerodynamic flow measurements only air at 10 g/s was inserted.

5.1 Aerodynamic flow measurements

The air flow inside the burner was measured by performing time-resolved PIV in the burner. The objective of air flow measurements was to characterize the air flow inside the burner, in the absence of fuel droplets. Presence of fuel droplets inside the burner can affect the flow inside the burner. It is not possible to study the velocity fields of air flow inside the burner when droplets are present. Therefore, it was necessary to study air flow and droplets' flow separately. For aerodynamic measurements, small solid particles (ZrO_2) of diameters 2-3 μm were used as tracers. Measurements were performed in both axial and transverse planes.

Mean and fluctuations of Mie-scattering images in an axial plane at the center of the burner, are shown in Fig. 5.1. Mean of the images is plotted over 10000 images acquired at 10 kHz. Fluctuations are plotted by calculating the standard deviation of Mie-scattering intensity values over the same number of images. Fluctuations of the Mie-scattering intensity depicts the main region of the flow coming out of the injector.

Pair of instantaneous Mie-scattering image frames were used to calculate the aerodynamic velocity fields in the axial plane at the center of the burner. As a

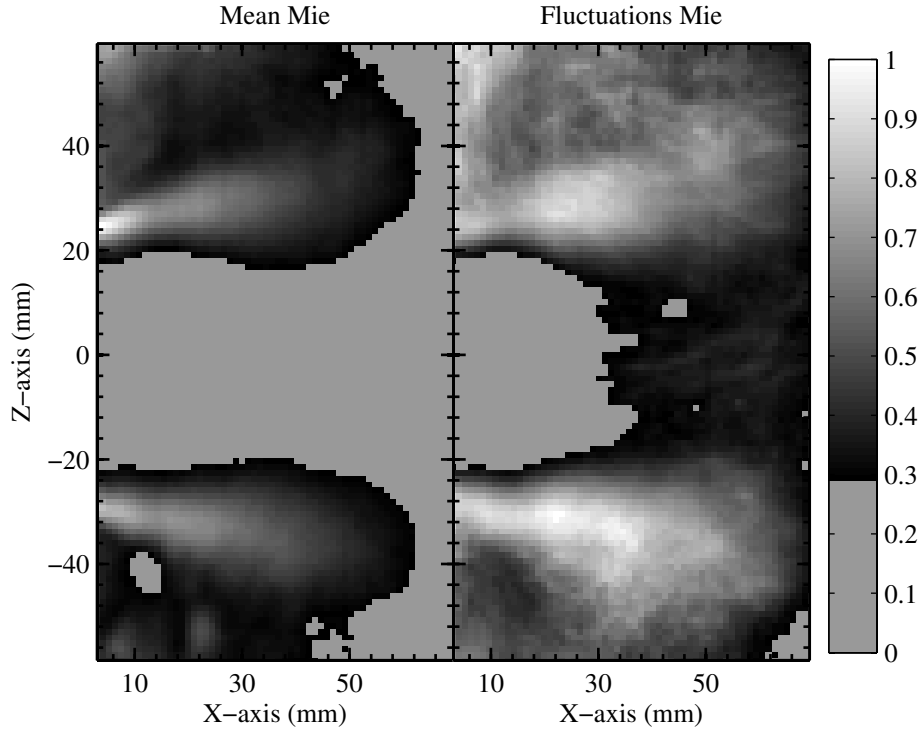


Figure 5.1: Mean and fluctuations of Mie-scattering intensity in an axial plane, averaged over 1 s, i.e. 10000 image frames.

result of 10 kHz image acquisition, time difference between two consecutive images used for velocity field calculations was 100 μ s. Aerodynamic measurements were performed in this axial plane because later ignition experiments were performed by moving the location of the spark in the same vertical plane located at the center of burner. Velocity fields were calculated from the image frame pairs using Dynamic studio (Dantec Dynamics). Image correlation between the images were calculated for an initial interrogation region of 256×256 pixels and a final interrogation region of size 32×32 pixels. A peak height validation of 1.2 and a median filtering of size 3×3 allowing a maximum variation of 0.3. Mean of velocity field components over 1 s are shown in Fig. 5.2. Maximum axial velocities of the order of 11 m/s and radial velocities of the order to 3 m/s were observed. Fig. 5.3(a) shows velocity vector field inside the burner and fig. 5.3(b) shows corresponding streamlines.

The accuracy of the velocity field measurements can be measured in terms of the number of validated vectors during velocity field calculations. A validated velocity vector means that the velocity vector was calculated by correlation of interrogation areas with peak ratio of at least 1.2. Percentage of valid velocity vectors at each location inside the burner are shown in Fig. 5.4(a). Percentage

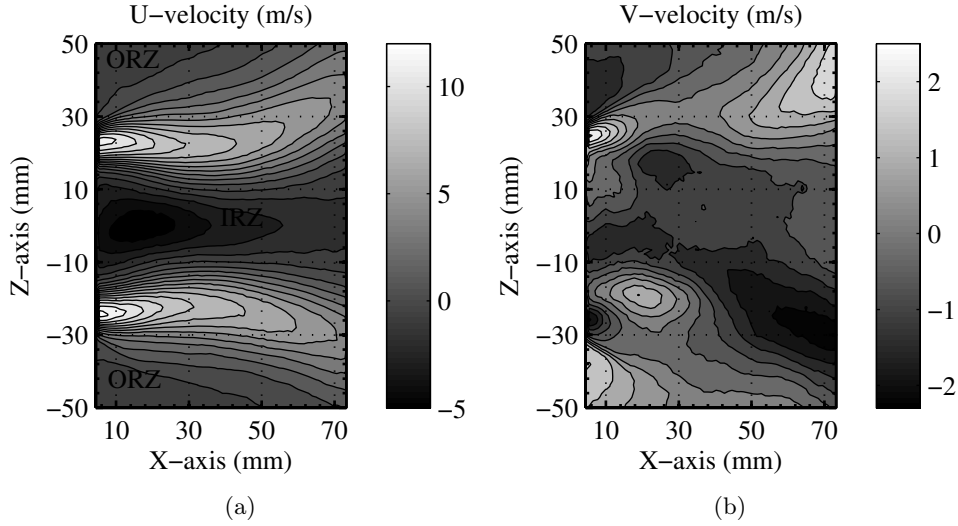


Figure 5.2: Mean axial (a) and vertical (b) components of aerodynamic velocity fields, mean calculated over 10000 velocity fields (1 s).

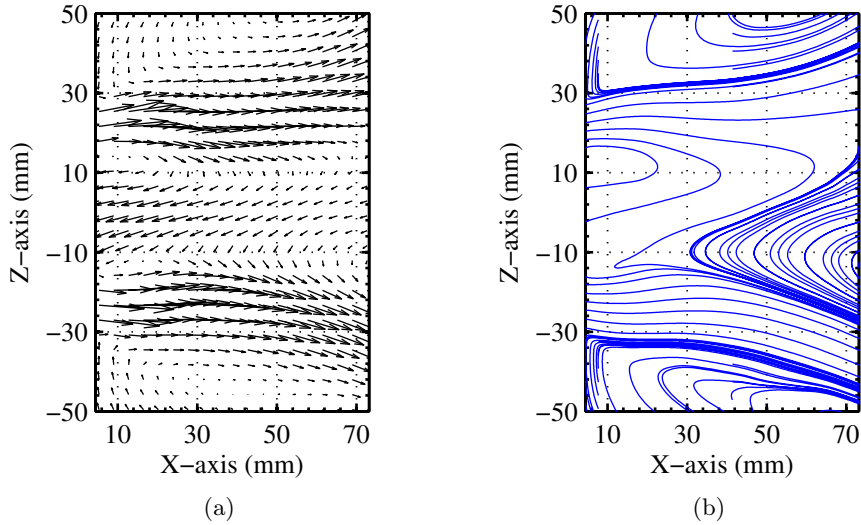


Figure 5.3: Velocity vectors (a) and streamlines (b), representing the mean aerodynamic flow inside the burner, mean calculated over 10000 velocity fields (1 s).

of validated vectors in the primary flow region was of the order of 50-70%, while it was very close to 100% in the region outside the primary flow coming out of the injector. The mean peak 1-to-peak 2 ratio is plotted in Fig. 5.4(b). In the primary flow zone, the mean peak ratio values were of the order of 2-3 and of the order to 4-5 in the other regions. This means that the velocity calculations are generally very accurate in the whole axial plane.

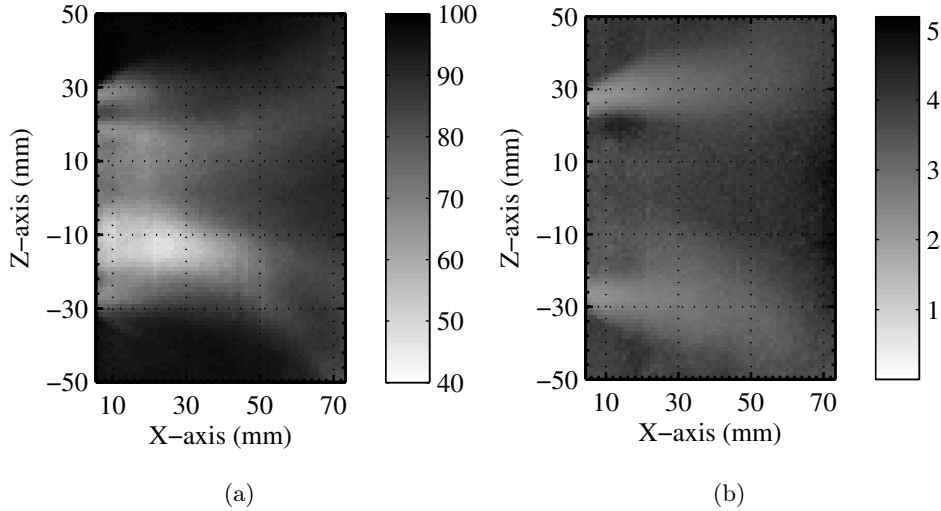


Figure 5.4: (a) Percentage of validated vectors for velocity field measurements in axial plane.; (b) Mean of peak ratios during velocity field calculations.

In axial velocity field (Fig. 5.2(a)), around the center of the burner smaller magnitudes of negative axial velocities were also observed. These negative axial velocities corresponded to internal recirculation zone (IRZ).

Transverse field measurements were also performed inside the burner at axial distances from 5 mm up to 60 mm in steps of 5 mm. Images of Mie-scattering by small seeding particles were acquired at an acquisition rate of 20 kHz. Mean and fluctuations of Mie-scattering images in a transverse plane at an axial distance of 25 mm are shown in Fig. 5.5. Mie-scattering images show the injector in the background, which remained constant in all the images.

The correlation of instantaneous images was performed using Dynamic Studio (*Dantec Dynamics*) and using the same correlation parameters as axial velocity field calculations. The time difference between two subsequent images was 50 μ s. Mean values of two velocity components in transverse planes are shown in Fig. 5.6.

In order to better visualize the flow field in transverse planes, the azimuthal and radial components of the velocity fields were calculated. Mean radial and azimuthal components of velocity fields at various axial distance from the injector are shown in Fig. 5.7 and Fig. 5.8, respectively. Mean values were calculated using only the validated velocity vectors.

Fig. 5.7 shows negative values of radial velocity components at radial distances of 12 to 20 mm which are high specially for axial distances of 15 to 25 mm. This denotes presence of strong inner recirculation zone at these axial locations. The outward radial velocities at radial locations greater than 20 mm had positive values. The values of these outward radial velocities decreased from 2 m/s at

axial location of 5 mm to 1 m/s at radial locations of 20 mm and then increased again to reach 2 m/s at axial location of 45 mm.

Fig. 5.8 shows that the azimuthal components of velocity fields increase with increase in axial distance, reaches a maximum around 20 mm, and then gradually decreases. Azimuthal velocity components increase from 4 m/s at axial location of 5 mm to 7 m/s at axial location of 20 mm and then decrease to 6 m/s at axial location of 45 mm. Axial locations having strong azimuthal velocities coincide with axial locations having strong radial velocities. The negative values of azimuthal velocity correspond to clockwise movement of the flow.

The accuracy of aerodynamic flow measurements in transverse planes can also be measured in terms of number percentage of validated vectors at each location in a transverse plane and the value of peak ratios in the correlation map used for calculating velocity fields. These parameters for transverse plane at an axial location of 25 mm is shown in Fig. 5.9.

The number of validated vectors are high all over in the transverse plane except along the circumference, where there are some discontinuities along a ring at an axial distance of approximately 25 mm. This ring corresponds to the edge of the injector as can also be seen in Fig. 5.5. Mean peak ratio values are also lower along this ring as can be seen in Fig. 5.9(b). Therefore, it could be concluded that velocity calculations are accurate except at radial locations of the edge of the injector, which interferes with the Mie-scattering images and there by with velocity calculations as well.

Histogram of the horizontal velocity components values in a transverse plane at an axial location of 25 mm is shown in Fig. 5.10. Histogram is plotted at a location along the vertical axis, where the magnitude of velocity was high. It shows that velocity magnitude fluctuates significantly as a very sharp peak

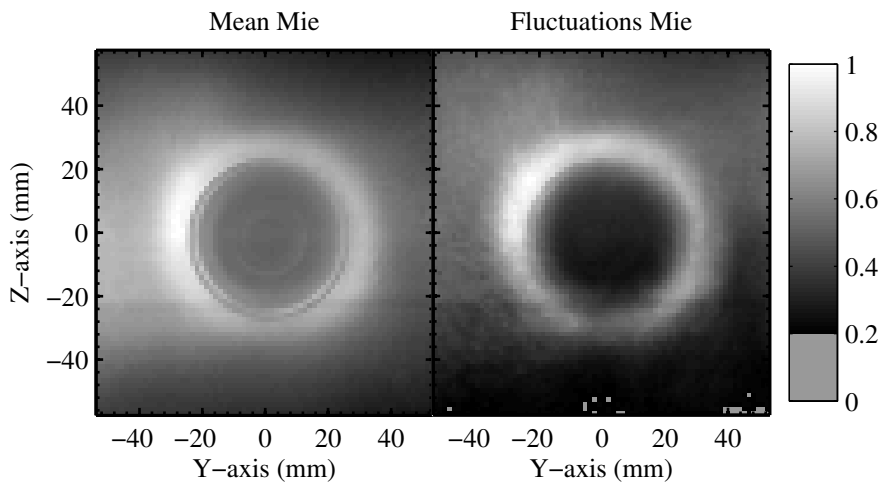


Figure 5.5: Mean and fluctuations (over 0.5 s) of Mie-scattering intensity in a transverse plane at an axial distance of 25 mm.

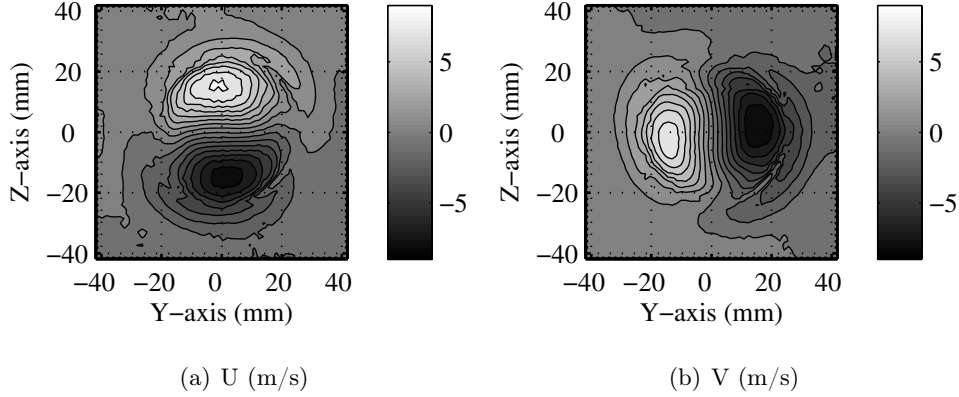


Figure 5.6: Mean U (axial) and V (vertical) components in transverse planes at an axial distance of 25 mm, Mean calculated over 10000 velocity fields (0.5 s).

is not present in the histogram. These fluctuations could be because of some inherent modes present in the flow and therefore, frequency domain analysis was necessary to understand these fluctuations.

The frequency domain analysis of the aerodynamic flow was also performed using Welch's technique (Section 4.2). Spectral analysis of Mie-scattering images acquired in axial as well as transverse planes was performed. It was attempted to look for dominant frequencies at all locations in the axial plane. It has been shown in previous experiments using the same burner (Providakis (2013)) that the flow inside the burner was dominated by the Precessing Vortex Core (PVC), which is a characteristic of the strongly swirled flows. The frequency of the PVC for the current flow conditions was measured to be of the order to 500-550 Hz. Analysis of Mie-scattering images showed frequencies corresponding to PVC but were not very dominant throughout the axial as well as transverse planes.

Similarly, frequency domain analysis of velocity fields was also performed. Axial planes of aerodynamic flow velocities did not show any particularly dominant frequencies. It was attempted to find the frequency of PVC in the axial plane, which was present near the injector exit but was not very well resolved. Analysis of velocity field components in transverse planes also did not show any particularly dominant frequencies. The PVC frequency was observed at some locations but even that was not very strong.

5.2 Droplets' size measurements

The characterization of the droplets coming out of the given injector, for different flow conditions has already been performed by using Phase Doppler Anemometry (PDA) (Providakis et al. (2011); Providakis (2013)). For the

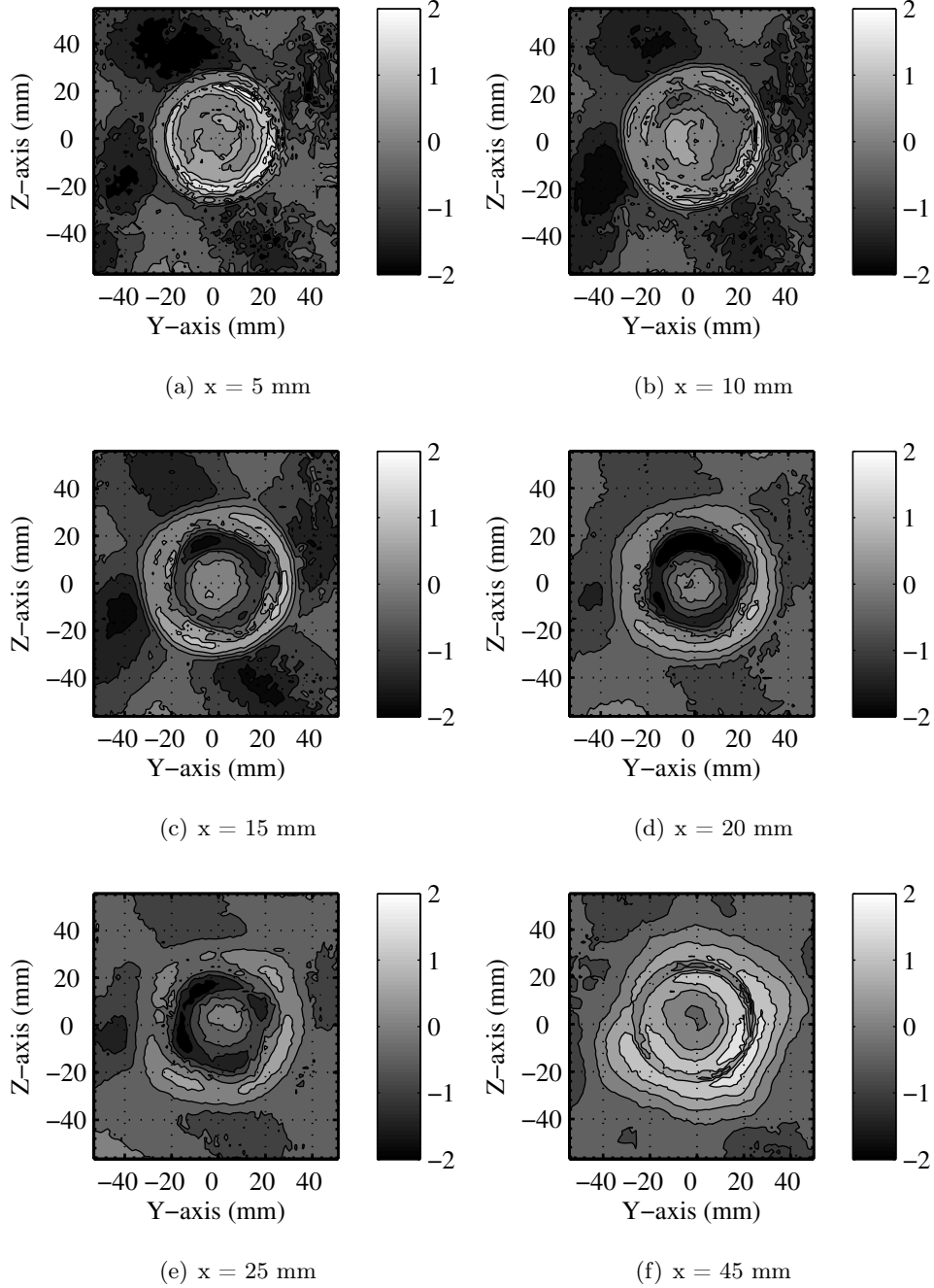


Figure 5.7: Radial velocity fields for different axial locations inside the burner.

flow conditions used during ignition experiments, the measurement of droplet sizes at different axial and radial (z -axis) positions were performed. Axial locations were chosen from 5 mm from the exit of the injector up to 60 mm in

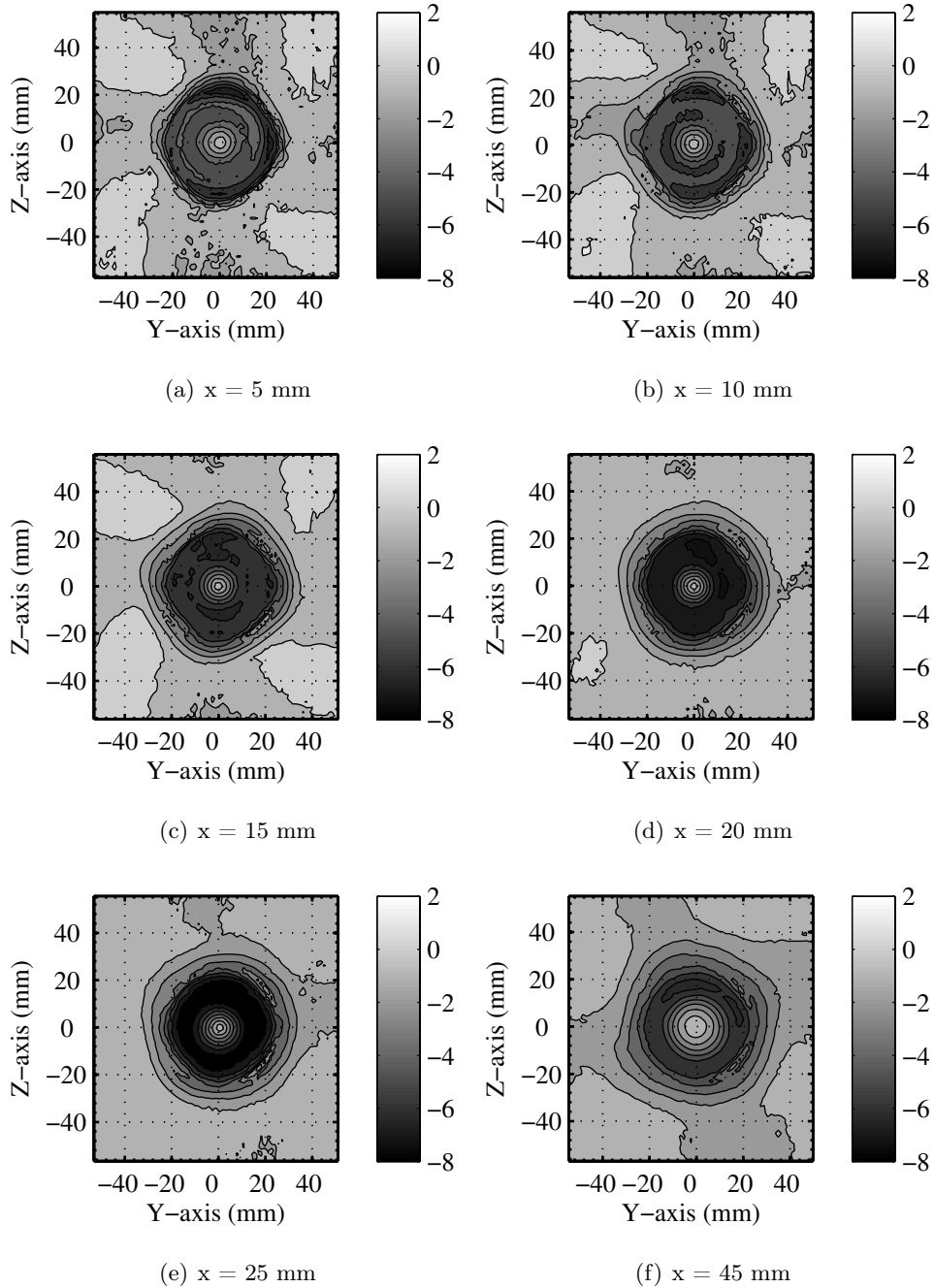


Figure 5.8: Azimuthal velocity fields for different axial locations inside the burner.

steps of 5 mm. Measurements were performed at a y-location of 15 mm. An axis symmetric distribution of droplets could be assumed. At the selected y-location, the measurement point was changed from $z = 0$ mm up to the point

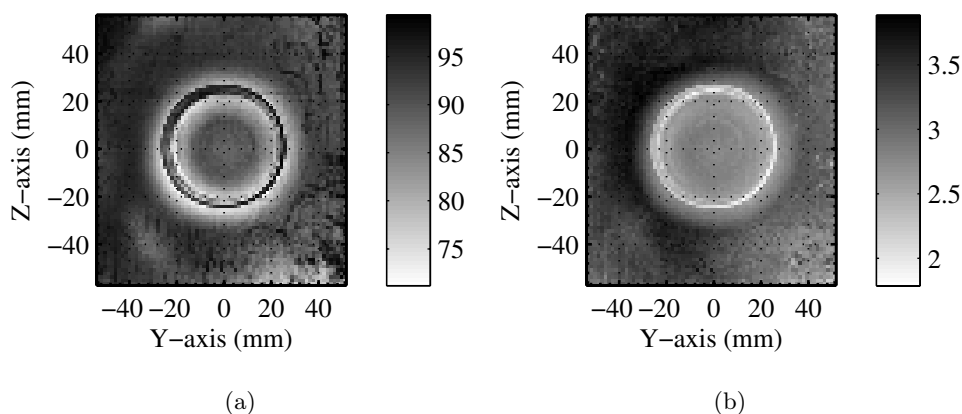


Figure 5.9: (a) Percentage of validated vectors for velocity field measurements in a transverse plane at an axial location of 25 mm.; (b) Mean of peak ratios during velocity field calculations for the transverse plane

where droplets were present. Measurements were repeated at each axial location. Data acquisition was performed for 100% dodecane through the pilot stage and a constant preheating temperature of 200 °C.

Fig. 5.11 shows histograms of droplet sizes for a few axial as a function of radial distance of the measurement point from the center of the burner. For 5 mm axial location, diameter values corresponding to peaks in histograms change from 17.5 μm for $r = 0$ up to 23.5 μm for $z = 10$ mm. Broadening of the peak with increase in vertical/radial distance represents presence of droplets of more diverse sizes. With increase in axial distance, diameter of the spray cone

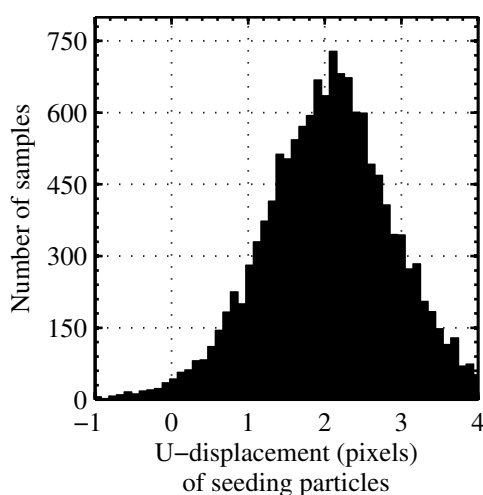


Figure 5.10: Histogram of horizontal velocity component at $y = 0$ mm and $z = 12$ mm for a transverse plane at an axial distance of 25 mm.

increases and therefore droplets are present up to higher radial distance.

The size of the droplets remain in the range of 17-25 μm . For the locations of spark in ignition experiments, i.e. axial locations between 15-35 mm and radial location ranging 5-35 mm, the peak diameter of the droplets ranges between 20-25 μm .

Fig. 5.12 shows Sauter mean Diameter (D_{32}) of the droplets at various axial distance from the exit of the injector. For each axial location, (D_{32}) is plotted at various vertical locations. At the center of the burner, the size of the droplets remains approximately 30 μm even for axial distance of up to 60 mm. With increase in vertical/radial location of the measurements, the size of the droplets increases gradually reaching 40 μm around the edges of the spray.

5.3 Droplets' flow measurements

The flow of droplets in the burner is very important as it provides the movement of fuel inside the burner. Images of Mie-scattering from droplets were acquired to calculate droplets' velocity fields. Mean and fluctuations of Mie-scattering intensity in an axial plane at the center of the burner are shown in Fig. 5.13. The plot for fluctuations of Mie-scattering intensity better shows the expansion of fuel spray inside the burner. It could also be used to calculate the angle of fuel spray cone for given flow conditions. The mean spray cone angle was estimated to be 46° .

Velocity fields of droplets in the axial plane were calculated using the same correlation parameters as in previous velocity calculations. Mean of droplets' velocity fields over 1 s is shown in Fig. 5.14. Maximum axial velocity of the order of 10 m/s and radial velocity of the order to 3 m/s was observed.

Mie-scattering intensity from the fuel droplets was also measured in transverse planes at different axial locations of 13, 18, 23, and 28 mm from the injector. The axial locations of the transverse measurements were chosen to coincide with the axial locations of the laser-induced sparks during ignition experiments. The images were acquired at an acquisition rate of 10 kHz. Mean Mie-scattering intensity at an axial location of 23 mm and intensity fluctuations are shown in Fig. 5.14. The plot of fluctuations clearly shows that droplet cone at this axial location has an internal diameter of approximately 20 mm and an outer diameter of approximately 80 mm.

Velocity field of droplets was calculated in transverse planes using the Mie-scattering from droplets. Velocity fields were calculated using the same correlation parameters as in previous sections. Mean radial and azimuthal components of the velocity fields in transverse planes at various axial locations are shown in Fig. 5.16 and Fig. 5.17, respectively. In radial velocity fields a positive value denotes velocity vectors away from the center and vice-versa. The radial velocity decreases with increase in axial distance. The expansion of spray cone with axial distance can also be visualized in Fig. 5.16. Radial component of

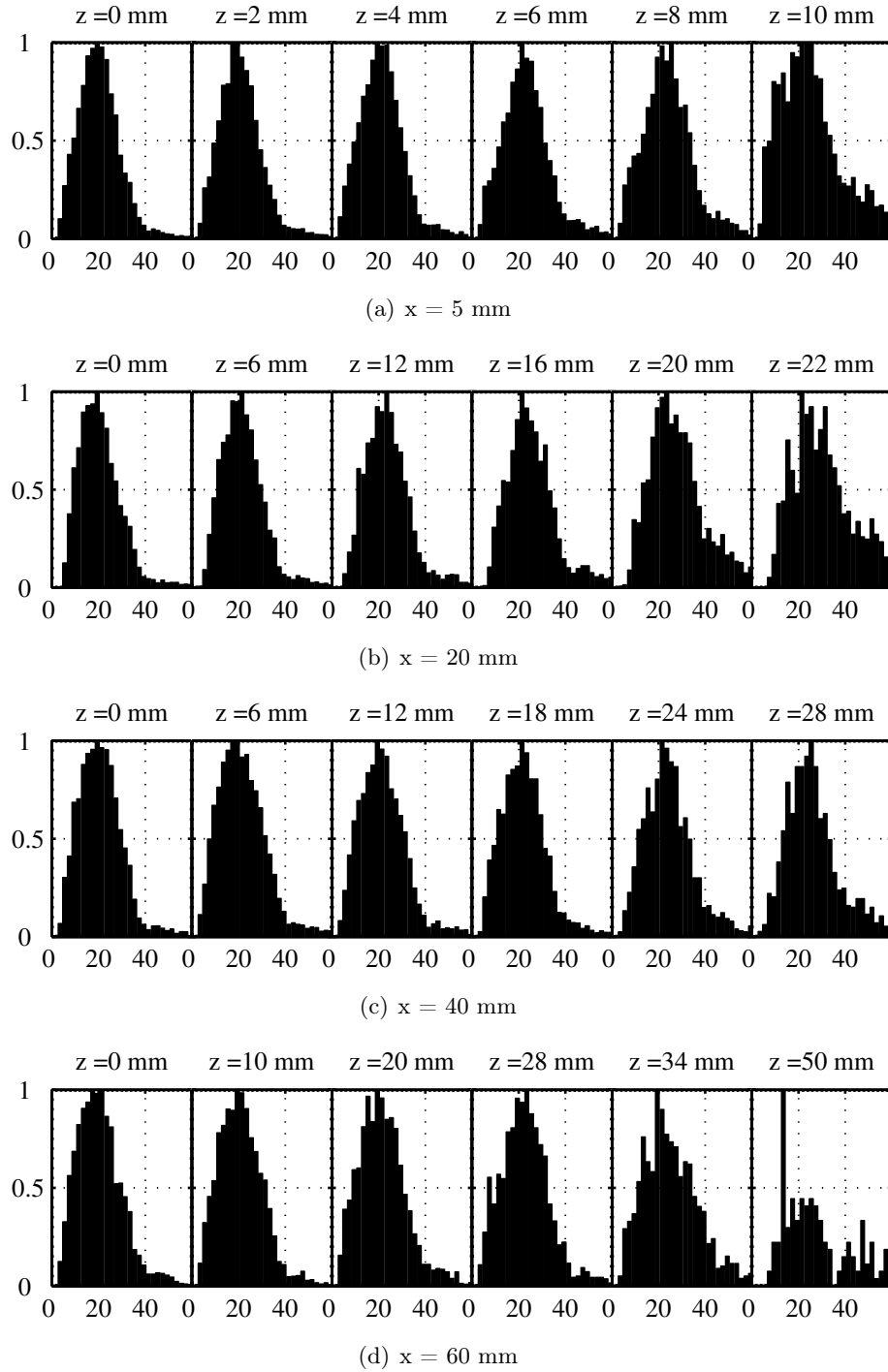


Figure 5.11: Histogram of droplet diameters (μm), at axial locations of (a) 5 mm, (b) 20 mm, (c) 40 mm, and (d) 60 mm. At each axial location, histograms are plotted at few vertical locations z .

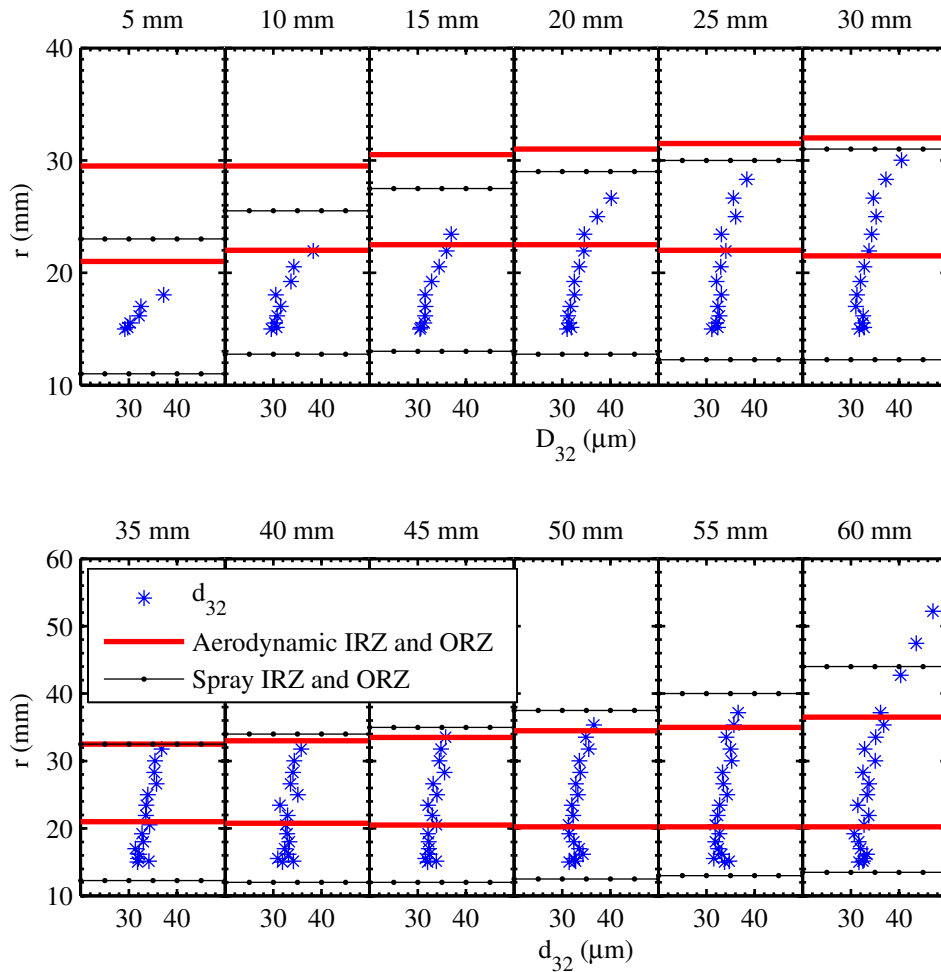


Figure 5.12: Sauter Mean diameter of droplets coming out of injector at various axial locations as a function of radial location, Aerodynamic and spray recirculation zone also simultaneously plotted.

velocity decreases from 4 m/s at an axial distance of 13 mm to 2.5 m/s at an axial distance of 28 mm.

A negative value of azimuthal velocity in Fig. 5.17 denotes clockwise-movement of the spray and vice-versa. High values of azimuthal velocity are results of a strong PVC inside the burner. The azimuthal component also provides a measure of the out-of-plane movement of droplets during measurements in an axial-plane. It is interesting to note that the value of azimuthal component increases with increase in axial distance. However, the strength of the PVC should decrease with axial distance. Moreover, the expansion of the spray as a function of axial distance is not observed in azimuthal component plots.

As seen in Fig. 5.14, droplets were present only in part of the burner, and

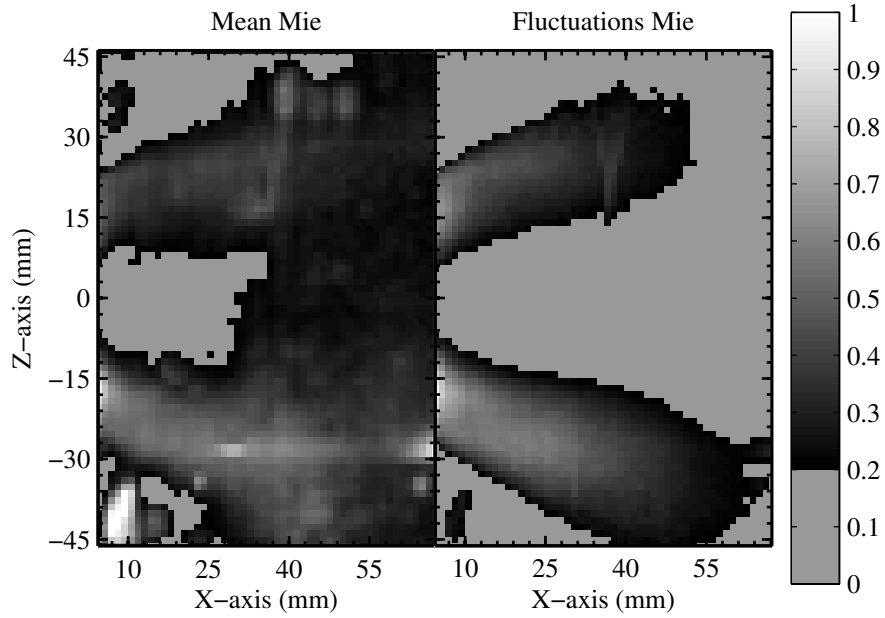


Figure 5.13: Mean and fluctuations of Mie-scattering intensity in an axial plane, averaged over 1 s.

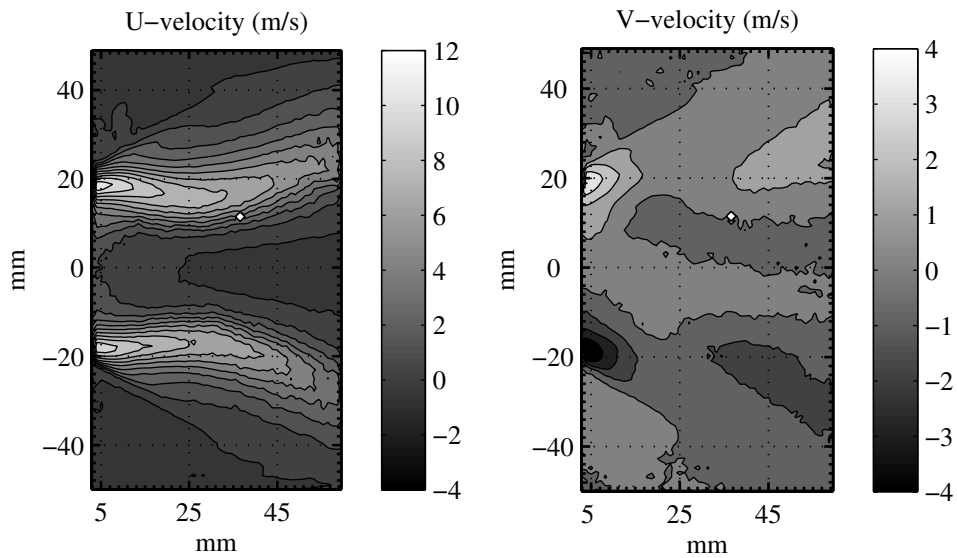


Figure 5.14: Mean axial (U) and vertical (V) components of droplets velocity fields, calculated over 1 s

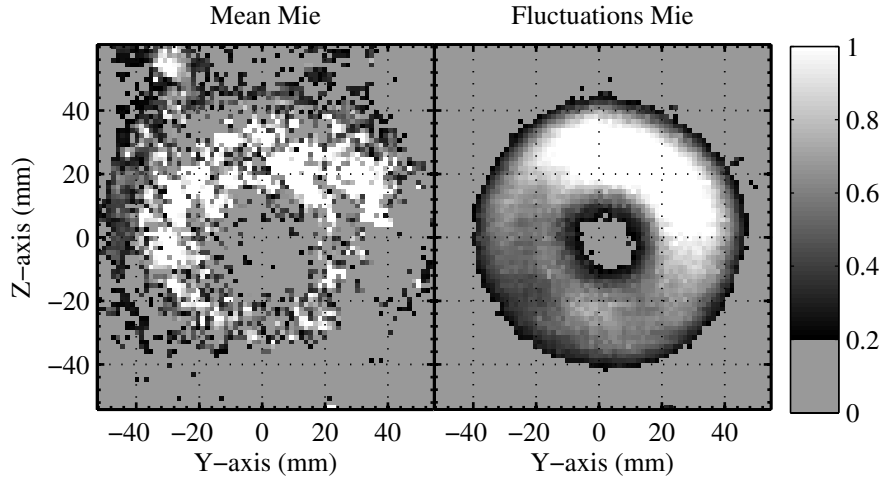


Figure 5.15: Mean and fluctuations (over 1 s) of Mie-scattering from fuel droplets in a transverse plane at an axial distance of 23 mm.

the accuracy of the velocity field measurements can be good only at locations where droplets were present. The accuracy of the velocity field calculations can be measured in terms of the ratio of peaks during the correlation of images used for velocity calculations. A higher peak 1 to peak 2 ratio corresponds to more accurate velocity measurements. The validation criteria used during the calculations of velocity required a minimum peak ratio of 1.2, and the vectors having lesser peak ratios were rejected/substituted. Fig. 5.18(a) shows mean of peak ratio values for transverse velocity field calculations at an axial distance of 23 mm. Mean values were calculated using only the validated vectors. Number of validated vectors at each location inside the burner are also shown as percentage in Fig. 5.18(b).

Fig. 5.18(a) shows that peak ratio values are highest in the same region where Mie-scattering intensity is high (Fig. 5.14). In the center of the burner, the percentage of validated vectors as well as the peak height ratio is low, thereby leading to lesser accuracy of measurements up to a radius of 10 mm. The accuracy of measurements is high for radius values in the range of 10-18 mm. The accuracy of the measurements again decreases from 18 mm radial distance up to approximately 30 mm. The accuracy further increases up to the axial distance of 40 mm. This proves that velocity calculations are more accurate at the edges of the spray cone. Similar trends were observed in transverse planes at other axial locations.

Fig. 5.19 shows histogram of v-velocity (y-direction) component calculated in a transverse plane at a location of $y = -20$ mm, $z = 20$ mm, and $x = 13$ mm. The mean value of the velocity component at this location was 4.1 m/s. Only validated vectors have been used to plot histogram in Fig. 5.19. It shows a high level of fluctuations in the velocity components as a result of high level

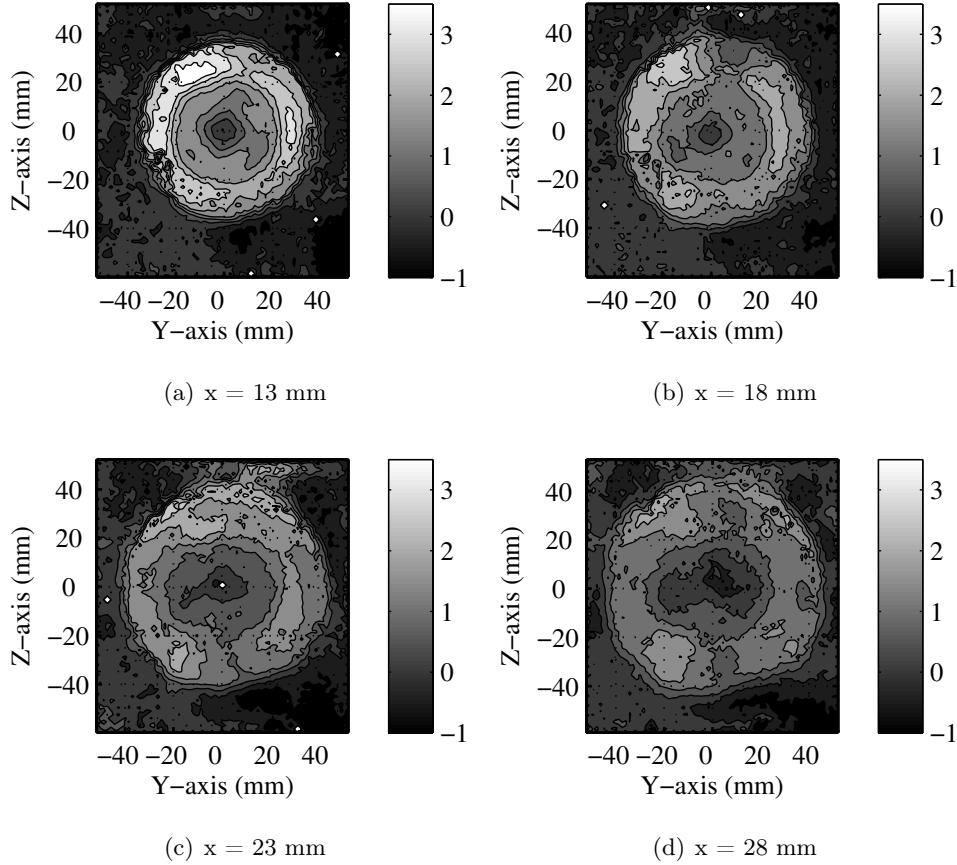


Figure 5.16: Radial velocity fields (m/s) for droplet flow at different axial locations inside the burner.

of fluctuations in the droplet flow. In order to understand the reason for high fluctuations, it was necessary to perform the frequency domain analysis of the droplet flow.

The velocity calculations were checked for the presence of peak-locking error. The measurements in the region of the spray were devoid of this error but this error was present outside the spray cone. Fig. 5.20 shows histogram of pixel displacement corresponding to vertical velocity component at $y = 0$ mm, $z = 48$ mm in a transverse plane at an axial distance of 13 mm. It shows presence of integer displacement values which represents peak-locking error. This error occurs when the size of the particles are smaller than a pixel of the PIV camera. This error was observed only around the edges, where velocity calculations were not accurate as already shown in Fig. 5.18. It was verified that this error was not present inside the spray cone.

The frequency content of the flow was calculated by using calculating FFT of Mie-scattering values at each location inside the burner. “Welch” method

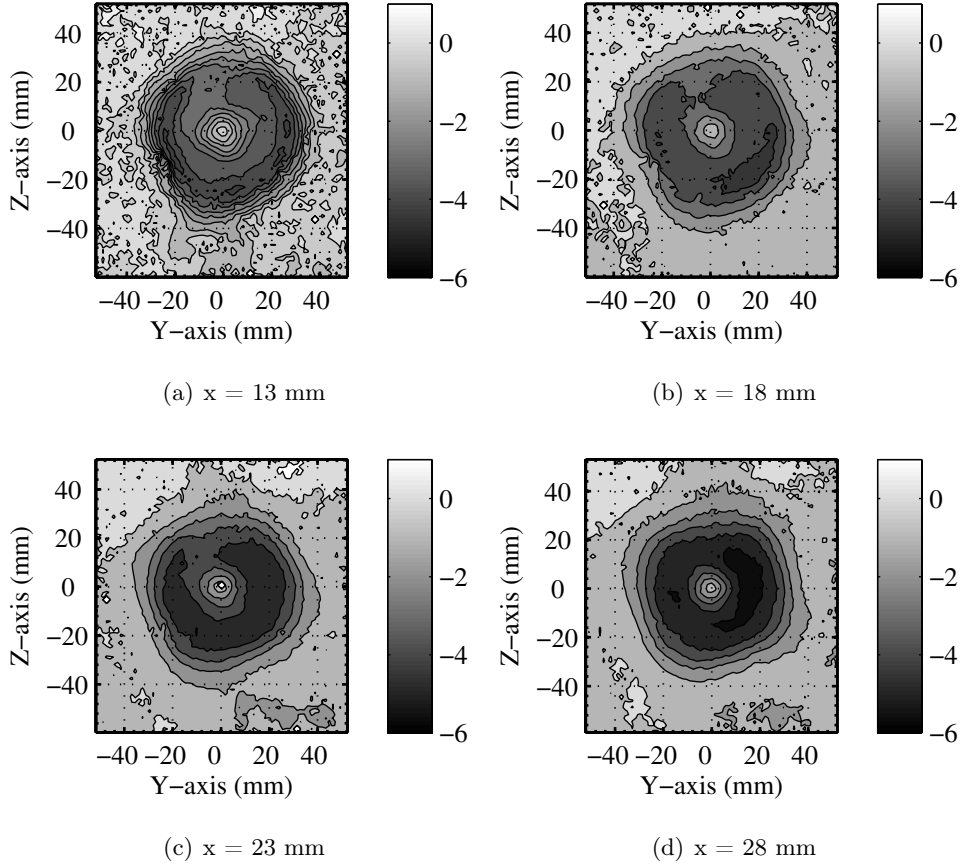


Figure 5.17: Azimuthal velocity fields for droplet flow at different axial locations inside the burner.

was used to calculate the dominant frequencies present. Mie-scattering images in transverse planes did not show any dominant frequencies. Similar analysis was performed for velocity components. A peak frequency corresponding to the PVC frequency was observed at few locations inside the burner. Values of dominant frequencies inside the burner are shown in Fig. 5.21(a) for a transverse plane at an axial location of 13 mm. Vertical components of velocities were used in the calculation of frequency. Analysis of horizontal components also shows similar results. It can be seen that dominant PVC frequency was observed only at few locations in the transverse plane. Fig. 5.21(b) shows PSD as a function of frequency, calculated using vertical velocity components at a location of $z = 28$ mm, and $y = -20$ mm for the transverse plane measurements shown in Fig. 5.21(a). A dominant frequency of 542 Hz was seen at the chosen location, which should be the frequency of the PVC. With increase in axial distance, the presence of dominant frequency of the PVC diminished quickly and no particular dominant frequencies were seen at the axial distance of 28 mm.

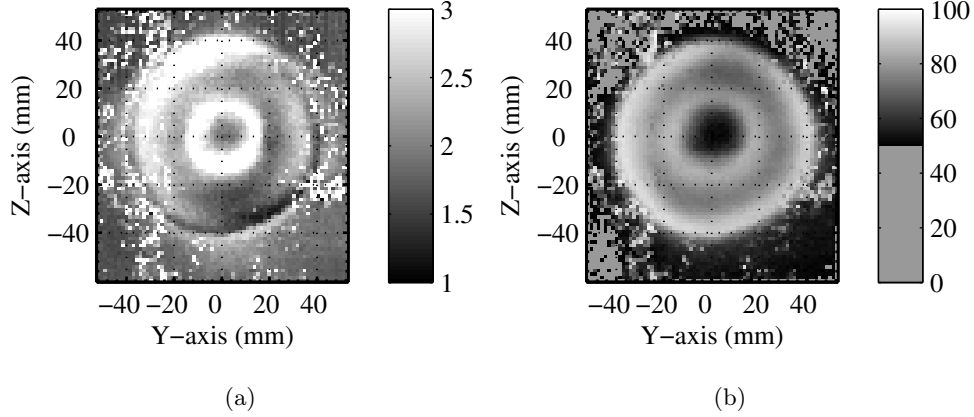


Figure 5.18: (a) Mean of peak ratios during correlation of images for velocity field calculations; mean calculated using only the validated vectors; (b) Percentage of validated vectors at each location inside the burner.

Frequency domain analysis was also performed in the axial plane. A dominant frequency of 536 Hz was found at the exit of the injector. This value also corresponds to the expected frequency of the PVC. The region where this frequency is dominant can be seen in Fig. 5.22(a). It shows that a clear PVC was seen up to axial distances of 25 mm. These results are in contrast with the measurements in transverse planes, where no dominant frequencies were seen in Mie-scattering images. In order to further understand the movement of PVC inside the combustor, a CPSD (cross power spectral density) analysis was performed on the Mie-scattering images. CPSD analysis was performed by calculating a cross-correlation between Mie-scattering intensity at each location in the axial plane with respect to a location just at the exit of the injector. If

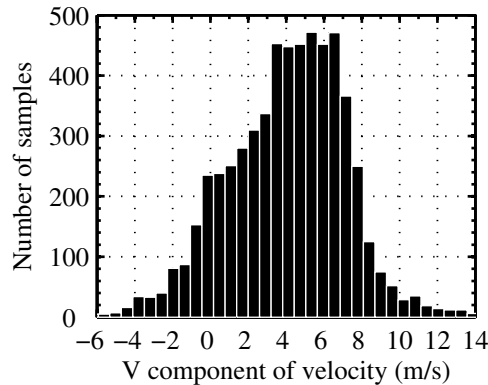


Figure 5.19: Histogram of vertical velocity component (m/s) at $y = -20$ mm and $z = 20$ mm for a transverse plane at an axial distance of 13 mm.

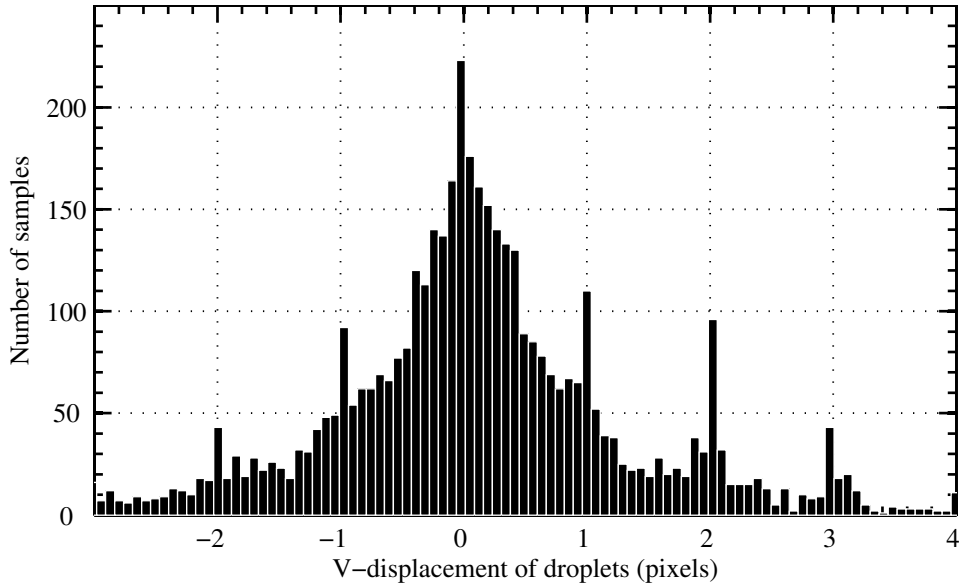


Figure 5.20: Histogram of vertical velocity component (displacement in pixels) at $y = 0$ mm and $z = 48$ mm for a transverse plane at an axial distance of 13 mm.

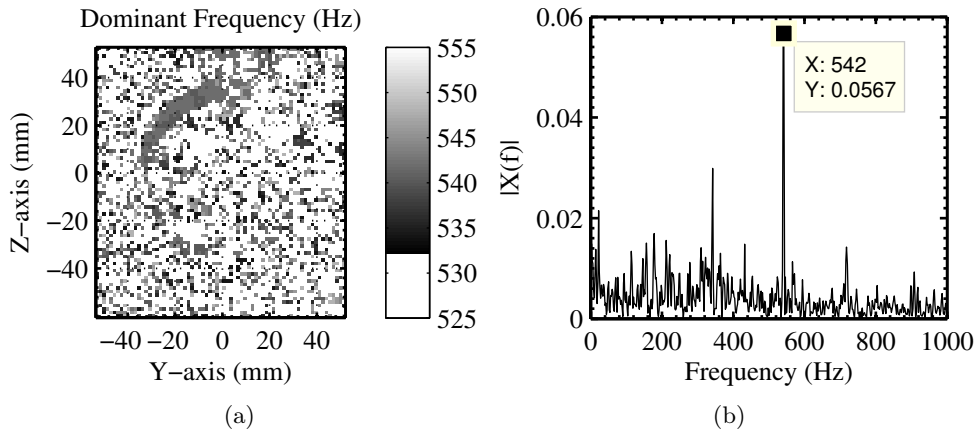


Figure 5.21: (a) Dominant frequencies inside the burner calculated using FFT of vertical velocity components; (b) Power spectral density as a function of wavelength at $z = 28$ mm, $y = -20$ mm, and an axial distance of 13 mm.

correlation existed between the two locations then the phase between the two locations was calculated. The phase values thus obtained for one of the tests are plotted in Fig. 5.22(b). Phase values change from positive to negative after half cycle of the PVC. This plot could also be used for calculating the pitch of the PVC.

Similarly, frequency domain analysis was also performed using velocity components in the axial plane. A dominant PVC frequency was observed in this

analysis as well for both axial and vertical components, as shown in Fig. 5.23. A strong PVC frequency was observed for up to axial locations of 35 mm, similar to Mie-intensity analysis.

5.4 Difference between droplets' and aerodynamic velocity fields

Measurement of both aerodynamic and droplets' velocity fields is important in order to understand the differences between the two. As it is not possible to perform these two measurements simultaneously during ignition experiments, these experiments were separately performed in both non-reactive and reactive conditions. In order to visualize differences between aerodynamic and droplets' velocity fields in transverse planes, mean of radial and azimuthal velocity components as a function of radial distance were calculated for measurements at each axial location. Fig. 5.24 shows profiles of radial and azimuthal velocity components for droplets' flow at $x = 13$ mm and 18 mm, and at $x = 15$ mm and $x = 20$ mm for aerodynamic flows. Fig. 5.24 shows that both radial and azimuthal velocity components are very different for droplets velocity field vis-a-vis the aerodynamic velocity field. Radial velocity profiles show that while aerodynamic flow has a strong central recirculation zone, droplets' flow is not affected by the central recirculation zone. This is apparent by the fact that aerodynamic flow have strongly negative radial velocities around radial distances of 20 mm. Azimuthal components also have a large difference, as the magnitude is very small for droplets' flow as compared to aerodynamic flows.

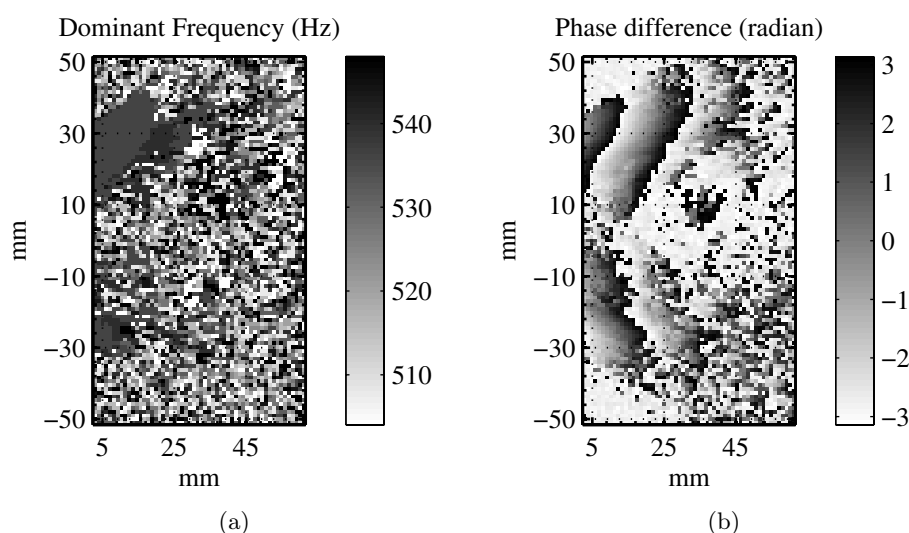


Figure 5.22: (a) Dominant frequencies in an axial plane inside the burner.; (b) Cross power spectral density analysis of Mie-scattering images in an axial plane.

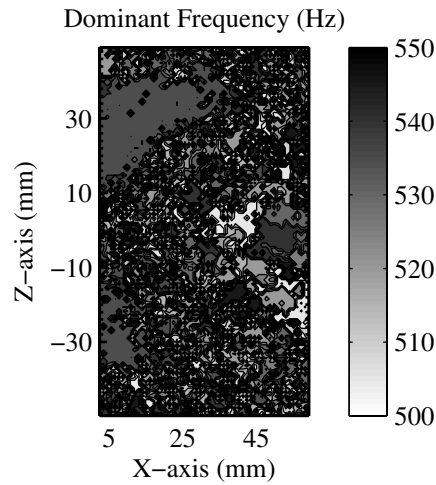


Figure 5.23: Dominant frequencies inside the burner calculated using FFT of vertical velocity components in the axial plane

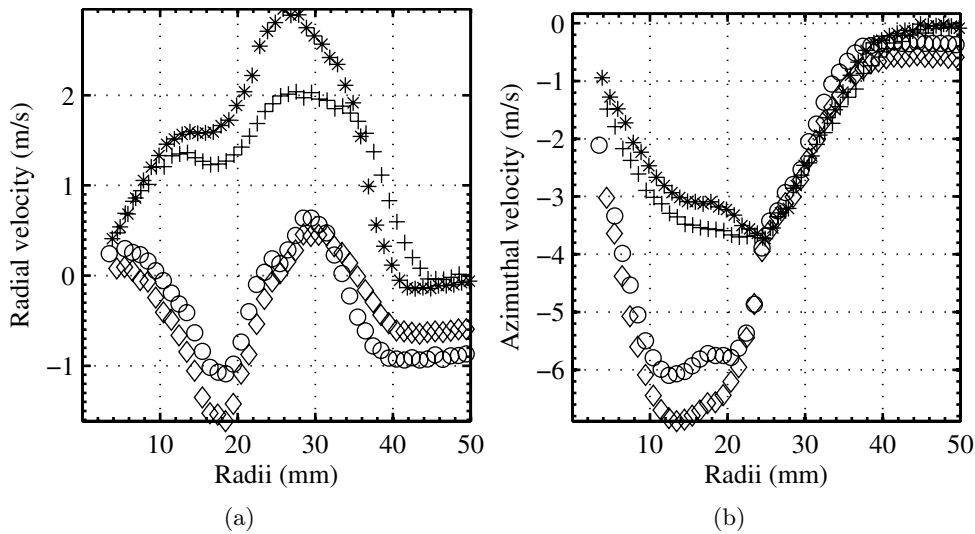


Figure 5.24: Comparison between aerodynamic and droplets' velocity fields: (a) Comparison of radial components and (b) comparison between azimuthal components; (*) $x = 13$ mm, droplets, (+) $x = 18$ mm, droplets, (o) $x = 15$ mm, aerodynamic, (◇) $x = 20$ mm, aerodynamic.

The difference in velocity fields of aerodynamic and droplets' velocity fields is shown in Fig. 5.25. The differences are shown in half plane as the other half is symmetric. At a vertical location of 25 mm, i.e. at the exit of the injector, the droplets' velocity is 6 m/s less than aerodynamic velocity field. This means that droplets do not follow the aerodynamic flow completely.

Frequency domain analysis of Mie-scattering images obtained by droplets show

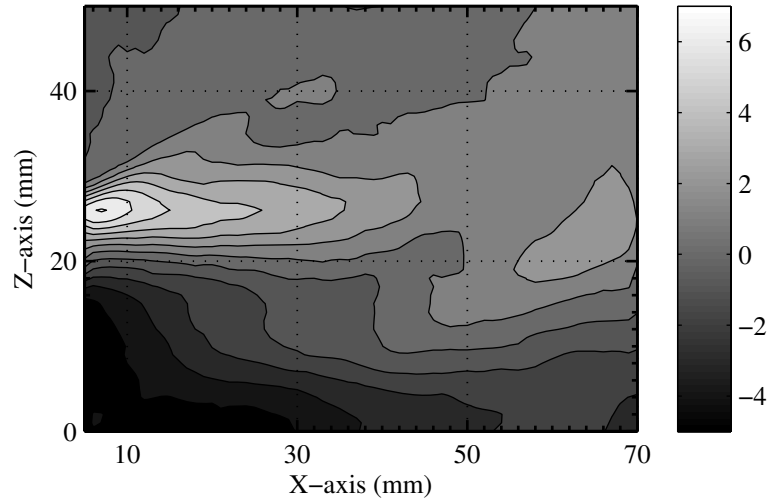


Figure 5.25: *Difference between aerodynamic and droplets' velocity fields in an axial plane.*

dominant frequencies of the PVC while aerodynamic flow measurements do not show the same. It can be concluded that while both droplets' and aerodynamic flows are important, measurement of one flow field is not sufficient to understand complete flow field inside the burner.

Chapter 6

Ignition at fixed location

In order to choose the best approach of measurements in ignition experiments, some test experiments were performed for a fixed spark location in the two-phase flow, turbulent TOSCA burner. These measurements were intended to identify the parameters which play a significant role in success and failure of an ignition attempt.

Simultaneous measurements including time-resolved axial plane PIV using Mie-scattering by droplets, LIPS, spark image, incident laser beam energy, Helium-Neon laser transmitted beam energy measurements were performed for 5 different runs. Each run was concluded when successful ignition was achieved. The location of the laser-induced spark was kept fixed with an axial location of 35 mm and a vertical location of 15-20 mm from the center of the burner. This location of spark was chosen to have not very high ignition probability, to allow for few unsuccessful shots measurements before successful ignition.

Laser-induced sparks were created at 3.33 Hz. The images of the sparks were also captured at 3.33 Hz. The spectrometer used for these measurements required continuous acquisition. Therefore, LIPS measurements were performed at 10 Hz with an exposure time of 100 ms. As a consequence each third spectrometer measurement contained emissions from a laser-induced spark. Time-resolved PIV of Mie-scattering by fuel droplets was performed at 20 kHz. On-board memory of the high-speed cameras allowed to capture 32932 frames (over 1.6466 seconds) at the chosen image resolution. The cameras were operated in end mode and image acquisition was manually stopped as soon as successful ignition was achieved. Therefore Mie-scattering images could be acquired around a maximum of 5 laser-induced sparks. In current experiments, Mie-scattering images could be acquired around 3 unsuccessful and 1 successful spark in each of the five runs.

6.1 Spark Measurements

6.1.1 Incident Laser energy

The chosen location had an ignition probability of 1 over 26, calculated using the 5 test runs comprising of simultaneous diagnostics. Fig. 6.1 shows that the incident laser energy achieved a constant level after a few, around 20, shots. Thus first 20 shots of laser-induced plasmas in each run were ignored during analysis. The ignition probability was calculated after removing these 20 shots from each of the runs.

It can be concluded from Fig. 6.1 that for same values of incident energy some sparks can result in successful ignition and some sparks in unsuccessful ignition.

6.1.2 Plasma Images

The images of the laser induced plasmas were acquired through an intensified CCD camera with no bandpass filter. The acquisition of the images started 1000 ns after the initiation of the plasma for an exposure time of 500 ns. Typical images of the spark (inverted in color) as captured by the ICCD are shown in Fig. 6.2.

It can be clearly seen that the deposition of the spark energy is greatly affected by the presence of droplets in the region of the spark. The density of droplets has an effect on the emission intensity of the plasma and also on the size of the plasma. Maximum and mean spark intensity for each laser induced spark are plotted in Fig. 6.3. High fluctuations in both mean and maximum plasma intensity were observed, even when the incident spark energy does not vary significantly.

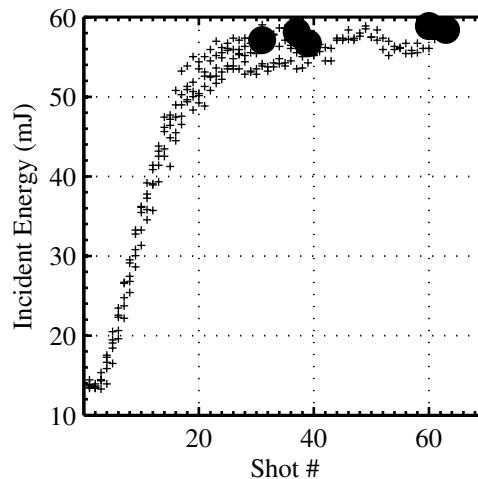


Figure 6.1: Variation of incident laser energy with shot number; Circles correspond to successful ignition and + correspond to unsuccessful ignition attempts.

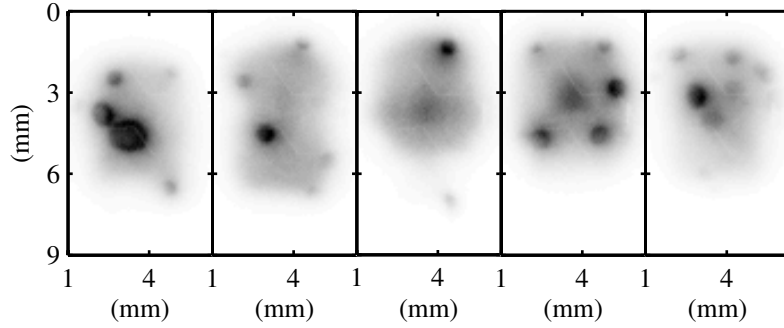


Figure 6.2: Images of spark as captured by the ICCD camera.

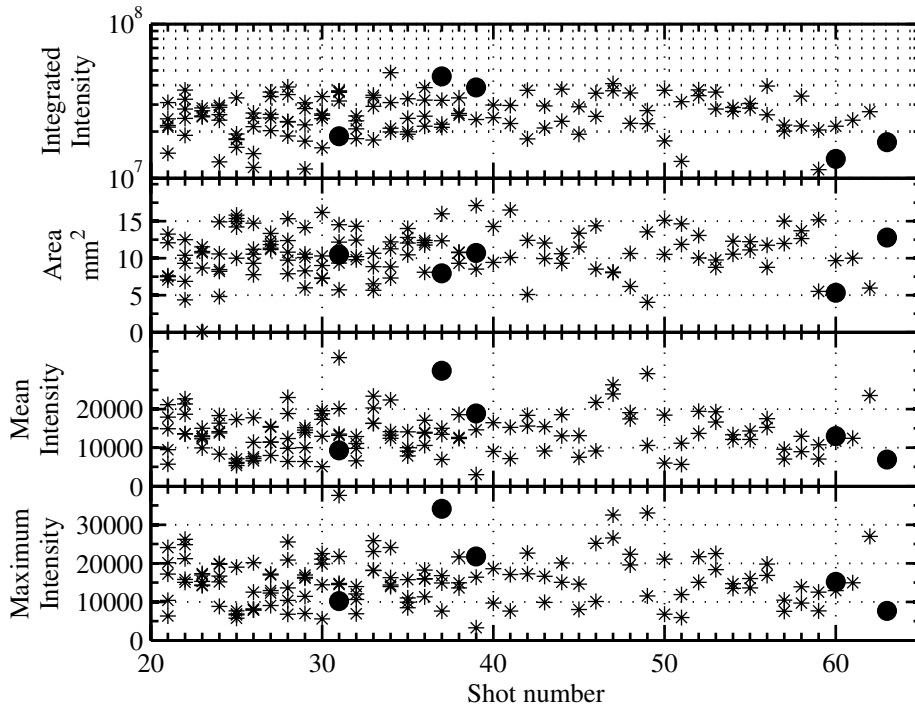


Figure 6.3: From top to bottom: Integrated spark intensity, Area of the laser induced spark, Mean intensity of the laser induced spark, Maximum intensity of the laser induced spark; Circles correspond to successful ignition and stars correspond to unsuccessful ignition attempts.

Second sub-figure of Fig. 6.3 shows area of the spark and it can be seen that for the same laser incident energy the area of the spark changes considerably, between $5\text{-}15\text{ mm}^2$. Thus the area of the plasma depends on the physical

conditions at the breakdown location, and more importantly on the droplet density at the location of the spark. Top sub-figure of Fig. 6.3 shows the integrated intensities of the whole laser-induced sparks. Integrated intensity of a laser-induced spark can be assumed to be proportional to the energy of the spark. There are fluctuations in integrated intensity as well but the order of fluctuations is not very high as compared to other parameters.

It can be concluded that these properties of plasma do not, themselves, provide a definite set of values to distinguish ignition and non-ignition sparks. Therefore, images of the sparks are not enough to distinguish between igniting and non-igniting sparks.

6.2 Spectral analysis

Spectral measurements acquired through the spectrometer provide a qualitative measure of the hydrogen to oxygen ratio in the region of the spark. The spectrometer was used in a continuous mode at a rate of 10 Hz, with an integration time of 100 ms. The laser induced spark is created at a frequency of 3.33 Hz, thus every third measurement of spectrometer gives integrated spectral emission from a laser-induced spark. A typical spectral measurement is shown in Fig. 6.4(a).

The peak around 656 nm, corresponding to hydrogen atomic emission, and 780 nm, corresponding to oxygen emission were measured and area of the peaks was calculated. Hydrogen peak area was calculated by integrating signal in the

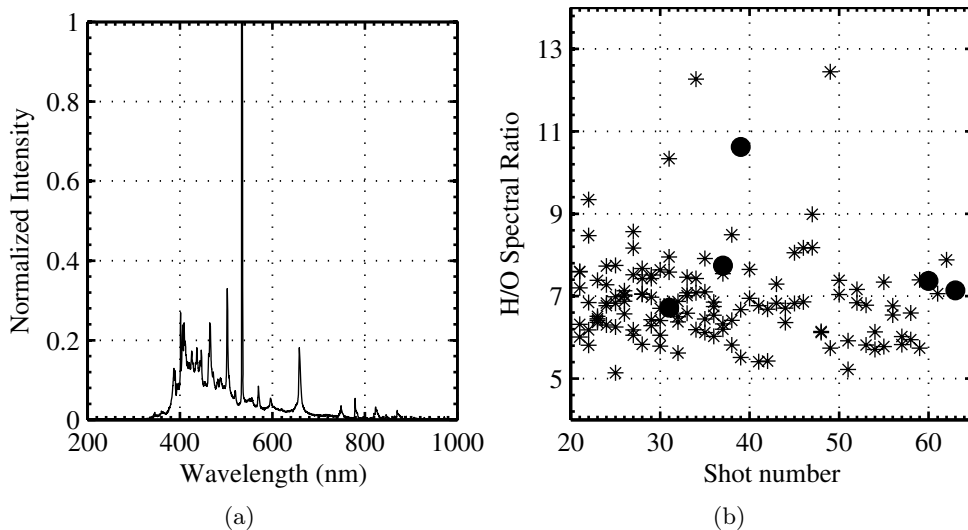


Figure 6.4: (a) Typical Spectral measurements from a laser induced spark; and, (b) Hydrogen to oxygen spectral ratio; Circles correspond to successful ignition and stars correspond to unsuccessful ignition attempts.

range of 641 and 671 nm, after removing the continuum emissions around the peak. Similarly, oxygen peak area was calculated using signal in the range of 775 and 788 nm. The range values for peak area calculations were decided using the peak values in typical spectral emissions.

The ratio of the areas of the two peaks provides the ratio of hydrogen to oxygen emission, which can be related to equivalence ratio through a calibration step, although the calibration step was not performed. The mean spectral ratio for all sparks was 6.96 with a standard deviation of 1.12. It shows a high shot-to-shot variation of the spectral ratio. The hydrogen to oxygen ratio is plotted for all the successful and unsuccessful shots as shown in Fig. 6.4(b).

The ratio of hydrogen and oxygen spectral emissions does not provide a clear distinction between igniting and non-igniting shots. However, a lean ignition limit seems to exist as ignition occurs for a hydrogen-to-oxygen ratio greater than 6.5.

6.3 Flow measurements

Flow field measurements were performed in order to characterize the flow in the burner, before and after the deposition of the spark energy.

6.3.1 Helium-Neon Analysis

The transmitted beam of Helium Neon laser was acquired with a photomultiplier at a rate of 16384 Hz. The analysis of the transmitted laser beam intensity was performed to provide the dominant frequencies in the droplet flow at the exit of the injector. Fast Fourier Transform (FFT) of the transmitted Helium-Neon laser beam intensity was performed using "pwelch" method for different frequency resolutions. The frequency spectrum obtained from the first run is shown in Fig. 6.5(a).

It shows a dominant frequency of 534 Hz, which is the frequency of the precessed vortex core. This value of dominant frequency is coherent with previous experiments performed in the same burner (Providakis (2013)). The dominant frequency values corresponding to the precessing vortex core was calculated for all the five runs. In order to see if dominant PVC mode in the flow should have a particular phase angle for successful ignition to occur, the Helium-Neon intensity measurements were filtered at corresponding dominant frequencies. The phase of dominant frequency was calculated at the time of laser-induced spark. The value of the phase angle for some shots, where simultaneous PIV measurements are available, is shown in Fig. 6.5(b). It can be inferred that ignition mostly occurs for positive values of this phase although the number of data points is not large enough to arrive at conclusive results. It was observed that the values of phase vary significantly with change in the width around peak frequency at which filtering was done. Therefore, the phase calculations were not very accurate and reliable.

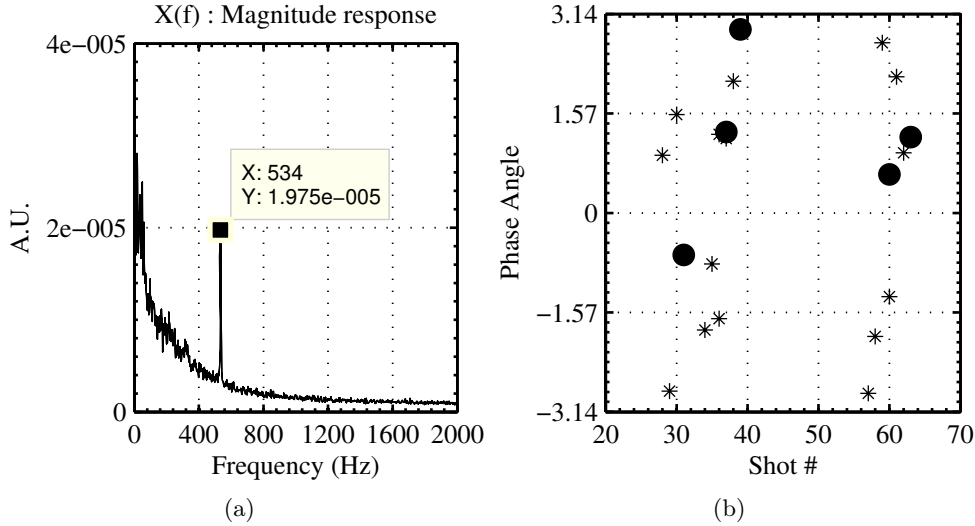


Figure 6.5: (a) Fast fourier transform of the helium neon laser transmitted energy measurements.; and, (b) Variation of phase of PVC at the times of spark, obtained from Helium Neon measurements; Circles correspond to successful ignition and stars correspond to unsuccessful ignition attempts.

In order to extract the time evolution of the PVC, wavelet transform technique was applied to the He-Ne transmitted intensity. Wavelet analysis technique (Section) provided change in frequency of the PVC with time. The PVC frequency variation with time for one of the tests is shown in Fig. 6.6. It can be seen that the frequency of the PVC decreases sharply just before the igniting spark. This phenomenon was observed in two tests out of five. A sharp decrease in frequency can also be responsible for successful ignition but no conclusive inferences could be drawn.

6.3.2 Mie-scattering image analysis

Frequency Domain Analysis

The Mie-scattering images were analyzed to find the dominant frequencies in the region of droplet flow. The exit of the injector, where the mean Mie-scattering intensity was maximum, was first analyzed to find the dominant frequency. Calculations of intensities at the exit of the injector show a dominant frequency in the range of 510 – 535 Hz for the five test runs, which is close to the expected frequency of the PVC. This observation is in coherence with the previous tests made on the same setup, and also in coherence with the frequencies observed from Helium Neon measurements. A region containing 11×11 pixels just outside the injector was selected, over which the mean intensity of Mie-scattering was calculated for each Mie-scattering image. The frequency spectrum is obtained from the fast fourier transform of 20000 shots

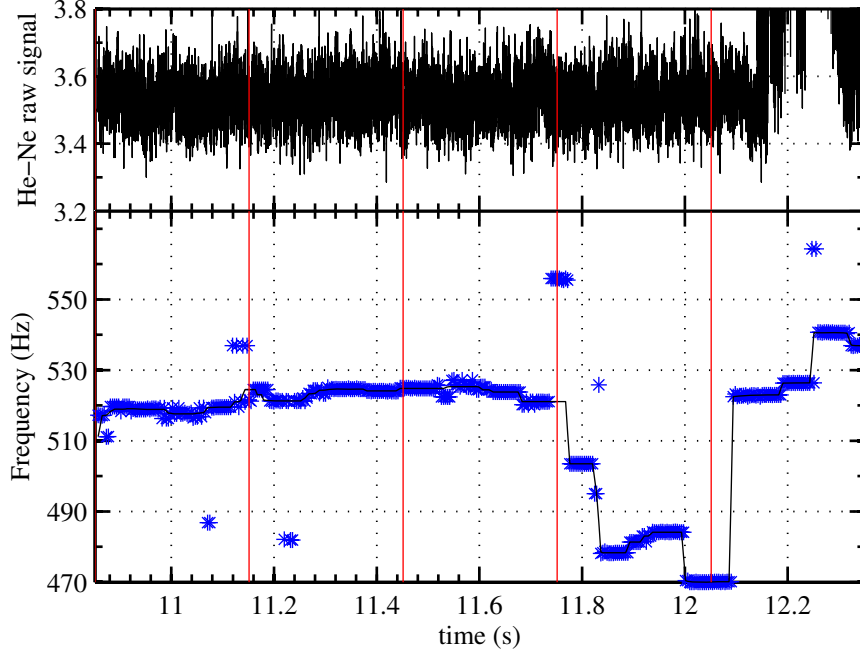


Figure 6.6: Temporal variation of PVC frequency (blue-bottom) and variation of He-Ne transmitted energy signal (black-top); red lines indicate locations of sparks, last spark corresponding to igniting spark.

acquired at a rate of 20 kHz, as shown in Fig. 6.7. This frequency spectrum was from the Mie-scattering images of the same run as He-Ne analysis presented in Fig. 6.5(a). The frequency from both the measurements is almost exactly the same.

Mie-scattering intensity in full image region was analyzed to find the presence of the dominant frequency, i.e. 534 Hz for test 1, so as to find region where PVC propagates. Regions of 11×11 pixels were selected in the whole image area, at a spacing of 5×5 pixels. The peak of power spectral density for frequency values around 530 ± 20 Hz were calculated. The peak values are shown in Figure. 6.8. It provides the region of expansion of the PVC. It should be noted that the peak of PSD at the PVC frequency is very high near the injector exit but not so high throughout the region. Therefore it can be concluded that strength of the PVC decreases with increase in axial distance.

The frequency domain analysis was also performed at the location of the spark. Fig. 6.9 shows the FFT of Mie scattering at the spark location. Even with different resolutions using pwelch method, no clear peak corresponding to the PVC frequency was observed. So, the frequency spectrum at the location of the spark can not be resolved at the PVC frequency.

The droplets at the exit of the injector can be representative of the droplets at the spark location, in addition to some constant time and phase delays. Thus

the analysis of the Mie-scattering intensity can be performed at the exit of the injector. At the exit of the injector, as already shown; the frequencies of the PVC were dominantly present. Thus the signal containing the Mie-scattering intensity in a small 11×11 pixels region was filtered at corresponding PVC frequency. The phase of the filtered signal is then plotted (Fig. 6.10) at the times of laser induced spark.

Fig. 6.10 shows the PVC phase values at the time of spark. First three points for each run correspond to unsuccessful ignition and the fourth one corresponds

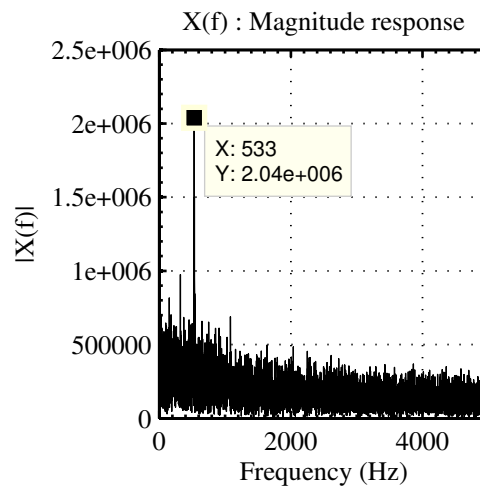


Figure 6.7: Fast fourier transform of the Mie scattering intensity at the exit of the injector.

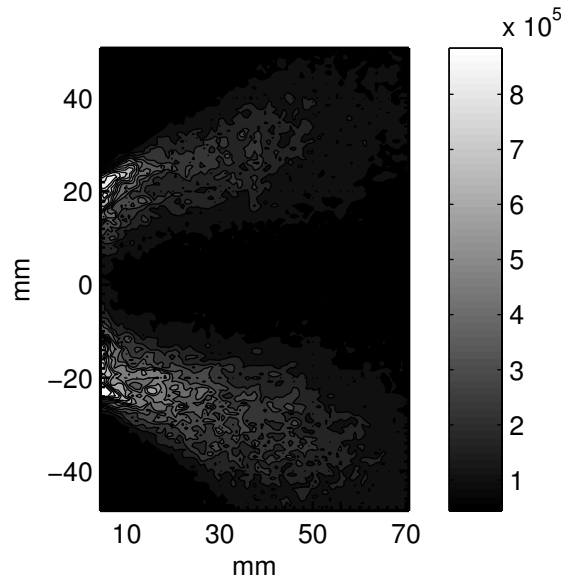


Figure 6.8: Expansion of the precessing vortex core (PVC).

ing the following parameters: a final interrogation area of 16×16 pixels after 3 refinement steps, a peak height validation ratio of 1.2, and a local median validation with an acceptance factor of 0.3.

Flow field patterns before and after the deposition of spark energy can play a significant role in success or failure of the ignition attempt, as it determines the movement of the initial flame kernel towards or away from the injector. Typical instantaneous and mean axial velocity fields in the current burner are shown in Fig. 6.11. Mean velocity fields over different time durations were calculated before and after the spark. It was attempted to look for the differences between mean velocity fields over different time durations corresponding to successfully igniting and failed sparks. Velocity profiles at the axial locations of spark were plotted for three non-igniting and one successfully igniting spark for each of the tests. Fig. 6.12 and Fig. 6.13 show profiles of vertical velocity component before and after the deposition of spark energy, respectively. The velocity profiles were plotted for three non-igniting and one igniting spark in each of the five test runs. Highlighted region in Fig. 6.12 and Fig. 6.13 corresponds to the location of laser-induced sparks, which was of particular interest to look for differences between the velocity fields. It was attempted to find differences between the profiles corresponding to igniting sparks vis-a-vis non-igniting sparks.

It was expected that a negative vertical velocity component would help in the convection of initial flame kernel towards the injector, but the current data sets

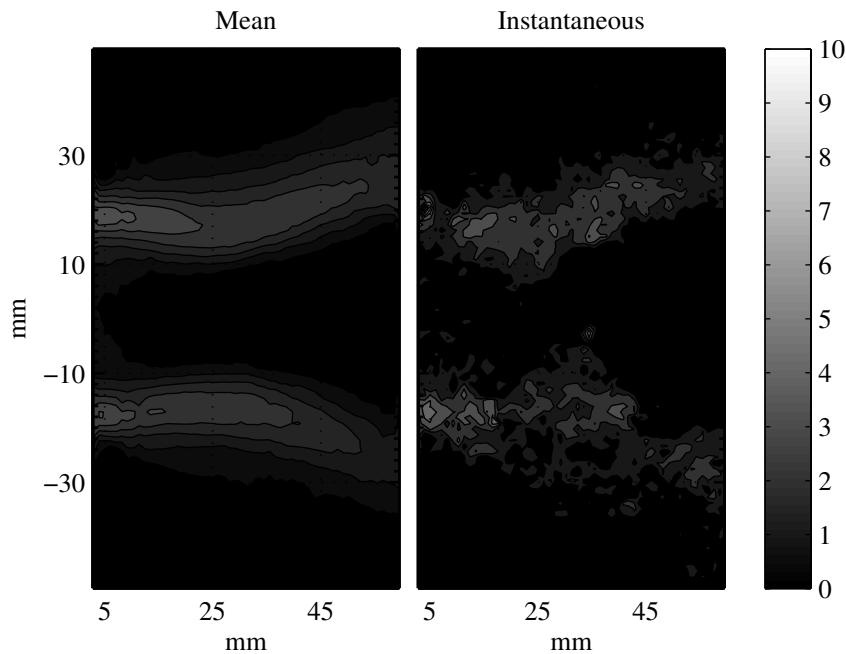


Figure 6.11: Mean (over 100 ms) and instantaneous axial velocity fields calculated using the Mie-scattering images of the droplets

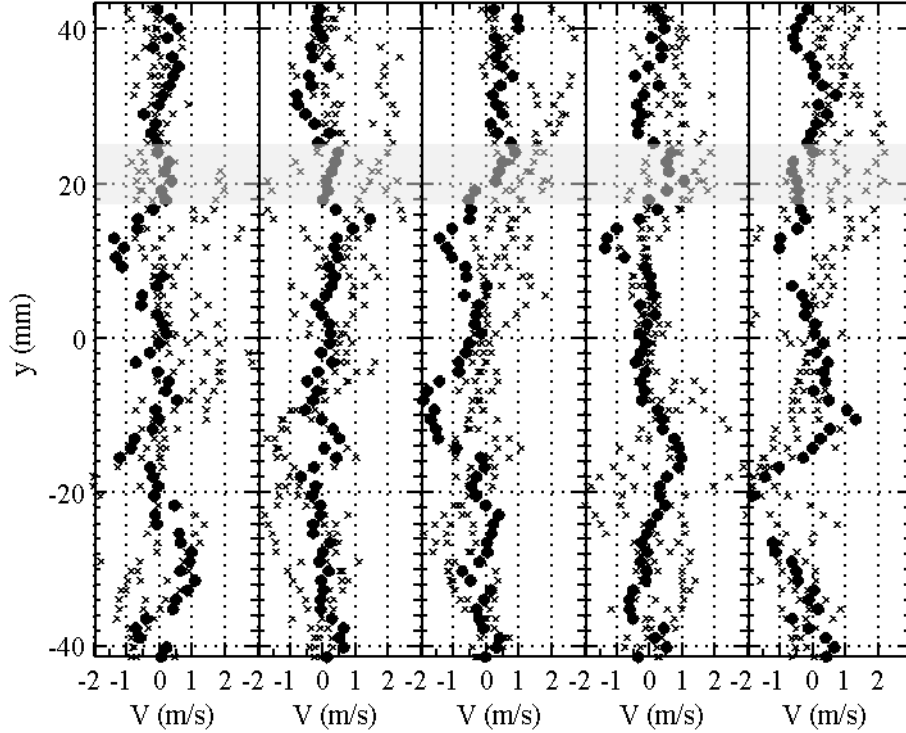


Figure 6.12: Mean (over 40 velocity fields \bar{I} PVC cycle) of vertical velocity components at the axial location of the spark before spark energy deposition; \times corresponds to non-igniting sparks and \bullet corresponds to successfully igniting spark; from left to right: test 1-5.

did not represent this phenomenon. It was also attempted to look at velocity profiles averaged over different times, but no conclusive results was obtained. It can be concluded based on the current data sets that no clear discrimination was found between velocity fields corresponding to igniting and failed sparks after the spark.

6.4 Dynamics of flame propagation

In order to understand how the initial kernel travels back to the injector, a new post processing method was applied. This is based on the Dynamic Mode Decomposition (DMD) using a method proposed by Schmid (2010). This method can help in the extraction of spatially resolved dynamic modes and respective frequencies. The method was applied to a sequence of velocity fields obtained from the Mie-scattering images. As shown in Schmid (2010), if acquisition rate is more than three times the inherent frequency then accurate results can be obtained with this technique.

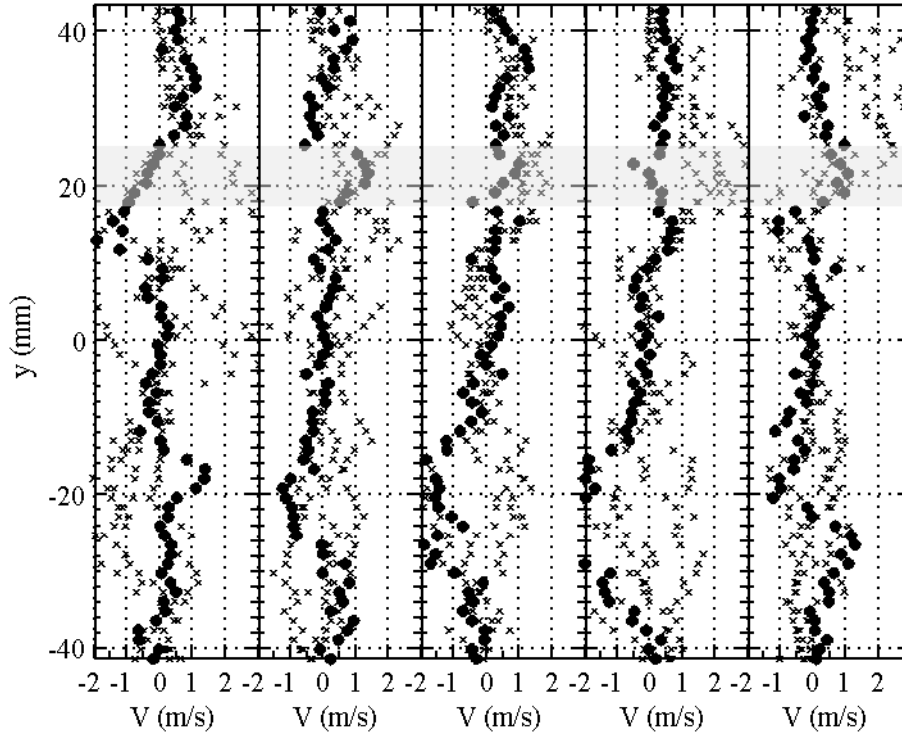


Figure 6.13: Mean (over 40 velocity fields $\bar{1}$ PVC cycle) of vertical velocity components at the axial location of the spark after spark energy deposition; \times corresponds to non-igniting sparks and \bullet corresponds to successfully igniting spark; from left to right: test 1-5.

In current study, Mie-scattering image acquisition was performed at 20,000 Hz and the frequency of the PVC was of the order of 500 Hz . Thus, this method can be applied in the framework of the measurements performed.

The objective of this study is to look at time evolution of the PVC inside the combustion chamber. Thus it is attempted to look at the eigenvalues corresponding to the mode at the frequency of the PVC. A sample of 400 subsequent velocity fields, corresponding to 20 ms, was chosen for the application and eigenvalues corresponding to the PVC frequency were calculated. Typical eigenvalues are shown in Fig. 6.14. The velocity fields used for this plot were calculated using Mie-scattering images acquired between 120 ms to 100 ms before the igniting spark in Test case 1.

Higher amplitudes of eigenvalues corresponding to the white and black colors in Fig. 6.14 show the presence and expansion of the PVC inside the burner. In order to look at the time evolution of this PVC, the analysis was applied to different set of samples. Samples of 400 fields, *i.e.* over 20 ms, were chosen starting from 150 ms before the spark up to 150 ms after the spark with an overlap of 50%.

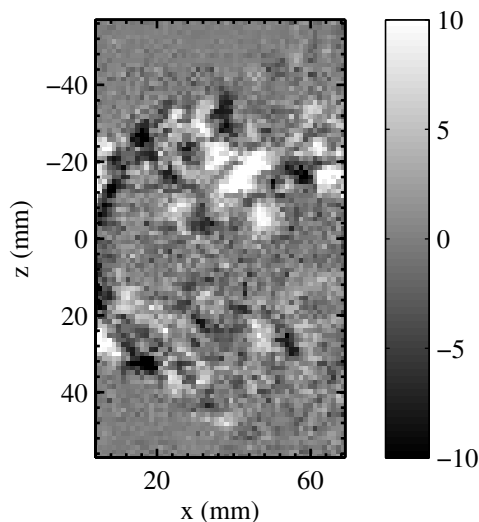


Figure 6.14: Typical magnitude of the eigenvalues corresponding to the PVC mode as obtained from DMD.

This time resolved analysis performed is shown for the shots before the spark in Fig. 6.15 and after the spark in Fig. 6.16. Higher magnitudes in these figures correspond to higher strength of the PVC.

Figure. 6.15 shows that the magnitude of the PVC mode remains almost constant before the igniting spark. Figure. 6.16 shows that the magnitude of the PVC mode increases significantly after approximately 60 ms from the spark. This change in the strength of the PVC is a result of change in the dynamics of the combustion chamber.

The objective of performing this time resolved analysis is to visualize the role of the PVC in the process of ignition. It was attempted to see how the strengthening of the PVC is related to the process of ignition and if it is the strengthening of the PVC that leads to the success of ignition or it is the ignition process that strengthens the PVC.

Thus the results of the DMD on PIV fields is simultaneously seen with the chemiluminescence images acquired simultaneously with the Mie-scattering images. In chemiluminescence images, flame is seen at approximately 62 ms after the spark, as can be seen in the images in Figure. 6.17. Now, the objective is to see if the strengthening of the PVC occurs before or after this time.

Dark black and white region in image 6 of Fig. 6.16, corresponding to analysis over images acquired between 60 to 80 ms, shows first clear instance of a strong PVC. This means that strengthening of the PVC occurred before 70 ms after the spark. No more information can be retrieved from the given plots. Thus DMD analysis is repeated with a higher temporal resolution, *i.e.* 200 samples, acquired over 10 ms are used with an overlapping of 50%. It gives a temporal

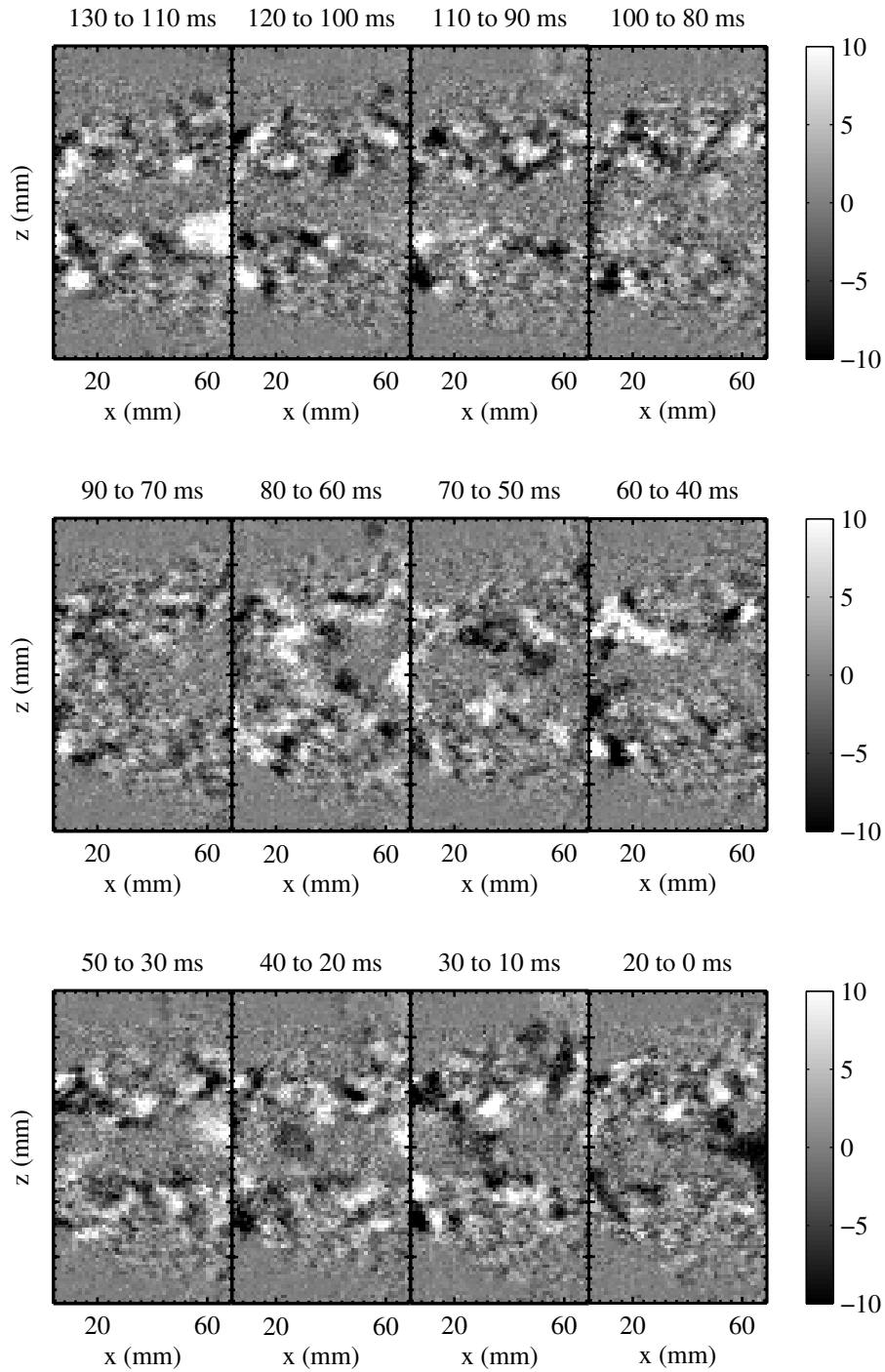


Figure 6.15: Time-resolved DMD before igniting spark, Test 1: images 1-12 show results using velocity fields, respectively, over (130-to-110 ms), (120-to-100 ms),, (30-10 ms), (20-0 ms) before the igniting spark

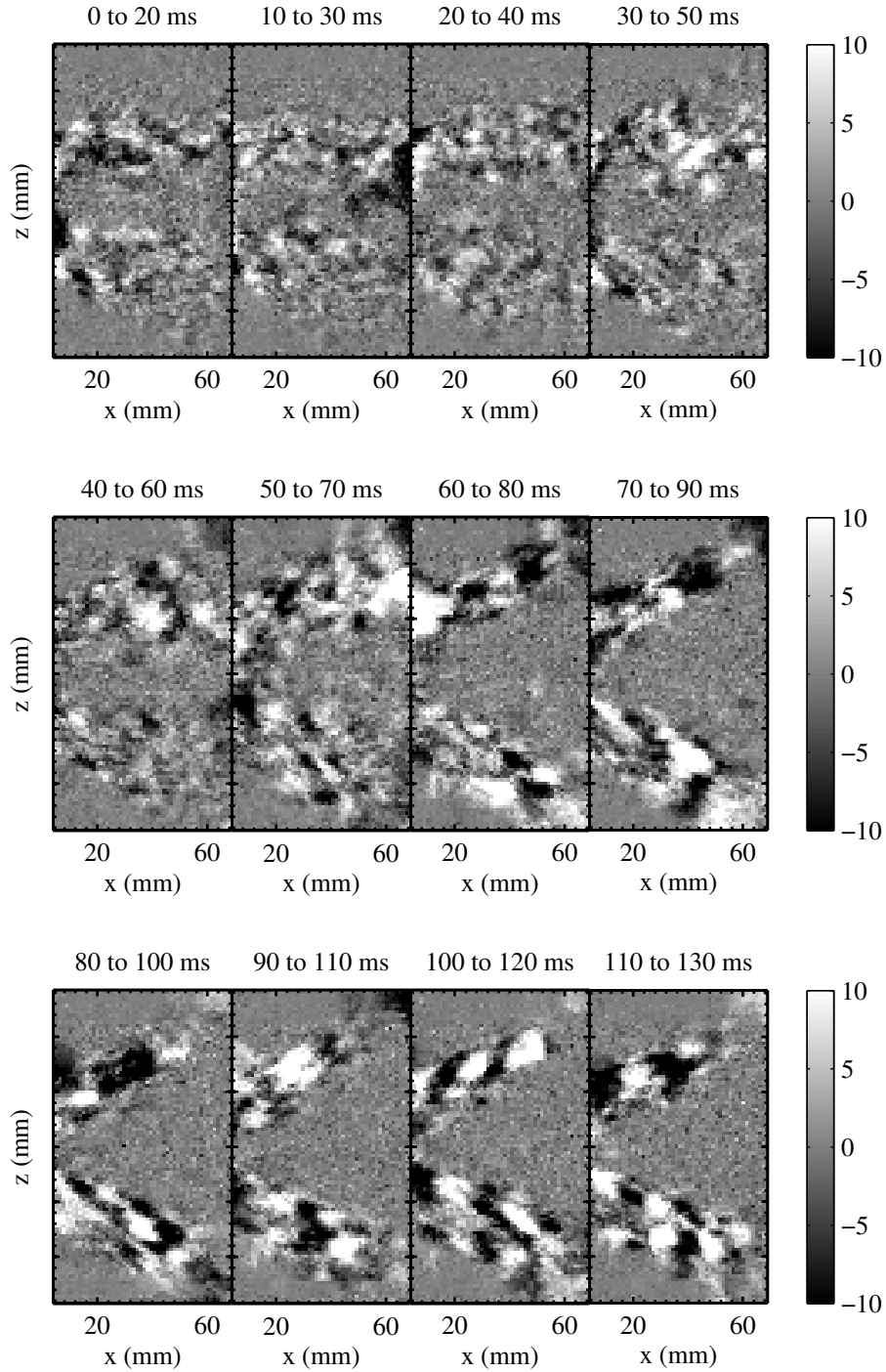


Figure 6.16: Time-resolved DMD after igniting spark, Test 1: images 1-12 show results using velocity fields, respectively, over (0-to-20 ms), (10-to-30 ms),, (30-10 ms), (20-0 ms) after the igniting spark

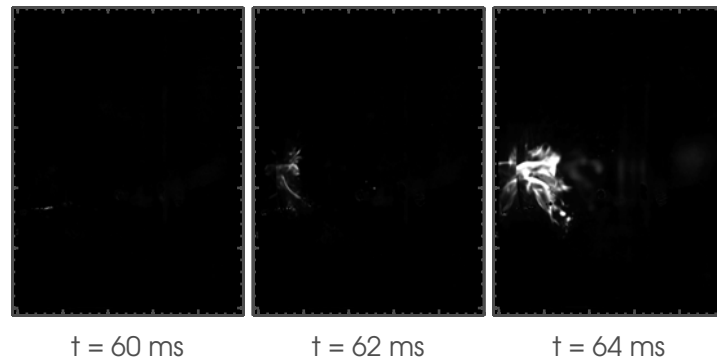


Figure 6.17: Chemiluminescence images acquired at 10 kHz, at respectively 60, 62, and 64 ms after the igniting spark.

resolution of 5 ms. Results of this analysis revealed that PVC strengthening occurs between 65 – 70 ms.

In order to find a more accurate measure of the starting time of strengthening of the PVC, this analysis was re-performed using different starting times for the sample. 200 samples were taken with starting time of samples differing by 0.25 ms. Thus the samples are taken over the times 54.75-64.75 ms, 55.00-65.00 ms and so on. First plot of Figure. 6.18 shows a first instance of strengthening of the PVC, which can be seen in the right top of the first image in this set of images. The subsequent images show strengthening of the PVC in the whole image map of the combustion chamber.

Figure. 6.18 concludes that PVC strengthening starts at about 64.75 ms after the spark. It can be concluded that it is the presence of the flame inside the combustion chamber that leads to the change in the PVC and not vice-versa.

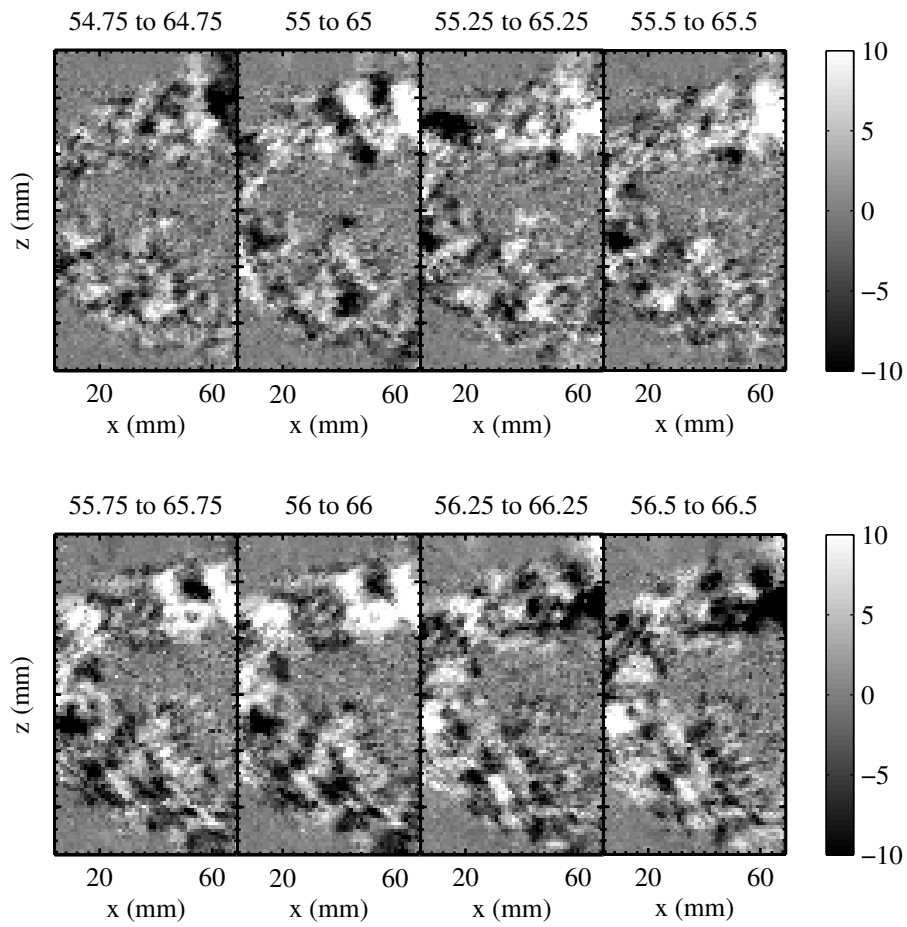


Figure 6.18: Time-resolved DMD after igniting spark, Test 1: images 1-8 show results using velocity fields, respectively, over (54.75-to-64.75 ms), (55.00-to-65.00 ms),, (56.5-66.5 ms), after the igniting spark

Chapter 7

Development of Two Dimensional Laser-Induced Plasma Spectroscopy (2DLIPS)

This chapter details the step-by-step development of Two-Dimensional Laser-Induced Plasma Spectroscopy (2D-LIPS) technique. 2D-LIPS is an extension of the conventional LIPS technique that provides the spatial variation of concentration ratios of two atomic emissions inside the region of a laser-induced spark. The two atomic emissions can be chosen so as to provide the spatially resolved equivalence ratio inside the region of the spark or to represent spatially resolved temperature of the plasma. This chapter details the objective, experimental setup, effects of various physical and experimental parameters on the measurements and the methods of concentration/equivalence ratio calculations.

7.1 Objective of 2D-LIPS Technique

Optical emission spectroscopy (OES) of Laser-induced plasmas (LIPs), which is known as Laser-Induced Plasma Spectroscopy (LIPS) or Laser-Induced Breakdown Spectroscopy (LIBS), is used since many years for applications from metal surfaces characterization (Lee et al. (2004), Ershovpavlov et al. (2008)) to gas mixture description (Itoh et al. (2001); Phuoc (2006b)). This technique allows quantitative and instantaneous measurements of atomic concentrations in a small volume. The principle is that a plasma is generated by focussing a laser beam and the light emitted by the plasma is collected through an optical fiber connected to an imaging spectrometer. This gives a spectrally resolved emission which is analyzed to recover the atomic composition of the medium at the location of the plasma. In the last few years the technique has also been used for combustion systems. The pioneer work of LIBS application to combustion studies was shown by Schmieder (1982). Phuoc and White (2002a) used

simultaneous measurements of the H_α line at 656.3 nm and the O(I) triplets in the range of 777.2 – 777.5 nm for the measurement of equivalence ratio in non-reacting and reacting jets of methane and air. Zimmer and Tachibana (2007b) used this technique for equivalence ratio measurement in oscillating combustion environment. For quantitative measurement of equivalence ratio using the LIPS technique, they considered the effect of plasma excitation on atomic concentrations. Excitation of the plasma was measured using ratio of hydrogen emissions of first and second terms of Balmer's series. Taking into account excitation within the plasma increased the accuracy of LIPS measurements as compared to conventional approaches. Conventional Laser Induced Plasma Spectroscopy (LIPS) has been used to measure equivalence ratio in some more studies; Phuoc (2006a); Ferioli and Buckley (2006); Zimmer et al. (2007); Zimmer and Yoshida (2008)).

This technique is valid within the hypothesis of optical thin emission of spectral lines and local thermodynamic equilibrium (Stavropoulos et al. (2005), Cristoforetti et al. (2010)). Moreover, this spectral emission strongly depends also on the plasma properties like electron density and temperature as well as on self-absorption problems (Aragon and Aguilera (2008)). The complete system of both plasma generation and acquisition equipment has to be carefully set to measure the species populations. The influence of different parameters like laser energy, laser wavelength, or focal length of converging optics for instance have already been reported (Aguilera and Aragon (2004); Aguilera et al. (2004); Chen et al. (2000); Phuoc and White (2002a)) for solids, liquids or gases.

This non-intrusive technique is really efficient for the determination of gas composition and proves to work for various types of gases, from inert (Zimmer et al. (2007); Shudo and Oba (2009)) to very complex gases (Zimmer and Yoshida (2008)). The effect of pressure has also been investigated recently showing that the method is robust and efficient (Shudo and Oba (2009); Zimmer and Yoshida (2011)) even up to 5 MPa. However, one strong limitation is that, when the light emission is collected through an optical fiber to the spectrometer, the measurement is averaged over all the plasma volume leading to two drawbacks : (1) the accuracy of the measurement may be dropped if small scale concentration fluctuations resides in the plasma and (2) the information obtained is reconstructed at one point.

To tackle such limitation, Beduneau and Ikeda (2004) and Kawahara et al. (2007) used a Cassegrain optics system coupled with an ICCD spectrometer through multiple fibers to spatially cover a larger area of measurement. However, the number of fibers is limited and the spatial discretization is fixed. Another approach was used by Aguilera et al. (2003) for the study of spatial characterization of a plasma created on the surface of a solid. A narrow vertical region of the plasma is imaged onto a spectrometer which is attached to a CCD whose rows are grouped. This provides one dimensional variation of spectra. And then the spectrometer system is shifted in horizontal direction to have spatial variation of plasma properties. This approach works only for mean

quantities. More similar studies are recently reviewed in [Aragon and Aguilera \(2008\)](#).

A different approach to yield spatial resolution is to use intensified cameras with appropriate bandpass filters. In this approach images of the laser-induced plasmas are acquired with two or more cameras equipped with band pass filters corresponding to different atomic emissions. The images acquired by the cameras contain different atomic emissions. By comparing the emission intensity at different wavelengths corresponding to different atomic emissions, the medium at the plasma location can be spatially characterized. The main advantage of this evolution is that the plasma is observed on a 2D camera sensor and the information may be recovered with good spatial resolution that may be adjusted a posteriori to achieve the highest signal to noise ratio. Additionally, image post-processing used in common optical diagnostic using the mathematical tools like the inverse Abel transform can be carried out to eliminate the integration along the line of view and achieve a true planar description of the phenomenon ([Aguilera et al. \(2003\)](#)). However, up to now, no simultaneous measurements were proposed on single shot basis for the characterization of gaseous flows with a two dimensional spatial resolution.

According to conventional LIPS theory, spectral intensity at particular wavelengths corresponds to particular atomic emissions ([Zimmer et al. \(2007\)](#)). In order to apply the 2D-LIPS technique to the measurement of equivalence ratio, it is necessary to adapt the technique to simultaneously measure intensity of two atomic emissions which can be related to equivalence ratio. The choice of atomic emissions depends mainly on the fuel being used. Hydrogen emissions at 656.3 nm and oxygen emissions triplets around 777.3 nm are very often used ([Phuoc \(2006a\)](#), [Phuoc and White \(2002a\)](#)) to relate to the equivalence ratio but in some other studies hydrogen, carbon, and nitrogen emissions have also been used ([Zimmer and Tachibana \(2007b\)](#), [Ferioli and Buckley \(2006\)](#), [Zimmer and Yoshida \(2011\)](#)).

The objective of the following study was to capture the images of the plasma simultaneously with two intensified cameras fitted with band pass filters; and to relate the ratio of image intensities observed to the ratio of concentrations of the desired atoms. The objective was to achieve a high single shot accuracy. Development of the technique also required quantifying the effects of various parameters on the intensity measured by the intensified cameras.

The experimental setup presented in [Fig. 3.2](#) was used for the following experiments. Laser-induced plasmas were created at the center of the burner ([Fig. 3.1](#)) in premixed flow of air or a methane-air mixture. The Reynolds number of the flow was kept constant at 1200 corresponding to a flow velocity of approximately 0.9 m/s in the center of the burner. A constant co-flow of Nitrogen/Air with velocity of 0.45 m/s was also kept in order to shield the central flow.

7.2 Energy Measurements

7.2.1 Incident and Transmitted Energies

In order to measure the spark energy of the laser-induced plasmas, experiments were performed with laser-induced sparks created in air flow. The incident and transmitted energies of the laser beam were measured. The spark energy is defined as the difference between the incident energy and the transmitted energy of the laser beam after taking into account the energy losses at various lens interfaces. Energy measurements through two energy meters (see Fig. 3.2) were performed for various laser pulse energies. The energy of the laser beam was varied by changing the Q-switch setting of the laser. The range of energy values was chosen to accommodate incident energies less than breakdown threshold up to incident energies for which 100% shots resulted in laser-induced sparks. The readings of the two energy meters for various Q-switch setting are shown in Fig. 7.1(a).

Fig. 7.1(a) shows that for low values of readings of energy meter A (less than 1.6 on x-axis of Fig. 7.1(a)), the readings of two energy meters follow a linear curve. Those shots correspond to incident energies smaller than the breakdown threshold. These linear curve following shots were used to calculate the calibration coefficient for incident energy measurements. The coefficient was obtained by dividing readings of energy meter B by readings of energy meter A. The coefficient value was calculated to be 50.14. This takes into account losses/reflections at all optical elements except the last converging lens. This coefficient value was multiplied to readings of energy meter A in order to obtain incident energy values. The value of the coefficient implied that for laser beam energies less than breakdown threshold energy meter A reads approximately

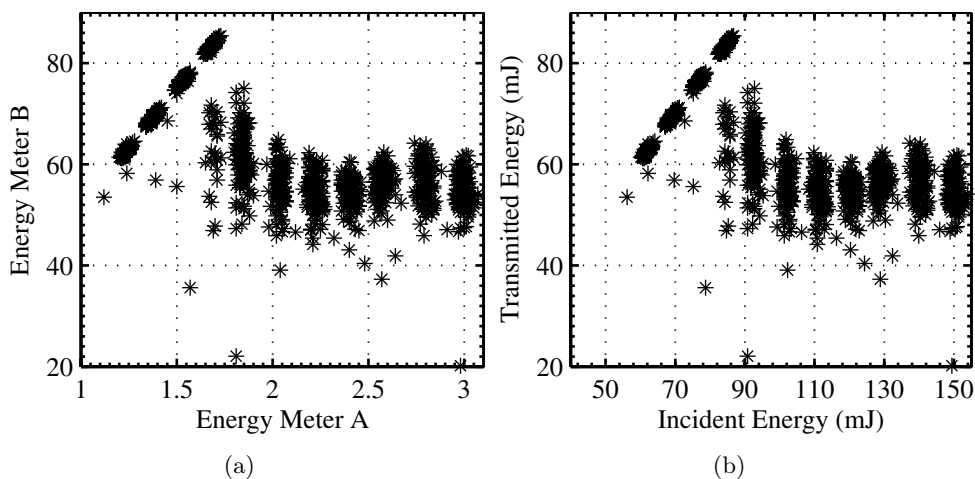


Figure 7.1: Laser Energy Measurements: (a) Variation of readings in the two energy meters; (b) Transmitted energy of the laser beam as a function of incident energy.

2 % of energy meter B. The reflection of the pulse energy from the beam splitter was less than the design reflectance (10%) because the beam splitter was designed for 532 nm wavelength but was used for 1064 nm reflections in the current measurements. The readings from energy meter A were multiplied by this coefficient to obtain incident laser beam energies and corresponding incident and transmitted energies plot is shown in Fig. 7.1(b).

7.2.2 Breakdown Threshold

Breakdown threshold or the energy of laser beam required to cause the breakdown of air and create a spark has been widely studied. Changes in the experimental conditions and changes in the experimental setup can result in a change in the energy required to cause breakdown or breakdown threshold.

The occurrence of breakdown is decided by the laser beam irradiance in the focal region, which is dependent on a number of setup parameters. Experimental setup can be changed by changing laser beam properties or the beam converging lens. The effect of change in laser beam wavelength and laser pulse duration on breakdown threshold is reviewed in [Morgan \(1978\)](#). Beam profile decides the energy density and distribution in the focal region and thus also affects the breakdown threshold. The effect of change in focal length of the converging lens on breakdown threshold has been quantified in [Beduneau et al. \(2003\)](#). Many other parameters of the laser system; laser beam diameter, laser beam divergence, laser pulse frequency also affect the breakdown process.

Laser induced breakdown is also slightly affected by the composition of the gas in which breakdown occurs. [Morgan \(1978\)](#) reviews the breakdown thresholds for different gases keeping all other parameters constant and also the effect of change in pressure on breakdown threshold. The effect of impurities in the gas on the breakdown threshold has also been mentioned.

Fig. 7.1(b) shows the incident and transmitted energies of the laser beam. The region of linear incident and transmitted energy variation is the region where incident energy is below breakdown threshold. Based on these values of incident and transmitted energies, the percentage of laser beam shots that successfully creates spark is plotted as a function of incident energy in Fig. 7.2.

Breakdown threshold is defined as the incident energy at which 50% of incident laser beams create spark. From Fig. 7.2, the approximate value of breakdown threshold can be concluded to be 88 mJ. It can also be seen that for values greater than 91 mJ, 100% of the laser shots resulted in spark. The value of the breakdown threshold was considerably high as compared to other breakdown threshold energy values available in the literature (e.g. [Beduneau and J. \(2003\)](#)). The reason for considerably high breakdown threshold values is the divergence of the laser beam being used for creation of the laser-induced sparks. The laser had a high beam divergence by design. A high divergence of the laser made it difficult to create laser induced sparks and a higher amount of energy was required to create the sparks. The sparks that were created

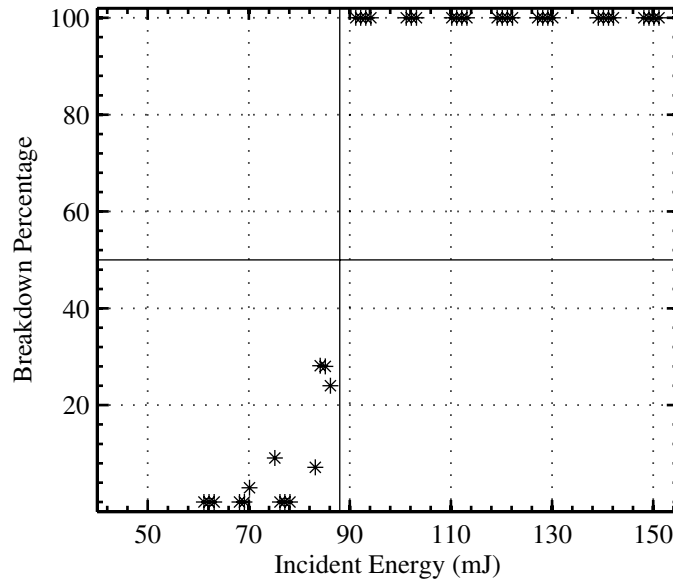


Figure 7.2: Probability of breakdown as a function of incident laser energy.

near the breakdown threshold energy values were also much bigger in size than the ones presented in literature. The bigger size of the laser-induced sparks is desirable for the development of 2D-LIPS technique as bigger size of the spark provides information at higher number of points, resulting in a higher measurement volume.

7.2.3 Spark Energy

It was assumed that the difference between the incident and transmitted energies is absorbed in the spark. The variation of spark energy as a function of incident energy is shown in Fig. 7.3(a). The percentage of energy absorbed increases as a function of incident energy as shown in Fig. 7.3(b). For the current values of incident energies, up to 60% of the incident energy was absorbed in the spark.

7.2.4 Effect of Laser Pulse Frequency

A pulse frequency of 1 Hz is often used for laser ignition experiments so as to avoid the effects of previous breakdown on the generation of plasma. In order to quantify the effect of change in pulse frequency on breakdown threshold, an experiment was conducted with three different laser pulse frequencies. Fig. 7.4(a) shows the variation of transmitted laser beam energy as a function of incident energy for three laser pulse frequencies.

The values of incident and transmitted beam energies were normalized by the values of breakdown threshold calculated for laser-induced plasmas created in

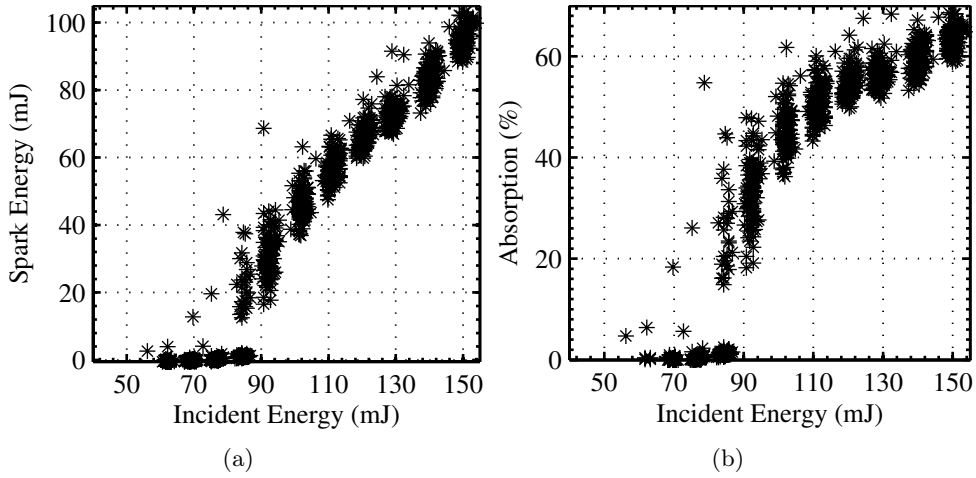


Figure 7.3: *Laser Energy Measurements: (a) Spark Energy as a function of incident energy, and (b) absorption percentage of the laser beam energy as a function of incident energy.*

air flow at 1 Hz. Fig. 7.4(a) shows that there was no significant difference between breakdown threshold energy for 2 Hz and 1 Hz. But the breakdown threshold energy for 5 Hz was slightly smaller. This effect can be more clearly observed in the variation of breakdown probability with incident energy as shown in Fig. 7.4(b). The reason for slight change in breakdown threshold can be the change in laser beam properties.

It can be concluded that there is no change in breakdown threshold for small laser pulse frequencies but small changes in breakdown thresholds are possible for high laser pulse frequencies.

7.2.5 Effect of Presence of Droplets

Experiments for quantifying the effect of presence of droplets were performed for several droplet densities. The objective of this study was to analyze the feasibility of performing simultaneous PIV measurements with laser induced spark ignition. Droplets of Edward's oil No.12 with typical size 2-3 μm were inserted in the air flow and the density of the droplets was varied from zero to a very high level. These oil droplets will be used as seeding particles during simultaneous PIV experiments. The accuracy of the PIV experiments depends on the density of seeding droplets, where a high density results in higher accuracy of velocity measurements. The incident energy of the laser beam was also changed from lower than breakdown threshold up to more than incident energy corresponding to 100% breakdown probability in air.

Fig. 7.5 shows the variation of transmitted energy as function of incident energy for different seeding droplet densities. There is small difference in the two lower subplots corresponding to zero and low droplet densities, where only a few laser

shots appear to be affected by the presence of droplets. But in the top sub-figure, breakdown of laser beams occur even for very low incident energy of the spark and a very high number of laser beams were affected by the presence of droplets. For high density of droplets, experiments were not performed for higher incident energies as almost all laser shots were affected by droplets. The laser induced sparks affected by the presence of droplets could be easily identified by the images of the plasmas acquired by the ICCDs equipped with filters corresponding to oxygen emissions (FB780-10, Thorlabs). Fig. 7.6 shows laser-induced plasmas generated in presence of droplets. Images were acquired 1500 ns after the deposition of spark energy with an exposure time of 90 ns.

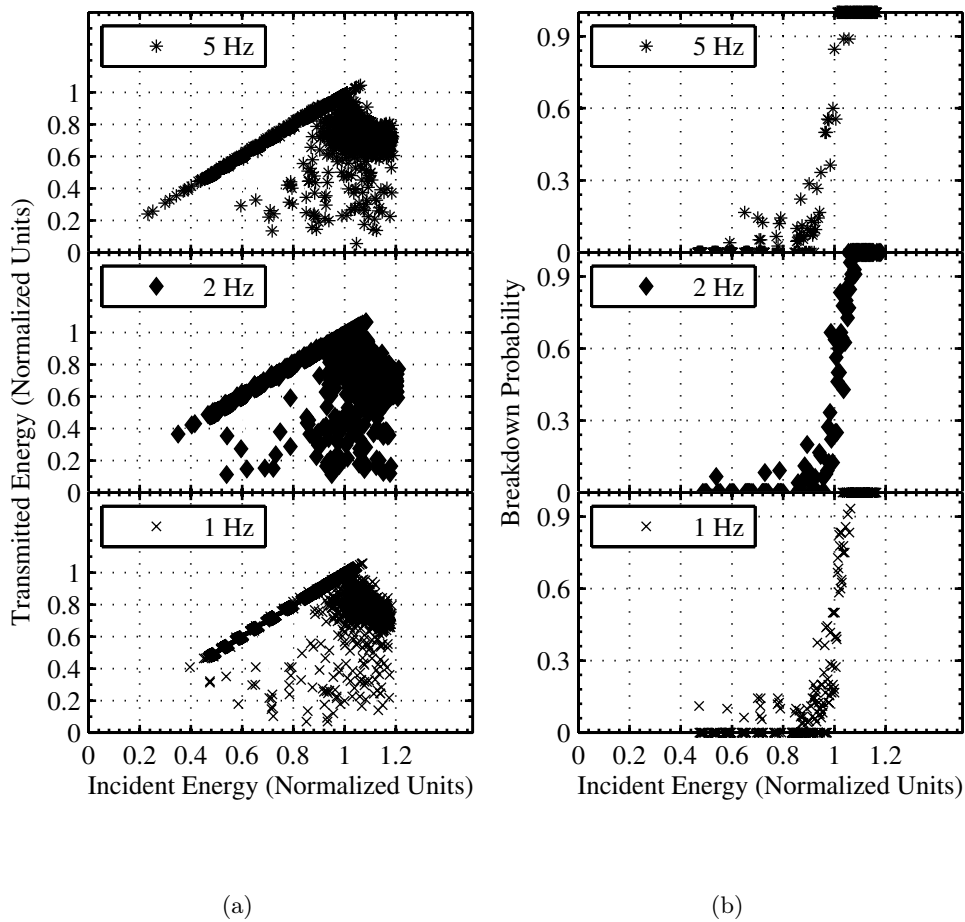


Figure 7.4: Effect of laser pulse frequency on breakdown: (a) Incident vs Transmitted Energy for different laser pulse frequency; and, (b) Breakdown probability as a function of incident laser energy.

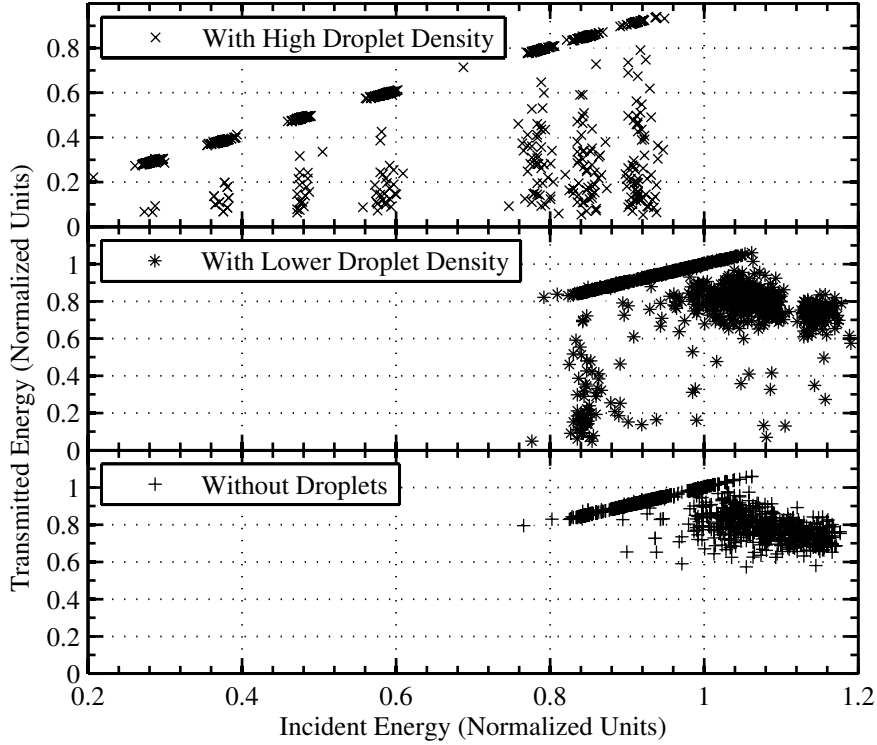


Figure 7.5: *Incident Vs Transmitted energy for different seeding droplet densities.*

The left plasma image shows the type of plasma generated in the absence of droplets. The plasmas affected in the presence of droplets can be seen in the rest of the plasma images in Fig. 7.6. Some of the affected plasma have very different sizes as the laser energy is deposited in very small area. Some of the affected plasmas also occur as multiple sparks. As for low densities of seeding droplets, only a few laser beams were affected; those affected shots were discarded during further analysis.

It can be concluded that low density of droplets affects only a few laser induced plasmas and the affected plasmas can be easily identified and removed. A very high density of seeding droplets can not be used as it erroneously affects the laser-induced plasmas. Therefore a trade-off had to be achieved between the number of plasmas affected and the accuracy of the velocity field measurements that can be achieved with lower seeding density.

7.3 Spectral Measurements - LIPS

Laser-induced plasma spectroscopy data is spatially integrated but temporally resolved measurement of plasma emission intensity. Two important parameters in LIPS measurements are the starting and exposure time of the measurements.

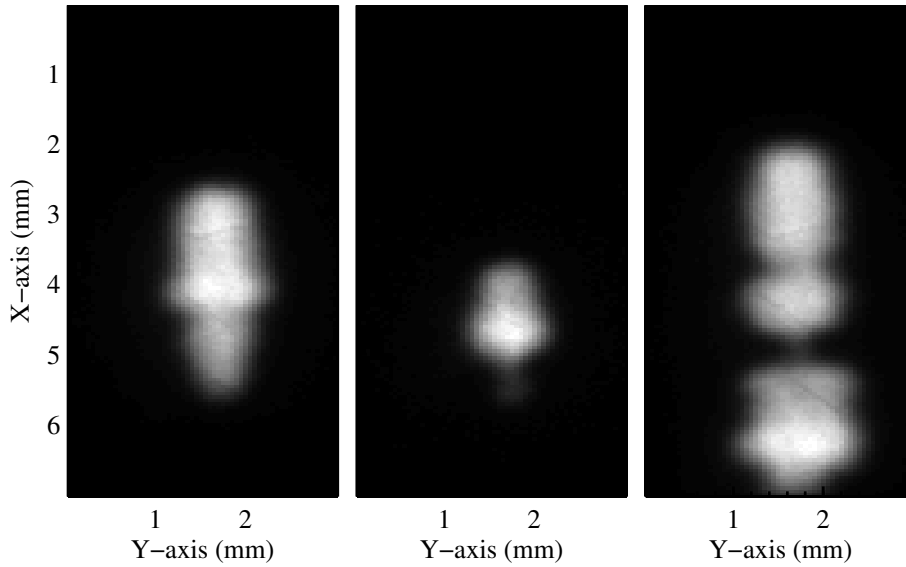


Figure 7.6: Typical images of laser-induced plasmas generated in presence of droplets. Images acquired through oxygen filter ($\lambda = 780 \pm 10 \text{ nm}$), 1500 ns after the deposition of spark energy with a 90 ns exposure.

The time of acquisition of measurements can be accurately controlled by using a BNC 555 Pulse delay generator (*Berkeley Nucleonics*). The PTG attached to the ICCD cameras was used to control the gate width or exposure time of measurements. The reference point for the start of measurements was chosen to be the time of starting of plasma emission, as seen by the spectrometer. The process of measurement of time of initial occurrence of the plasma is shown in the following section.

7.3.1 Initial occurrence of plasma

Laser-induced plasma is formed after the laser is fired, and the time of firing of laser depends on Q-Switch setting, which also determines the energy and the profile of the laser beam. Quality switch (Q-switch) setting is a time delay with respect to the flash lamp. The time of initial occurrence of plasma was measured with respect to the time of flash lamp.

The time of initial occurrence of plasma for the spectrometer measurements as well as ICCD acquisitions were individually identified with respect to the flash lamp delay. Initial occurrence of the plasma in individual measurements were measured for a gate width of up to 2 ns. The delay for which plasma signal first appeared in the equipments was noted to be the time of initial occurrence. Thus the accuracy of plasma occurrence time measurement was 2 ns. The time of initial occurrence of plasma was calculated for fixed Q-switch settings. A change in Q-switch settings required re-calibration of initial times

of occurrences of plasmas.

7.3.2 Time of acquisition

It is known that the spectral emissions from laser-induced plasmas are a function of time and they vary significantly during the life-time of laser induced plasmas. It is also known that during initial stages of plasma, there are mainly ionic emissions. Atomic emissions are present after a few hundred nano-seconds and finally molecular emissions can be detected. Those delays depend on density (pressure - temperature) and on gaseous composition at the location of spark. The intensity seen by the ICCD through a bandpass filter is not only the intensity of atomic emissions but there are some continuum background emissions as well. 2D-LIPS is an imaging technique, in which a band pass filter was used for image acquisition. A part of all emissions with wavelengths within ± 10 nm of center wavelengths of the filter were acquired. Therefore, precaution was taken to select the peaks corresponding to the wavelengths around which there are no other atomic emissions except the desired one.

The bandpass filters that were used, FB780 – 10, FB660 – 10, and FB750 – 10 from *Thorlabs*, have some transmission properties that were taken from the specification sheets provided with the filters (Appendix B). This gives the value of percentage transmission of intensity through the filter as a function of wavelength. A band pass filter with 10 nm FWHM transmits a percentage of intensity for a wavelength range of about 20 nm. Thus, in order to calculate the atomic concentration as seen by the camera, it is important to know the amount of desired atomic emission intensity present in the total intensity seen by the camera. Simultaneous emission spectra acquired by the spectrometer were used to obtain this information. The spectrum recorded with a plasma emitting in a homogeneous gas is equivalent to the spatial integration of emission recorded by the ICCD cameras. A typical spectral measurement from a laser-induced plasma generated in a homogenous mixture of methane and air is shown in Fig. 7.7.

A new parameter, α_λ , was defined which provided the ratio of atomic emissions over the total intensity seen by the ICCD camera. This parameter α_λ was calculated using the spectra acquired with the spectrometer, the knowledge of atomic emission wavelengths obtained from the NIST online database ([Kramida et al. \(2012\)](#)), and the transmission properties of the band pass filter mounted in front of the ICCD camera provided by the specification sheet. In the present study, the purpose was to show feasibility of the 2D-LIPS technique and the measurement of the concentration of oxygen, nitrogen, and hydrogen in a mixture of methane and air. Hydrogen, nitrogen and oxygen atoms emit mainly around 656, 742 – 746, and 777 nm, respectively. So, α_λ was defined as

$$\alpha_\lambda = \frac{I_s}{I_c}$$

where,

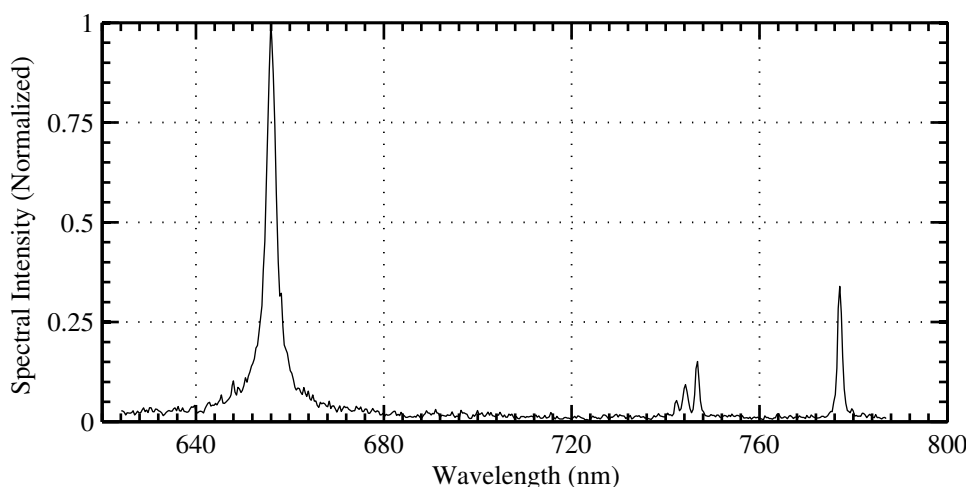


Figure 7.7: Example of single shot spectral emission obtained in methane-air mixture with an equivalence ratio of 0.6, for an integration time of 90 ns at a delay of 1500 ns from plasma formation.

λ = center wavelength of a particular atomic emission.

I_c = total intensity seen by the camera through a particular band pass filter; it was obtained by multiplying emission intensity at each wavelength observed with the spectrometer by the transmissivity of filter at that wavelength.

I_s = Intensity of atomic emission obtained by subtracting the continuum around a peak as recorded by the spectrometer from the total spectral intensity (area of the peak) at the emission wavelength.

Fig. 7.8 shows the the various intensities used in calculating the value of α around the 777 nm wavelength. It can be seen that the continuum level was selected based on the mean of spectra intensity around the peak. Intensity seen by the camera is calculated by multiplying the transmission efficiency of the band pass filter with spectra intensity at corresponding wavelengths, which is the same as ' I_c '. And, amount of oxygen seen by camera is calculated by subtracting the continuum level from the spectral intensity for the wavelengths corresponding to oxygen atomic emissions, which is same as ' I_s '.

In order to quantify the effect of time from the starting of the plasma on the plasma properties, experiments were performed for different time delays between 200 ns to 3000 ns. The time from the starting of the plasma up to 200 ns after the starting was not useful for these measurements as there were very high ionic emissions making it impossible to capture atomic emissions. Integration time of the measurement was increased from 10 ns for 200 ns delay up to 200 ns for 3000 ns delay. The integration time is decided depending on the intensity of the spectra as observed by the spectrometer. The intensity seen by the spectrometer should not be very high, as it will saturate the ICCD and intensity could not be kept very low, in order to have enough signal. 100 shots

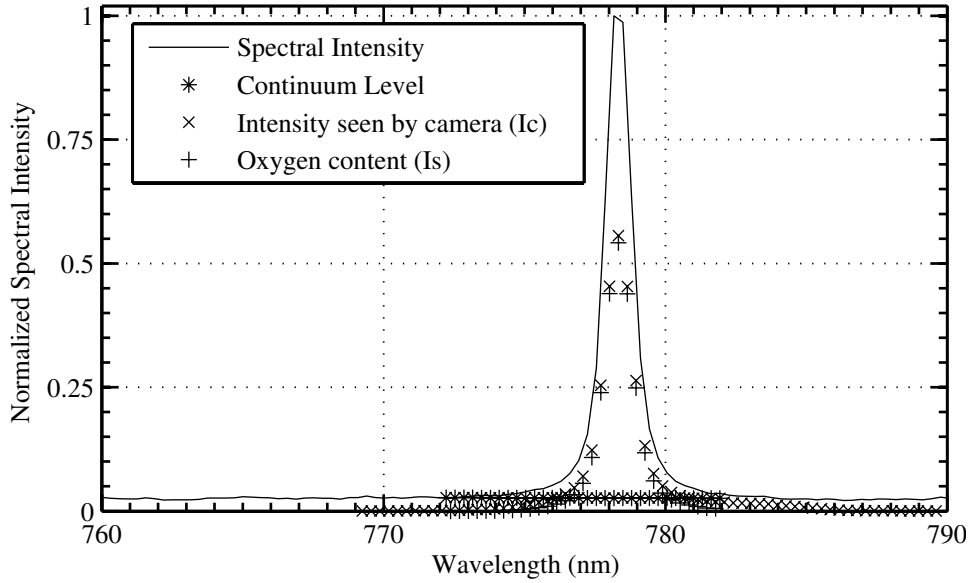


Figure 7.8: Mean spectra and various values used in calculating α

were recorded for each delay setting and last 90 were used for the analysis, in order to have constant laser beam properties.

The normalized intensity of the plasma spectral emission for each delay was calculated by dividing the intensity observed by the spectrometer minus the background with the corresponding integration time and further dividing it with the same value calculated for the delay of 200 ns. Images of the plasma were simultaneously acquired for same integration times and delays with respect to the starting of the plasma. The area of the plasma was calculated by counting the number of pixels on the image (after background subtraction) having a intensity greater than 20 % of the maximum intensity of the image.

The mean values of α_λ , area, normalized intensity, and aspect ratio are presented in Fig. 7.9 as a function of the time delay after the initial occurrence of the plasma.

The variation of normalized intensity of the plasma shows that the intensity of the plasma decays exponentially (Fig. 7.9). In this case the intensity after 2000 ns from the starting of the plasma was only about 10% of the intensity after 200 ns from the starting of the plasma. It is necessary to have enough intensity of the plasma in order to achieve sufficient signal-to-noise ratio for single shot study. The area of the plasma first increased with time, achieved a maximum around 1400 ns, and then decreased again (See Fig. 7.9). A higher area of the plasma means that more pixels on the ICCD have information of intensity values, and thus concentration ratio values can be retrieved at more number of points, i.e. a higher measurement area or volume. Aspect ratio of the plasma (L/w in Fig. 7.9), defined as the ratio of maximum length and maximum width of the plasma, also first increased with time and then decreased. If the

laser induced plasma is supposed to be axi-symmetric, then a higher aspect ratio means that the cross sectional area of the plasma is relatively low. Thus a higher aspect ratio means lesser effect of the along-the-sight integration on the measurements.

Spectral properties of plasma were also a function of delay. The parameter α_{777} , already defined as a measure of oxygen emission intensity seen by the camera, increased with time, reached maximum values of the order of 0.7 around a delay of 1300 ns and then remained almost constant up to 2500 ns. The variation of α_{744} shows a similar tendency. The maximum magnitude of α_{744} is of the order of 0.5. Thus the magnitude of α_{744} is less than α_{777} which means that if these

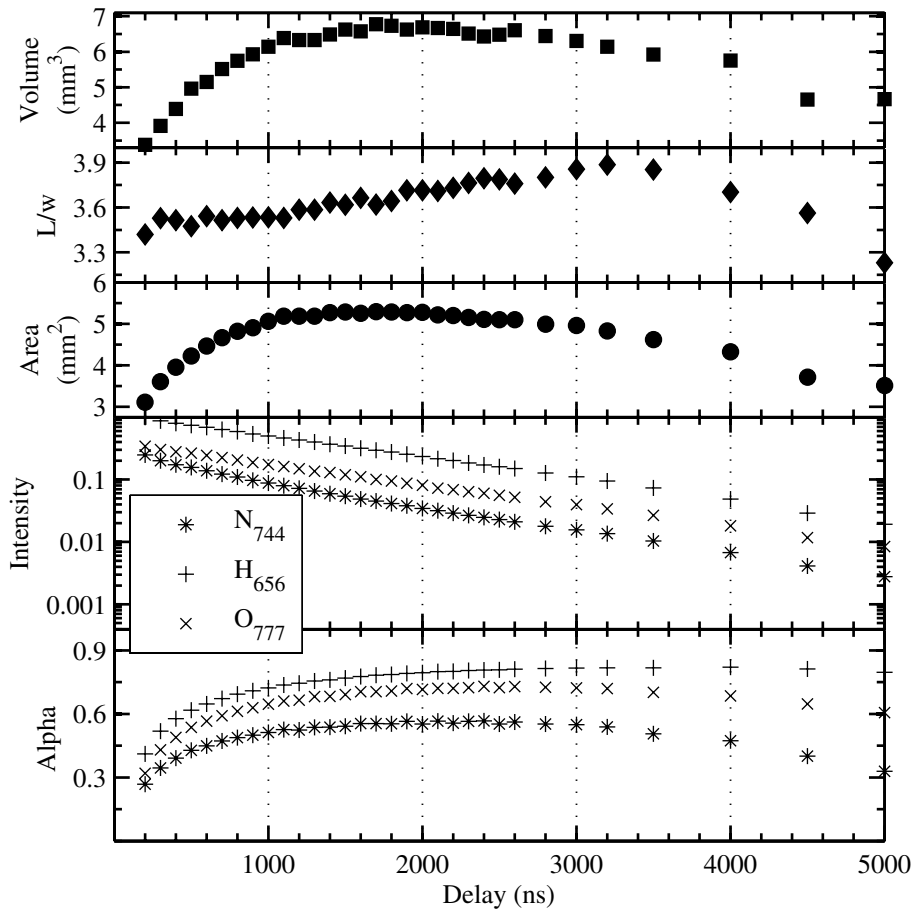


Figure 7.9: Effects of delay after plasma formation on, from top to bottom: (1) volume of the plasma, (2) aspect ratio of the plasma, (3) area of the plasma image, (3) normalized intensity for different atomic emission and (4) α for the same atomic emissions, as a function of time after the initial occurrence of plasma; plasma created in premixed air-methane mixture with an equivalence ratio of 0.6.

peaks are used for the identification of nitrogen and oxygen peaks respectively, then oxygen will be more accurately measured as compared to nitrogen. The magnitude of α_{656} (corresponding to hydrogen emission) was much higher in comparison with other two atomic emissions and it also followed the same pattern as the parameter for other two atomic emissions. The absolute values of these parameters were a function of the instantaneous peak heights of the different atomic emissions or the local equivalence ratios. Nevertheless, this study provided the times of acquisition to obtain best results from 2D-LIPS measurements. Considering all parameters together, the region between 1300-1700 ns seems to be most suited to the requirements of 2D-LIPS technique.

7.4 Image acquisition

The 2D-LIPS technique requires to image the plasma simultaneously with two ICCD cameras equipped with two different bandpass filters. Images of the plasma were recorded for same delays and integration times as spectrometer measurements. Fig. 7.10 shows mean plasma images for different starting times of measurements. The variation of size of these plasma measurements as a function of starting time of measurements is already shown in Figure. 7.9.

To compute the ratio of light intensity acquired by the two cameras, the two cameras have to be set with exactly the same field of view. As each pixel on the ICCD cameras corresponds to approximately $50 \times 50 \mu\text{m}$ field of view, a μm order accuracy is required in the spatial alignment. This order of spatial

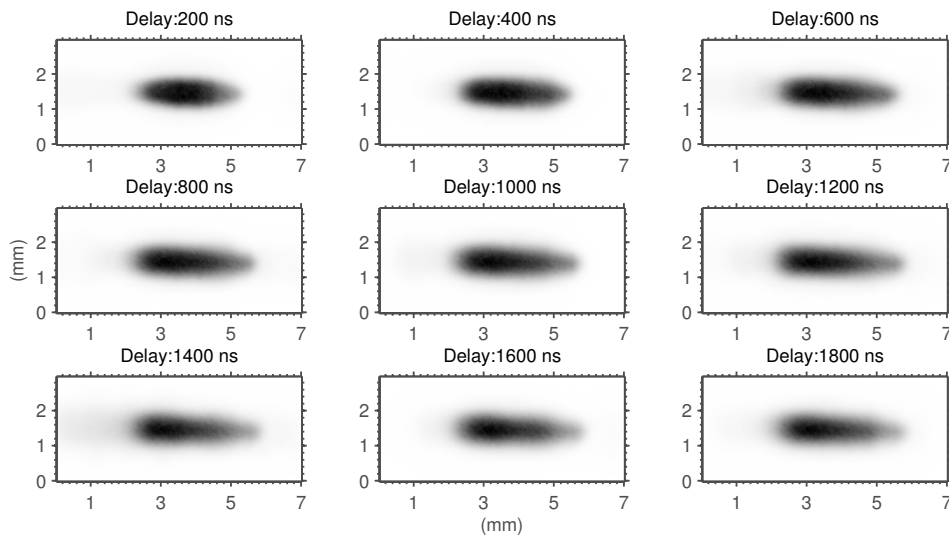


Figure 7.10: Mean Images of laser-induced plasmas in air, acquired with oxygen filter for different delays with respect to the initial occurrence of plasma; Spark energy = 30 mJ

accuracy in the alignment of ICCDs could not be obtained physically. Therefore, after best possible physical alignment, pixel order accuracy was obtained using numerical image processing techniques.

7.4.1 Image correlation

The correlation of the two images simultaneously obtained by the ICCD cameras was an important step in the development and use of the 2D-LIPS technique. Various methods were attempted to obtain best correlation between the images from the two ICCD cameras.

7.4.1.1 Correlation through PIV measurements

For this correlation approach, the experimental setup was modified to create a laser sheet just above the nozzle. Emission wavelength of the laser beam was changed to first harmonic, i.e. 532 nm by adding the doubling crystal in front of the laser. A plano-concave lens of focal length -500 mm in combination with a bi-convex lens of focal length 250 mm was used to create a sub-millimeter thick laser sheet. This laser sheet was used to illuminate droplets of Edward oil n°12 with size of the order of $2 - 3 \mu\text{m}$ injected in the central region of the burner. Both ICCDs were equipped with band pass filters having center wavelength of 530 nm (*FB530-10, Thorlabs*), in order to allow the cameras to acquire the Mie-scattering from the oil droplets. The simultaneous images of droplets were captured for identical delays with respect to laser and for identical integration times. Background corrected droplet images were imported in Flow Manager, a *DANTEC DYNAMICS* software tool, generally used for PIV. An adaptive correlation was performed on the images with the following parameters: an initial interrogation window size of 256×256 pixels, a final interrogation window size of 16×16 pixels, 50% interrogation area overlapping, no filter, a moving average validation with acceptance factor of 0.1 and a peak validation with minimum peak ratio of 1.15. Correlation of these images allowed computation of transfer matrix between the two cameras to correct translation, rotation and magnification between the Mie-scattering images.

The displacement matrix, thus obtained, is a property of the relative position of the cameras. The same displacement matrix could be applied to the images of plasma captured with the same cameras irrespective of the filters in front of the cameras. The displacement matrix, after interpolation, was used to transform the plasma images acquired with same cameras.

However, another step was performed to achieve sub-pixel accuracy and to remove the difference that might have occurred due to the change in filters. The plasma images obtained after the first transformation were imported to Flow Manager and another correlation was performed with identical parameters as earlier. The second transformation provided an exact match in the position of the plasma on the two images. This was confirmed by correlating the final

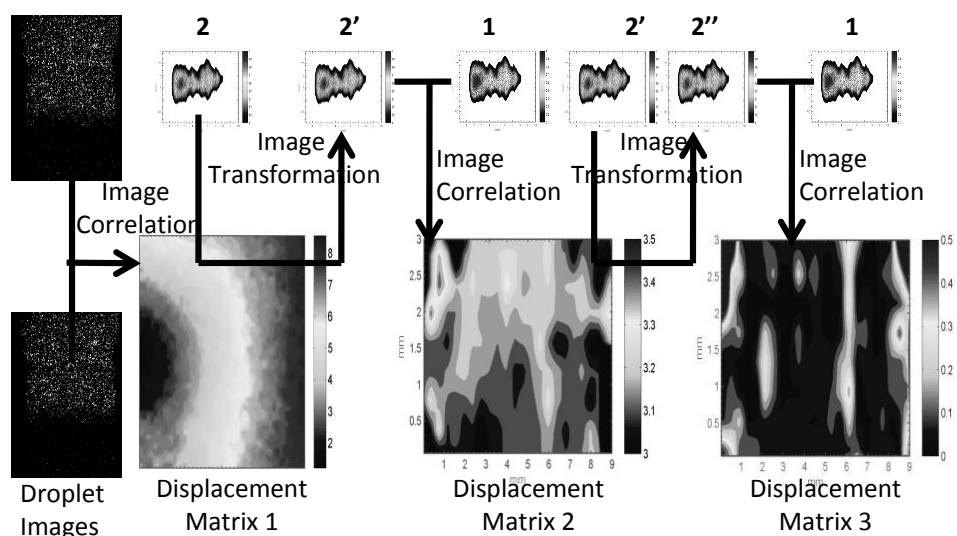


Figure 7.11: *Image Correlation Procedure.*

plasma images and noticing that the displacement matrix thus obtained had elements smaller than 0.3 pixels.

Using this two step calibration procedure, a sub pixel accuracy in the location of the plasma was achieved as shown by the final displacement matrix in Fig. 7.11. This calibration procedure was used for analysis of experiments performed with sparks created in a flow of air. The velocity of the air flow was kept constant at 0.9 m/s. Filters corresponding to nitrogen emissions were installed on both ICCD cameras. The spark energy corresponding to fix Q-switch setting was 97.2 ± 3.1 mJ. The intensity ratio of the two images acquired by the ICCD cameras showed fluctuations of the order of 10 %. The fluctuations were higher specially around the edges of the plasma as can be seen in the intensity ratio plot shown in Fig. 7.12. The reason for these undesirable issues could be not-so-good first image correlation or second correlation step where correlation was not good for pixels around the edges.

7.4.1.2 Correlation through grid image and PIV processing

In order to avoid changing the filters from the ones corresponding to the desired atomic emissions to the ones corresponding to Mie scattering of droplets, another method of first image correlation step was attempted. In this method, a planar grid (See Fig. 7.13) was installed in the plane containing the location of the spark and perpendicular to the axis of the ICCD cameras. The grid was illuminated by a spot light and the image of the grid was acquired by the ICCD cameras for very high exposure times. The filter in front of the ICCD cameras was kept the same as the desired atomic emission measurements. The gain and exposure time of both the cameras were individually adjusted to obtain good

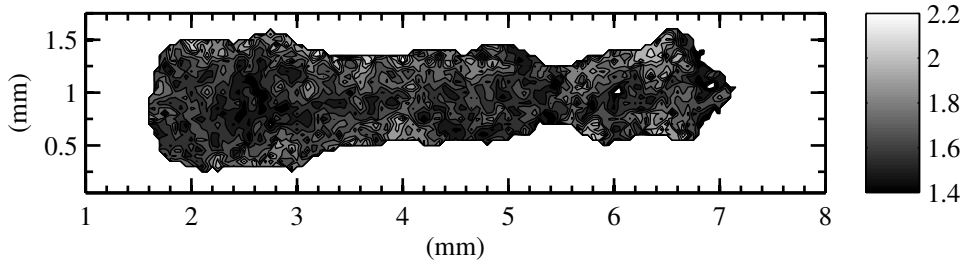


Figure 7.12: Intensity ratio of images obtained after image correlation using PIV measurements; Images acquired with nitrogen filters on both cameras, laser-induced spark of energy 94.8 mJ created in a constant flow of air.

enough signal to noise ratio. In this method initial field of views of the two cameras could be better aligned because they were aligned by focussing the cameras on a stationary grid image while instantaneous droplet images were used in the the previous method. Droplet images were different for each frame making the process of alignment difficult.

The images of the grid acquired through two ICCD cameras were correlated using the PIV image correlation tool, *Dynamic Studio* by *Dantec Dynamics*. The parameters for correlation of images was kept same as in previous method. The correlation matrix thus obtained was used to transform one of the images of the laser-induced plasma. The second step to achieve sub-pixel accuracy was performed by correlating the images obtained after first transformation. The displacement between the transformed images was calculated using the image correlation tool, *Dynamic Studio*.

This calibration procedure was used for analysis of experiments performed with

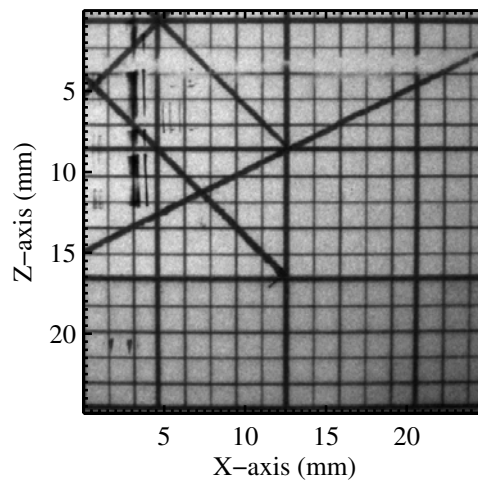


Figure 7.13: Typical image of the grid used for initial image calibration.

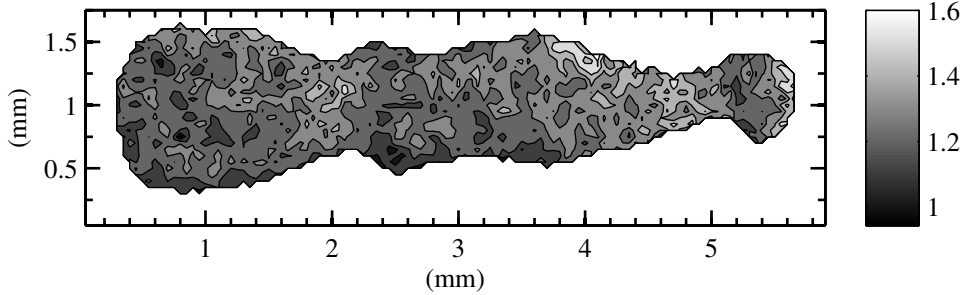


Figure 7.14: Typical intensity ratio (O/N) obtained using image correlation through a grid image and image processing with Flow Manager; Images acquired with oxygen and nitrogen filters on ICCD cameras, laser-induced spark of energy 117 mJ created in a constant flow of air.

laser-induced sparks in a constant flow of air. Spark energy corresponding to constant Q-switch setting was 116.6 ± 3.1 mJ. Camera 1 was equipped with filter corresponding to nitrogen emissions ($\lambda = 750 \pm 10$ nm) and camera 2 was equipped with filter corresponding to oxygen emission ($\lambda = 780 \pm 10$ nm). Images corresponding to oxygen emissions were divided by images corresponding to nitrogen emissions to obtain intensity ratio.

This method of image correlation resulted in slightly better intensity ratios as fluctuations of the order of 9 % were observed. However, this method also resulted in some issues around the edges of the plasma as can be seen in a typical intensity ratio calculated after correlation of images using this approach as shown in Fig. 7.14.

7.4.1.3 Correlation through grid image and bounding box approach

A bounding box approach was attempted as an alternate approach to reduce the number of steps in the image correlation process which might be leading to high fluctuations in the calculation of intensity ratios. The correlation of plasma images with PIV software also needed to be avoided. As a first step, a grid image was acquired and used for first correlation in the same way as in the previous method.

In second step, a bounding box was selected around the plasma images. This step ruled out the need to calculate the translation between the two plasma images through PIV processing techniques. The size of the two bounding boxes provided the magnification between the images. The first step was performed carefully to take care of rotation and magnification between fields of views of the two cameras. And the bounding box approach was then applied to the images obtained after one image transformation.

After first image transformation, an intensity threshold was applied to the plasma images. The pixels having intensity level less than a threshold, which

was selected as a few percentage of the maximum intensity for that plasma shot were ignored. A rectangular box was selected around the remaining pixels. It was observed that the width and length of these boxes in the two images had a maximum difference in the range of 0-2 pixels for bounding box sizes of the order of 100×40 pixels. This proved that first transformation had already corrected most of the translation and rotation that was present in the field of view of the two ICCD cameras. One of the image frames was resized to have the same size as that of the second image frame.

This calibration procedure was used for analysis of experiments performed with laser-induced sparks in a constant flow of methane-air mixture with equivalence ratio of 0.9. Spark energy corresponding to the constant Q-switch setting was 112.5 ± 5.0 mJ. Camera 1 was equipped with filter corresponding to hydrogen emissions ($\lambda = 660 \pm 10$ nm) and camera 2 was equipped with filter corresponding to oxygen emission ($\lambda = 780 \pm 10$ nm). Images corresponding to oxygen emissions were divided by images corresponding to hydrogen emissions to obtain intensity ratio.

This method of the image correlation provided better intensity ratio calculation measurements as compared to previous two approaches. Although intensity ratio calculations showed fluctuations of order of 9 %, which is same as the previous approach but fluctuations are not particularly high around the edges as shown in Fig. 7.15. Therefore, this approach was selected for calculations of intensity ratio in 2D-LIPS experiments.

7.4.2 Calculation of intensity ratio

Images obtained after correlation and transformation were processed to find the ratio of intensities and compute the concentration of atoms based on this ratio. The images represent line of sight integrated measurements of the plasma emission intensity. In the current experiments the variation of concentration

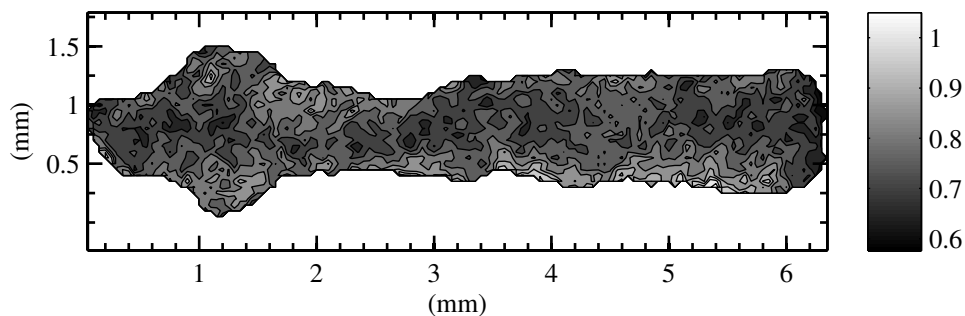


Figure 7.15: Typical intensity ratio (O/H) obtained using bounding box approach; Images acquired with oxygen and hydrogen filters on ICCD cameras, laser-induced spark of energy 110.4 mJ created in a constant flow of methane-air mixture with equivalence ratio of 0.9.

along the line of sight was ignored. Therefore, inverse Abel transform can be performed on laser-induced plasma images before calculating the intensity ratio. Nevertheless, not too much variation is expected in intensity ratio calculations, as dividing two images nullifies the effects of line-of-sight integration. However, Abel transform was applied to some of the images and the results are presented in Section 8.2.2.

The two image frames obtained from the previous step were divided to obtain the intensity ratios. Typical intensity ratio calculation step is shown in Fig. 7.16. It shows the selection of bounding box comprising pixels with intensity values greater than 33% of the maximum intensity of the corresponding image frames. The division of these frames provided intensity ratio inside the region of plasma. The fluctuations in intensity ratio could be reduced by applying digital filters but it resulted in degradation of spatial resolution. The methods for improvement of intensity ratio are presented in the following section.

7.4.3 Accuracy of intensity ratio calculations

Some mathematical tools were utilized to obtain most accurate intensity ratios. Data acquired during experiments presented in Section 7.4.1.3 was used for this analysis. The threshold of intensity selected for bounding box size calculations was varied from about 10% to 50% in small steps in order to calculate the effect of threshold level on the accuracy of calculations. Fig. 7.17 shows the variation of standard deviation as a function of intensity ratio threshold. The standard deviation is the mean of standard deviations of 90 intensity ratio plots. The absolute standard deviation was also divided by the mean of intensity ratio to obtain relative standard deviation. Fig. 7.17 also shows the variation in number of pixels where intensity ratio information was available. It can be seen that both level of fluctuations and measurement area or number of pixels with useful information reduces with an increase in intensity threshold. The reason for lower level of fluctuations with higher intensity threshold is the removal of pixels closer to edges which have relatively higher fluctuations. An undesired consequence of the increase in accuracy was the decrease in the number of pixels/points or measurement area where information was available. Thus a trade-off between the accuracy required and measurement volume required had to be achieved.

As another step to reduce the fluctuations of the intensity ratio, digital filtering of the data was performed. Different finite impulse response (FIR) filters of type *average* were attempted and their effect on the level of fluctuations was quantified. The size of the filter decided the resulting spatial resolution. The original spatial resolution was 50 μm ; a filter of size 2×2 results in a resolution of 100 μm and so on. A fixed intensity threshold of 33% was used for the calculations for effects of FIR filters. Fig. 7.18 shows the effect of size of FIR filter or corresponding spatial resolution on the level of fluctuations in intensity

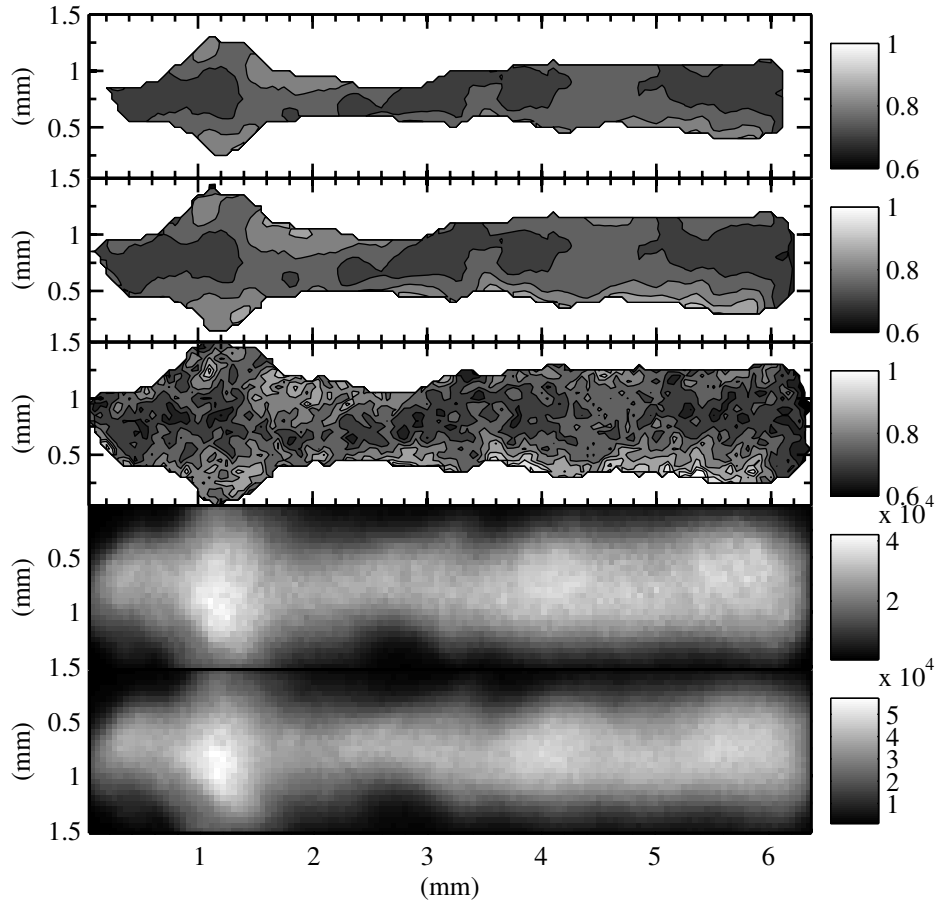


Figure 7.16: Steps of intensity ratio calculation for a laser-induced plasma of spark energy 110.4 mJ, generated in an air-methane mixture of equivalence ratio 0.9. From bottom to top: (a) Image from camera 1 corresponding to hydrogen emission. (b) Image from camera 2 corresponding to oxygen emissions. (c) Intensity ratio obtained after division of images (O/H) (fluctuations 8.19 %). (d) Intensity ratio obtained after applying an average filter of size 4×4 pixels, therefore resulting in a spatial resolution of $200 \mu\text{m}$ instead of actual resolution of $50 \mu\text{m}$ (fluctuations 5.73 %). (e) Intensity ratio obtained after removal of edges using a disk of size 2 (fluctuations 4.37 %).

ratio and the measurement area where information is available. An *average filter* of size 4×4 pixels provides a mean fluctuation level of approximately 0.07 or 7%.

Therefore the combined application of 33% intensity ratio threshold and an FIR filter of size 4×4 reduces the level of fluctuations from 0.145 (corresponding to no filter and 10% intensity threshold) to 0.07. As an undesired consequence the number of points where information is available is also reduced from approximately 3500 to 1700. The intensity threshold and the size of the filters

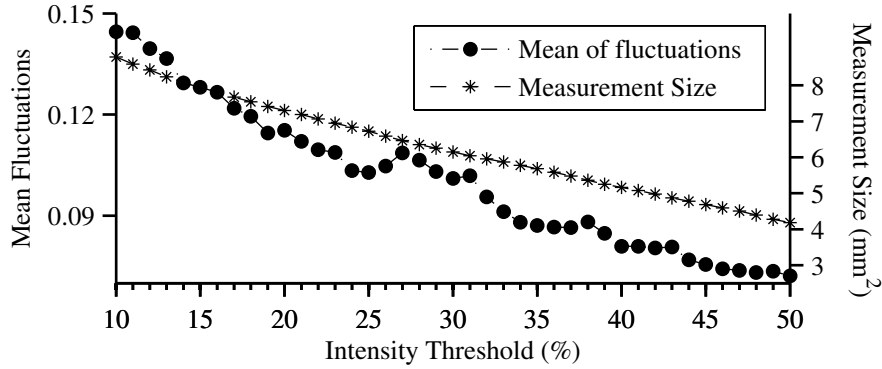


Figure 7.17: Variation of standard deviation in calculations of intensity ratio and the number of points/pixels where intensity ratio information is available for different levels of intensity ratio threshold.

can be decided on the basis of required accuracy and measurement volume. These parameters also depend on the shape and properties of the laser-induced plasmas and therefore should be decided on the basis of given laser and plasma generation systems.

Another step in order to reduce edge effects on intensity ratio was to remove the edges. In order to remove edges, disks of different sizes were chosen and pixels along the edges of the intensity ratio values were removed using “imerode” function of MATLAB[®]. The results of edge removal are shown in Fig. 7.19. It shows that fluctuations are considerably reduced with increasing size of disk for removal of edges. This points to the fact that fluctuations are higher closer to the edges as compared to the center of the plasmas. However, the reduction in fluctuations results in big loss of the measurement area. Thus a big size of disk

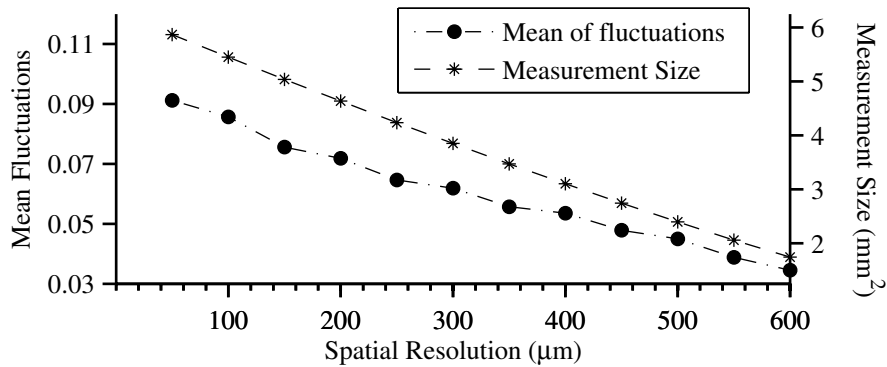


Figure 7.18: Variation of standard deviation in calculations of intensity ratio and the number of points/pixels where information is available with size of digital FIR filters or resulting resolution of measurements.

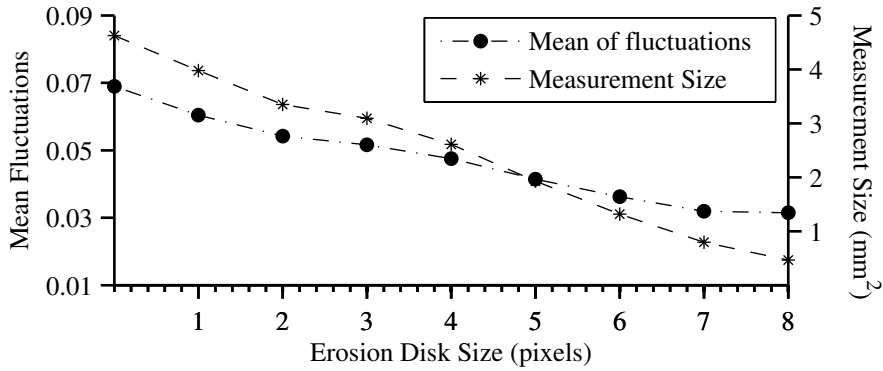


Figure 7.19: Variation of standard deviation in calculations of intensity ratio and the number of points/pixels where information is available with size of erosion disk for a fixed filter size of 4 and an intensity threshold of 33%.

for edge removals should be chosen only if a very high accuracy of measurements is required.

A combination of all these methods can be used to obtain good intensity ratio values from the two ICCD images. However, a trade-off has to be decided between the accuracy and measurement volume depending on the application of the 2D-LIPS technique.

Chapter 8

Application and validation of 2D-LIPS

The objective of the development of 2D-LIPS technique was to measure spatially resolved equivalence ratios in combustible environments. However, in order to validate the technique, 2D-LIPS was first applied to measurements in non-reactive spatially varying mixtures and then to reactive non-premixed mixtures.

8.1 Validation in non-reacting conditions

For the validation of 2D-LIPS technique, a laminar mixing layer of nitrogen and air flows was created using the experimental setup presented in Fig. 3.2 and the co-flow burner presented in Fig. 3.1. Air was injected through the central nozzle at a velocity of 0.9 m/s while nitrogen was injected in the annular region at a velocity of 0.3 m/s. The Reynolds number of the inner jet was equal to 1200 leading to a laminar flow; this configuration allowed to create a steady mixing layer above the lip of the nozzle with a concentration of oxygen changing from 21% in the center to 0% in the annular region. Plasma was formed at a height of 2 cm from the nozzle lip. The location of the plasma was moved through the central to the annular region of the nozzle to measure the whole mixing layer thickness. In the present configuration, the Peclet number of the flow was significantly larger than unity so the mixing layer geometry was determined by the gas velocity profile and mass diffusion could be neglected. ICCD cameras were equipped with band pass filters corresponding to oxygen and nitrogen emission peaks.

Now, the bounding box approach was applied to the data acquired for the measurement of mixing layer in the air-nitrogen co-flow. The ratio of oxygen-to-nitrogen emission was calculated using the two simultaneous images. Intensity ratio calculations using the bounding box approach for a typical case are pre-

sented in Fig. 8.1. Four sub-figures of Fig. 8.1 show the bounding boxes selected around the two images, the resized frame, and the intensity ratio obtained by dividing the two frames. The pixels where intensity ratio values were calculated was fewer than the pixels where plasma emission intensity values were available. Application of post-processing techniques, presented in Section 5.5.2.1, reduced the number of pixels where intensity ratio information could be accurately calculated. The intensity ratio sub-figure shows the variation of intensity ratios of images corresponding to camera 2 and camera 1. Camera 2 corresponded to oxygen atomic emission and camera 1 corresponded to nitrogen atomic emission. The central region of the burner (containing air) was towards the left of these frames, and annular region (containing nitrogen) was towards the right of these frames. The laser beam direction was from right to left. The intensity ratio variation inside the plasma region shows higher oxygen-by-nitrogen ratio towards the left and lower oxygen-by-nitrogen intensity ratio towards the right. It shows the potential of 2D-LIPS technique for measurements of spatially resolved concentration ratios. However a calibration step was performed to relate

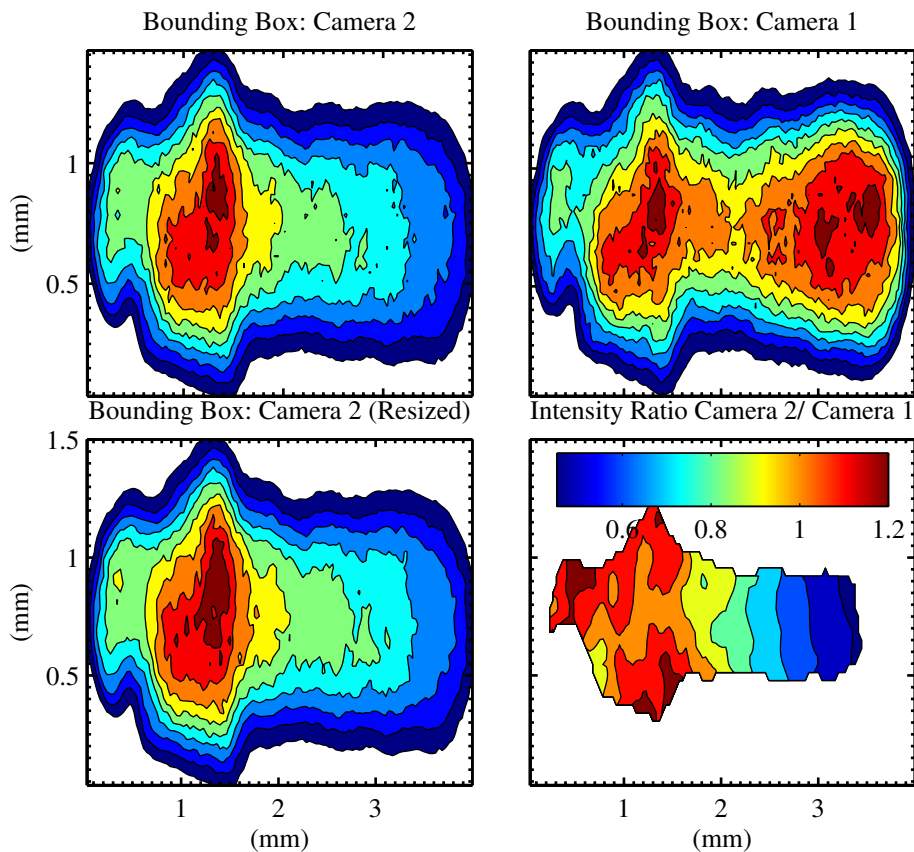


Figure 8.1: Typical intensity ratio calculations using the bounding box approach in the region of concentration gradient.

intensity ratio values to concentration ratio values.

8.1.1 Calibration Intensity Ratio and Concentration

The intensity ratio obtained from the 2D-LIPS technique corresponds to a particular atomic concentration ratios. To relate an intensity ratio to a relative concentration of oxygen versus nitrogen, a calibration was required with different mixtures containing different known oxygen versus nitrogen concentrations. The setup presented in Fig. 3.2 was used and a fully premixed mixture of nitrogen and air was injected through the central element of the nozzle. The concentration of oxygen was linearly varied from 0 % – i.e. nitrogen – to 21 % – i.e. air.

To find the calibration curve for relating intensity ratio of the cameras to concentration ratio, mean of intensity ratio at all pixels for a single shot was calculated. Mean and error-bar of 100 such values for a fixed concentration is plotted in Fig. 8.2. This plot acts as a map to calculate the concentration ratio for non premixed flows. It can also be noted in Fig. 8.2 that the value of image intensity ratio for zero oxygen concentration is not zero, which was because the intensified cameras still capture the background continuum for the corresponding wavelength range.

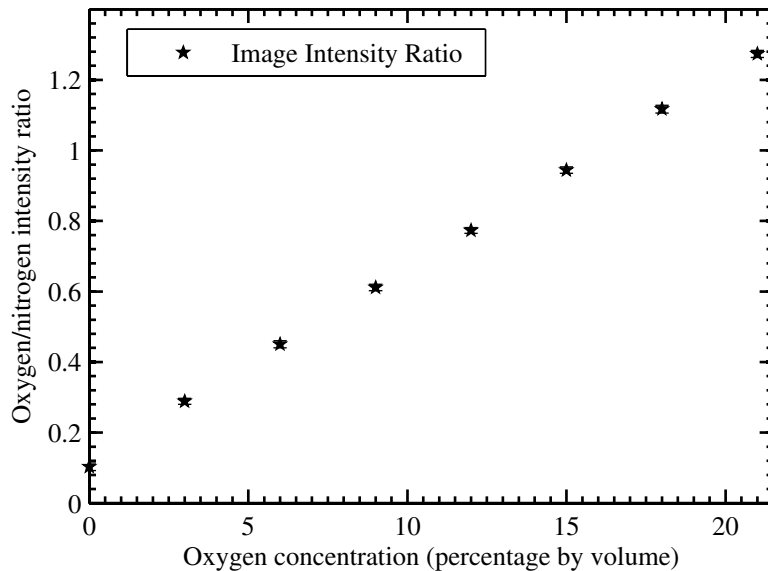


Figure 8.2: Evolution of the image intensity ratio of oxygen over nitrogen emissions as a function of the oxygen concentration.

8.1.2 Comparison between LIPS and 2DLIPS

During the calibration step, when the mixture was perfectly premixed, spectral intensity ratios of oxygen and nitrogen were obtained simultaneously with a conventional spectrometer (LIPS). A linear relation between the spectral intensity ratio and the concentration was found as can be seen in Figure 8.3. The spectral measurements were acquired at same time and for same exposure time as that of images.

The fluctuations shown in Figure 8.3 can be used to compare the 2D-LIPS and 0D-LIPS (conventional LIPS) technique, if both are used for single point measurements. For spectral data, fluctuations are a measure of shot to shot fluctuations and for 2D-LIPS data, fluctuations are the fluctuations in mean intensity ratio over the whole plasma images. The intensity ratio obtained by images has fluctuations of the order to 1% while the spectral intensity ratio has fluctuations of the order to 10%.

This proves that if 2D-LIPS is used as an alternate to the conventional LIPS technique, then single shot accuracy of concentration ratio measurements can be greatly increased.

8.1.3 Measurement of mixing layer

During experiments with non-premixed flow, when the location of the plasma was changed, the actual mixture at the location of the plasma changed from air to pure nitrogen. The plasma location was changed in steps of 1 mm,

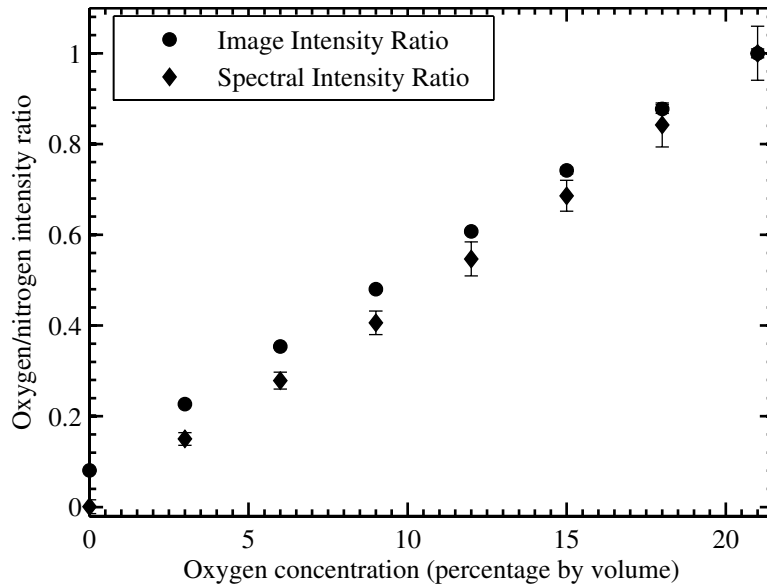


Figure 8.3: Comparison of 0D-LIPS and 2D-LIPS technique: Mean and fluctuations of 2D-LIPS and 0D-LIPS measurements as a function of oxygen concentration.

and the size of the plasma was of the order of 4 mm. Therefore parts of the plasma at one location overlapped with parts of plasma at nearby locations. In order to measure the mixing layer width, the intensity ratio at a fixed vertical location was chosen, where intensity ratio was plotted as a function of horizontal direction. The mean and fluctuations of all intensity ratio values obtained from 2D-LIPS technique is plotted as a function of axial distance in Fig. 8.4. Intensity ratio measurements shown in Fig. 8.4 show constant level of fluctuations in intensity ratio values above central part of the burner. The level of fluctuations increases in the mixing layer where concentration of oxygen decreases and that of nitrogen increases. Then the level of fluctuations again decreases at radius of approximately 15 mm location, where pure nitrogen is expected. Further, the level of fluctuations again increases as nitrogen flow traps some ambient air. These result show that the level of fluctuations is low in region of constant concentration while it is higher in region of concentration gradients.

8.1.4 Reason for fluctuations in mixing layer

In order to find the reason for fluctuations in measurements, specially in the region of gradients, it is first necessary to verify if these fluctuations were not because of actual concentration fluctuations in the mixing layer. Simultaneously acquired spectral and velocity measurements were used to retrieve that information. The measurements performed for calibration of intensity ratio to obtain concentration ratio provided the expected level of uncertainty in perfectly pre-mixed conditions. Fig.8.5 shows the uncertainty in the measurements of oxy-

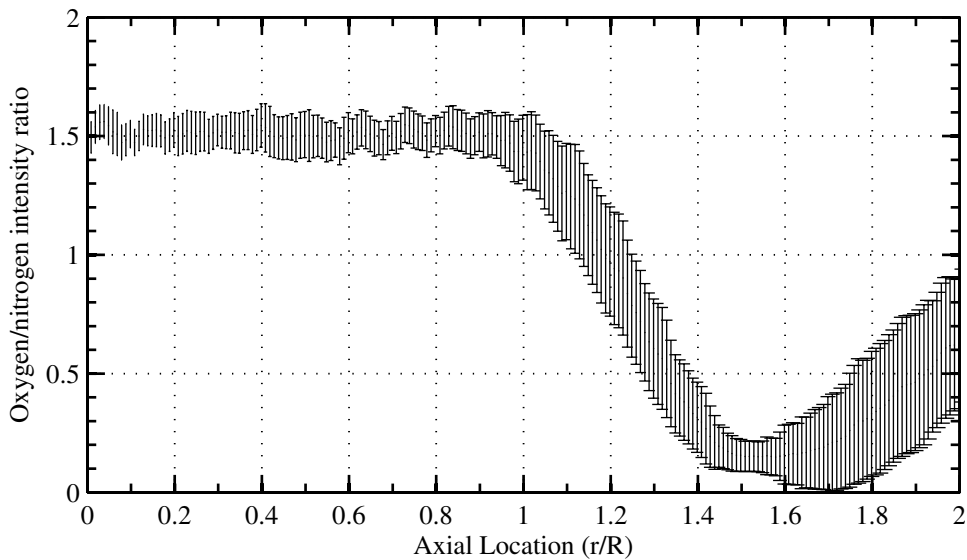


Figure 8.4: Variation of oxygen-by-nitrogen intensity ratio as a function of axial distance from the center of the burner.

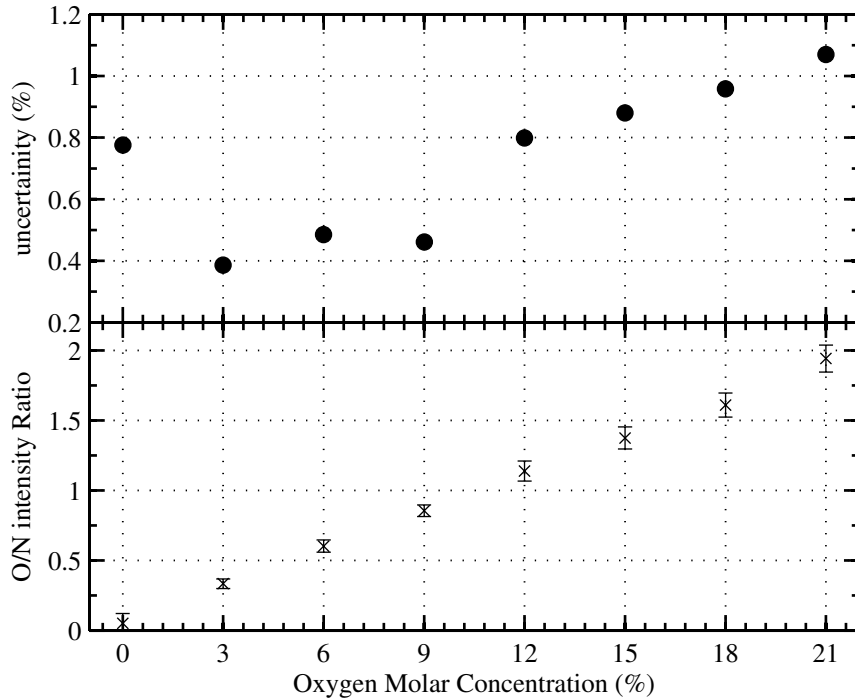


Figure 8.5: Analysis of the spectral data in premixed conditions. From bottom to top: (a) Oxygen/Nitrogen ratio as calculated from spectral measurements as a function of input oxygen concentration (b) uncertainty in the measurements of oxygen concentration for given input oxygen concentration.

gen concentration for given oxygen concentrations in premixed gases. For 3% oxygen concentration, an uncertainty of 0.4% was observed which means LIPS measurements show measured oxygen concentration between 2.6 and 3.4%. Approximately linear variation of uncertainty with concentration shows that fluctuations in measurement are constant and independent of actual concentration.

Now, the calculations of the spectral data was performed for the mixing layer experiments. Fig.8.6 shows the mean level of relative fluctuations as a function of location above the burner. Top subfigure of Fig.8.6 shows the difference between uncertainty in actual measurements and the expected uncertainty corresponding to the mean level of oxygen concentration (Using Fig.8.5). This proves fluctuations observed in the region of gradients is much higher than the fluctuations observed in the region of constant concentration. The uncertainty in the region of gradients reach up to a level of 1% higher than the expected uncertainty as obtained from calibration experiments. This concludes that the reason for these fluctuations must be physical fluctuations of concentration in the region of concentration gradients.

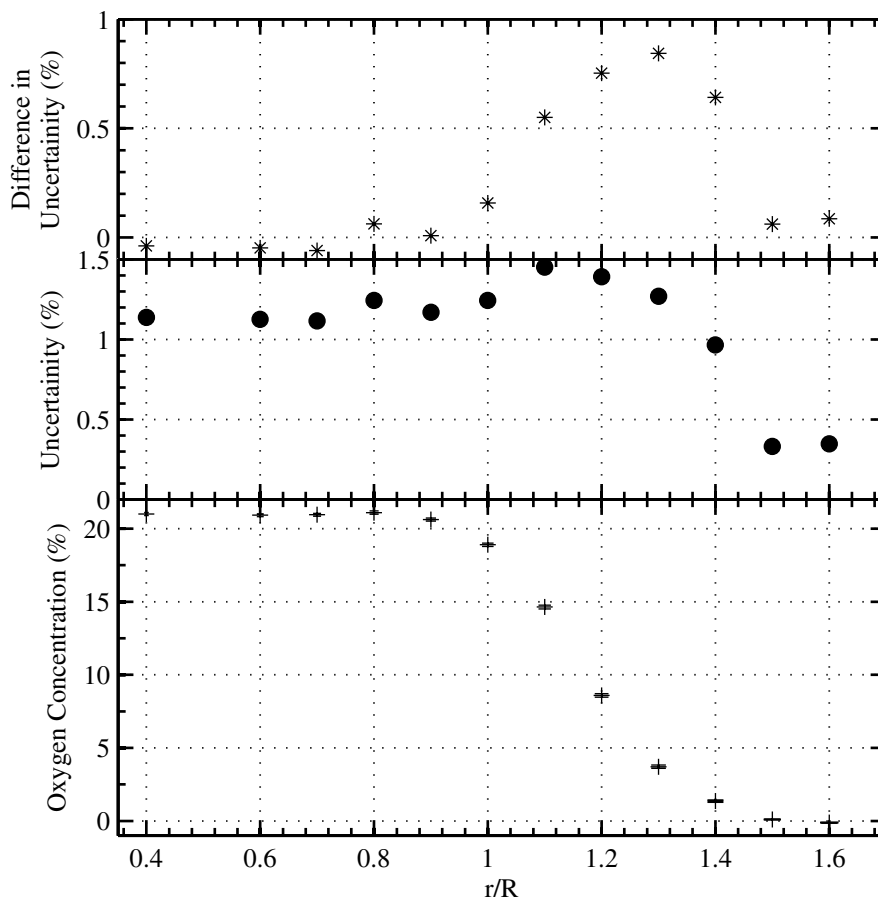


Figure 8.6: Analysis of the spectral data across the mixing layer. From bottom to top: (a) error bar showing calculated Oxygen concentration and corresponding fluctuations. (b) Uncertainty in the calculation of oxygen concentration. (c) Difference in the uncertainty in oxygen concentration as compared to the uncertainty corresponding to the same mean oxygen concentration in the premixed measurements.

Spectral measurements alone can not provide enough justification for the fluctuations in measurements obtained by 2D-LIPS technique. In order to confirm actual fluctuations of concentration in the region of gradients, it is also necessary to measure the velocity field in the region of the plasma.

8.1.5 Simultaneous PIV and 2D-LIPS

The setup used for performing simultaneous PIV is already presented in Fig. 3.2. Droplet generators were connected to the supply of both air and nitrogen flows. Images of Mie-scattering from droplets were acquired in the two frames of the PIV camera, 200 and 80 μ s before the laser-induced sparks. 200 shots of

simultaneous measurements were acquired for each location of the burner. The location of burner with respect to the plasma was changed from center to the annular region in steps of 1 mm. Measurements were performed at a total of 18 locations across the burner. Inserting seeding droplets in the studies of laser-induced plasmas is difficult as higher density of droplets affects the breakdown process. Therefore an optimum density of droplets had to be chosen so that not many sparks are affected and the accuracy of velocity field measurements is not highly compromised.

8.1.6 Analysis of PIV measurements

The images obtained from PIV cameras were correlated using the *Dynamic Studio (DANTEC DYNAMICS)* tool. An initial interrogation window of 256×256 and a final interrogation window of 32×32 was used, along with peak height validation of 1.2 and a moving average filtering of size 3×3 with a value of 0.1. PIV cameras also saw small intensity because of the reflection from the beam splitter being used for 2D-LIPS measurements. The effect of these reflections was reduced by subtracting the mean of 200 PIV shots at the same location from each shot. For the selected settings of droplet density and time difference between frames, it was not possible to go to lower final interrogation window, so as to allow at least 8 particles in final interrogation window.

The maximum displacement between the two PIV frames in the region of maximum velocity is of the order of 0.8 pixels, which means that the accuracy of PIV measurements can not be very good. But the velocity field obtained can still be used for qualitative comparison with the 2D-LIPS measurements. A typical velocity measurement is shown in Fig. 8.7. The laser induced plasma is located near the the center of this velocity field. The velocity field shown in Fig. 8.7 is plotted after removing bad vectors and replacing them with mean of nearby vectors. A median filtering has also been performed to obtain this velocity field.

8.1.7 Results of simultaneous PIV and 2DLIPS measurements

The objective of simultaneous PIV and 2DLIPS was to find the reason for high fluctuations in the 2DLIPS measurements, mainly in the region of concentration gradients. The idea was to use velocity measurements to see if we have actual fluctuations of concentration which was leading to fluctuations in the 2DLIPS measurements. Thus the mixing layer was measured with both velocity and 2D-LIPS. The velocity measurements at one vertical location are presented in Fig.8.8. The shots for which the laser-induced sparks were affected by the presence of droplets were removed during the analysis. The bad shots were identified based on the intensity of the sparks, the number of energy deposition zones i.e. multiple sparks, the simultaneous LIPS measurements.

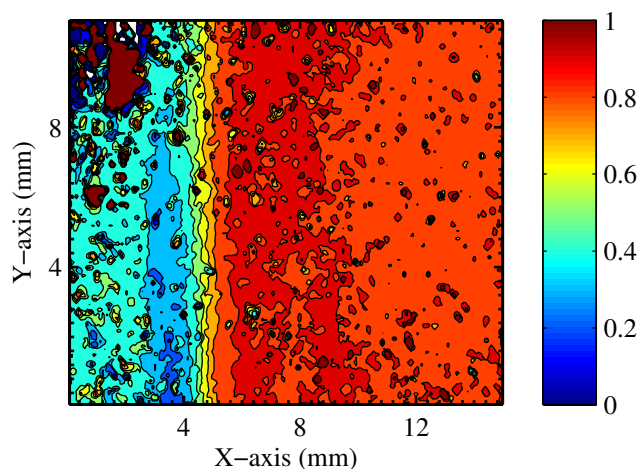


Figure 8.7: *Velocity field measurement above the burner using PIV.*

Approximately 50% shots were removed during the rejection process. Mean and fluctuations of remaining shots has been plotted for final analysis. Only the measurements in the region of interest corresponding to the 2DLIPS images has been used, and the measurements at different axial locations are overlapped to give mean velocity profile and fluctuations as a function of axial location. Fig.8.8 and Fig.8.4 show that both velocity and concentration have approximately the same width of mixing layer, The mixing layer width is approximately 5 mm, from axial distance of 10 mm up to about 15 mm. The mixing

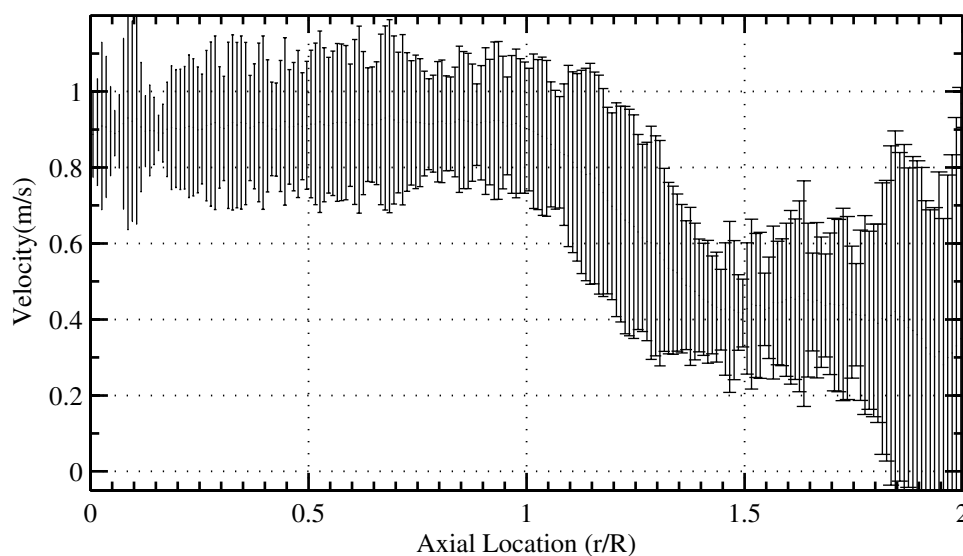


Figure 8.8: *Velocity Measurements and fluctuations at vertical location of the plasma as a function of horizontal location.*

layer in the concentration field is the region between which oxygen concentration changes from 21 % to 0 % approximately. And the mixing layer in velocity field is the region between which velocity changes from the velocity of central flow to the velocity of annular flow, i.e. in Fig.8.8 velocity changes from 0.9 to about 0.4 m/s.

Higher fluctuations of concentration in the region of gradients corresponds to higher fluctuations in velocity measurements in the same region of mixing layer. Figure.8.9 presents the absolute uncertainty of velocity and concentration measurements as a function of location across the burner. This shows that fluctuations in concentrations start at the same location when fluctuations in velocity start. Figure.8.9 also shows the fluctuations in the velocity field in the annular region are relatively very high. This means that the flow in annular region is not very uniform, which is leading to fluctuations in the mixing layer, which in turn is leading to fluctuations in the concentration measurements. Velocity measurements reconfirm the prediction that it is actual shot to shot fluctuations of concentration which leads to fluctuations in 2D-LIPS measurements in the current setup.

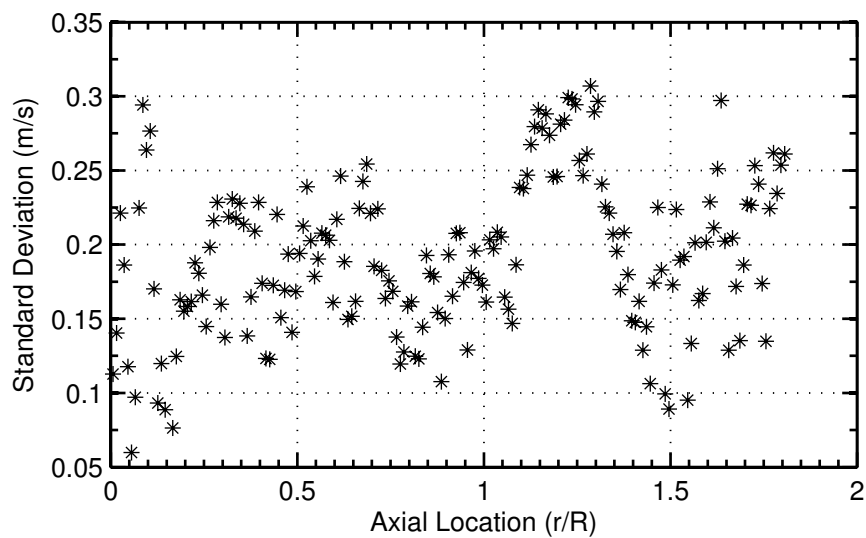
8.2 Ignition studies in a laminar stratified burner

The final objective of the 2D-LIPS technique is to help in the study of ignition in turbulent sprays by the measurement of spatially resolved equivalence ratios. In this section, 2D-LIPS measurements were performed in gaseous combustible mixtures. Similar to non combustible mixtures, measurements were performed in premixed methane-air, for calibration of the technique. The equivalence ratio of the premixed flow was varied from 0.2 to 0.9 while the Reynold's number of the flow was kept constant at 1500.

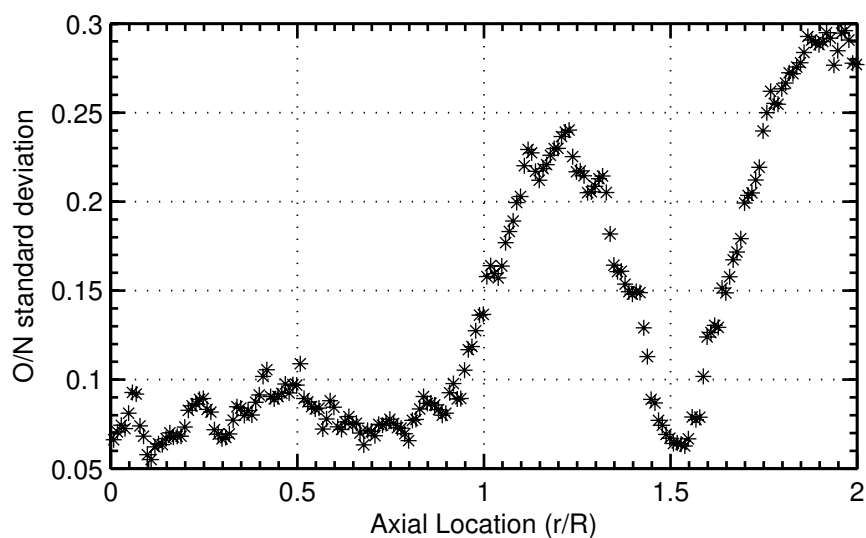
8.2.1 Calibration Measurements

Integrated equivalence ratio measurements were performed with conventional LIPS technique. The spectrometer presented in Section 3.1 was centered at 720 nm to allow capture of oxygen emission, i.e. 777 nm, as well as hydrogen emission, i.e. 656 nm. Typical spectral measurement for a mixture of methane-air has already been shown in Fig. 7.7.

100 shots for each equivalence ratio from 0 to 0.9, in steps of 0.1, were recorded. Measurements were not performed for equivalence ratio of 1.0, because there was successful ignition for each shot at an equivalence ratio of 1 and the flame needed to be extinguished after each spark. Ignition was also achieved for few shots at equivalence ratios 0.8 and for many shots at 0.9. Measurements were stopped and flame was blown off when successful ignition occurred. Measurements were then continued thereafter. The ratios of spectral emission intensity of hydrogen and oxygen emissions are presented in Fig. 8.10.



(a)



(b)

Figure 8.9: Absolute uncertainty in (a) velocity and (b) concentration measurements.

An approximately linear variation of the intensity ratio as a function of equivalence ratio is observed. A constant Q-switch setting of $295 \mu\text{s}$ was used for these measurements, which resulted in a spark energy of the order of $72.9(\pm 3.3\%) \text{ mJ}$, which is much higher than minimum ignition energy. The plot shown in Fig. 8.10 would be used for calibration of intensity ratio to obtain equivalence ratio.

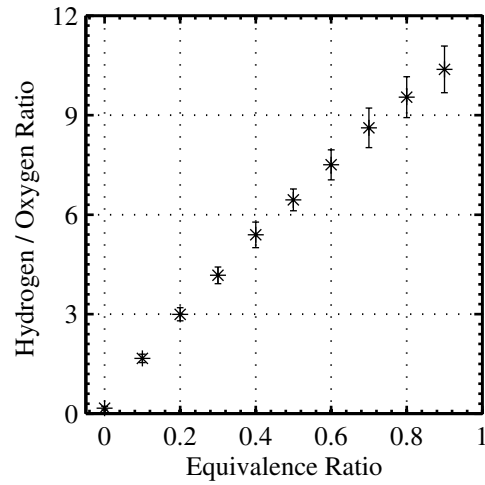


Figure 8.10: Variation of Hydrogen-Oxygen ratio obtained by LIPS as a function of equivalence ratio.

Two-dimensional laser-induced plasma spectroscopy measurements were also simultaneously performed for the calibration step. The processing of the two camera image frames for each shot was carried using the bounding box approach as explained in Section 7.4.1 and intensity ratio was calculated using methods presented in Section 7.4.2. The mean of the intensity ratios obtained from 2D-LIPS for different equivalence ratios is shown in Fig. 8.11.

The ratio obtained by 2D-LIPS also follows a linear curve with equivalence ratio. This curve would be used to obtain equivalence ratio from intensity ratio values in non-premixed measurements.

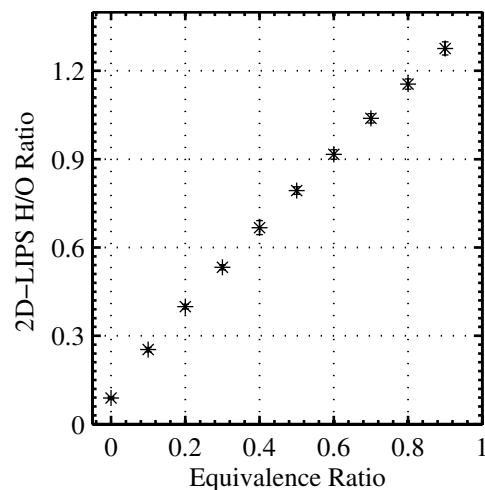


Figure 8.11: Variation of Hydrogen-Oxygen ratio obtained by 2D-LIPS as a function of equivalence ratio.

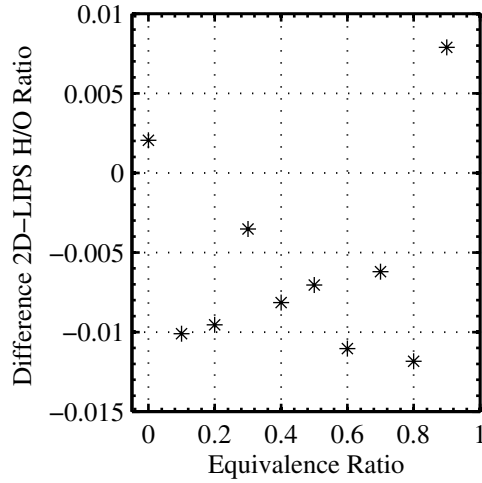


Figure 8.12: Difference between the mean H/O ratio calculated by 2D-LIPS for two different spark energies of 73 mJ and 113 mJ.

Effect of spark energy

At this stage, it was attempted to find the effect of spark energy on 2D-LIPS measurements. Therefore, these measurements are performed for another Q-switch setting of 285 μs , which resulted in a spark energy of 113.6($\pm 3\%$) mJ. The difference between the atomic emission ratios for the two spark energies is shown in Fig. 8.12. It can be seen that the difference is very small, less than 1% of the actual ratio values. Therefore, it can be concluded that the 2D-LIPS measurements are independent of spark energy of the laser-induced sparks.

8.2.2 Spatial variation of spark energy

The spatial distribution of spark energy is an important parameter, when it comes to understanding ignition in non-premixed mixtures. The images obtained by the ICCD cameras can be used as a measure of spatially resolved spark energy. The images obtained by ICCD cameras as shown in two top sub-figures of Fig. 8.1 show that spatial variation of image intensity is different for different filters. However the laser-induced plasma images shown in two bottom sub-figures of Fig. 7.16 show same intensity variation even for different bandpass filters. These two set of plasma images show that local concentration affects the intensity seen by a single camera. In case of laser-induced plasmas created in premixed flows, plasma images with any bandpass filter can be used to find spatial variation of spark energy. While in case of non-premixed flows the intensity seen by an ICCD camera does not provide spark energy variation. Therefore, it was attempted to look at the effect of local concentration on intensity seen by an ICCD camera equipped with a fixed band pass filter. The plasma images acquired during the calibration experiments presented in

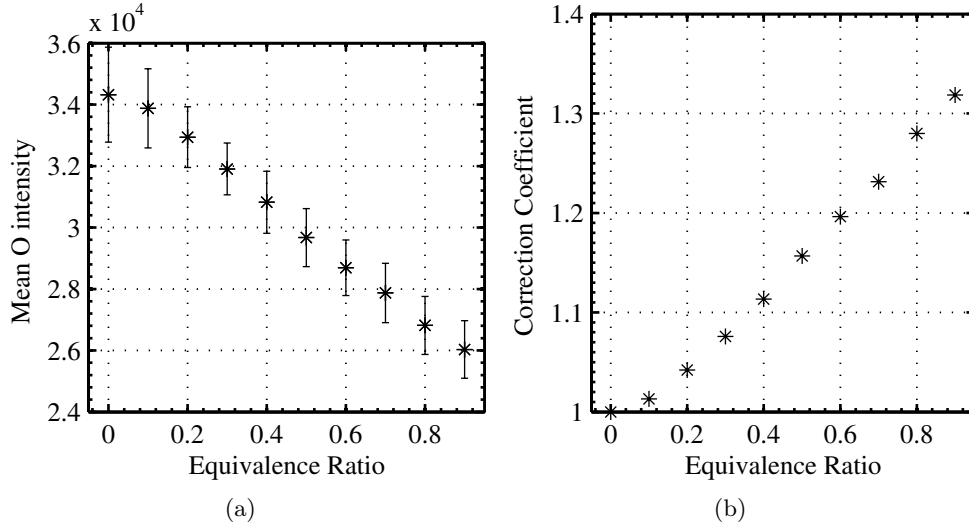


Figure 8.13: (a) Mean intensity of oxygen images as a function of equivalence ratio; and, (b) Correction factor for oxygen image intensity as a function of local equivalence ratio in order to obtain local spark energy.

Section 8.2.1 were used for these calculations. The variation of mean intensity of images, acquired with bandpass filter corresponding to oxygen emissions, as a function of equivalence ratio is shown in Fig. 8.13(a). It shows that intensity of oxygen atomic emission varies linearly with equivalence ratio.

Linear variation of oxygen intensity as a function of equivalence ratio was used to correct oxygen image intensity as a function of local equivalence ratio. The correction coefficient is shown in Fig. 8.13(b). 2D-LIPS provided local equivalence ratio at each pixel location inside the plasma. Therefore, correction to oxygen intensity could be applied at each pixel inside the plasma. The correction nullified the effects of equivalence ratio variation. After the correction, the corrected oxygen emissions images could be used as the measurement of spatial variation of spark energy.

The images of the laser-induced sparks acquired with ICCD cameras correspond to a measurement of emission intensity integrated along the line-of-sight. In order to obtain true two-dimensional variation of the spark energy, Abel transformation technique using onion peeling (Dasch (1992)) was performed on the images. For the application of this technique, laser-induced plasmas were assumed to be symmetric about the axis of the laser beam. This also implied an assumption on the local concentration to be axis-symmetric about the laser beam axis. Abel transformation of an image acquired in a premixed methane-air flow is shown in Fig. 8.14.

The Abel transformed images had fairly constant values except close to the center, where high accuracy could not be expected as a drawback of the Abel transformation technique. It shows almost constant energy deposition through-

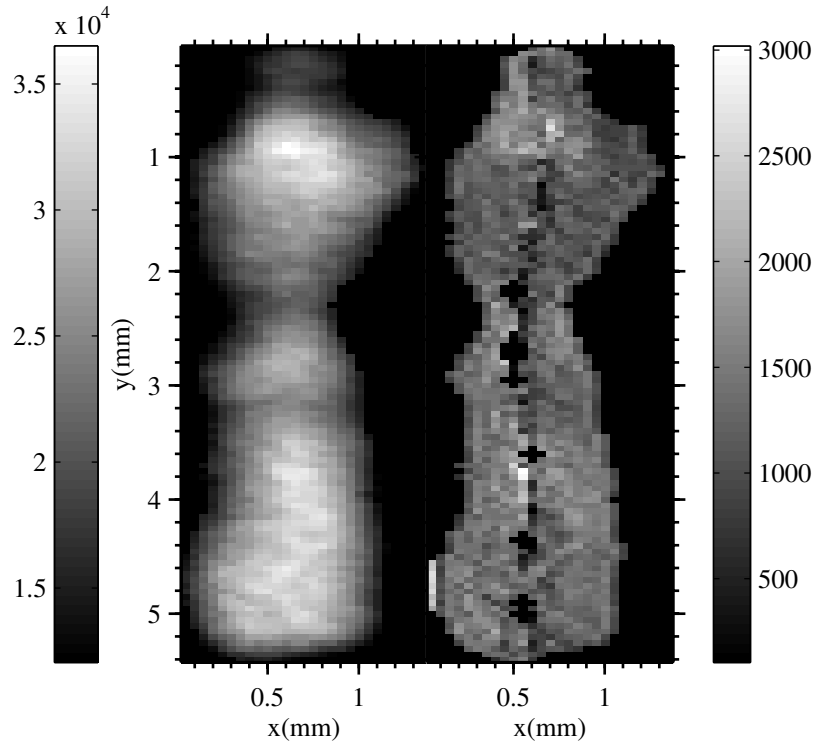


Figure 8.14: Raw ICCD image corresponding to oxygen emissions and Abel transformed image to look at spatial variation.

out the plasma region for plasmas created in premixed flows.

In order to calculate spatial variation of spark energy, the spark energy obtained by energy meter measurements was distributed as a function of intensity at each pixel of the acquired emission image of a plasma. And then the Abel transform was performed to calculate spatial variation of spark energy.

Chapter 9

Ignition experiments in two-phase burner

Ignition experiments at different spark locations were performed inside the two-phase flow burner presented in Section 3.2. 2D-LIPS experiments were performed simultaneously with other diagnostic techniques. The objective of these experiments was to define the conditions leading to a complete ignition in the two-phase burner.

9.1 Spark Locations

In order to choose the best locations for laser-induced sparks, a map of ignition probability in a small region of the burner was determined. Spark locations were chosen in the x-z plane inside the burner. Laser-induced plasmas were created at 3.33 Hz while keeping a constant Q-switch delay of 250 μ s. The incident laser beam energy had maximum fluctuations of the order of 7 %, as measured just before the laser beam entry into the burner and a mean value of 60 mJ for the induced spark. Laser beam was inserted from the top of the burner. The map of ignition probability is shown in Fig. 9.1(a). The ignition probability map covers a wide a range of ignition probabilities from 0 to about 60%. The objective of the ignition probability measurement was to identify zones of high and low ignition probabilities and therefore a different number of sparks were studied depending on the position. As a consequence, statistically required number of measurements were not performed but current investigation is dedicated to single shot events rather than statistically based analysis.

In order to perform ignition analysis in regions of different physical conditions and different ignition probabilities, seven different points were chosen inside the burner as depicted in Fig. 9.1(b). These points had a wide range of ignition probabilities, *i.e.* from non-ignitable locations to locations which could easily be ignited. Furthermore, the average ignition delay between the laser emission and the complete combustion of the chamber is provided for the seven different

locations. One can notice that typical delays are relatively small, of the order of 6 to 9 ms. This is a relatively low delay as compared to more practical combustors. This may be explained by the fact that the spark is introduced directly or close to the inner recirculation zone. In practical systems, usually the position of the spark plug is located in the outer recirculation zone. The aim of the present research is the development of the measurements and associated post-processing techniques and therefore the difference in the position is not considered to be a problem. Furthermore, there seems to be a link between ignition delay and ignition probability because position ‘a’ presents both a high probability together with a smaller ignition delay. On the opposite, position ‘g’ with 7.5% probability is also characterized by a longer ignition delay, of the order of 9 ms. These delays correspond to approximately four to five PVC cycles (see Chapter 5).

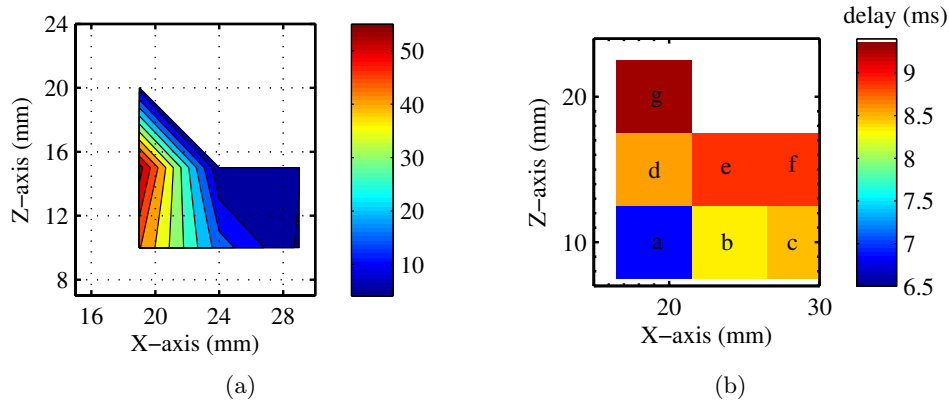


Figure 9.1: (a) Ignition probability (percentage) at few locations inside the chamber, (b) Locations of the laser-induced spark chosen for ignition experiments together with typical ignition delay.

9.2 Experimental Conditions

Two-dimensional laser-induced plasma spectroscopy technique was used for spatially resolved equivalence ratio measurements during ignition experiments in the two-phase flow burner. The images of the laser-induced sparks were simultaneously acquired with two ICCD cameras. Separate filters corresponding to hydrogen ($\lambda = 660 \pm 10$ nm) and oxygen ($\lambda = 780 \pm 10$ nm) emissions were installed in front of the two ICCD cameras as shown in Fig. 3.7. The images were acquired 1500 ns after the starting of the plasma with an exposure time of 90 ns. The timing of the measurements was decided on the basis of the analysis presented in Fig. 7.9.

The images corresponding to the oxygen emission were modified using the image of a grid acquired with both cameras using the approach presented in Sec-

tion 7.4.1.3. As a second step, a correlation was performed between two modified images. Those were obtained by using an intensity threshold of 10%, a 4×4 average filter and an edge erosion disk of size 2. A lower intensity threshold was chosen as compared to results presented in chapter 7 to avoid problems with low intensity of hydrogen emissions at some of the locations. 2D-LIPS analysis provided two important information; spatial variation of emission intensity and spatial variation of concentration ratio. As shown in Section 8.2.2, spatial variation of emission intensity can provide a quantitative measure of spatial variation of spark energy after multiplication with a coefficient. This coefficient was shown to be a function of local concentration ratio in Fig. 8.13(b).

During these experiments, integrated spark energy measurements through transmitted energy measurements could not be performed because of optical access limitations. Assuming a shot-to-shot constant spark energy (around 60 mJ), spatial variation of corrected oxygen emission intensity was used as a representation of spatial variation of spark energy.

Images of Mie-scattering by fuel droplets were simultaneously acquired in the axial plane at an acquisition rate of 10 kHz. These images were used to estimate the concentration of liquid fuel and to calculate the velocity fields using a multi-pass cross-correlation approach (*Dynamic Studio* from *Dantec Dynamics*). However, due to limitations in memory of the camera, full resolution images could only be captured for four sparks, including the successful one. Therefore, for detailed discussions between failed events and ignition events, only four sparks could be considered at most. In parallel to the 2D-LIPS measurements, a conventional LIPS system was also used with an optical fibre placed at 45° to the direction of flow (Fig. 3.7). Overall flow rates of air and dodecane inside the burner were kept constant at an air flow rate of 10 g/s with an initial temperature of 473K and a global equivalence ratio of 0.7. Fuel (dodecane) was inserted through the Pilot stage of the injector, in the center of the combustion chamber.

9.3 Results and Discussions

In the following sections, different locations of laser-induced plasmas are discussed. This section begins with the laser-induced spark at position ‘b’ as this location features many of the different patterns existing to establish a flame in the combustion chamber. This location is detailed whereas only main conclusions will be provided for the other locations.

9.3.1 Location ‘b’

This location ‘b’ corresponds to a position of 24-25 mm from the injector in axial direction, and 8-13 mm from the axis of the burner in radial direction (see Fig. 9.1(b)). The typical size of the created spark was $1 \times 1 \times 5 \text{ mm}^3$. According to the initial studies, this position corresponds to an ignition probability of the

order of 17.5 % (Fig. 9.1(a)). To better visualize the position of this spark with respect to the mean flow patterns, its position is simultaneously displayed with mean velocity fields in Fig. 9.2. The mean location of the spark is represented by the black rectangle. It shows that the spark is located at the edge of the spray cone towards the inner recirculation zone (See Fig. 9.2(a)). The magnitude of the mean axial velocity component at the spark location was approximately between 2 and 4 m/s (from bottom to top of spark region) and vertical velocity component was of the order of 1.1 to 1.3 m/s (Fig. 9.2(b)).

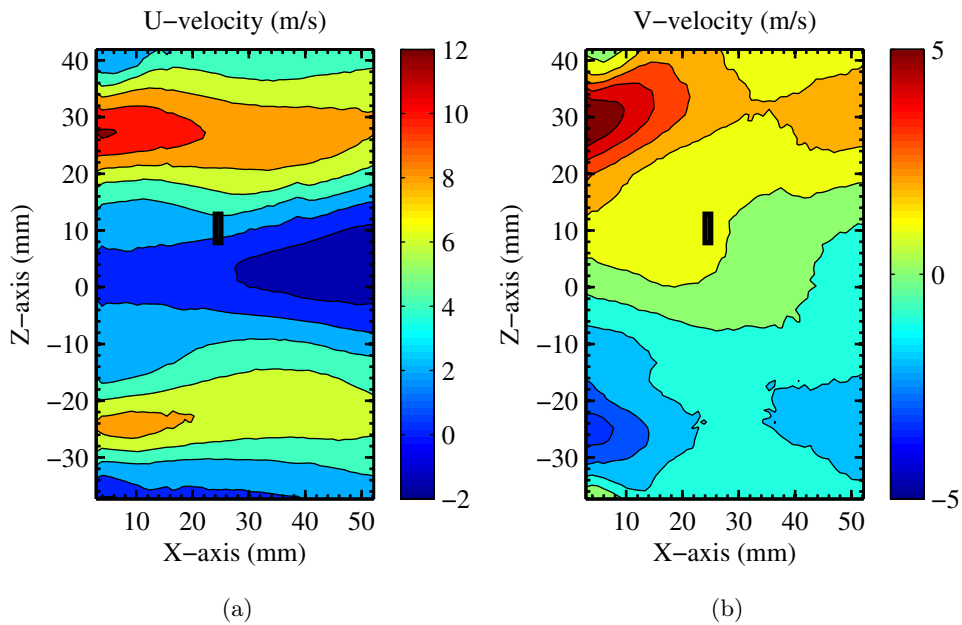


Figure 9.2: Location of laser-induced spark for location *b* (small black rectangle) shown in mean velocity fields.

Seven ignition experiments were performed at this location of spark. The number of sparks required to achieve successful ignition were successively 2, 3, 11, 3, 6, 14, and 1. The analysis of simultaneous LIPS, 2D-LIPS, and Mie-scattering images was performed to understand the reasons for success/failure of individual ignition attempts. Eyssartier et al. (2011) and Eyssartier et al. (2013) proposed different criteria to explain the complete ignition of an aeronautical combustion chamber, starting from the conditions to obtain an initial kernel that shall afterwards be successfully convected. In the following, a similar decomposition is proposed, but based on experimental results. First, conditions for having an initial kernel are determined and then the conditions for its propagation are examined. For conventional LIPS measurements, the ratio of atomic emissions was obtained by dividing the areas below the peaks corresponding to hydrogen (656 nm) and oxygen (777 nm) emissions.

9.3.1.1 Influence of local equivalence ratio

As originally proposed in Zimmer et al. (2007), the measurement of local equivalence ratio may be a good parameter to discriminate between success and failure of ignition attempts. When applying this conventional technique to the two sparks created during Test#1, measured overall H/O ratios were 3.60 and 3.48 respectively. Therefore, conventional LIPS predicted Spark#1 to be more probable to ignite as compared to Spark#2. However, sparks created in a spray tend to be longer than those obtained in gaseous conditions and therefore a mean concentration ratio may not be sufficient to understand the phenomena. 2D-LIPS measurements provide information on spatially resolved oxygen emission and spatially resolved H/O emission ratio. Results obtained when analyzing the data of 2D-LIPS measurements for Test#1 at location b are shown in Fig. 9.3(a) and Fig. 9.3(b) with respectively spatial variation of corrected oxygen image intensity and hydrogen-to-oxygen intensity ratio.

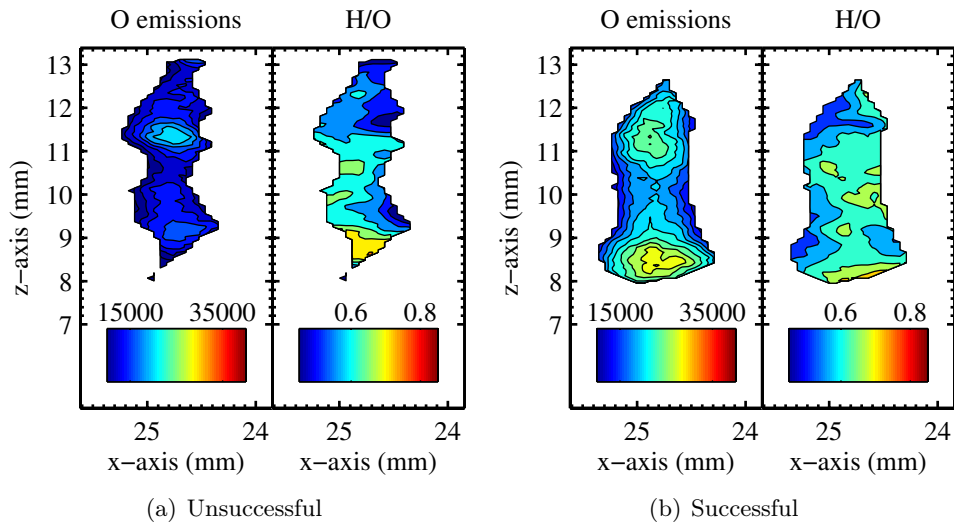


Figure 9.3: (a) Location b; Test#1, Analysis of 2D-LIPS experiments for Spark#1 which failed to ignite, (b) Location b; Test#1, Analysis of 2D-LIPS experiments for Spark#2 which successfully ignited.

The comparison between the two sparks using 2D-LIPS measurements shows that although Spark#1 had higher atomic ratio in some regions of the spark, its energy was lower, as revealed by the corrected oxygen emission intensity. Therefore, the creation of an initial kernel was not possible. On the other hand, spark#2 had higher energy as well as high H/O at the locations of high energy (bottom part of the plasma) which may have led to the creation of an initial flame kernel. It is known that the presence of high local spark energy as well as high equivalence ratio is required for successful ignition and those quantities may be experimentally determined using 2D-LIPS.

Test#3 at location b required 11 sparks to ignite. Simultaneous velocity field measurements could only be recorded for 4 sparks, due to memory limitation of the camera. Therefore only three unsuccessful sparks before the successfully igniting spark could be fully analyzed. LIPS measurements for these four sparks provided H/O values of 3.6, 2.4, 3.4, and 3.3 respectively. Therefore Spark#4 was not the most probable to ignite as compared to other sparks. 2D-LIPS analysis for the four laser-induced sparks is shown, respectively in Fig. 9.4(a), 9.4(b), 9.4(c), and 9.4(d). Spark#1 and Spark#2 had very low spatial variation of spark energy along with low values of H/O. Spark#3 had high spark energy deposited in two separate regions, but the regions of high spark energy did not coincide with the regions of high H/O. Spark#4 had smaller spark energies than Spark#3 but high H/O ratio was seen in a large part of the spark, thereby resulting in successful creation of kernel and ignition. As a conclusion, it seems that this Test#3 could mainly be explained by the fact that only one spark had a good mixture fraction value combined with a good energy.

The reason for successful ignition by Spark#3 of Test#4 was obtained by 2D-LIPS measurements, where a high H/O region coinciding with high spark energy region was found for the igniting spark (For analysis of 2D-LIPS measurements, Refer to Appendix. D.2). In this case, even LIPS measurements estimated higher H/O for the igniting spark.

Similarly for Test#5 (Refer to Appendix. D.2), 2D-LIPS provided justification for the igniting spark, while LIPS suggested otherwise. Analysis of measurements corresponding to Test#6 (Refer to Appendix. D.2) showed much better spark energy and slightly better H/O in spark region leading to successful ignition.

Test#7 required only a single shot to ignite. This was because of a region of extremely high H/O occurring inside the region of the plasma as shown in Fig. 9.5. This strong signal may be a consequence of the presence of a cloud of droplets in the plasma. The size of a single droplet was about $20\mu\text{m}$ and may not have resulted in such a pattern. Due to the PVC, some centrifugation effects may have created a locally high concentration of droplets that interacted with the electromagnetic wave of the laser.

Whereas many tests could be explained with 2D-LIPS, some undetermined events were noticed for Test#2. Test#2 at location b required three sparks to ignite. H/O ratios by conventional LIPS measurements was measured to be 3.0, 3.7, and 2.8 successively. Results of 2D-LIPS measurements for the three successive sparks are shown in Fig. 9.6(a), 9.6(b), and 9.6(c), respectively.

2D-LIPS analysis for Test#2 shows that Spark#2 had higher probability to ignite because of high energy along with high H/O in two regions of the spark. Spark#1 seems least probable to ignite, owing to very low H/O. Spark#3, which actually successfully ignited, lies between Spark#1 and Spark#2 in terms of its potential to generate an initial flame kernel. Therefore, 2D-LIPS analysis

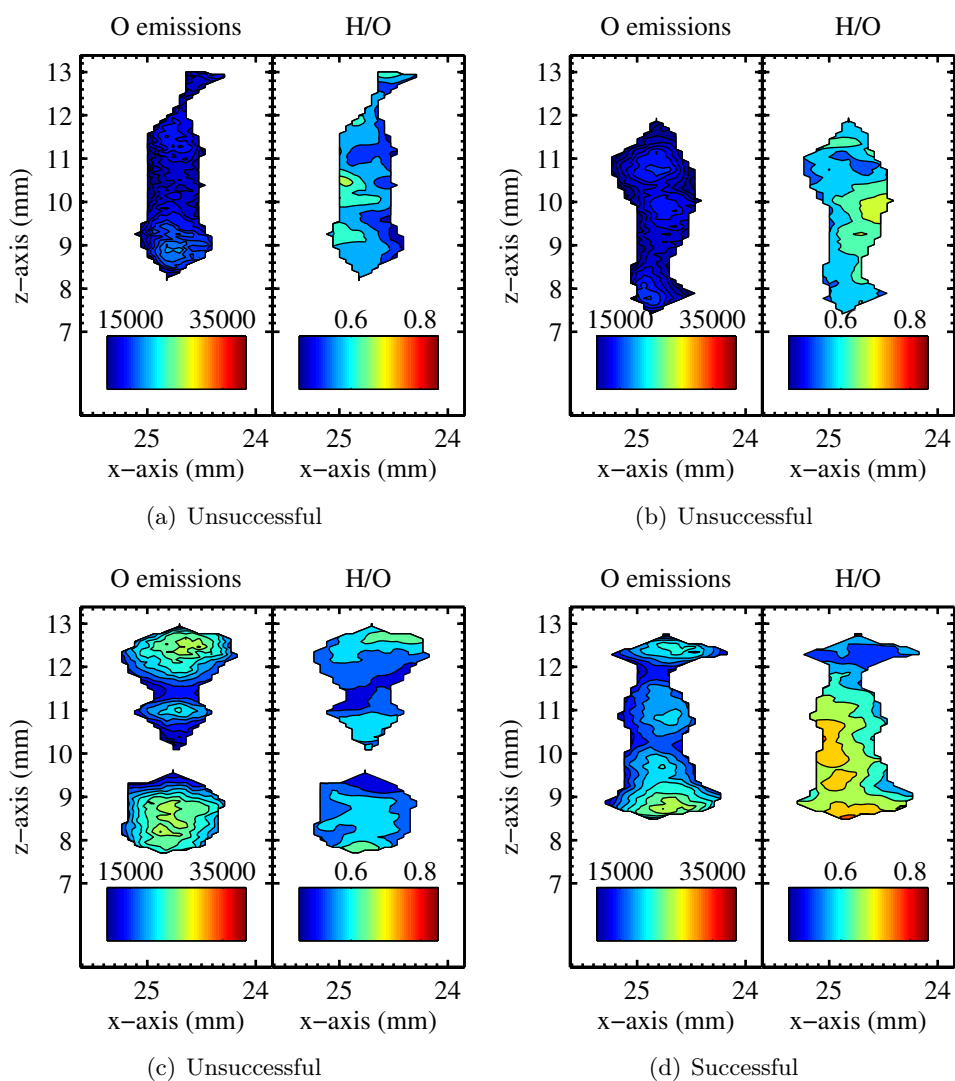


Figure 9.4: (a) Location b; Test#3, Analysis of 2D-LIPS experiments for Spark#1 which failed to ignite, (b) Location b; Test#3, Analysis of 2D-LIPS experiments for Spark#2 which failed to ignite, (c) Location b; Test#3, Analysis of 2D-LIPS experiments for Spark#3 which failed to ignite, (d) Location b; Test#3, Analysis of 2D-LIPS experiments for Spark#4 which successfully ignited.

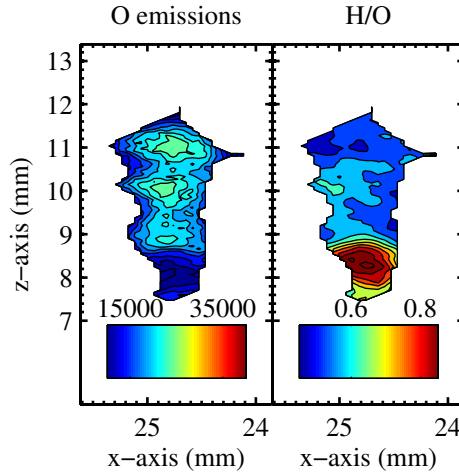


Figure 9.5: Location b; Test#7, Analysis of 2D-LIPS experiment where single shot ignition occurred.

suggests that Spark#2 was more probable to ignite as compared to Spark#3, which however had local condition for creating the initial kernel.

The reason for the Spark#2 to fail could not be understood with this analysis and will be further discussed in the section devoted to flow dynamics.

As an intermediate conclusion, it can be noticed that out of seven tests performed at location 'b' in the burner, six could be explained on the basis of 2D-LIPS measurements. It should particularly be noted that conventional LIPS measurements could not help in understanding the reason for successful ignition. This underlines the need for spatially resolved concentration and spark energy measurements. Among all tests performed at this location, only Test#2 could not be understood by measurements of local concentration within the spark.

Previous analysis of 2D-LIPS measurements showed that simultaneous presence of high energy (corrected oxygen emissions) as well as high hydrogen-to-oxygen ratio was required for successful ignition. It was also concluded that such regions of spark may lead to the formation of the initial flame kernel. In order to estimate the size of the initial flame kernel based on 2D-LIPS measurements for each spark, a threshold on the H/O ratio and a threshold on the corrected oxygen intensity was selected. The region of the spark which was above both these thresholds was set as being part of the initial flame kernel. Test#1 at location 'b' of the spark required two sparks to ignite. Fig. 9.7 shows the different steps to obtain initial flame kernel size for those two sparks. Thresholds were individually applied to corrected oxygen images and hydrogen-to-oxygen ratios. The values of the thresholds were chosen to be 15000 for corrected oxygen image intensity and 0.6 for hydrogen-to-oxygen ratio. Finally the regions of the spark which were above both thresholds were calculated, which provided

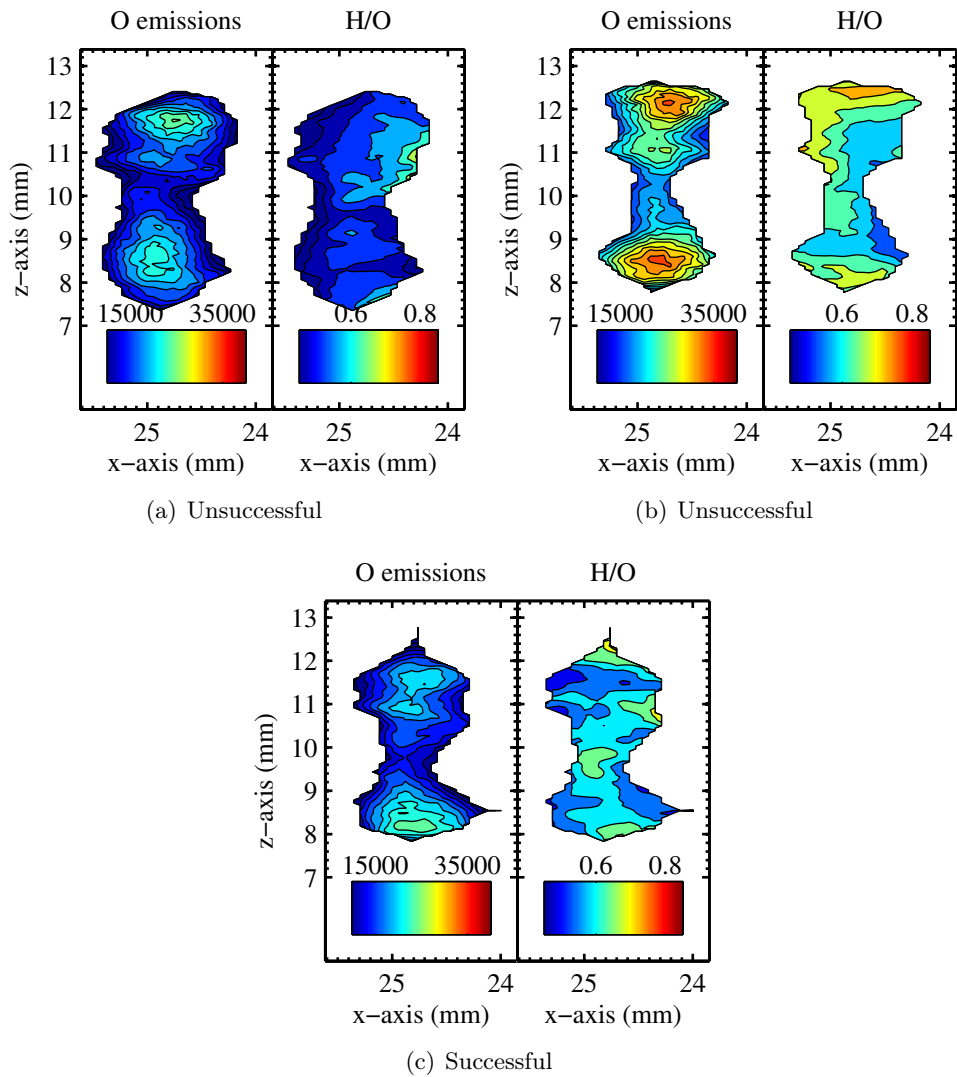


Figure 9.6: (a) Location b; Test#2, Analysis of 2D-LIPS experiments for Spark#1 which failed to ignite, (b) Location b; Test#2, Analysis of 2D-LIPS experiments for Spark#2 which failed to ignite, (c) Location b; Test#2, Analysis of 2D-LIPS experiments for Spark#3 which successfully ignited.

an estimate of initial flame kernel size. The middle images of sub-figures in Fig. 9.7(a) and Fig. 9.7(b) correspond to cases for which individual thresholds have been applied, either on corrected oxygen intensity or on H/O ratio. Finally, the common region of both high corrected oxygen intensity and high H/O ratio is provided in the right-side of the figures. This allows an estimate of the initial flame kernel for both unsuccessful and successful spark respectively. It can be seen that the successfully igniting spark had a much larger area of the region above both thresholds as compared to the failed attempt.

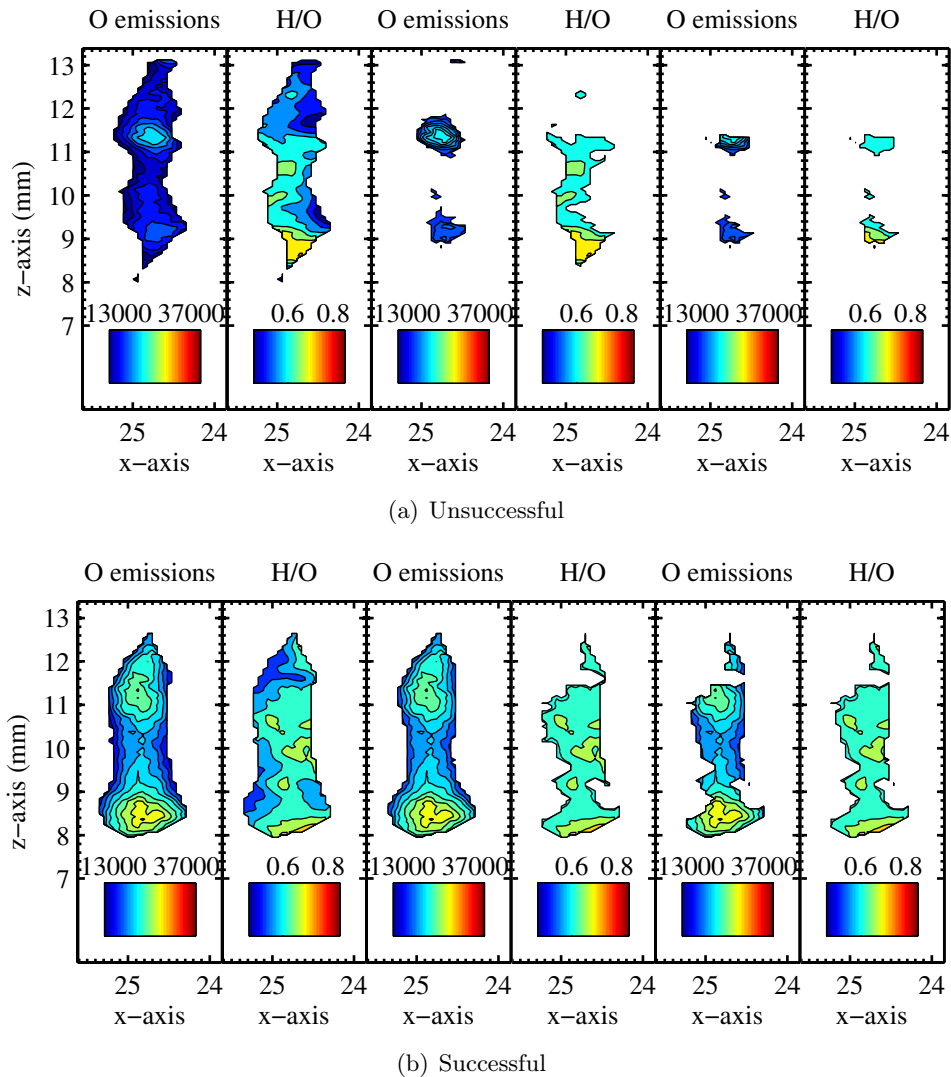


Figure 9.7: Location b; Test#1, Calculation of initial flame kernel size for (a) unsuccessful and (b) successful sparks, From left to right: Oxygen intensity and H/O ratio as obtained by 2D-LIPS, regions above thresholds separately applied to H/O and oxygen image intensity, and regions above both the thresholds.

The area of the initial flame kernel was similarly calculated for all igniting and non-igniting sparks. The area of the selected region for all igniting and non-igniting sparks at location 'b' is displayed in Fig. 9.8. The size of the spark has been plotted as a function of mean hydrogen-to-oxygen ratio inside the selected area. Fig. 9.8 shows that successfully igniting sparks had a higher initial flame kernel size as compared to non-igniting sparks. It can be seen also that for high H/O ratio, the initial kernel size may be a bit smaller than for lower ratios. This comes from the fact that a high mixture fraction will have a smaller critical kernel size. The heat released by richer mixtures can more easily be higher than heat losses due to convection (see Appendix. C). This analysis explains reasons for all sparks except one created during Test#2. Fig. 9.8 does not show the sparks for which initial flame kernels of zero or very small size were calculated. It is however mandatory to conduct further analysis to explain why one of the spark during Test#2 did not ignite despite having a large initial flame kernel size.

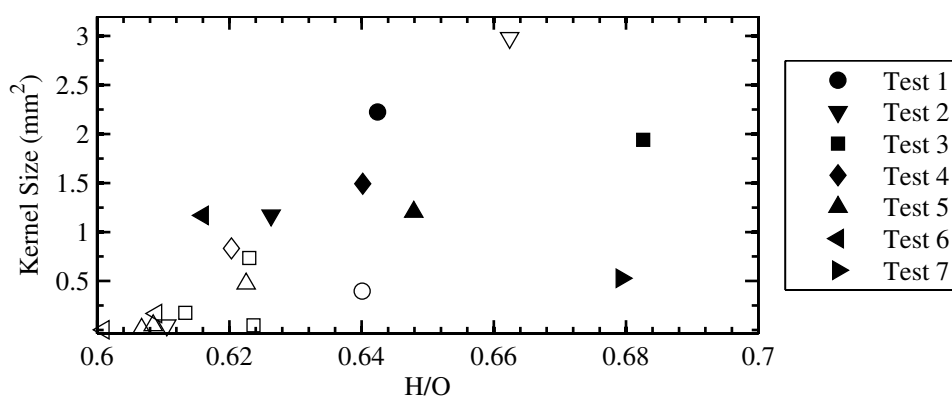


Figure 9.8: Size of the initial flame kernel as a function of mean H/O inside the kernel. Filled markers represent successful sparks and blank markers represent unsuccessful sparks.

2D-LIPS provided information on mixture fraction inside the spark region but in order to achieve successful ignition, presence of favorable conditions in the region around the spark is also required. Mie-scattering from dodecane can be used as a qualitative measure of presence of fuel inside the burner (see [Providakis \(2013\)](#)). Mie-scattering intensity before different sparks was compared to provide an estimate of the presence of fuel inside the combustion chamber, close to the spark. As seen in Fig. 9.8, there were eight sparks which had the potential to ignite (by 2D-LIPS analysis) but seven lead to a complete ignition. Therefore, Mie-scattering intensity before each of those eight sparks was compared. Radial profiles of mean Mie-scattering intensity taken at the axial location of the sparks are shown in Fig. 9.9.

Fig. 9.9 shows that the Mie-scattering intensity for the failed spark is lower than that of all igniting sparks. This tends to support the fact that although the

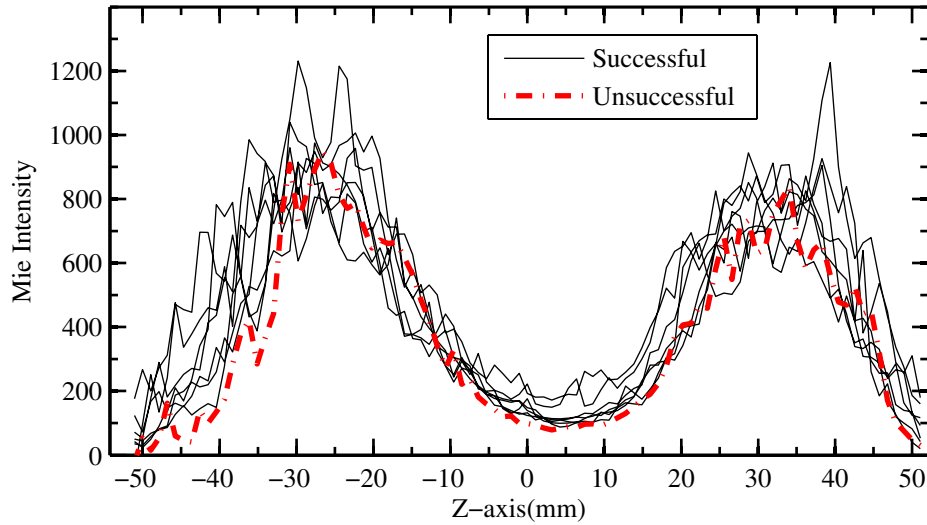


Figure 9.9: Radial profiles of mean Mie-scattering intensity (over 10 ms, before sparks) at axial location of the sparks created at location 'b'; Seven successful and one unsuccessful sparks compared.

initial flame kernel was big enough, favorable mixture fraction was not present in nearby regions and therefore the kernel might not have grown. This may explain the reason for failure of one of the sparks created during Test#2 but some more analysis was performed concerning the dynamics of the flow to see potential effects of the PVC on ignition characteristics.

9.3.1.2 Flow dynamics

In order to see possible flow dynamics effects on the ignition process, two different data have been extracted from the Mie-scattering images. Those images were used to calculate velocity field in the axial plane containing the sparks and afterwards the dynamics of the PVC was determined.

Fig. 9.10 shows profiles of axial and vertical velocity components at the axial location of the two sparks created during Test#1. The velocity profiles were plotted using the mean velocity fields computed over 10 ms (*i.e.* 100 instantaneous velocity fields) before each spark. The sparks were located at approximately 8-13 mm from the center of the burner in the radial direction. The profile of vertical component of velocity (Fig. 9.10(b)) at the axial location of the spark shows negative velocity magnitude close to the spark location. The presence of negative velocity before spark would have helped the convection of initial flame kernel towards the injector. Moreover, the axial component of velocity (Fig. 9.10(a)) shows lower velocities in the center before the igniting spark. Lower velocities in the center correspond to a wider inner recirculation zone, which would have eased the initial flame kernel to convect further towards

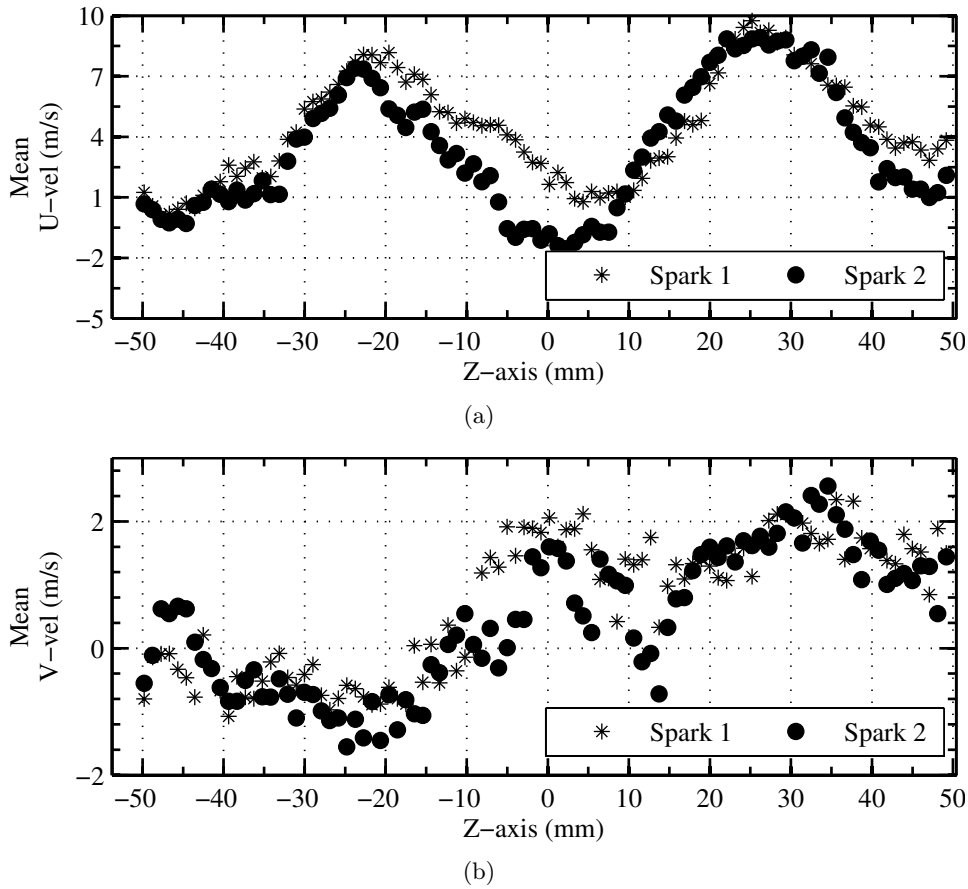


Figure 9.10: Location *b*; Test#1, Analysis of PIV measurements for 2 consecutive sparks. Spark#1 failed to ignited while Spark#2 successfully ignited. Velocity profiles at the location of spark have been plotted as a function of radial distance (*Z*-axis); spark located at 8-13 mm. Profiles plotted using mean velocity fields (over 100 instantaneous fields equivalent to 10 ms) before the deposition of spark energy.

the injector.

Velocity profiles before the four sparks of Test#3 are shown in Fig. 9.11. No particular difference between velocity field before non-igniting and igniting sparks was observed in the axial direction. It is worth noting that in the present case, the velocity profile does not exhibit a wide inner recirculation zone. This did not prevent the spark to be convected towards the injector. This suggests that a wide inner recirculation zone is not a necessary condition for complete ignition of the combustion chamber. On the radial profile, one can see that the igniting spark had a very low radial velocity, close to zero. This means that any initial kernel may just have to propagate upstream the main direction. Other sparks, like Spark#1 and Spark#2 had on the opposite a stronger radial velocity, which may have led to a stretch of the initial kernel, making the convection

more difficult to achieve.

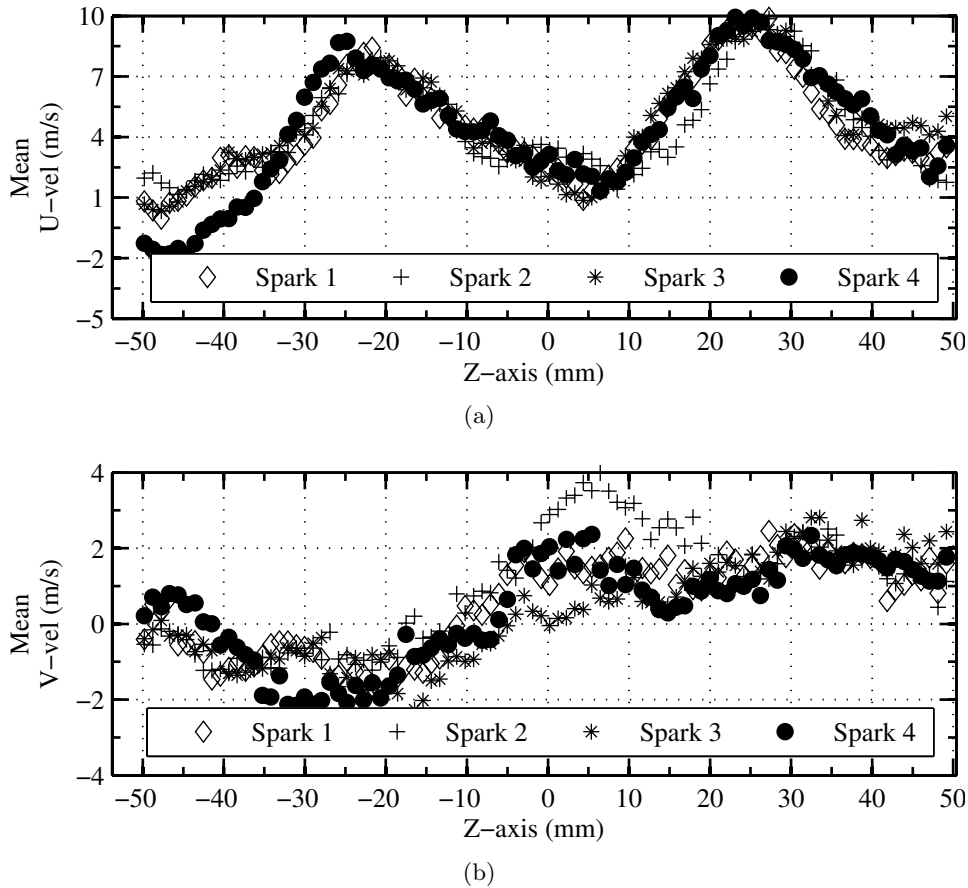


Figure 9.11: Location b; Test#3, Analysis of PIV measurements for four consecutive sparks. Spark#1, Spark#2 and Spark#3 failed to ignited while Spark#4 successfully ignited. Velocity profiles at the location of spark have been plotted as a function of radial distance; spark located at 8-13 mm. Profiles plotted using mean velocity fields (over 100 instantaneous fields equivalent to 10 ms) before the deposition of spark energy.

For the Test#4 and Test#5, the velocity profiles did not show any difference between igniting and non-igniting sparks whereas vertical components were lower for the ignition spark of Test#6. All those tests were already discussed on a 2D-LIPS base. However, to understand potential flow effects, velocity profiles before the three sparks of Test#2 are shown in Fig. 9.12. It seems that no significant difference was observed between the mean velocity profiles taken just before the different sparks. This tends to mean that the actual flow just before the spark may not be sufficient to describe the dynamics and further treatment is required.

As shown in Chapter 5, the flow in the two-phase burner had a strong characteristic precessing vortex core (PVC). The strength of this PVC can also affect

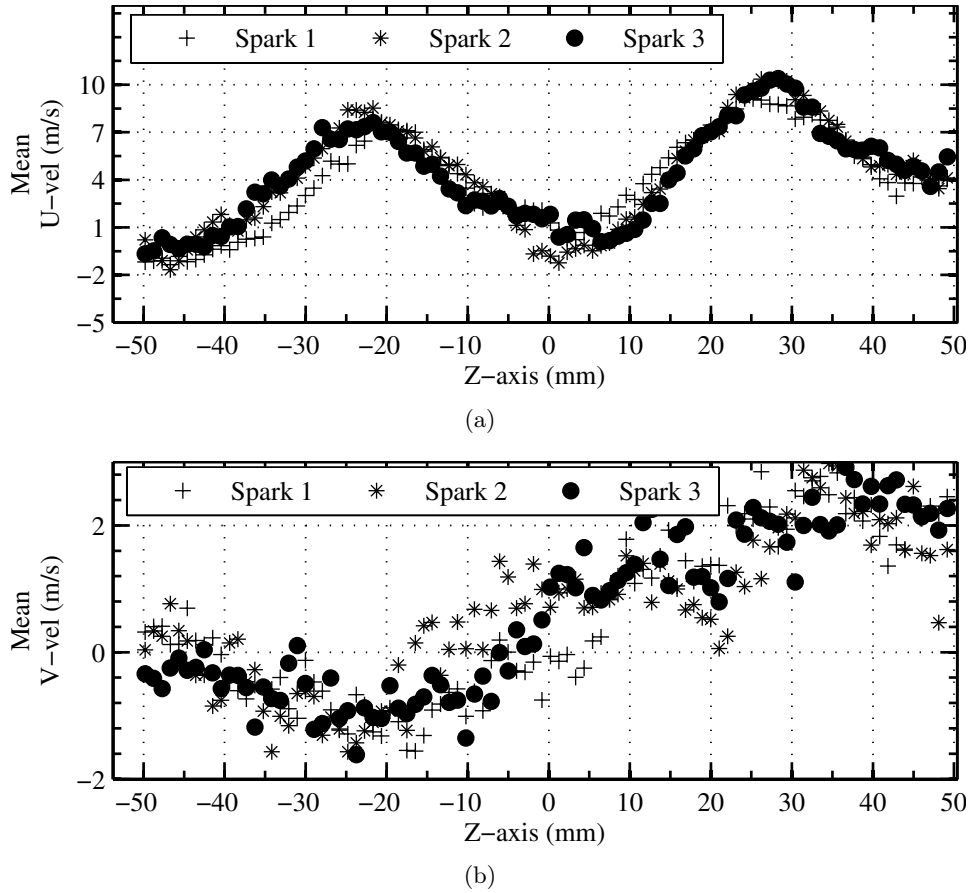


Figure 9.12: Location *b*; Test#2, Analysis of PIV measurements for 3 consecutive sparks. Spark#1 and #2 failed to ignited while Spark#3 successfully ignited. Velocity profiles at the location of spark have been plotted as a function of radial distance; spark located at 8-13 mm. Profiles plotted using mean velocity fields (over 100 instantaneous fields equivalent to 10 ms) before the deposition of spark energy.

the process of ignition. In order to look at temporal variation of PVC strength, Dynamic Mode Decomposition (DMD) analysis (Section 4.4) was performed on the Mie-scattering images acquired before the sparks. The strength of the PVC can be measured in terms of the peak-to-noise ratio value corresponding to the PVC frequency and surrounding frequencies. It has been shown that this comes with typical uncertainties that were quantified in the DMD section. It has been shown that the signal to noise ratio was precise within the order of 0.15, regardless the number of samples used and the initial magnitude (ranging from 1.05 to 1.50). This uncertainty has to be recalled in the next analysis. DMD analysis was performed only for the eight sparks which were highly probable to ignite (as provided by 2D-LIPS analysis). Fig. 9.13 shows variation of PVC strength (defined as being the ratio between the peak in the DMD and

the surrounding modes) for seven igniting and one failed spark. The strength of PVC at each time ‘t’ was calculated using the set of images between time ‘t’ and the spark. Higher the number of images used for DMD analysis, higher will be the frequency resolution and accuracy of calculations. A minimum of 100 Mie-scattering images (corresponding to 10 ms in Fig. 9.13) were used for this DMD analysis.

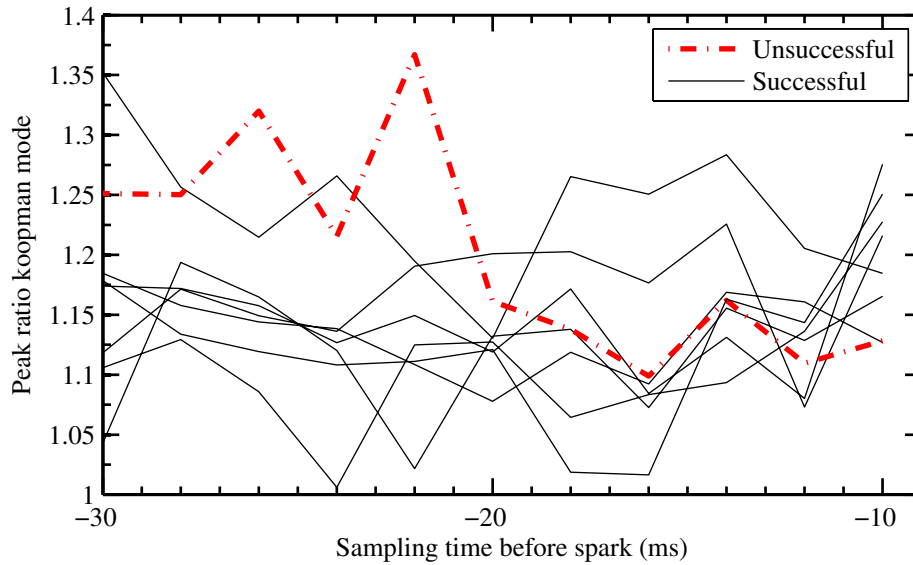


Figure 9.13: Variation of PVC strength before sparks for 7 igniting and 1 failed sparks.

Fig. 9.13 shows that the strength of the PVC corresponding to the failed spark seems to decrease with time before the spark. This location of spark lied inside the inner recirculation zone (IRZ). Pressure in the IRZ is a function of the PVC strength; higher the strength of the PVC, lower will be the pressure in IRZ. Lower the pressure in the IRZ, easier would be the convection of initial flame kernel towards the injector. Therefore, a lower strength of PVC, before the spark for the failed spark (Fig. 9.13), corresponds to unfavorable conditions for the initial flame kernel to convect towards the injector, resulting in failure. The change in PVC strength can also be represented by the slope of the PVC strength curves shown in Fig. 9.13. Therefore, the final PVC strength just before the spark (calculated using Mie-scattering images over 10 ms before the spark) and its difference with respect to initial PVC strength (calculated using Mie-scattering images over 30 ms before the spark) are plotted in Fig. 9.14. As shown in Fig. 9.14, a point with lower final PVC strength (y-axis in Fig. 9.14) and higher drop in pvc strength (x-axis in Fig. 9.14) is less probable to ignite. Therefore a spark in left-down part of Fig. 9.14 has less potential to ignite in terms of PVC strength.

It can be concluded from Fig. 9.13 and Fig. 9.14 that one of the sparks from

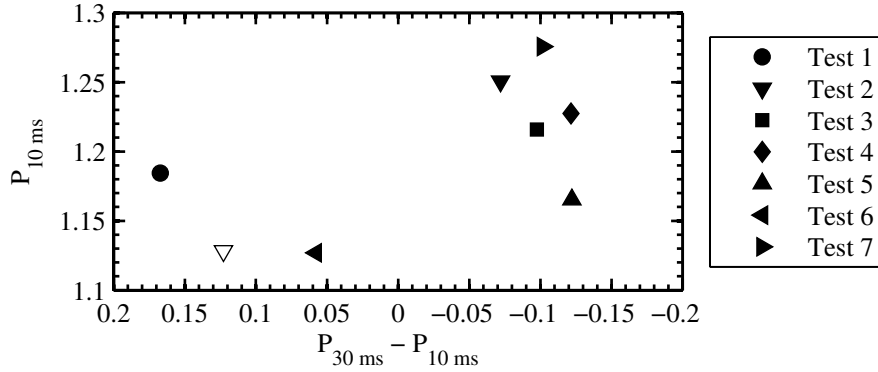


Figure 9.14: Strength of the PVC 10 ms before the spark as a function of decrease in the strength of PVC, for sparks created at location ‘b’

Test No.	No. of sparks for ignition	2D-LIPS	LIPS	Velocity field	PVC
1	2	Yes	No	Yes	No
2	3	No	No	No	Yes
3	11	Yes	No	No	Yes
4	3	Yes	Yes	No	Yes
5	6	Yes	No	No	Yes
6	14	Yes	Yes	Yes	No
7	1	Yes	Yes	NA	Yes

Table 9.1: Summary of ignition experiments at location *b* inside the burner. *Yes* represents successful prediction of fate of ignition attempt and *No* represents failure in prediction of fate of ignition attempt by the given technique. *NA* represents cases when single shot ignited and therefore velocity fields’ comparison could not be performed.

Test#2 at location ‘b’ had less potential to ignite due to lower PVC strength and a decreasing dynamics. As a consequence of which it could not ignite despite having a large initial flame kernel. The accuracy of this processing is estimated to be within 0.1 for the measurement of the strength of the PVC. Therefore, one has here tendencies rather than absolute frontiers.

A summary of ignition tests performed at location ‘b’ is proposed in Table. 9.1. This table recollects the explanations for the success of the igniting spark by emphasizing the main physical mechanisms.

Similar analysis was performed at other locations of the spark to find out possible explanation for success/failure of individual ignition attempts.

9.3.2 Location ‘a’

This location of spark corresponded to 19-20 mm from the injector in axial direction, and 8-13 mm from the center of the burner in radial direction. The typical size of the spark was 1 mm-by-5 mm. Fig. 9.1(a) predicts a very high ig-

nitiation probability of 45 % at this location. Five ignition tests were performed at this location. Number of sparks needed for successful ignition were successively 5, 2, 2, 1, and 1.

2D-LIPS analysis for individual tests at this location are shown in Appendix. D.1. Final results of 2D-LIPS analysis at this location is shown in Fig. 9.15.

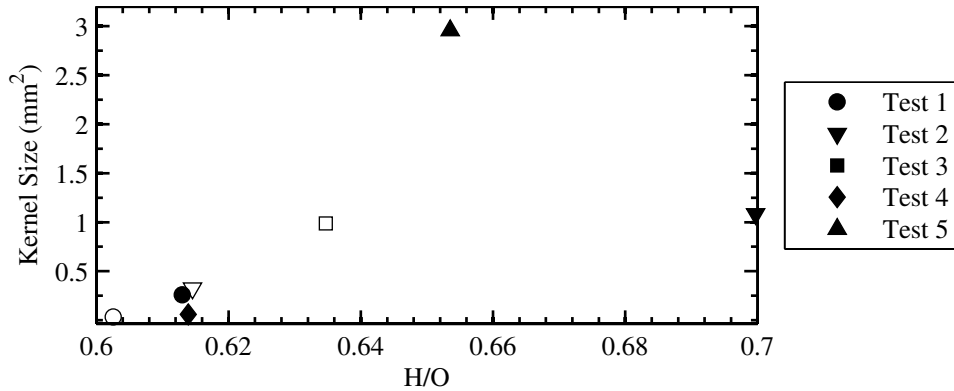


Figure 9.15: Size of the initial flame kernel as a function of mean H/O inside the kernel for sparks created at location ‘a’. Filled markers represent successful sparks and blank markers represent unsuccessful sparks.

It can be seen in Fig. 9.15 that Test#3 could not be explained as the kernel size was calculated to be zero by the selected criteria. Test#1 and Test#4 ignited even with very small initial kernel size. As a result of 2D-LIPS analysis at location ‘a’, conditional probability of ignition has increased from 5/11 to 4/6.

Reason for failed spark during Test#3 could be explained by comparison of velocity field before the igniting and non-igniting sparks. Radial profiles of vertical velocity components at axial location of the two sparks during Test#3 is shown in Fig. 9.16. It shows a significantly lower radial velocity for successfully igniting spark and a very high vertical velocity component for the failed spark created during Test#3. A higher vertical velocity component makes it difficult for the initial flame kernel to convect towards the injector.

Mie-scattering intensity analysis was performed for 5 igniting and 2 non-igniting sparks (one corresponding to Test#2 and the other corresponding to Test#3, which are shown to be well placed to ignite by 2D-LIPS analysis). Radial Mie-scattering profiles at the axial location of the spark are shown in Fig. 9.17. Fig. 9.17 shows that the failed sparks had slightly lower amount of fuel in the region around spark (spark located at $z = 8-13$ mm), but it is not conclusive. Therefore, Mie-scattering measurements could not justify the failure of one spark each in Test#2 and Test#3.

PVC strength analysis by DMD was also performed at location ‘a’ of spark; final results of which is presented in Fig. 9.18.

PVC strength analysis does not provide very useful information. It can be con-

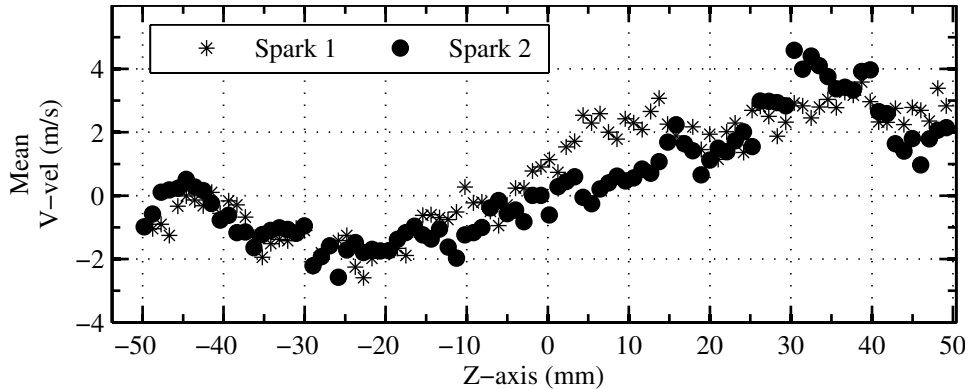


Figure 9.16: Location *a*; Test#3, Analysis of PIV measurements for 2 sparks. Spark#1 failed to ignite while Spark#2 successfully ignited. Velocity profiles at the location of spark have been plotted as a function of radial distance; spark located at 8-13 mm. Profiles plotted using mean velocity fields (over 100 instantaneous fields equivalent to 10 ms) before the deposition of spark energy.

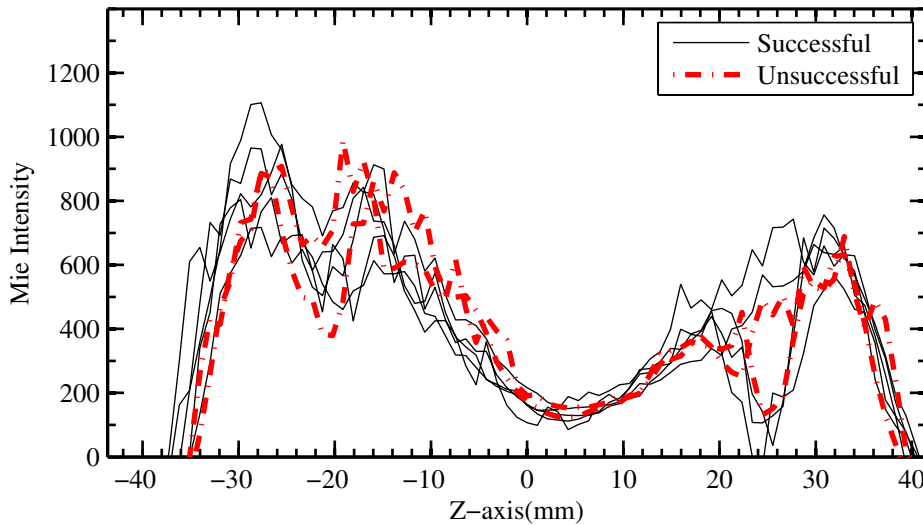


Figure 9.17: Radial profiles of mean Mie-scattering intensity (over 10 ms, before sparks) at axial location of the sparks created at location 'a'; Five successful and two unsuccessful sparks compared.

cluded from these simultaneous measurements that conclusive reasons could not be derived for 2 sparks (one corresponding to Test#2 and another to Test#3), which failed to ignite. Test#3 could not be completely understood as 2D-LIPS predicted no initial flame kernel for igniting spark.

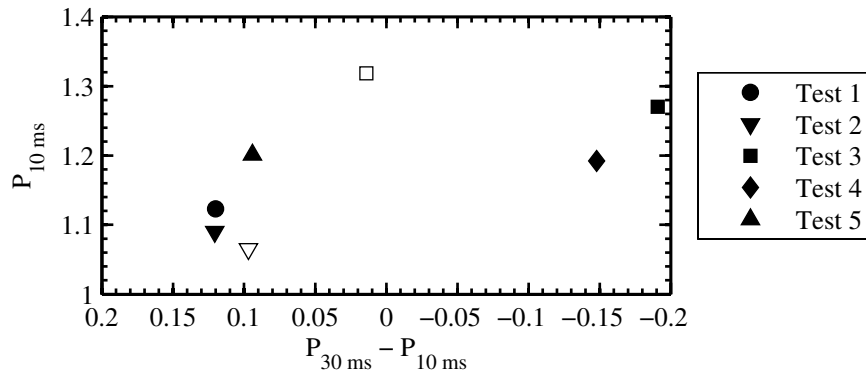


Figure 9.18: Strength of the PVC 10 ms before the spark as a function of decrease in the strength of PVC, for sparks created at location ‘a’

9.3.3 Location ‘c’

This location of spark corresponded to 29-30 mm from the injector in axial direction, and 8-13 mm from the center of the burner, in radial direction. Fig. 9.1(a) predicts a very low ignition probability of approximately 4 % at this location. Five ignition tests were performed at this location. Number of sparks needed for successful ignition were successively 55, 21, 3, 3, and 39. 2D-LIPS analysis for individual tests at this location are shown in Appendix. D.3. Final results of 2D-LIPS analysis at this location is shown in Fig. 9.19.

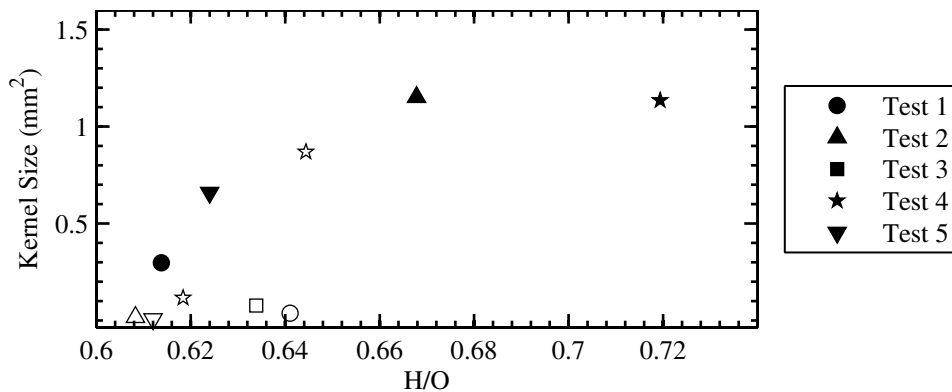


Figure 9.19: Size of the initial flame kernel as a function of mean H/O inside the kernel for sparks created at location ‘c’. Filled markers represent successful sparks and blank markers represent unsuccessful sparks.

It can be seen in Fig. 9.19 that Test#3 could not be explained as the kernel size was calculated to be zero by the selected criterions. Moreover, there was one spark from Test#4 which also seemed to have the potential to ignite. Mie-scattering analysis was performed for five successfully igniting sparks and one spark from Test#4 which could not ignite. Radial Mie-scattering profiles

at the axial location of the spark are shown in Fig. 9.20.

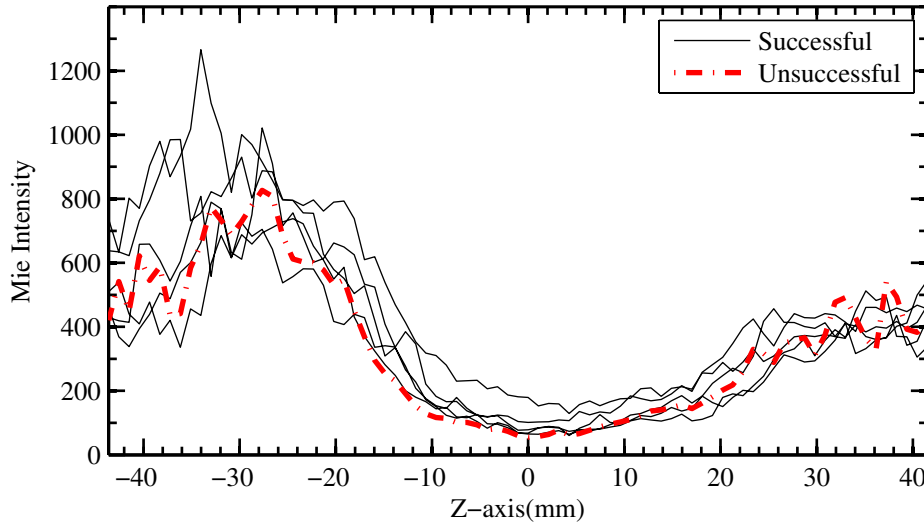


Figure 9.20: Radial profiles of mean Mie-scattering intensity (over 10 ms, before sparks) at axial location of the sparks created at location 'c'; Five successful and one unsuccessful sparks compared.

Fig. 9.20 shows that unsuccessful sparks had slightly less amount of fuel in the region around the spark, which would have lead to failure.

PVC strength analysis (Fig. 9.21) also shows that the failed spark had lower PVC strength just before the spark.

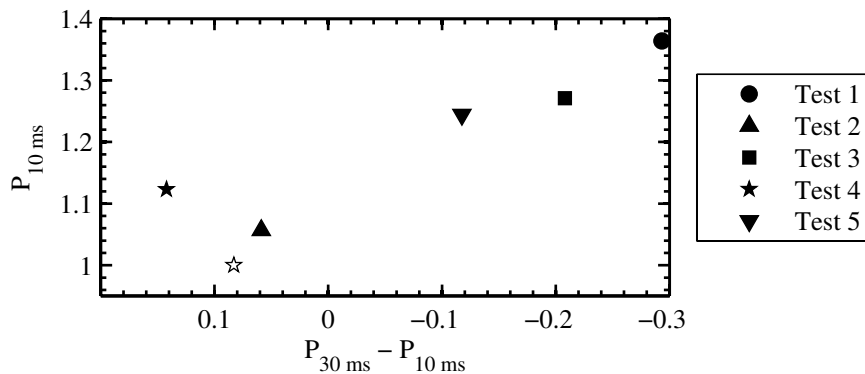


Figure 9.21: Strength of the PVC 10 ms before the spark as a function of decrease in the strength of PVC, for sparks created at location 'c'

As a result of simultaneous measurements at location 'c', all sparks except the igniting spark of Test#3 could be explained.

9.3.4 Location 'd'

This location of spark corresponded to 19-20 mm from the injector in axial direction, and 13-17 mm from the center of the burner in radial direction. Fig. 9.1(a) predicts a very high ignition probability of approximately 57 % at this location. Only four ignition tests were performed at this location due to frequent single shot ignitions. Number of sparks needed for successful ignition were successively 1, 4, 1, and 1. 2D-LIPS analysis for individual tests at this location are shown in Appendix. D.4. Final results of 2D-LIPS analysis at this location is shown in Fig. 9.22.

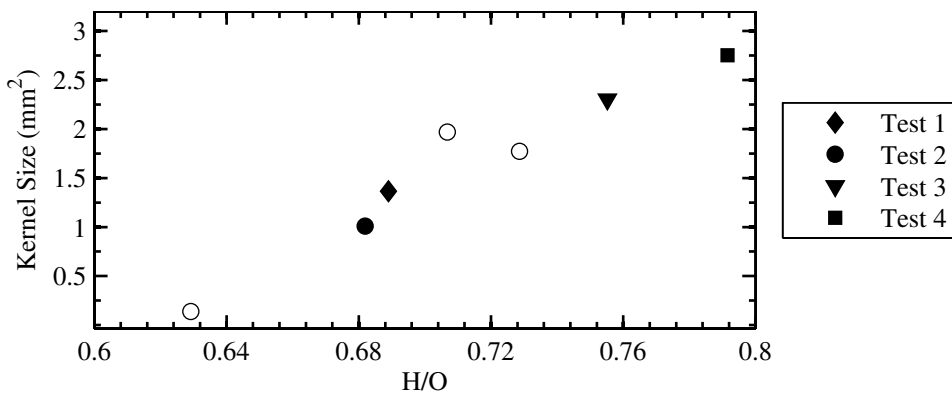


Figure 9.22: Size of the initial flame kernel as a function of mean H/O inside the kernel for sparks created at location 'd'. Filled markers represent successful sparks and blank markers represent unsuccessful sparks.

It can be seen in Fig. 9.22 that 2 unsuccessful sparks for Test#2 also had a big initial flame kernel, nevertheless they could not ignite. Mie-scattering analysis was performed for three successfully igniting sparks (Tests#2, #3, and #4) and two sparks from Test#2 which could not ignite. Radial Mie-scattering profiles at the axial location of the spark as shown in Fig. 9.23 did not provide any criteria to distinguish successful and unsuccessful sparks.

PVC strength analysis (Fig. 9.24) clearly shows that the failed sparks had lower PVC strength just before the spark and higher drop in PVC strength. A lower strength of PVC was responsible for failure of two sparks in Test#2.

Therefore, PVC strength analysis combined with 2D-LIPS measurements could explain the reason for the fate of all ignition attempts.

9.3.5 Location 'e'

This location of spark corresponded to 24-25 mm from the injector in axial direction, and 13-17 mm from the center of the burner in radial direction. Fig. 9.1(a) predicts a low ignition probability of approximately 5 % at this location. Nine ignition tests were performed at this location. Number of sparks needed for successful ignition were successively 19, 57, 15, 3, 6, 11, 12, 31,

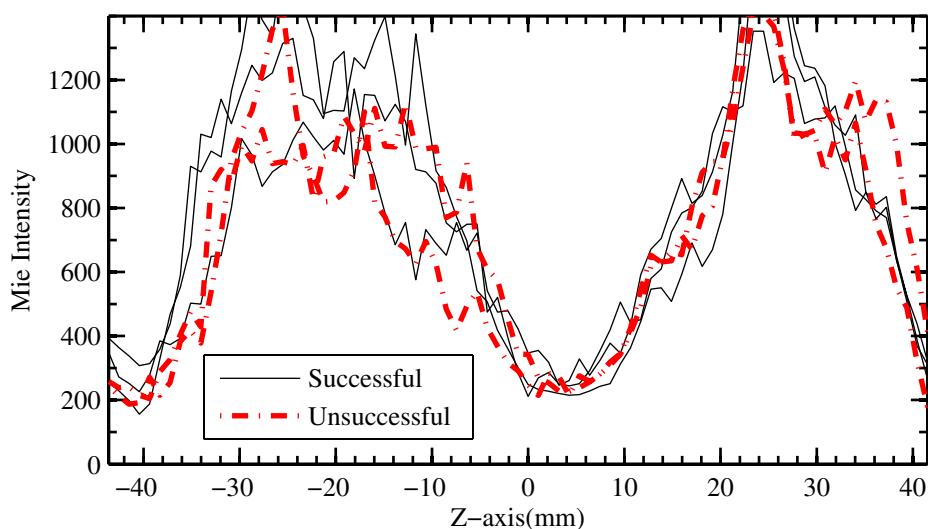


Figure 9.23: Radial profiles of mean Mie-scattering intensity (over 10 ms, before sparks) at axial location of the sparks created at location 'd'; Three successful and two unsuccessful sparks compared.

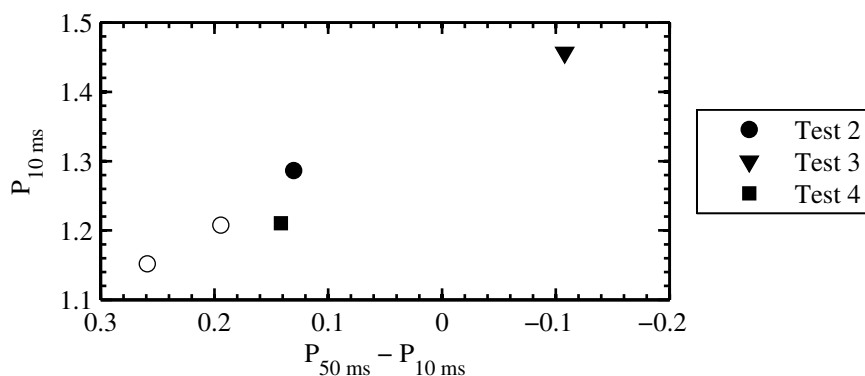


Figure 9.24: Strength of the PVC 10 ms before the spark as a function of decrease in the strength of PVC, for sparks created at location 'd'

and 21. 2D-LIPS analysis for individual tests at this location are shown in Appendix. D.5. Final results of 2D-LIPS analysis at this location is shown in Fig. 9.25.

Fig. 9.25 does not provide a very clear distinction between igniting and failed sparks. Although it generally (except for Test#3) shows that, igniting spark had a bigger initial flame kernel size as compared to failed sparks during the same test. Successfully igniting sparks are also more concentrated towards right-top of Fig. 9.25.

Mie-scattering analysis for all tests together did not provide clear distinction between non-igniting and igniting sparks. For few individual tests, comparison

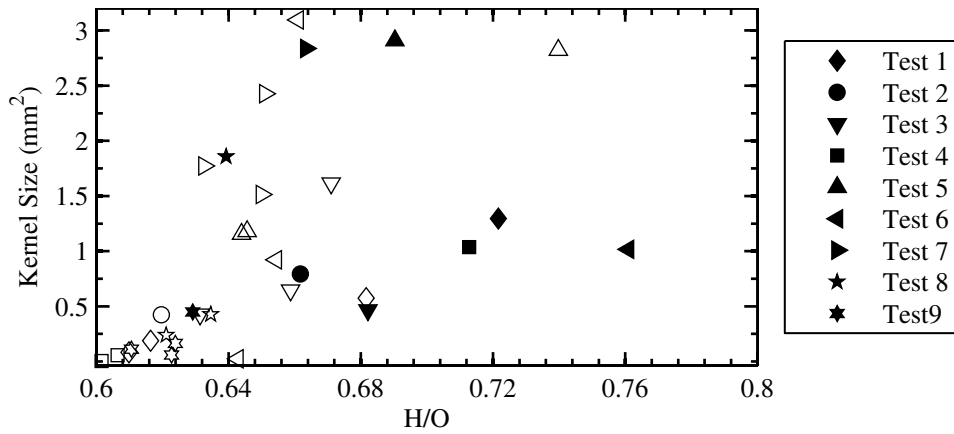


Figure 9.25: Size of the initial flame kernel as a function of mean H/O inside the kernel for sparks created at location 'e'. Filled markers represent successful sparks and blank markers represent unsuccessful sparks.

of Mie-scattering intensity before non-igniting and igniting sparks was useful and provided justification for failure of the few sparks.

PVC strength analysis (Fig. 9.26) also did not help in further distinction of failed and successful sparks.

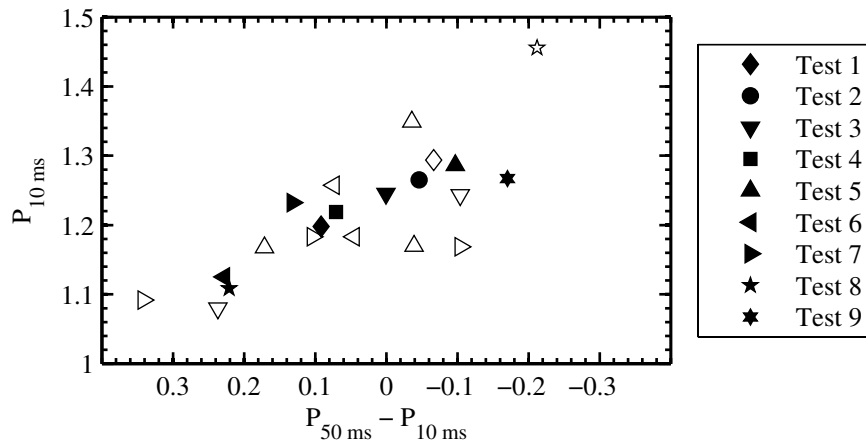


Figure 9.26: Strength of the PVC 10 ms before the spark as a function of decrease in the strength of PVC, for sparks created at location 'e'

At this location of spark, it can be concluded that only 2D-LIPS helps to understand some of the ignition cases. PVC strength analysis and Mie-scattering intensity were not useful.

9.3.6 Location ‘f’

This location of spark corresponded to 29-30 mm from the injector in axial direction, and 13-17 mm from the center of the burner in radial direction. Fig. 9.1(a) predicts a very low ignition probability of approximately 5 % at this location. Four ignition tests were performed at this location, out of which 2 tests did not result in ignition even after a long time (about 1 minute). Number of sparks needed for successful ignition for the two tests were successively 7, and 30. 2D-LIPS analysis for individual tests at this location are shown in Appendix. D.6. Final results of 2D-LIPS analysis at this location is shown in Fig. 9.27.

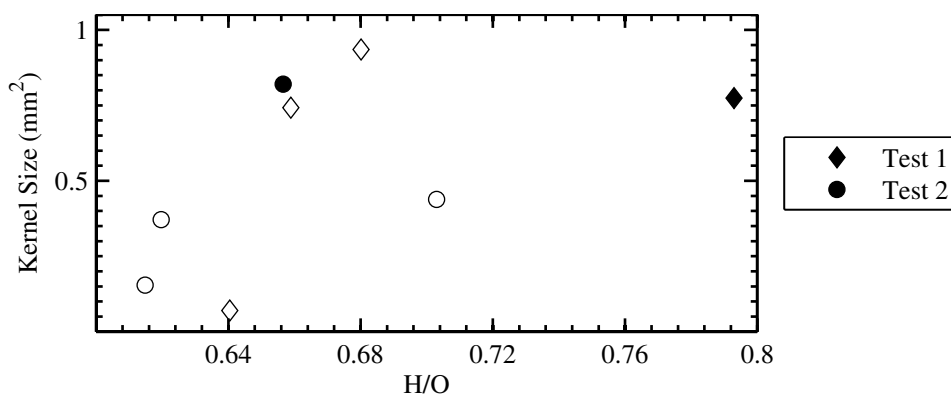


Figure 9.27: Size of the initial flame kernel as a function of mean H/O inside the kernel for sparks created at location ‘f’. Filled markers represent successful sparks and blank markers represent unsuccessful sparks.

Fig. 9.27 shows that the igniting sparks have high initial flame kernel size as compared to failed sparks (except for two failed sparks corresponding to Test#1). Mie-scattering analysis was performed for 4 sparks at the top of Fig. 9.27.

Mie-scattering analysis (Fig. 9.28) shows that the Mie-scattering intensity is significantly lower around the failed sparks, which could have been responsible for their failure.

PVC strength analysis (Fig. 9.29) shows a lower PVC strength and higher drop for failed sparks as compared to successful sparks.

Therefore, 2D-LIPS analysis combined with Mie-scattering and PVC strength analysis justifies the reason for the fate of all ignition attempts.

9.3.7 Location ‘g’

This location of spark corresponded to 29-30 mm from the injector in axial direction, and 17-20 mm from the center of the burner in radial direction. Fig. 9.1(a) predicts an ignition probability of approximately 7.5 % at this location. Seven ignition tests were performed at this location. Number of sparks

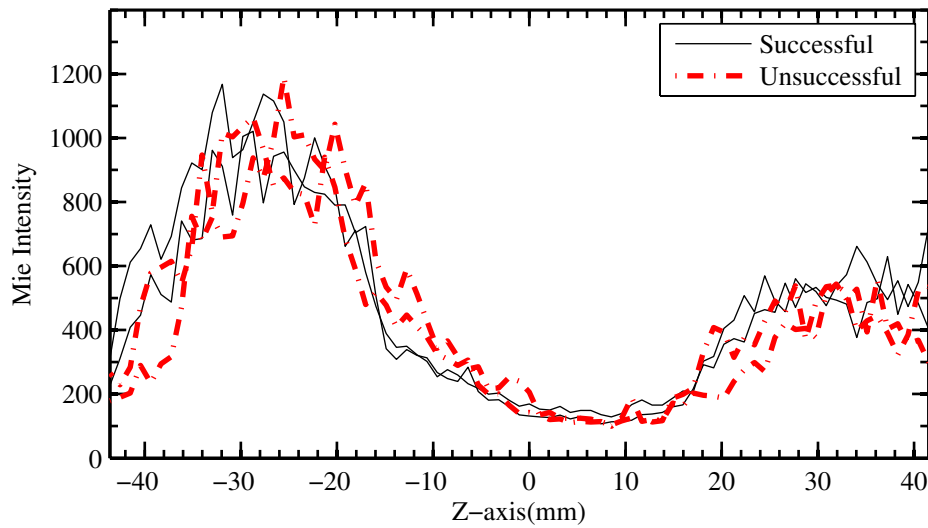


Figure 9.28: Radial profiles of mean Mie-scattering intensity (over 10 ms, before sparks) at axial location of the sparks created at location 'f'; Two successful and two unsuccessful sparks compared.

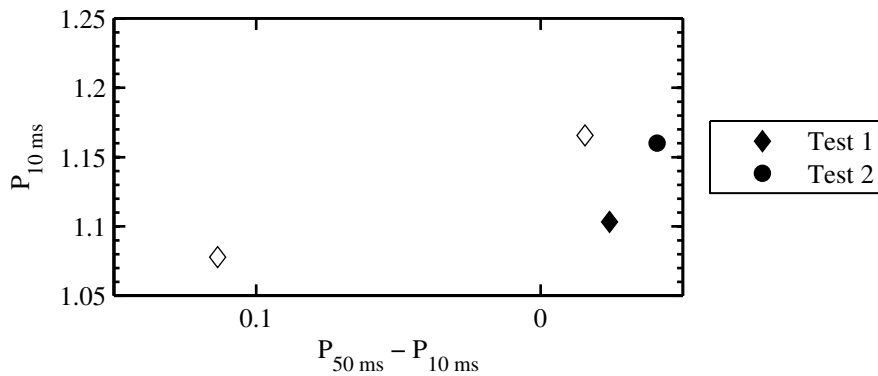


Figure 9.29: Strength of the PVC 10 ms before the spark as a function of decrease in the strength of PVC, for sparks created at location 'f'

needed for successful ignition for the seven tests were respectively 20, 29, 24, 4, 11, 3, and 2. 2D-LIPS analysis for individual tests at this location are shown in Appendix. D.7. Final results of 2D-LIPS analysis at this location is shown in Fig. 9.30.

Fig. 9.30 shows that most of the igniting sparks (5 out of 7) have high initial flame kernel size as compared to failed sparks (except Test#2 and #7). Even Test#2 and Test#7 have higher kernel size for ignited spark as compared to failed sparks from the same tests.

Fig. 9.30 shows that for Test#6 there were three sparks of almost the same size and equivalence ratio, the reason for failure of 2 of these sparks was shown by

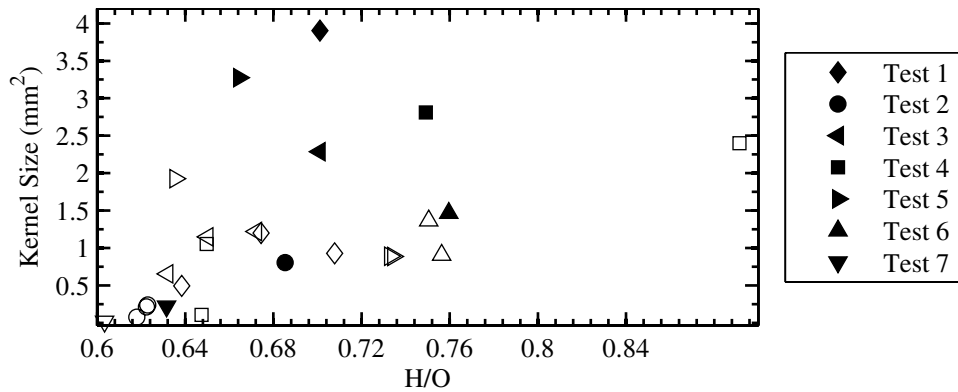


Figure 9.30: Size of the initial flame kernel as a function of mean H/O inside the kernel for sparks created at location 'g'. Filled markers represent successful sparks and blank markers represent unsuccessful sparks.

Mie-scattering intensity profiles as shown in Fig. 9.31.

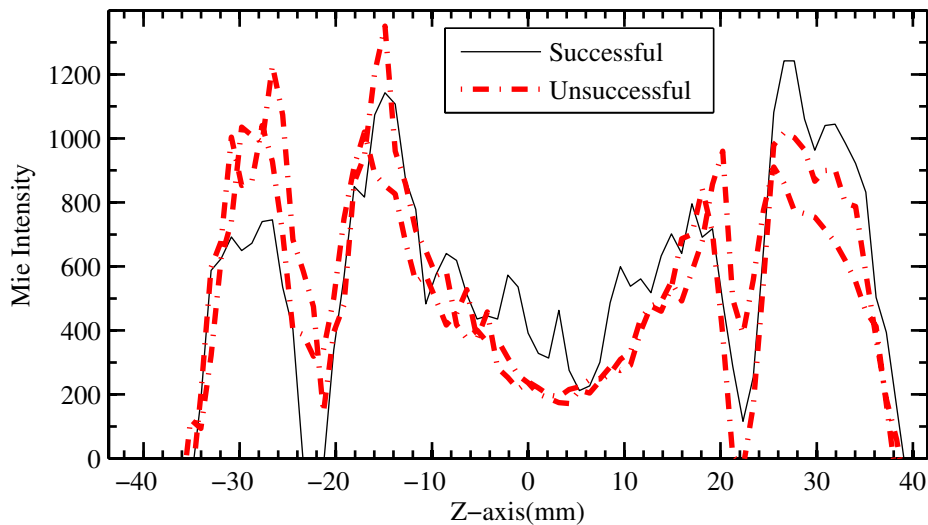


Figure 9.31: Radial profiles of mean Mie-scattering intensity (over 10 ms, before sparks) at axial location of the sparks created during Test#6 at location 'g'; Two unsuccessful and one successful sparks compared.

PVC strength analysis (Fig. 9.32) did not provide a criteria for distinguishing failed sparks from successful sparks.

Therefore, 2D-LIPS analysis and Mie-scattering intensity for few cases provided criteria to distinguish most of the igniting sparks from failed sparks. PVC strength analysis was not very useful in distinguishing failed sparks from successful sparks.

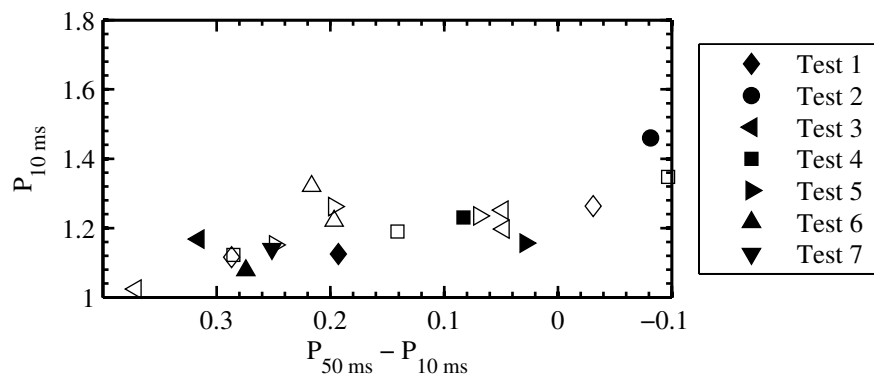


Figure 9.32: *Strength of the PVC 10 ms before the spark as a function of decrease in the strength of PVC, for sparks created at location 'g'*

Chapter 10

Conclusions and Perspectives

The process of ignition inside a modeled aeronautical combustion chamber has been studied through measurements of various physical parameters. It was shown that local as well as global physical parameters play a role in the determination of the fate of an ignition attempt and some criteria could be extracted in a simplified staged injector.

The principle of laser-induced plasma spectroscopy (LIPS) was extended to develop an imaging based approach, named 2D-LIPS. Two-dimensional laser-induced plasma spectroscopy (2D-LIPS) was developed for the measurement of spatially resolved equivalence ratios. Temporal synchronization of the measurements was carefully performed for atomic emission measurements based on detailed spectral analysis. Several image processing techniques were developed to perform the ratio, with a high spatial resolution, of two plasma images using essentially correlation based techniques. It was shown that accuracy of equivalence ratio measurements could be improved by further image processing at the cost of the spatial resolution. Quantitative measurements of equivalence ratios was performed in premixed gaseous burners and results showed that the 2D-LIPS has a much lower uncertainty than conventional LIPS approach. It was also suggested that 2D-LIPS measurements provided spatially resolved spark energies along with spatially resolved equivalence ratios.

Due to difficulties in the calibration, 2D-LIPS measurements in two-phase flows could only provide qualitative measurements of equivalence ratios in presence of droplets. Those measurements, coupled to the estimation of the local spark energy could be used to calculate the size of initial flame kernel which was shown to be critical for the success/failure of an ignition attempt. Those coupled measurements clearly showed the differences between the size of the initial flame kernel and the size of energy deposition region.

This technique was mainly applied in a combustion chamber allowing the study of air/dodecane configuration. In order to understand flow field inside a two-phase flow burner, measurements of both aerodynamic and droplets' flow were separately performed. It was seen that aerodynamic and droplets' flow field

were significantly different, in terms of both velocity magnitudes as well as recirculation zones. This is an important finding as it shows that the aerodynamic flow field can not be used as a representative of flow field in presence of sprays, due to the strong initial momentum induced by the spray.

Ignition is a highly transient phenomenon, therefore, understanding ignition in two-phase flows required various time and space resolved measurements. The objective of this thesis was to provide shot-to-shot comparison of ignition attempts based on simultaneous measurements of various quantities. A critical initial flame kernel size provided by 2D-LIPS analysis was shown to be very important for a successful ignition. The presence of fuel around the spark was also shown to play role in the ignition process, as shown qualitatively by the measurements of Mie-scattering of droplets. The dynamics of the Precessing Vortex Core (PVC), measured by time-resolved Planar Imaging Techniques could also affect the ignition process by allowing an easier convection of the kernel in the low-pressure region. Simultaneous diagnostics provided conclusive reasons for the failure or success of most of individual ignition attempts.

Another important conclusion was the incapability of conventional LIPS measurements to predict ignition. It showed that overall equivalence ratio inside the spark is not a relevant parameter for ignition studies. It also makes it difficult to design simple and small sensors aimed to discuss ignition probability in industrial applications without adding extra information on plasma energy for instance.

Perspectives

The ignition of an aeronautical combustion chamber remains a challenge as far as security is concerned. Due to turbulence, predicting the fate of a spark will still remain probabilistic. A descent number of samples can not be achieved through numerical analysis and therefore there is still a strong need for experimental investigations. This thesis could shed some lights on the initial creation of a kernel in a simplified combustion chamber. Many aspects still require a detailed attention in the near future and several directions are proposed. Two dimensional measurements are still a good trade-off and should be further investigated. For instance, it would be helpful to quantify the fuel vapor and liquid concentration before the spark using some tracer molecules, coupled to velocity fields of the complete combustion chamber and possibly a planar image of the flame front, with the radical OH. Those measurements should be performed at a high repetition rate to discuss some dynamics of the system. The coupled measurements of different quantities may help building some conditional rules for ignition and use similar criteria on numerical simulations.

Concerning the three dimensional movement of the kernel, it would be interesting to perform investigation, at first based on the natural emission of the flame. Having two (or more) high-speed cameras equipped with interferential filters centered on some radicals may be used to track the actual movement

of the flame base and performs detailed measurements of its dynamics. This would provide quantitative data to establish a more comprehensive scenario of the ignition process. Time-resolved quantitative velocity measurements are yet possible in non reacting gaseous conditions using Tomographic Particle Image Velocimetry. It would be interesting to extend this principle to the measurements of sprays based on a three dimensional Particle Tracking Velocimetry approach. Even though the volume of investigation would remain limited, it may provide a complete dataset of local conditions in a volume around the spark. This would require a full optical access which may be possible if a dedicated ignition chamber is used. A chamber may be designed to allow four planar accesses at the cost of no cooling. This may be possible as only the ignition part is of interest. Once a flame is attached on the burner, all fuel supplies may be cut off to lead to the extinction of the flame.

The 2D-LIPS technique may also be improved. At first, one has to find a proper way for calibrating in presence of droplets for both mixture fraction and absolute energy. This may be done by combining experimental results and some simulation tools. For instance, it would be interesting to see if in the presence of droplets, the lifetime of the different species is strongly modified and if quenching is an issue. Typical sprays used in the current experiments were relatively diluted so that those effects may have been negligible. Also, to properly take into account the correction due to background, it would be interesting to propose a new optical layout, still based on two cameras. However, with a proper design, each camera may look at the same object with two different filters each, using beam splitter and mirrors before the chip of the camera. This would allow a direct measurement of local background and possibly improve the signal to noise ratio of the technique. Some difficulties in ghost images may however limit the advantages of such an approach.

Concerning post-processing techniques, the Dynamic Mode Decomposition seems very promising but still requires a lot of care, especially for quantifying growing/fating events. In the present approach, a simple analysis was proposed and this lead to relatively large uncertainties. It would also be interesting to analyze different sets of data (pressure - velocity - density) and see their interactions through this decomposition, either through a multi-variable DMD or through an approach similar to the Extended-Proper Orthogonal Decomposition.

Appendix A

Potential of polarization-resolved laser-induced plasma spectroscopy for ignition studies

This report aims to explore the possibility of combining Laser induced plasma spectroscopy measurements (both 0D and 2D) with polarization resolved Laser induced plasma spectroscopy. An assessment of the advantage in terms of the increase in the value of alpha (which is defined as the ratio of atomic emission intensity to the total intensity observed by the ICCD cameras through a band pass filter) is performed.

The experiments performed by [Majd, Arabanian, and Massudi \(2010\)](#) demonstrate that the continuum level in the emission of a plasma generated on the surface of a metal can be highly reduced by the use of a polarizer. In that study, the signal-to-continuum ratio is increased from 2 to 6, which implies that about 40% reduction in continuum level was achieved. The proposed reason for which is a stronger polarization of continuum emission and weaker polarization of discrete line emission. The article presents a time integrated measurement of the plasma emissions, and it is well known that continuum emissions are much higher in the initial stages of the plasma lifetime, and decreases rapidly with delay ([De Giacomo, Gaudiuso, Dell'Aglio, and Santagata \(2010\)](#)). Nevertheless it can be assumed that polarization reduces continuum at all times during the lifetime of a plasma by the same factor. Thus, if one assumes that a 40 % reduction in continuum level can be achieved. Application of this reduction in continuum level to spectra obtained results in a increase in α_O from (0.7059 ± 0.0406) to (0.8024 ± 0.0288) . These are the values for mean and standard deviations for 40 shots acquired for a Q-switch setting of $325 \mu s$, a delay of 1500 ns from the start of the plasma and an integration time of 80 ns. Similarly, the value of α_N increase from (0.5738 ± 0.0477) to

(0.7084 ± 0.0360) . This means that significant increase in alpha values can be achieved if the assumptions are true.

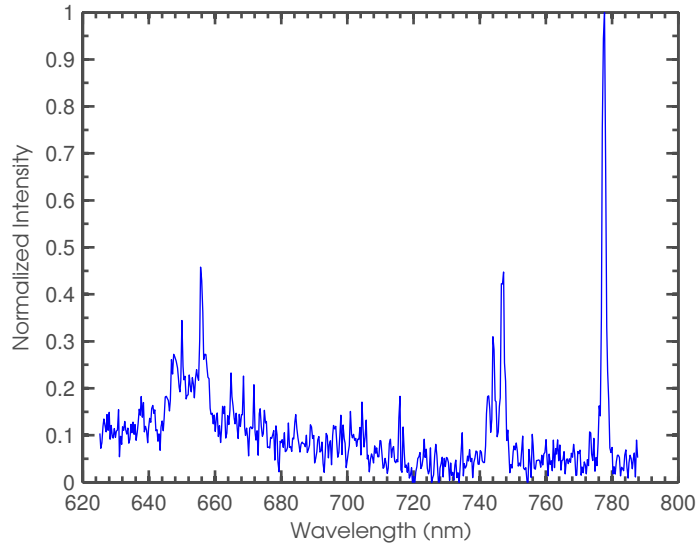


Figure A.1: *Spectral emission of a plasma created in air*

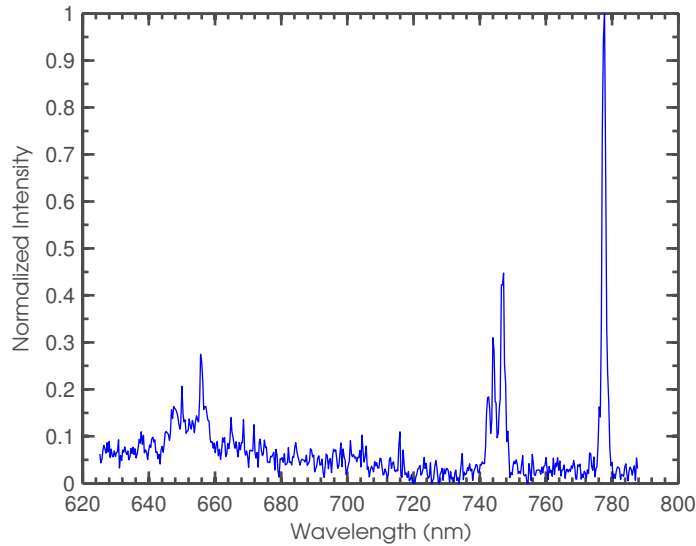


Figure A.2: *Spectra with synthetically reduced continuum level.*

Another study by [Zhao, Singha, Liu, and Gordon \(2009\)](#) using polarization resolved LIPS of femto-second laser generated plasmas on solid surface also showed similar increments in peak to continuum ratio for space and time integrated emission measurements.

But a recent study by [Asgill, Moon, Omenetto, and Hahn \(2010\)](#) presents a time resolved effect of polarization resolution of LIPS. This work is more relevant to our study as it studies the polarization effects of a laser induced plasma generated in a gaseous flow as well. In this study, for a plasma generated in nitrogen and spectra acquired at a delay of $1 \mu s$ for an integration time of $0.5 \mu s$, it is shown that such plasma has no polarization associated with either the continuum or atomic emissions. It is also shown that plasma generated on surfaces of solid may show some polarization effects, which are generally because of the fresnel reflections from the surface of solids. This may be a reason of high polarization effects observed in the previous studies. Thus the potential of polarization resolved LIPS in the current experimental procedure could not be proved, and the possibility of having any significant advantages is bleak. But it can be learnt that if some method is found by which we could reduce the continuum level, a significant increase in the values of α_λ could be achieved.

Appendix B

Transmission properties of band-pass filters used for 2D-LIPS measurements

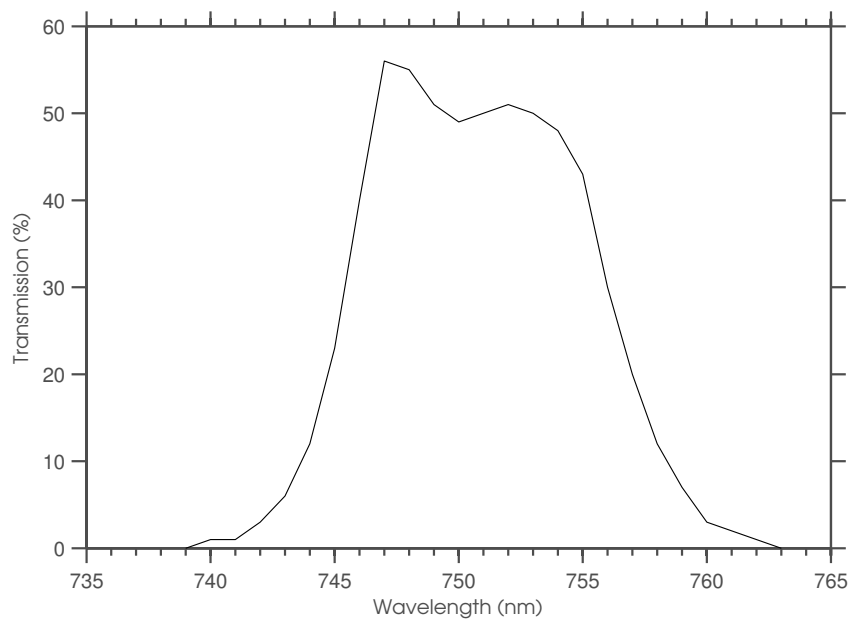


Figure B.1: *Transmission percentage as a function of wavelength for FB750-10*

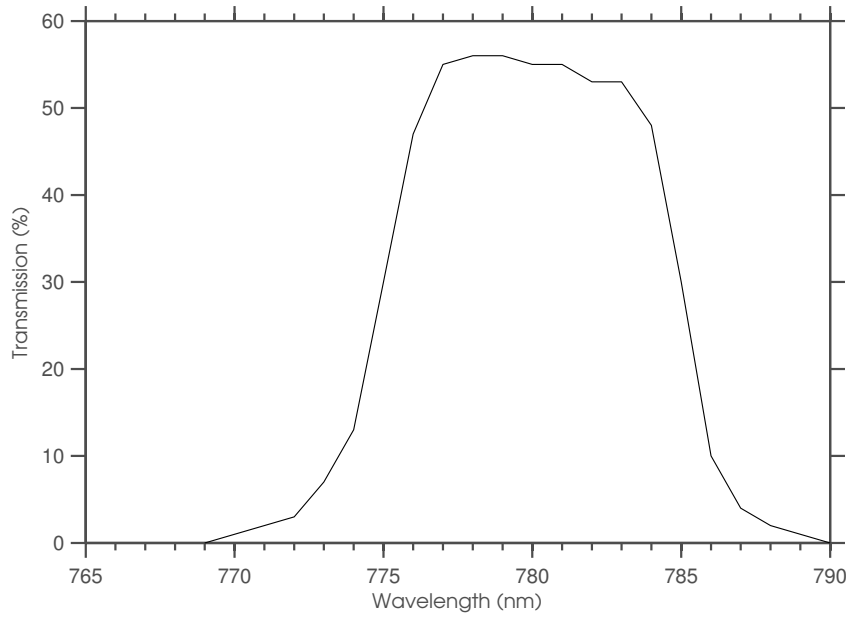


Figure B.2: *Transmission percentage as a function of wavelength for FB780-10*

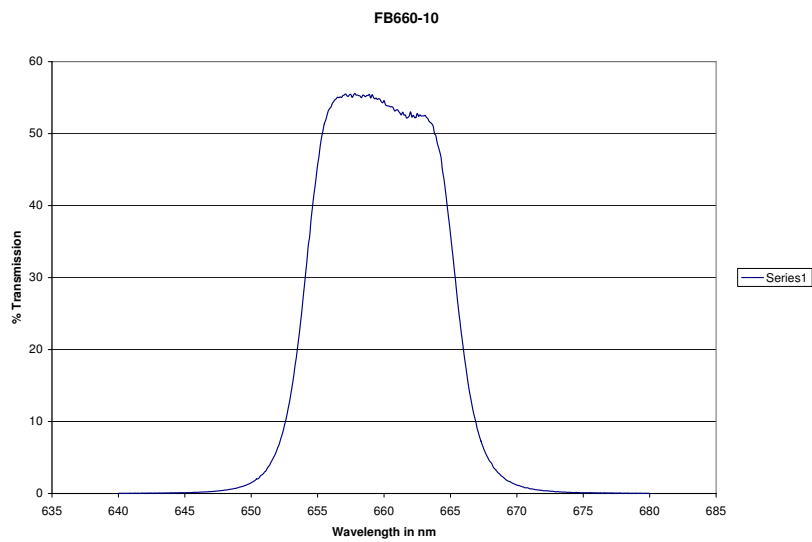


Figure B.3: *Transmission percentage as a function of wavelength for FB660-10*

Appendix C

Estimation of initial flame kernel size

Theoretical calculation of initial flame kernel size was performed using a spherical initial flame kernel. Deposition of spark energy in a small spherical region attempts to ignite some/all of the gas at the location of the spark.

During the laminar flow experiments in gaseous burner (Fig. 3.1). The flow of approximately 1 m/s was present and the width of the spark on the top of the burner could be approximated to be 1 mm. Therefore the ignition of gas at the location of the spark should have occurred within 1 ms, otherwise the hot gas region would be convected by the flow. Although, convected pockets of hot gases can help in the ignition process at a later stage. Or, auto-inflammation of the convected hot pockets can occur at a later stage.

Therefore, ignition process can be divided into following steps: (a) deposition of spark energy, (b) heating of mixture at the location of the spark. If the temperature of the mixture increased to a level which causes ignition delays smaller than convection time (1 ms in case of laminar burner), then ignition would occur for that pocket of mixture which satisfied the above condition.

Ignition delay of a premixed mixture is a function of initial temperature as shown in Fig. C.1. The plot was obtained by extrapolation of the data presented in Darabiha et al. (2010).

It can be seen in Fig. C.1 that for ignition delays less than 1 ms, an approximate initial gas temperature of 1440°C should be available. During ignition experiments in laminar gaseous burner, this temperature was achieved by the deposition of spark energy. The temperature of the gases before deposition of spark energy was 25°C. Thus spark energy should be enough to raise the temperature to approximately 1500 °C. Mass fraction of methane in a unburned mixture of methane-air with an equivalence ratio 0.7 can be calculated as,

$$Y_{m_{CH_4}} = \frac{0.7 \times M_{CH_4}}{0.7 \times M_{CH_4} + 2 \times (M_{O_2} + \frac{79}{21} \times M_{N_2})} = 0.0392 \quad (C.1)$$

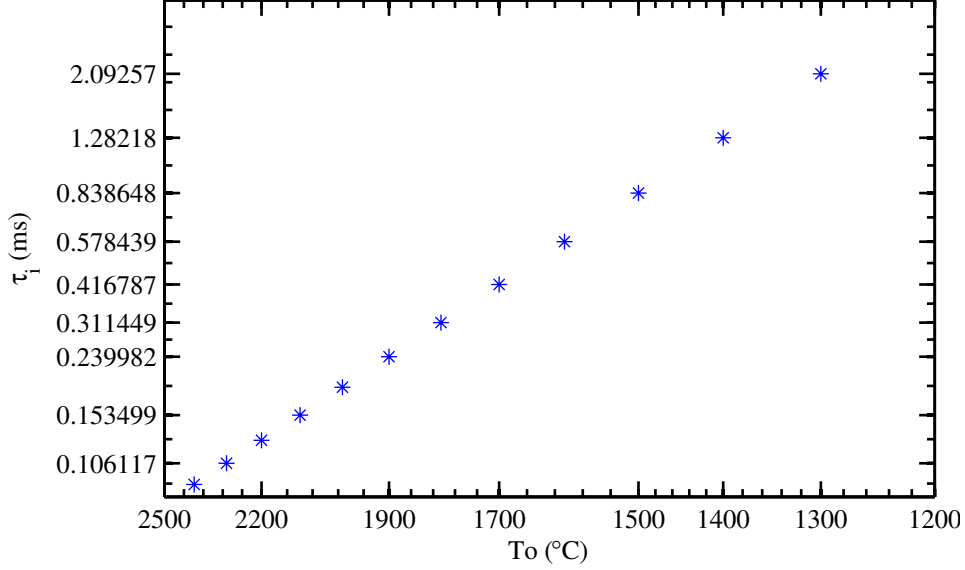


Figure C.1: Ignition delay, τ_i (ms) as a function of initial temperature, T_o ($^{\circ}$ C) for methane-air mixture.

Similarly, mass fraction of air in the same mixture was calculated to be,

$$Y_{m_{air}} = 0.9608 \quad (\text{C.2})$$

specific heat at constant pressure for air, $C_{p_{air}}$ was 1.005 KJ/kgK at 300 K. C_p is a function of temperature and increases with temperature to 1.216 KJ/kgK at 1500 $^{\circ}$ C..

Similarly, specific heat at constant pressure for methane, $C_{p_{CH_4}}$ was 2.226 KJ/kgK at 300 K. It is also a function of temperature and increases with temperature to 4.708 KJ/kgK at 1500 $^{\circ}$ C.

Therefore, for a change in mixture temperature from 25 $^{\circ}$ C to 1500 $^{\circ}$ C, the enthalpy change of the methane-air mixture can be calculated as

$$\Delta H = \int_{25}^{1500} C_{P_{CH_4}} Y_{m_{CH_4}} dT + C_{P_{Air}} Y_{m_{Air}} dT = 1856.4 \text{ kJ/kg} \quad (\text{C.3})$$

Each voxel in 2D-LIPS measurements corresponds to an approximate volume of $50^3 \mu\text{m}^3$. Whereas, density of methane-air mixture was 1.2535 kg/ m^3 . Therefore mass of each voxel of the mixture could be calculated as, Mass of each voxel = 1.567×10^{-13} kg.

Therefore energy required for each voxel to have an ignition delay less than 1 ms could be calculated as,

$$\text{Energy Required} = 1.567 \times 1856.4 \times 10^{-10} \text{ J} = 0.2909 \mu\text{J}.$$

If this much energy is supplied at each voxel with equivalence ratio of 0.7 then ignition would occur at that voxel.

It was seen that after Abel transformation of oxygen emission images (Section. 8.2.2) that a minimum incident energy of 3.5 μJ per voxel was required for ignition. If it is assumed that 7-8% of deposited energy is absorbed in the gases as shown by [Phuoc \(2004\)](#), than 0.24-0.28 μJ was actually deposited in the ignition. This is in confirmation with the results obtained by current theoretical analysis.

The next step was to calculate the size of initial kernel which would have sustained expansion.

It was supposed that 'r' was the critical radius of the initial flame sphere. Rate of energy generation at the edge of the kernel is a function of laminar flame velocity. It was assumed that the sphere expands at laminar flame burning velocity.

Laminar burning velocity $S_L = 0.2$ m/s for methane-air mixture of equivalence ratio 0.7.

Heat of combustion of methane $H_{comb_{CH_4}} = 50 \times 10^6$ J/kg.

Rate of heat generation

$$\begin{aligned} Gain &= 4\pi r^2 \times S_L \times \rho_{CH_4} \times H_{comb_{CH_4}} \\ &= 4\pi r^2 \times 0.2 \times 0.0392 \times 1.2535 \times 50 \times 10^6 \\ &= 6.1747 \times r^2 \times 10^6 \text{ J/s} \end{aligned} \quad (C.4)$$

Next step was to calculate convective losses. Rate of convective heat loss can be written as:

$$q = hcAdT \quad (C.5)$$

where, hc = convective heat transfer coefficient of the process. It is a function of Nusselt number (Nu) of the process and given as

$$hc = \frac{Nu \times \lambda}{D} \quad (C.6)$$

where, λ = thermal conductivity of the material (W/mK)

Nu for a sphere in a constant flow can be written on the basis of Reynolds number (Re) and Prandtl number (Pr) as given by [Taine and Petit \(2010\)](#),

$$Nu = 2.0 + 0.6 \times Re_D^{\frac{1}{2}} \times Pr^{0.31} \quad (C.7)$$

where, Re can be calculated as,

$$Re = \frac{\rho_{mix} U_{\infty} D}{\mu_{mix}} = \frac{1.2535 \times 1 \times 2 \times r}{1.779 \times 10^{-5}} = 1.4092 \times 10^5 \times r \quad (C.8)$$

Pr can be safely taken as 0.7, for gases. Therefore, Nu was calculated to be

$$Nu = 2.0 + 0.6 \times (1.4092 \times 10^5 \times r)^{\frac{1}{2}} \times 0.7^{0.31} = 2 + 201.66r^{\frac{1}{2}} \quad (C.9)$$

Thermal conductivity, λ of methane was found to be 0.030 and that of air to be 0.024. The thermal conductivity of the mixture can be calculated based on mass fraction of methane and air. The thermal conductivity of the mixture was calculated to be 0.0242.

$$hc = \frac{(2 + 201.66r^{\frac{1}{2}}) \times 0.0242}{2r} \quad (\text{C.10})$$

The temperature of the surface of the kernel was assumed to be same as adiabatic flame temperature for an equivalence ratio of 0.7 and ideal atmospheric conditions. The adiabatic flame temperature was found to 1837 K as calculated by CERFACS adiabatic flame temperature calculator available online at <http://elearning.cerfacs.fr/combustion/tools/adiabaticflametemperature/index.php>. Finally, rate of convection losses can be calculated as,

$$\begin{aligned} q_{convection} &= \frac{(2 + 201.66r^{\frac{1}{2}}) \times 0.0242}{2r} \times 4\pi r^2 \times (1837 - 298) \\ &= 234.00r \times (2 + 201.66r^{\frac{1}{2}}) \text{ J/s} \end{aligned} \quad (\text{C.11})$$

Radiation losses can also be taken into account. The radiation losses from any material are given by Stefan-Boltzman law.

$$q_{radiation} = \epsilon\sigma(Th^4 - Tc^4)A \quad (\text{C.12})$$

where, ϵ is the emissivity of an object. For radiation calculations, the flame kernel was assumed to be containing the products of combustion at the adiabatic flame temperature. ϵ was estimated to be order of 0.001, using CK-model for broadband emissions from the constituents of the flame kernel (Zhang (2010), and, Soufiani and Taine (1997)). The value is also in coherence with the emissivity values available in literature (Egbert (1942)). σ is the Stefan-Boltzman constant whose value is 5.6703×10^{-8} ($\text{W}/\text{m}^2\text{K}^4$). Th is the temperature of hot body, which was taken as the adiabatic flame temperature. Tc is the surroundings temperature which was 25°C .

$$\begin{aligned} q_{radiation} &= 0.001 \times 5.6703 \times 10^{-8} \times (1837^4 - 298^4) \times 4\pi r^2 \\ &= 8.1087 \times 10^3 r^2 \text{ W} \end{aligned} \quad (\text{C.13})$$

It can be concluded that radiation losses are significantly smaller than convection losses and the energy generated by the flame. All loss rates and rate of generation of combustion energy as a function of flame kernel radius are presented in Fig. C.2. It can be concluded that a minimum radius of 0.2 mm is required for an initial flame kernel for the flame kernel to sustain.

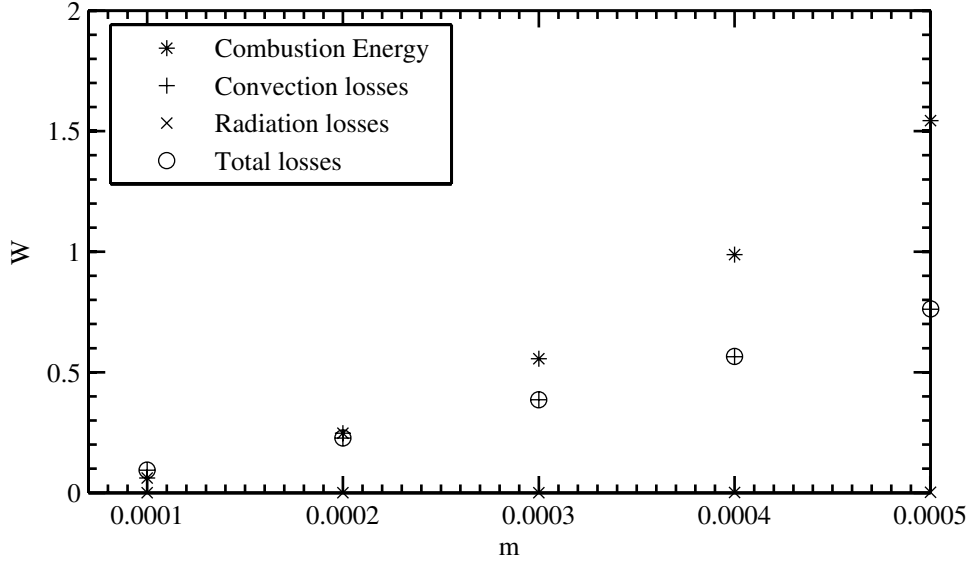
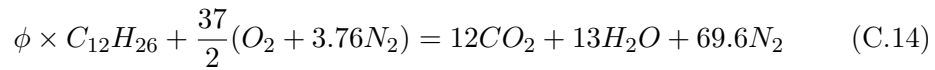


Figure C.2: Rate of generation of combustion energy and rate of convection and radiation losses as a function of initial spherical kernel diameter, for sparks created in premixed methane-air mixture with an equivalence ratio of 0.7.

Application to Dodecane

Similarly, calculations of initial flame kernel diameter can be performed for dodecane. Dodecane being liquid and an initial temperature of 200°C brings more complexity in to the process.



where, ϕ is the equivalence ratio of dodecane, which was kept globally constant at 0.7.

Properties of dodecane,

Lower Heating Value = 44150 kJ/kg

Thermal conductivity (liquid): = 0.1269 W/m.K

Flame speed (for $\phi = 0.7$) = 0.5 m/s (Kumar and Sung (2007))

Density of air at 200°C = 0.7458 kg/m³

Viscosity of air at 200°C = 1.45×10^{-5} Pa-s

Let us suppose an initial flame kernel diameter of 'r'.

Mass fraction of dodecane for an equivalence ratio of 0.7 was calculated using the equation similar to the one presented in Equation C.1.

Rate of heat generation,

$$\begin{aligned} q_{radiation} &= 0.001 \times 5.6703 \times 10^{-8} \times (1837^4 - 298^4) \times 4\pi r^2 \\ &= 8.1087 \times 10^3 r^2 W \end{aligned} \quad (C.15)$$

$$\begin{aligned}
Gain &= 4\pi r^2 \times S_L \times \rho_{mixture} \times H_{comb_{C_{12}H_{26}}} \\
&= 4\pi r^2 \times 0.5 \times 0.0181 \times 0.7458 \times 44.150 \times 10^6 \\
&= 3.7447 \times r^2 \times 10^6 J/s
\end{aligned} \tag{C.16}$$

Density of mixture was taken as that of air at 200°C, as dodecane having very small mass fraction won't affect the density of the mixture significantly. Next step is to calculate convective losses using the equations presented in Equations C.5 and C.6 The initial flame kernel was assumed to be in the internal recirculation zone with mean velocity of the order to 1 m/s.

$$Re = \frac{\rho_{mix} U_{\infty} D}{\mu_{mix}} = \frac{0.7458 \times 1 \times 2 \times r}{1.45 \times 10^{-5}} = 1.0287 \times 10^5 \times r \tag{C.17}$$

Therefore,

$$Nu = 2.0 + 0.6 \times (1.0287 \times 10^5 \times r)^{\frac{1}{2}} \times 0.7^{0.31} = 2 + 172.29634r^{\frac{1}{2}} \tag{C.18}$$

Thermal conductivity, λ of dodecane was found to be 0.1269 (for liquid dodecane) and that of air to be 0.04118 (at 200°C). For evaporated dodecane value of conductivity could not be found. Therefore conductivity of air was taken as the conductivity of mixture.

$$hc = \frac{(2 + 172.2963r^{\frac{1}{2}}) \times 0.04118}{2r} \tag{C.19}$$

The temperature of the surface of the kernel was assumed to be same as adiabatic flame temperature for an equivalence ratio of 0.7 and normal pressure and 200°C temperature. The adiabatic flame temperature for dodecane-air mixture at an equivalence ratio of 0.7 was taken to be 2100 K, same as that of kerosene.

$$\begin{aligned}
q_{convection} &= \frac{(2 + 172.2963r^{\frac{1}{2}}) \times 0.04118}{2r} \times 4\pi r^2 \times (2100 - 473) \\
&= 420.9725r \times (2 + 172.2963r^{\frac{1}{2}}) J/s
\end{aligned} \tag{C.20}$$

Radiation losses can also be taken into account.

$$q_{radiation} = 0.6 \times 5.6703 \times 10^{-8} \times (2100^4 - 473^4) \times 4\pi r^2 = 1.382 \times 10^4 r^2 W \tag{C.21}$$

Summary of rates of losses and combustion energy production as a function of flame radius can be seen in Fig. C.3

It can be concluded that for experiments with dodecane-air mixture with an equivalence ratio of 0.7, an initial flame kernel diameter of 0.75 mm, or an initial kernel area of approximately 1.8 mm² was required for the flame kernel to sustain and develop into flame. This initial flame kernel size is a function of equivalence ratio and can be calculated for different equivalence ratios as shown in Fig. C.4.

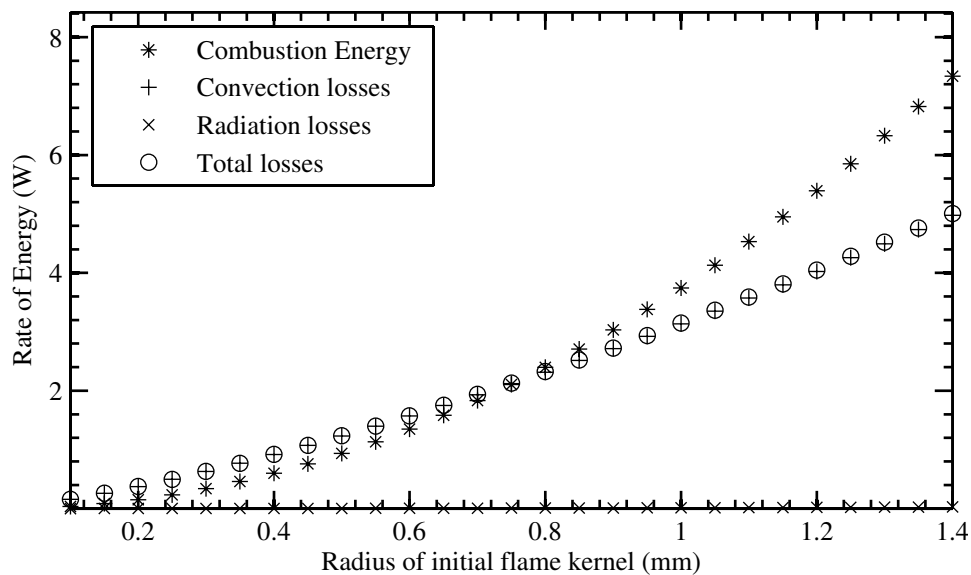


Figure C.3: Rate of generation of combustion energy and rate of convection and radiation losses as a function of initial spherical kernel diameter for dodecane.

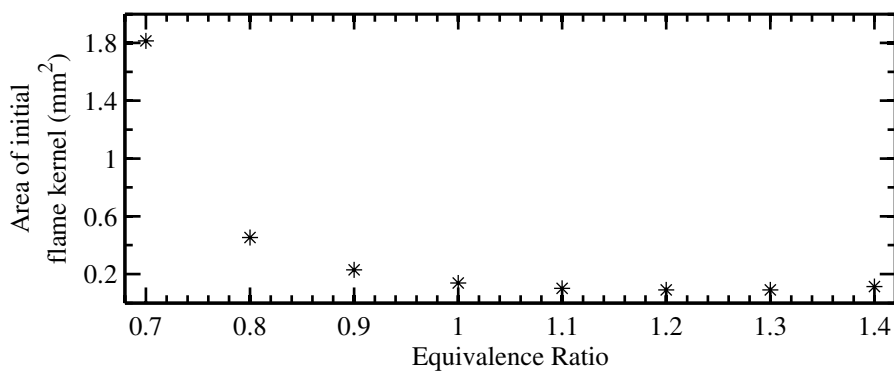


Figure C.4: Size of critical initial flame kernel as a function of equivalence ratio at the location of the spark.

C

Appendix D

Results of 2D-LIPS experiments.

2D-LIPS measurements are presented for all ignition tests performed in two-phase flow burner. The presence of simultaneous high oxygen emission intensity (or Spark energy) and high hydrogen to oxygen ratio can be seen in most of igniting sparks.

D.1 Location a

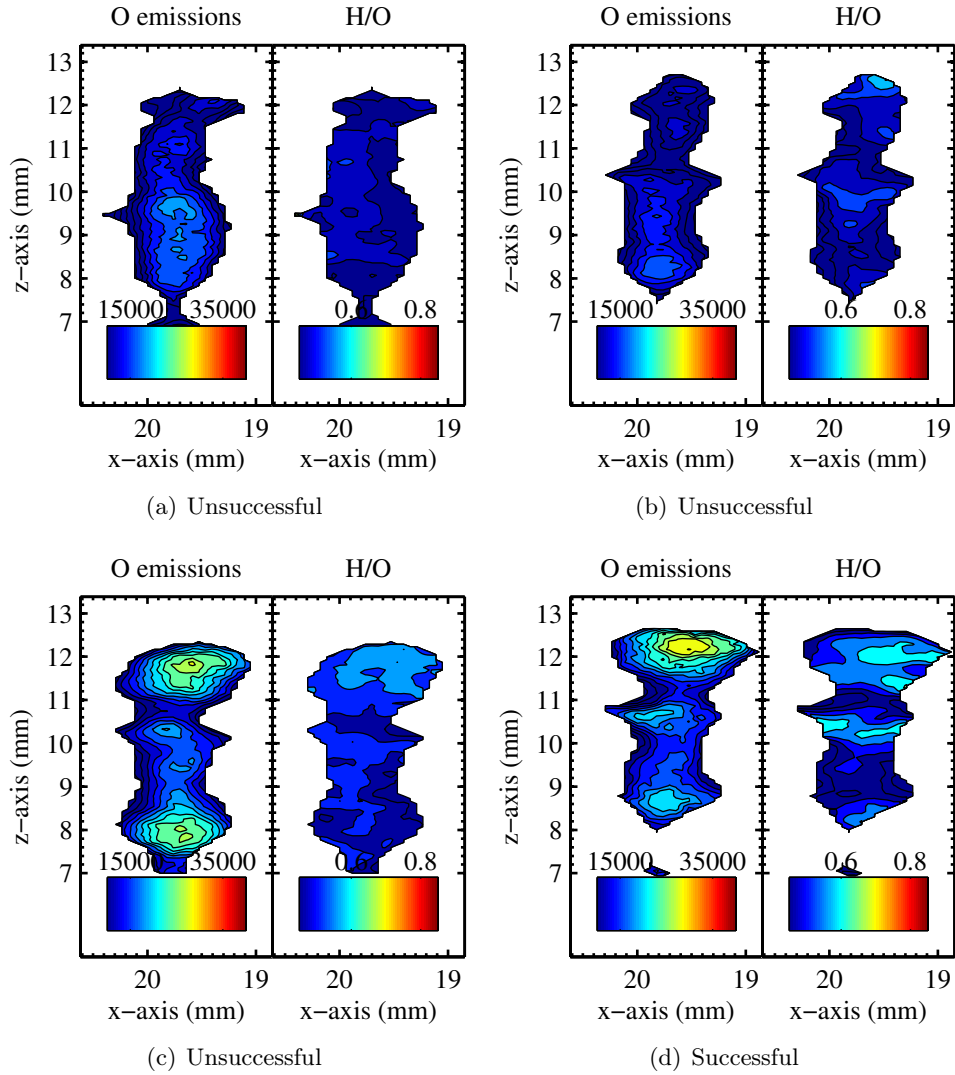


Figure D.1: Location a; Test#1, Analysis of 2D-LIPS experiments for (a) Spark#1, (b) Spark#2, and (c) Spark#3 which failed to ignite, and (d) Spark#4 which successfully ignited.

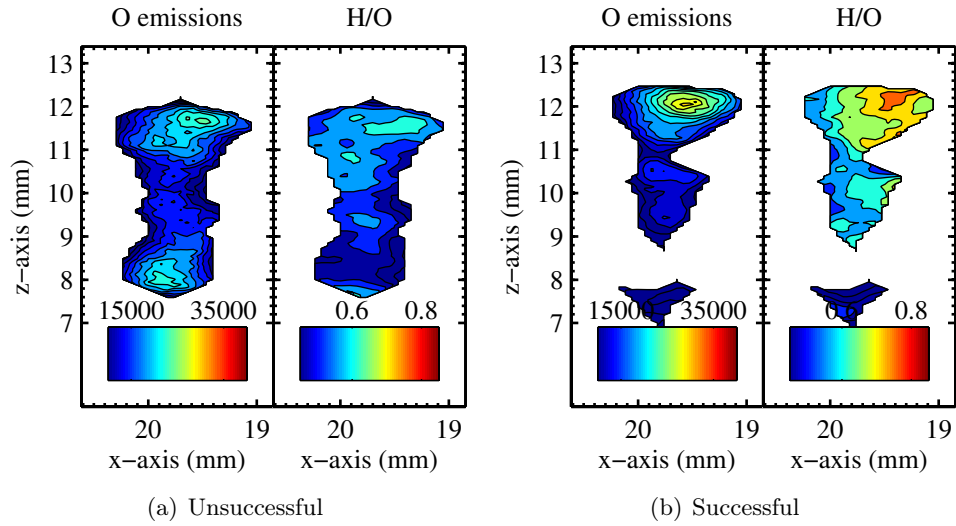


Figure D.2: Location a; Test#2, Analysis of 2D-LIPS experiments for (a) Spark#1 which failed to ignite, and (b) Spark#2 which successfully ignited.

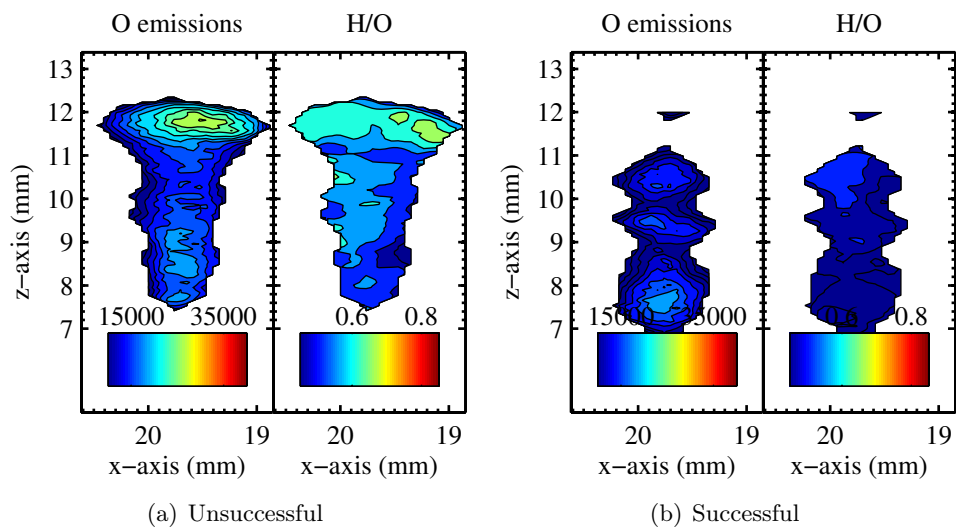


Figure D.3: Location a; Test#3, Analysis of 2D-LIPS experiments for (a) Spark#1 which failed to ignite, and (b) Spark#2 which successfully ignited.

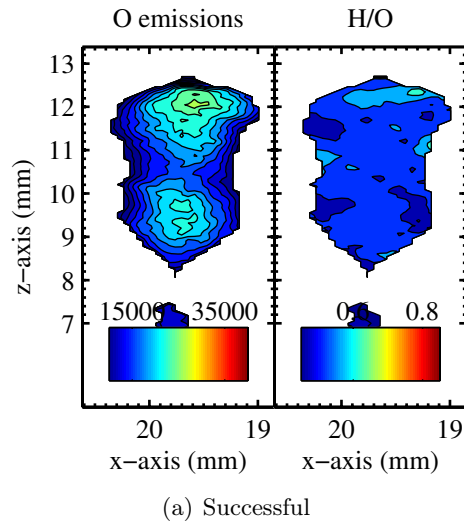


Figure D.4: Location a; Test#4, Analysis of 2D-LIPS experiments for (a) Spark#1 which successfully ignited.

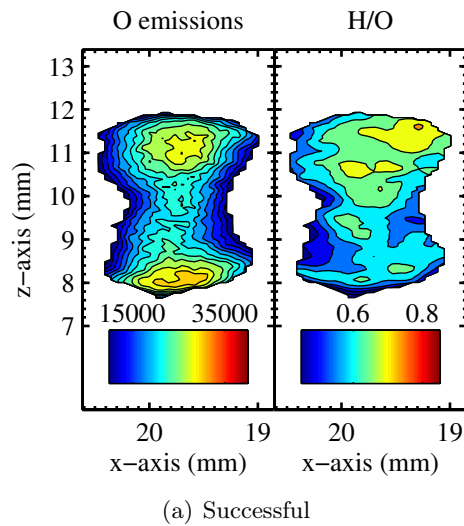


Figure D.5: Location a; Test#5, Analysis of 2D-LIPS experiments for (a) Spark#1 which successfully ignited.

D.2 Location b

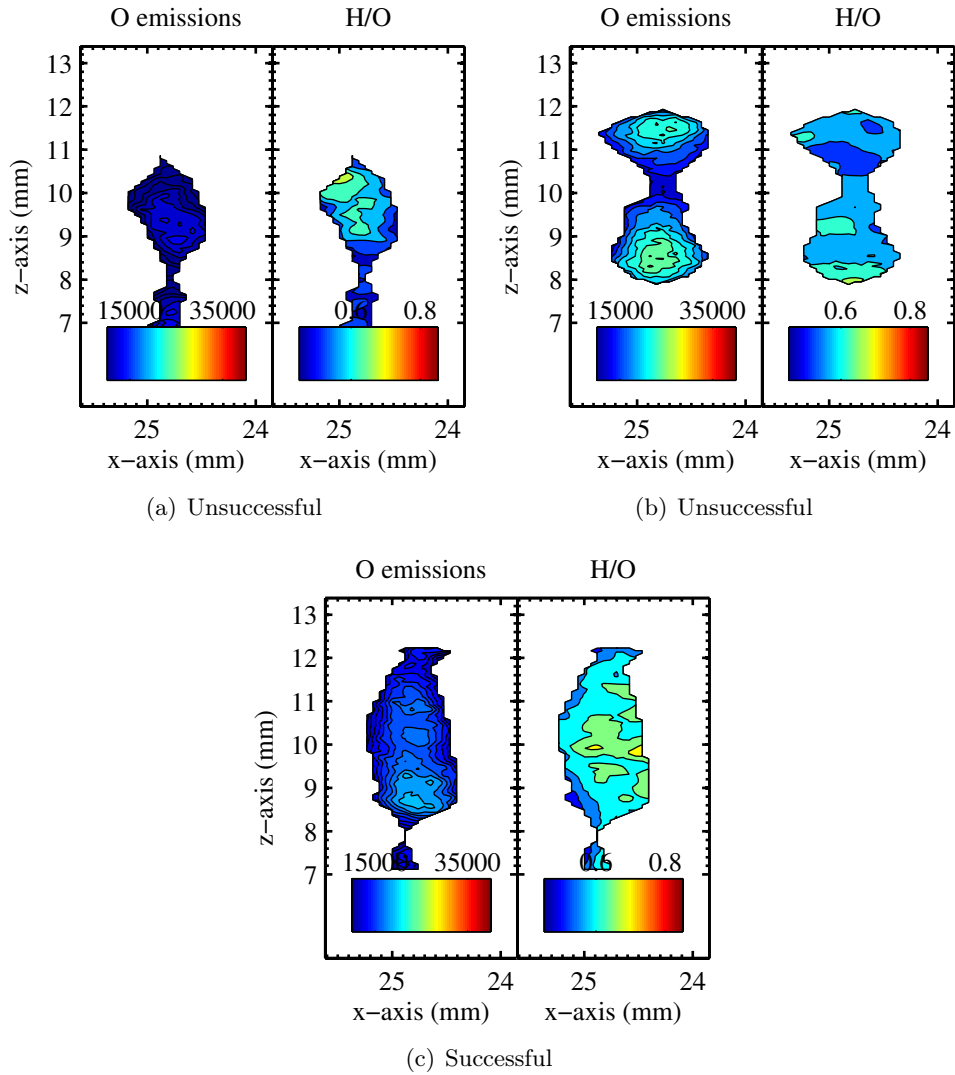


Figure D.6: Location b; Test#4, Analysis of 2D-LIPS experiments for (a) Spark#1, and (b) Spark#2 which failed to ignite, and (c) Spark#3 which successfully ignited.

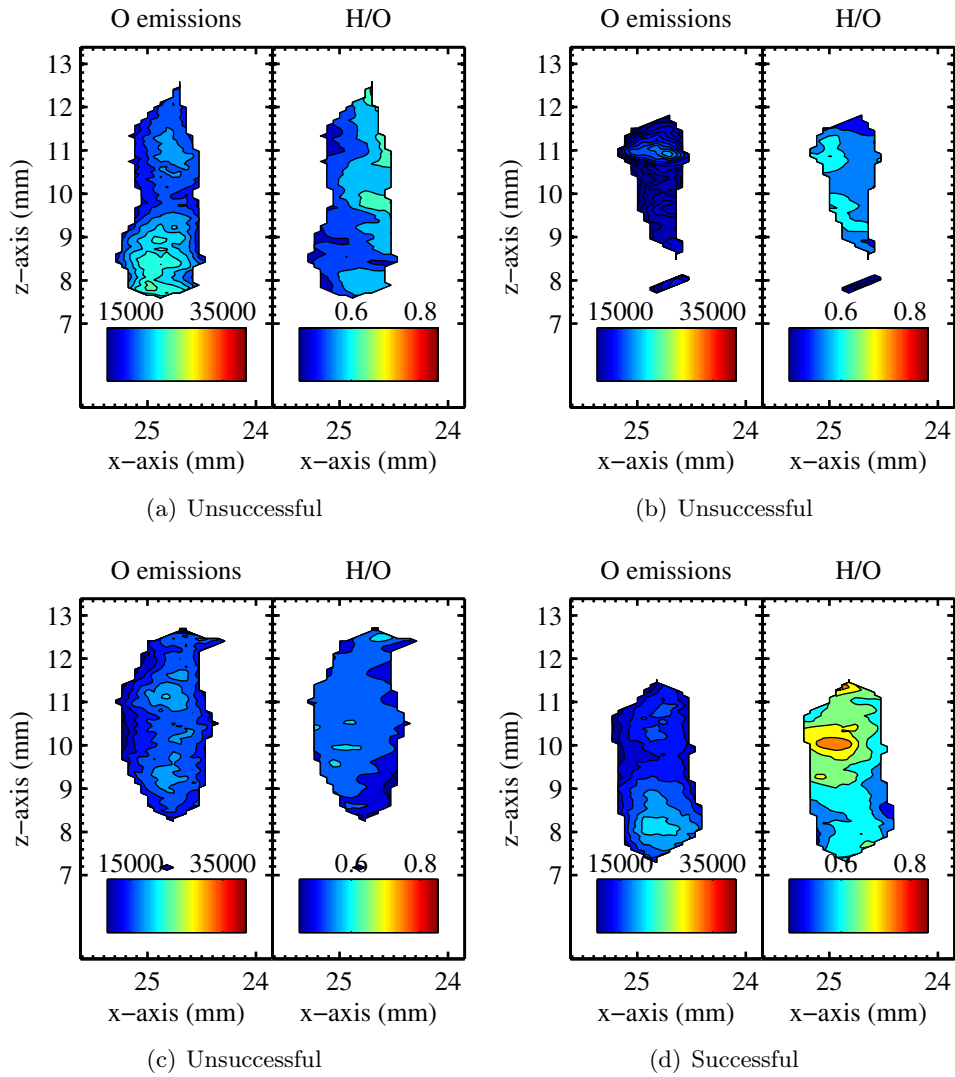


Figure D.7: Location b; Test#5, Analysis of 2D-LIPS experiments for (a) Spark#1, (b) Spark#2, and (c) Spark#3 which failed to ignite, and (d) Spark#4 which successfully ignited.

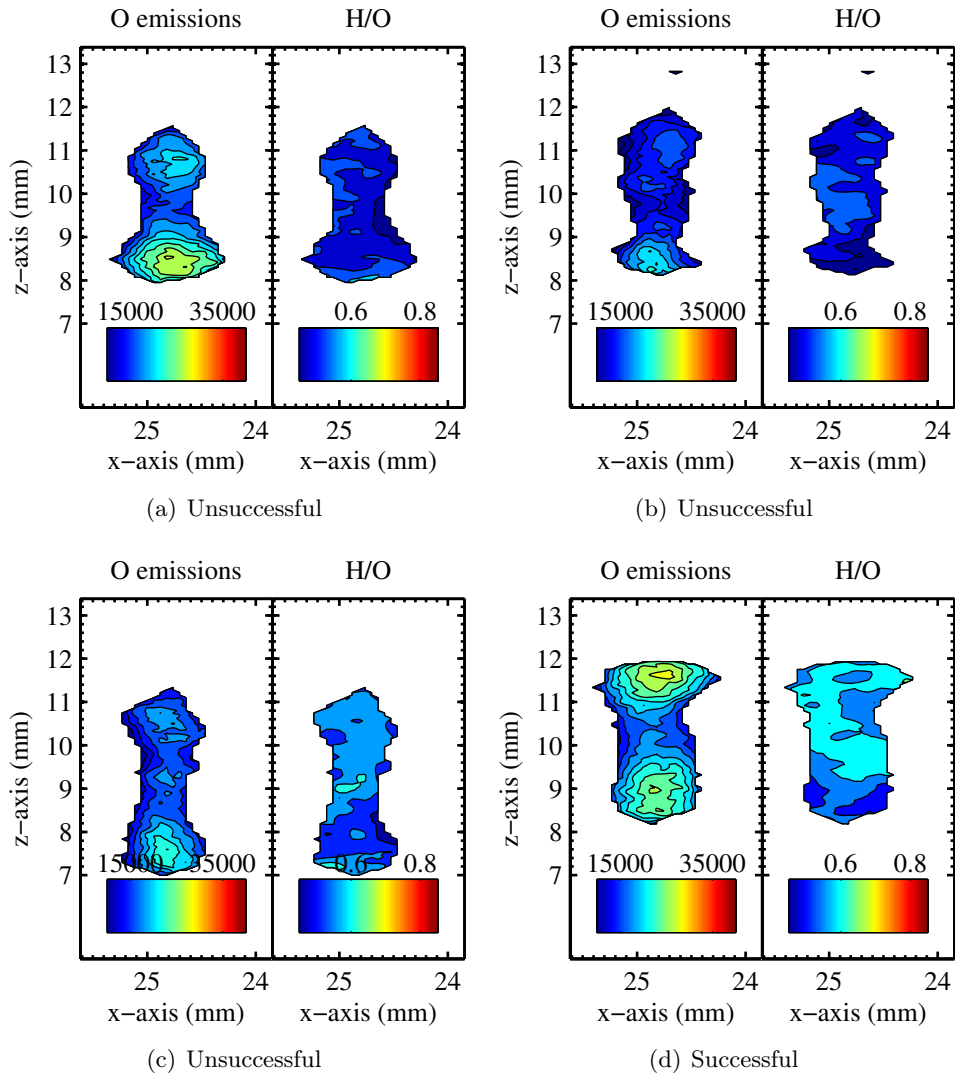


Figure D.8: Location *b*; Test#6, Analysis of 2D-LIPS experiments for (a) Spark#1, (b) Spark#2, and (c) Spark#3 which failed to ignite, and (d) Spark#4 which successfully ignited.

D.3 Location c

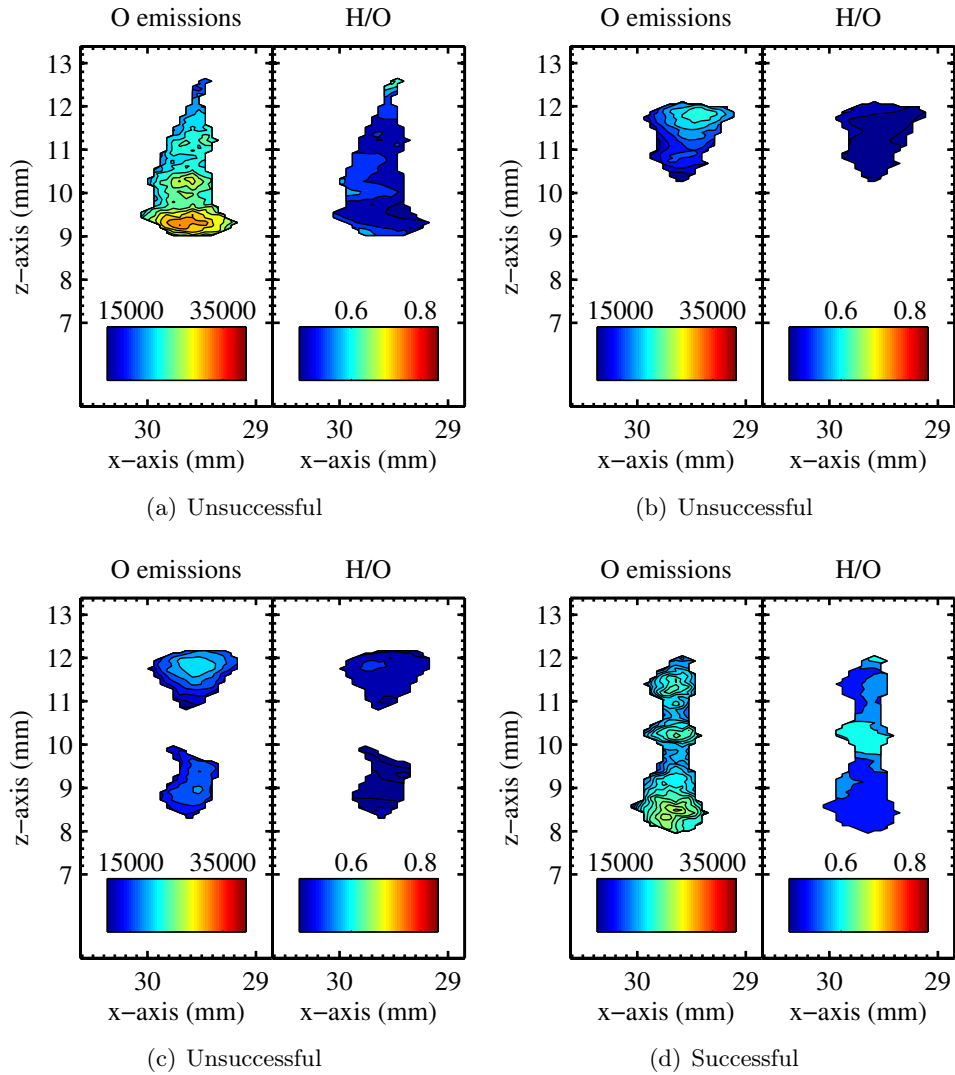


Figure D.9: Location c; Test#1, Analysis of 2D-LIPS experiments for (a) Spark#1, (b) Spark#2, and (c) Spark#3 which failed to ignite, and (d) Spark#4 which successfully ignited.

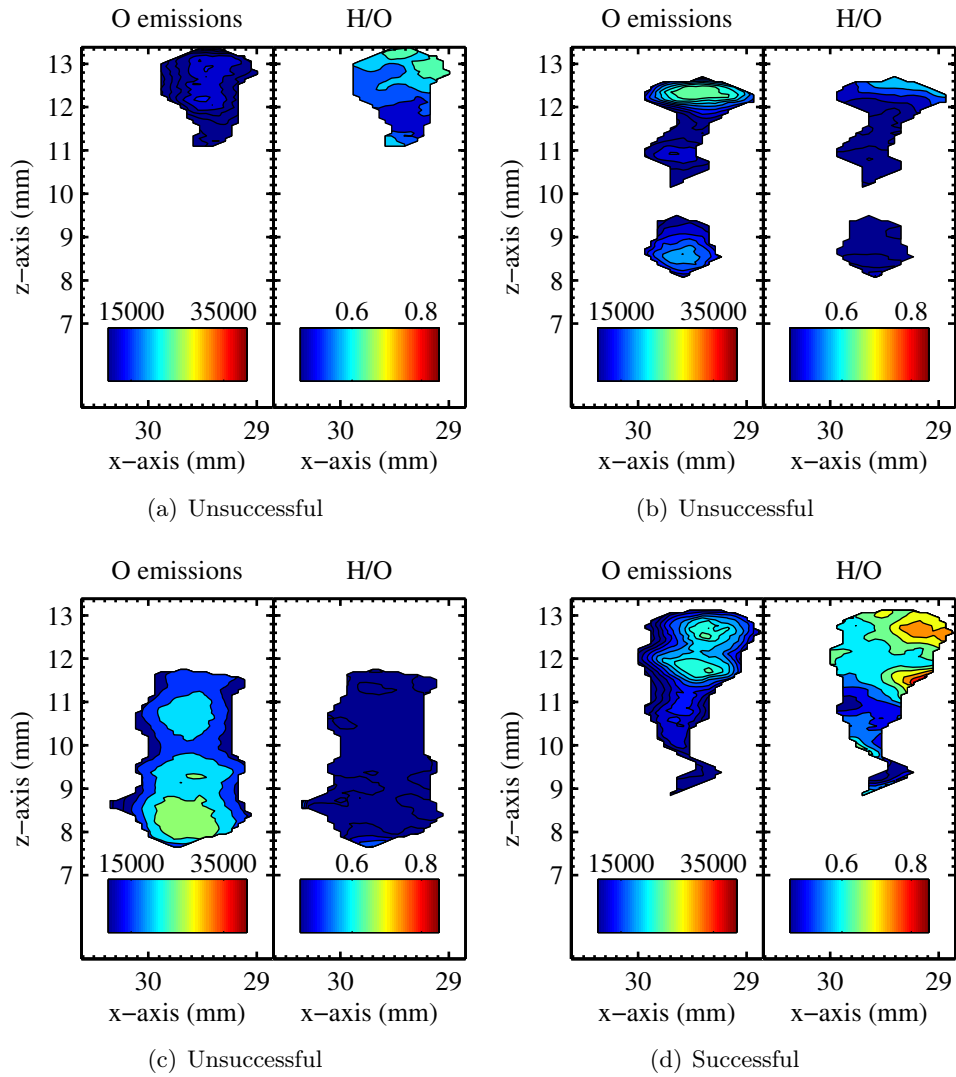


Figure D.10: Location *c*; Test#2, Analysis of 2D-LIPS experiments for (a) Spark#1, (b) Spark#2, and (c) Spark#3 which failed to ignite, and (d) Spark#4 which successfully ignited.

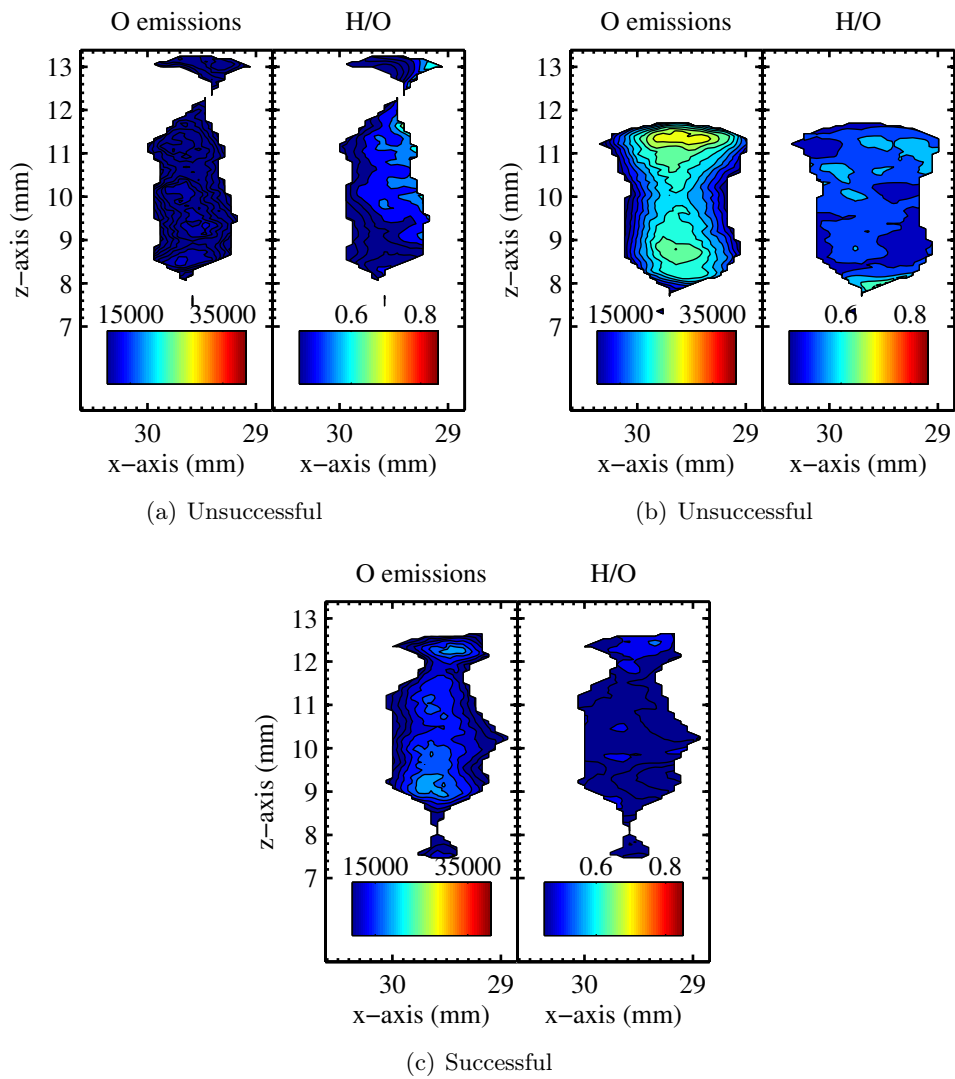


Figure D.11: Location c; Test#3, Analysis of 2D-LIPS experiments for (a) Spark#1, and (b) Spark#2 which failed to ignite, and (c) Spark#3 which successfully ignited.

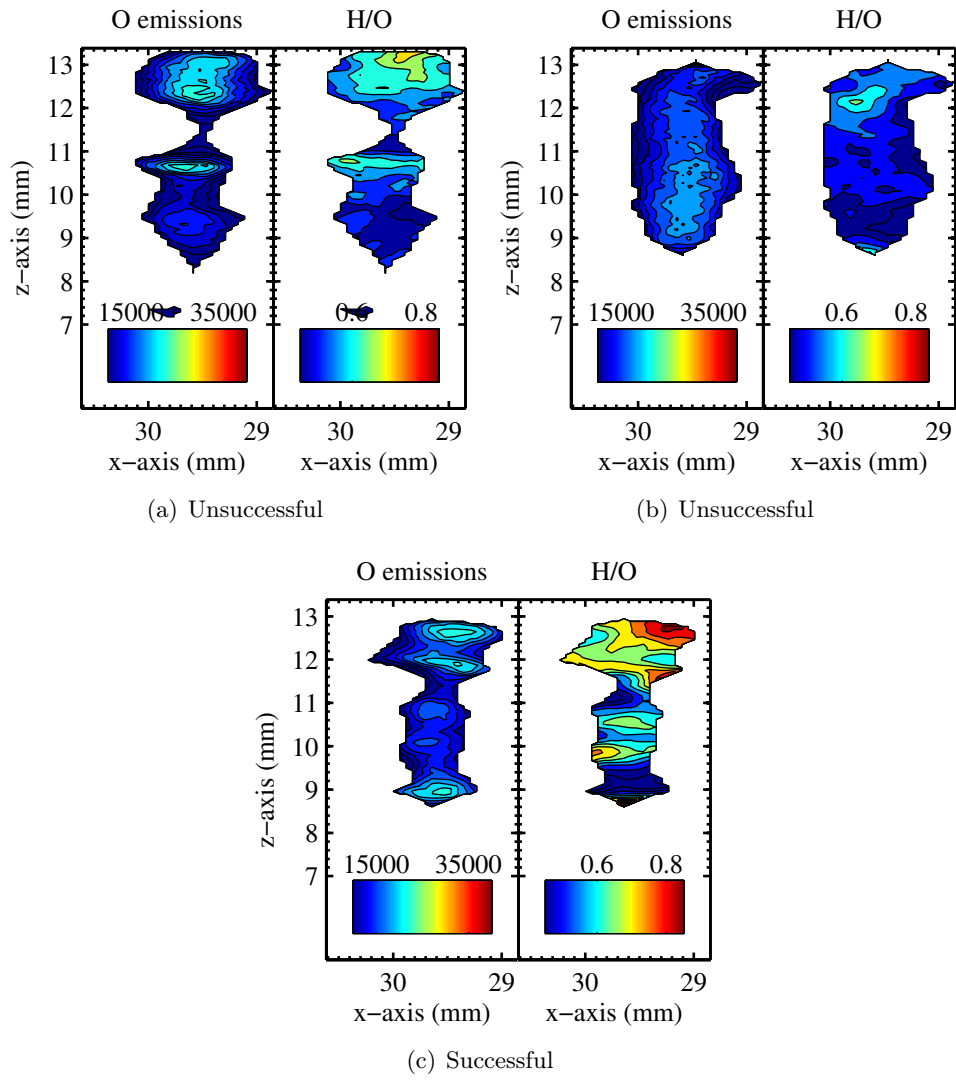


Figure D.12: Location *c*; Test#4, Analysis of 2D-LIPS experiments for (a) Spark#1, and (b) Spark#2 which failed to ignite, and (c) Spark#3 which successfully ignited.

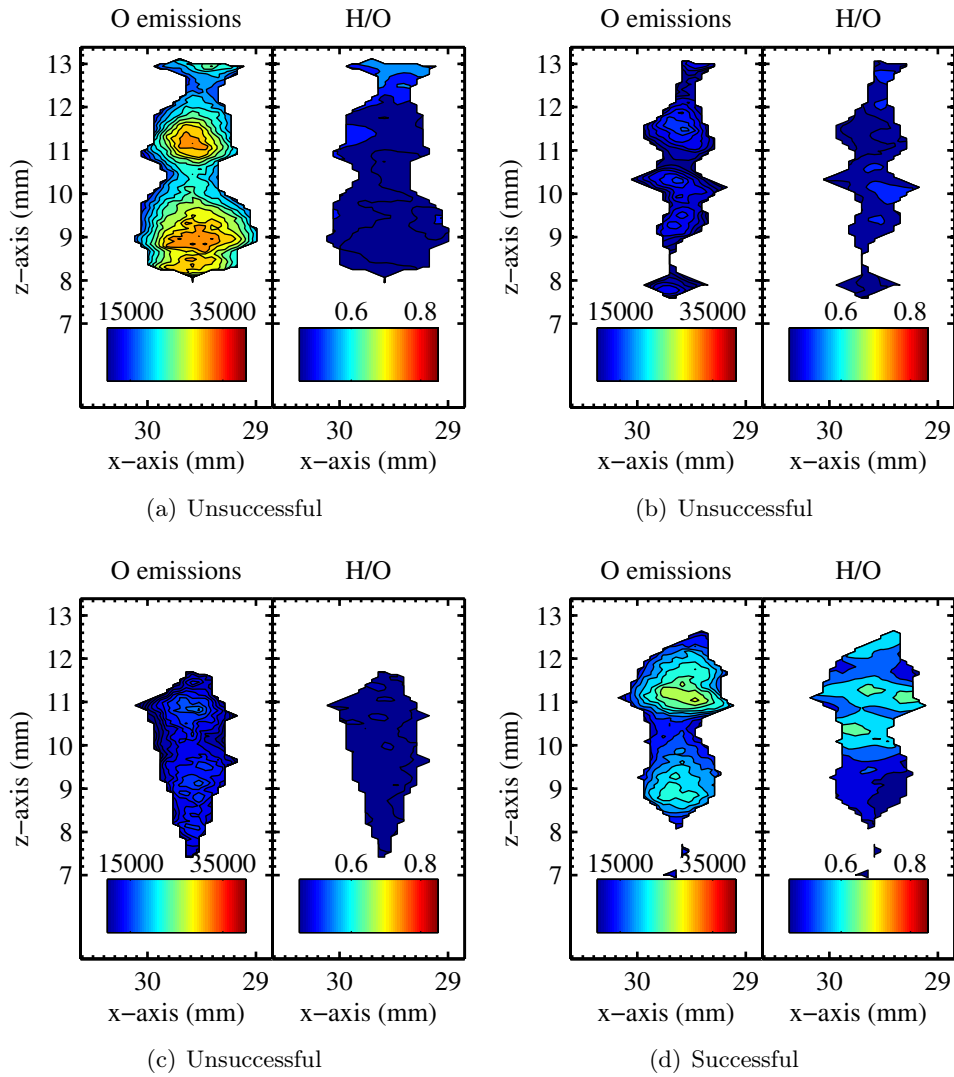
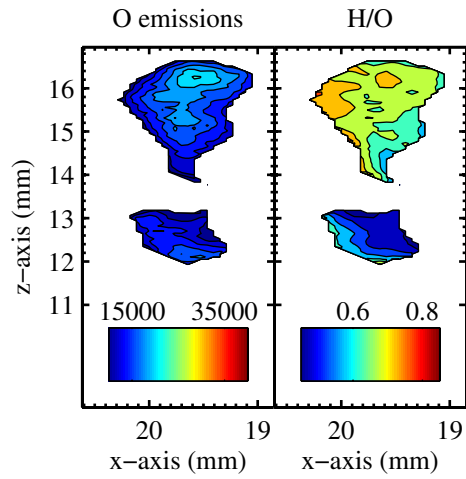


Figure D.13: Location c; Test#5, Analysis of 2D-LIPS experiments for (a) Spark#1, (b) Spark#2, and (c) Spark#3 which failed to ignite, and (d) Spark#4 which successfully ignited.

D.4 Location d



(a) Successful

Figure D.14: Location d; Test#1, Analysis of 2D-LIPS experiments for (a) Spark#1 which successfully ignited.

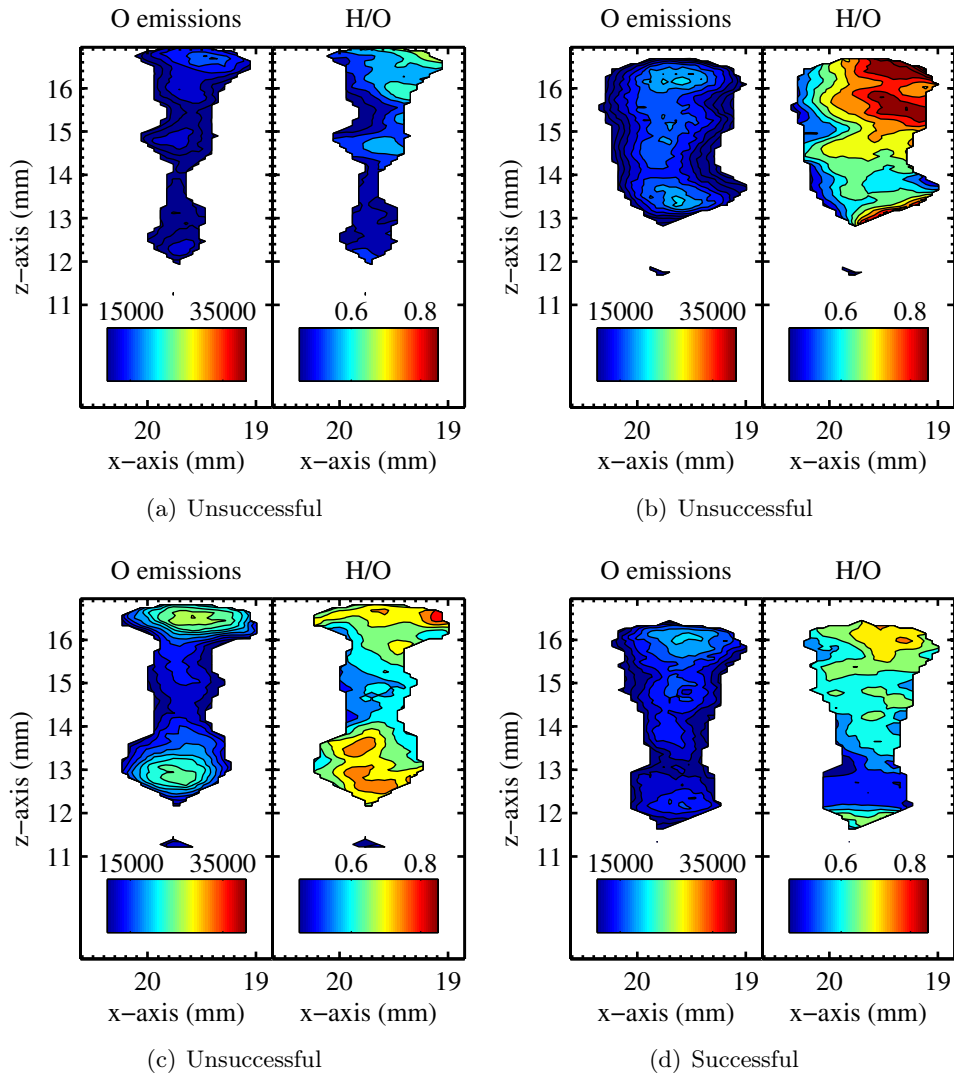


Figure D.15: Location d; Test#2, Analysis of 2D-LIPS experiments for (a) Spark#1, (b) Spark#2, and (c) Spark#3 which failed to ignite, and (d) Spark#4 which successfully ignited.

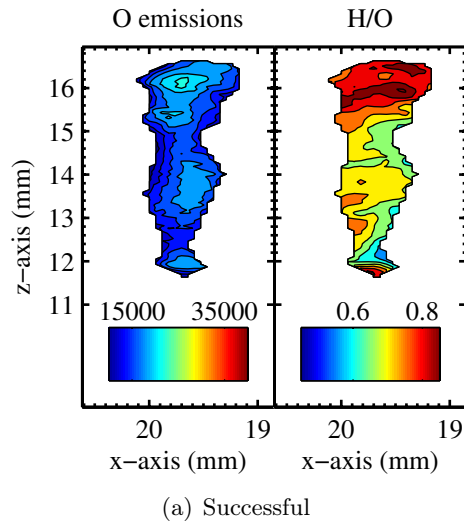


Figure D.16: Location *d*; Test#3, Analysis of 2D-LIPS experiments for (a) Spark#1 which successfully ignited.

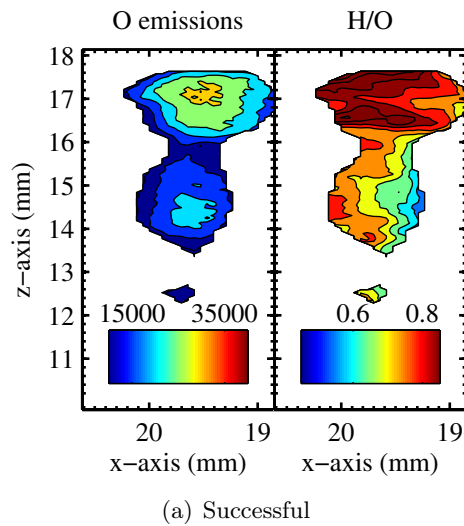


Figure D.17: Location *d*; Test#4, Analysis of 2D-LIPS experiments for (a) Spark#1 which successfully ignited.

D.5 Location e

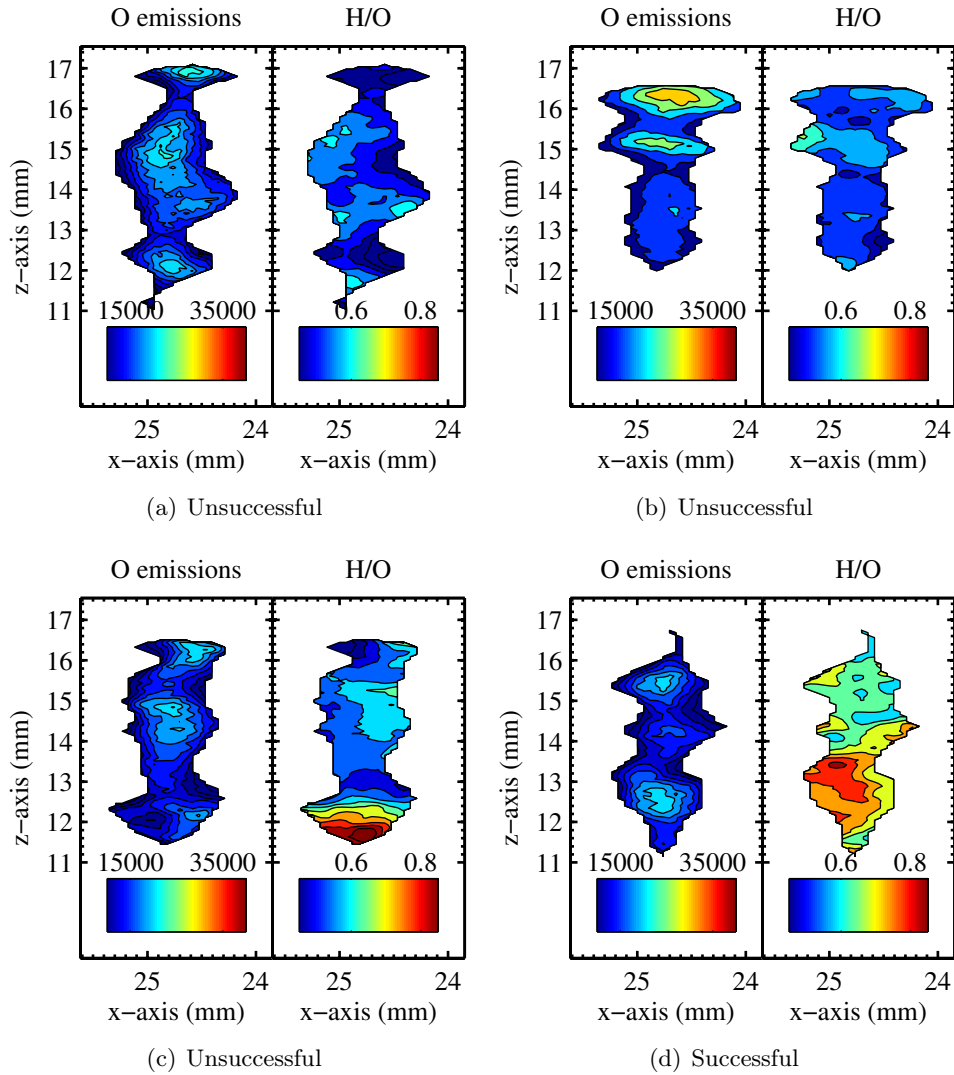


Figure D.18: Location e; Test#1, Analysis of 2D-LIPS experiments for (a) Spark#1, (b) Spark#2, and (c) Spark#3 which failed to ignite, and (d) Spark#4 which successfully ignited.

D.6 Location f

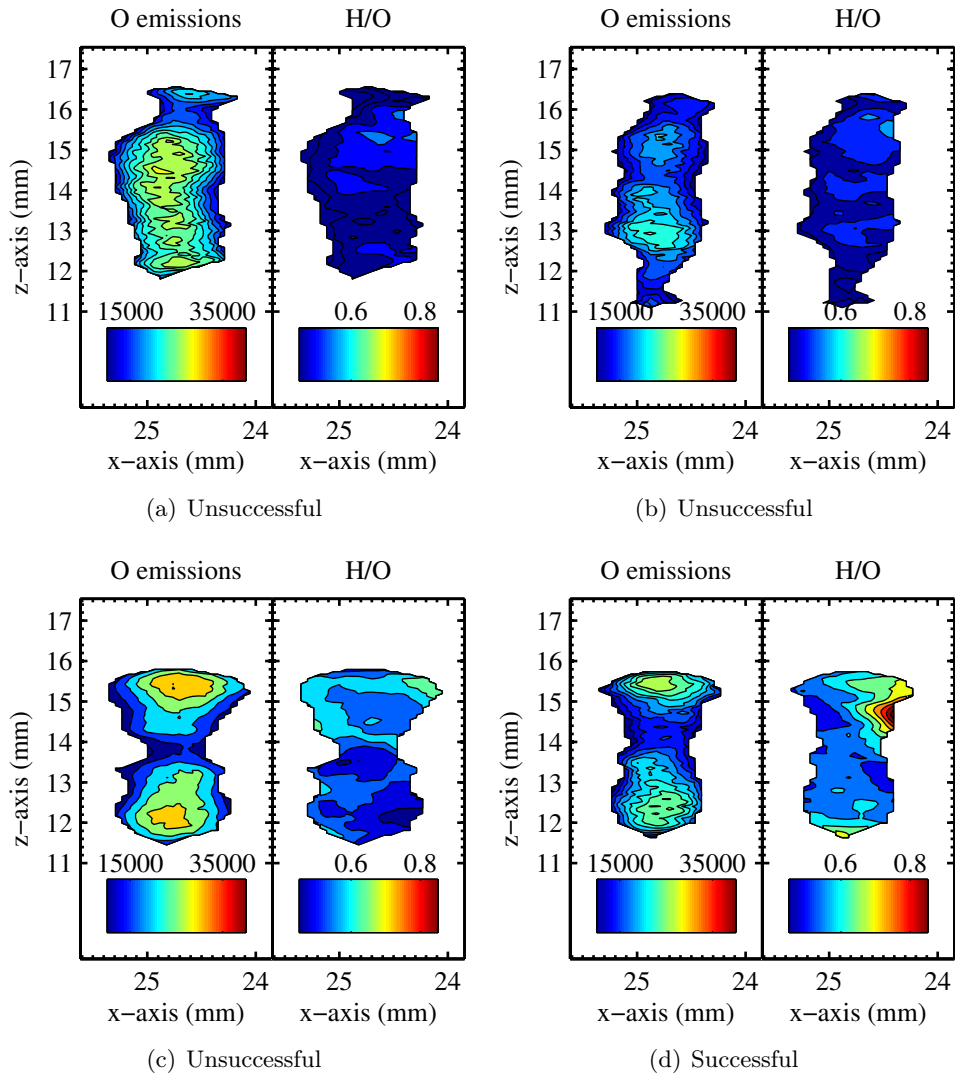


Figure D.19: Location *e*; Test#2, Analysis of 2D-LIPS experiments for (a) Spark#1, (b) Spark#2, and (c) Spark#3 which failed to ignite, and (d) Spark#4 which successfully ignited.

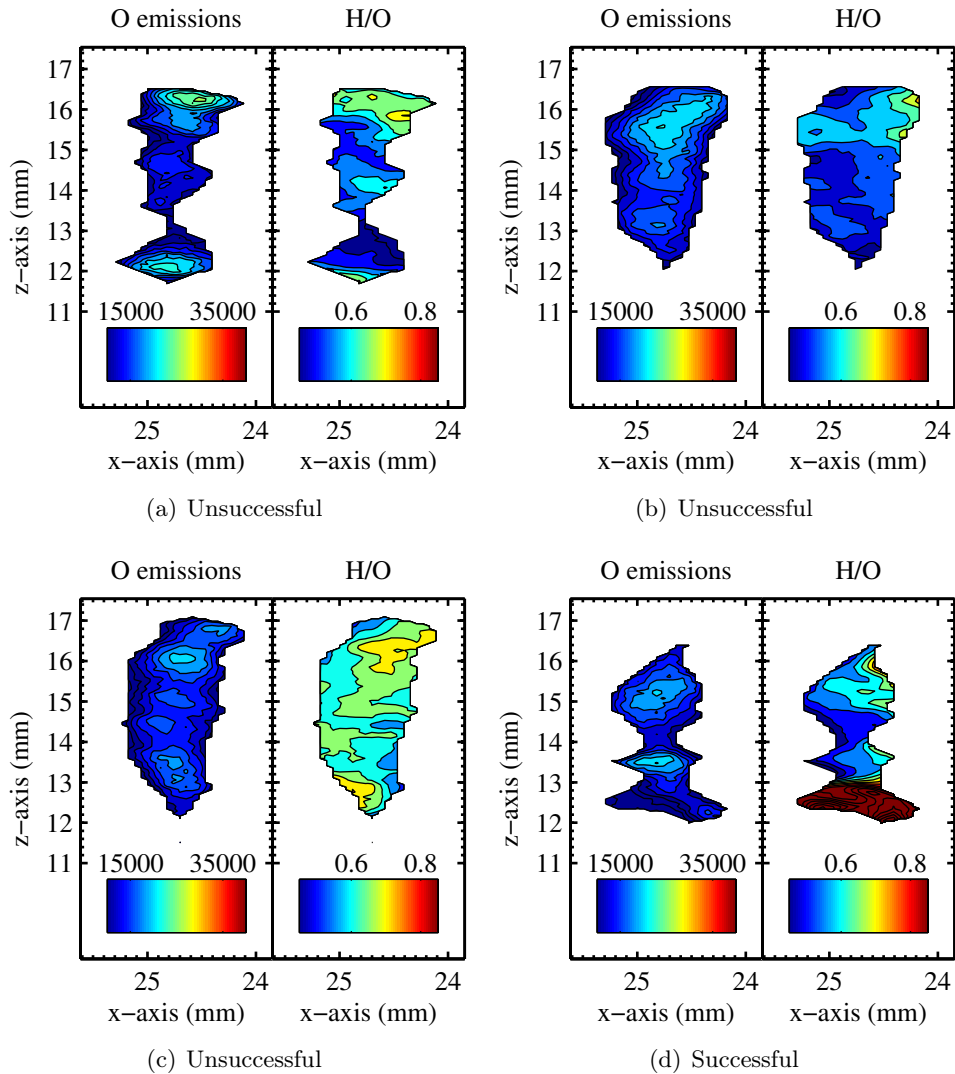


Figure D.20: Location e; Test#3, Analysis of 2D-LIPS experiments for (a) Spark#1, (b) Spark#2, and (c) Spark#3 which failed to ignite, and (d) Spark#4 which successfully ignited.

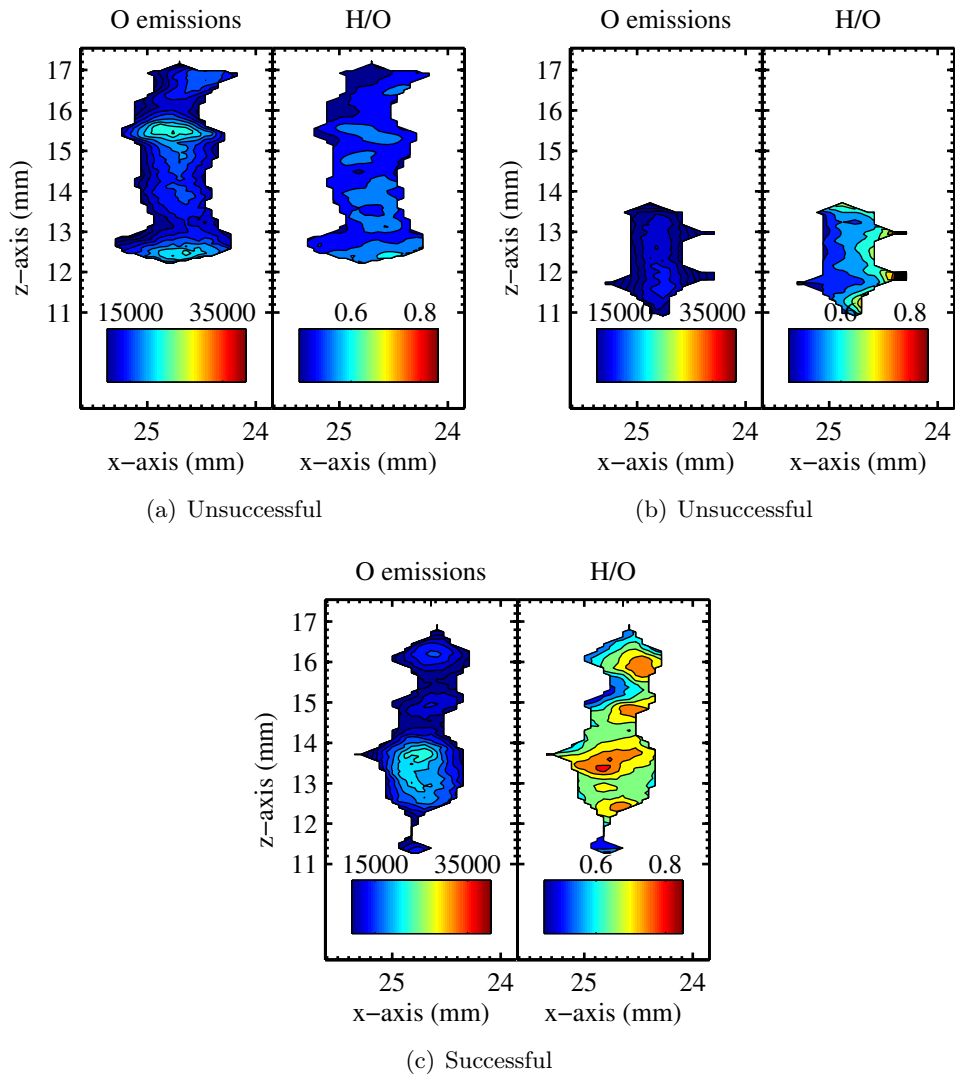


Figure D.21: Location e; Test#4, Analysis of 2D-LIPS experiments for (a) Spark#1, and (b) Spark#2 which failed to ignite, and (c) Spark#3 which successfully ignited.

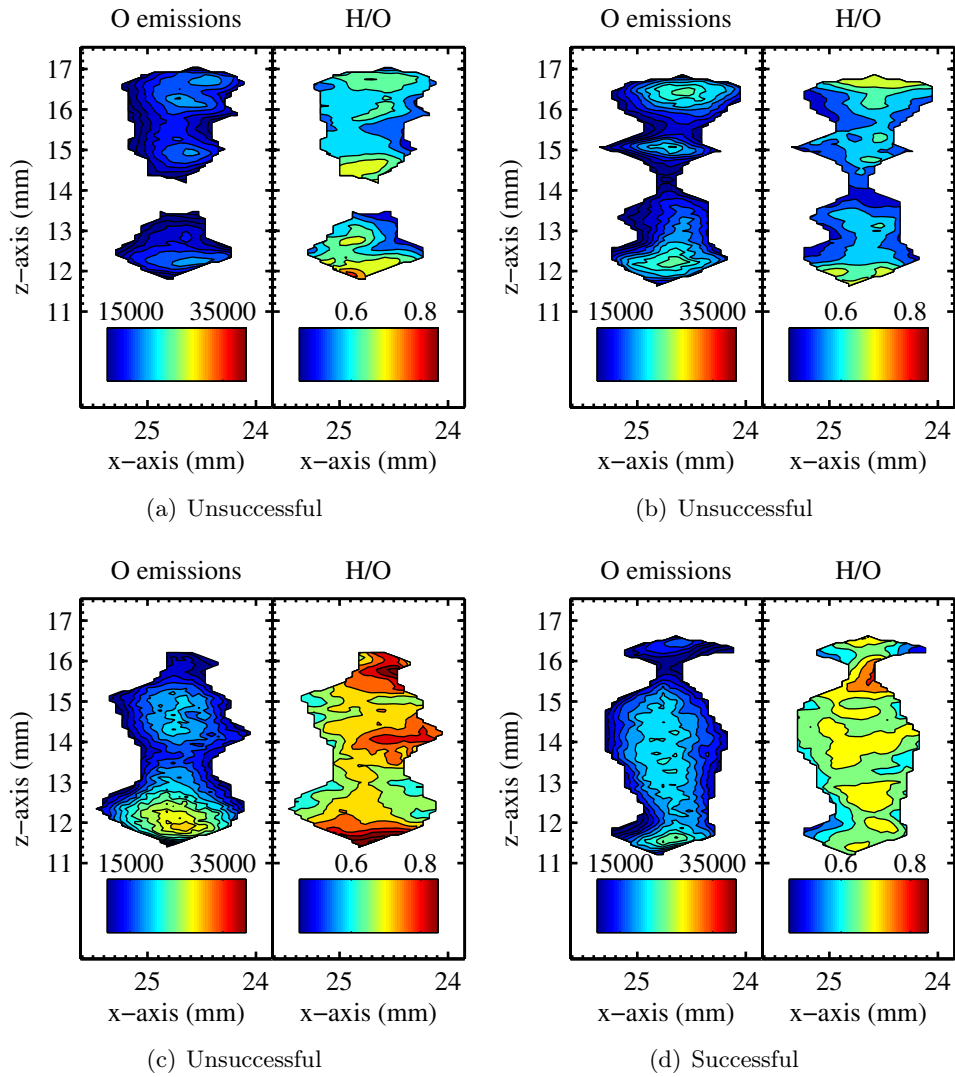


Figure D.22: Location e; Test#5, Analysis of 2D-LIPS experiments for (a) Spark#1, (b) Spark#2, and (c) Spark#3 which failed to ignite, and (d) Spark#4 which successfully ignited.

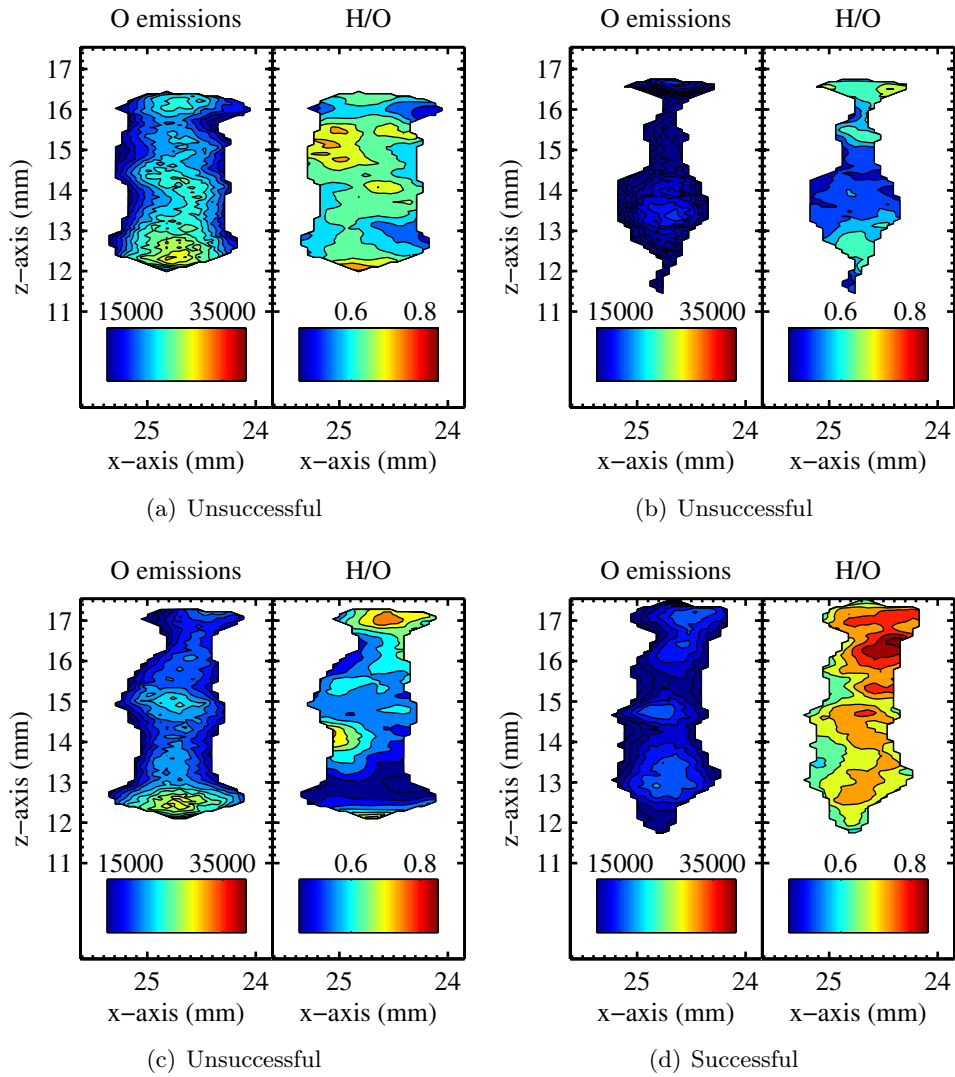


Figure D.23: Location *e*; Test#6, Analysis of 2D-LIPS experiments for (a) Spark#1, (b) Spark#2, and (c) Spark#3 which failed to ignite, and (d) Spark#4 which successfully ignited.

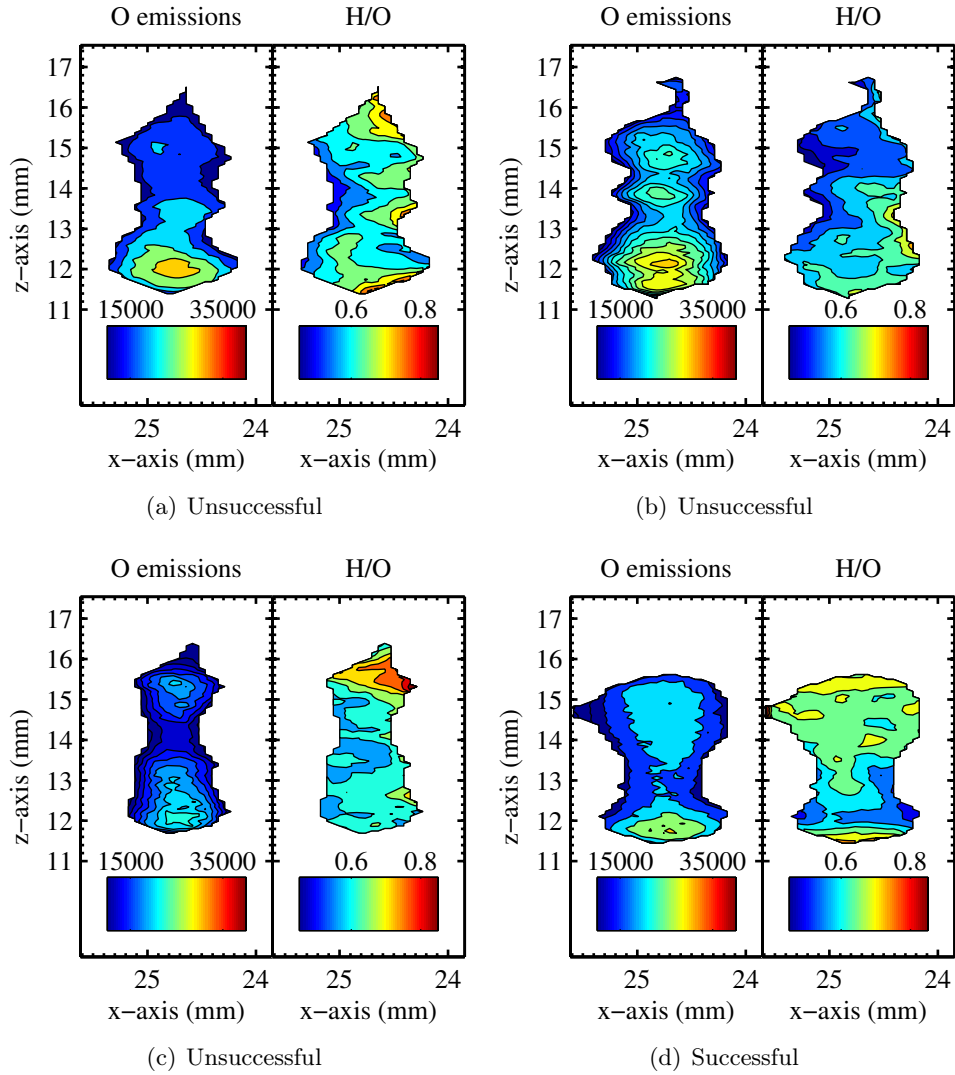


Figure D.24: Location *e*; Test#7, Analysis of 2D-LIPS experiments for (a) Spark#1, (b) Spark#2, and (c) Spark#3 which failed to ignite, and (d) Spark#4 which successfully ignited.

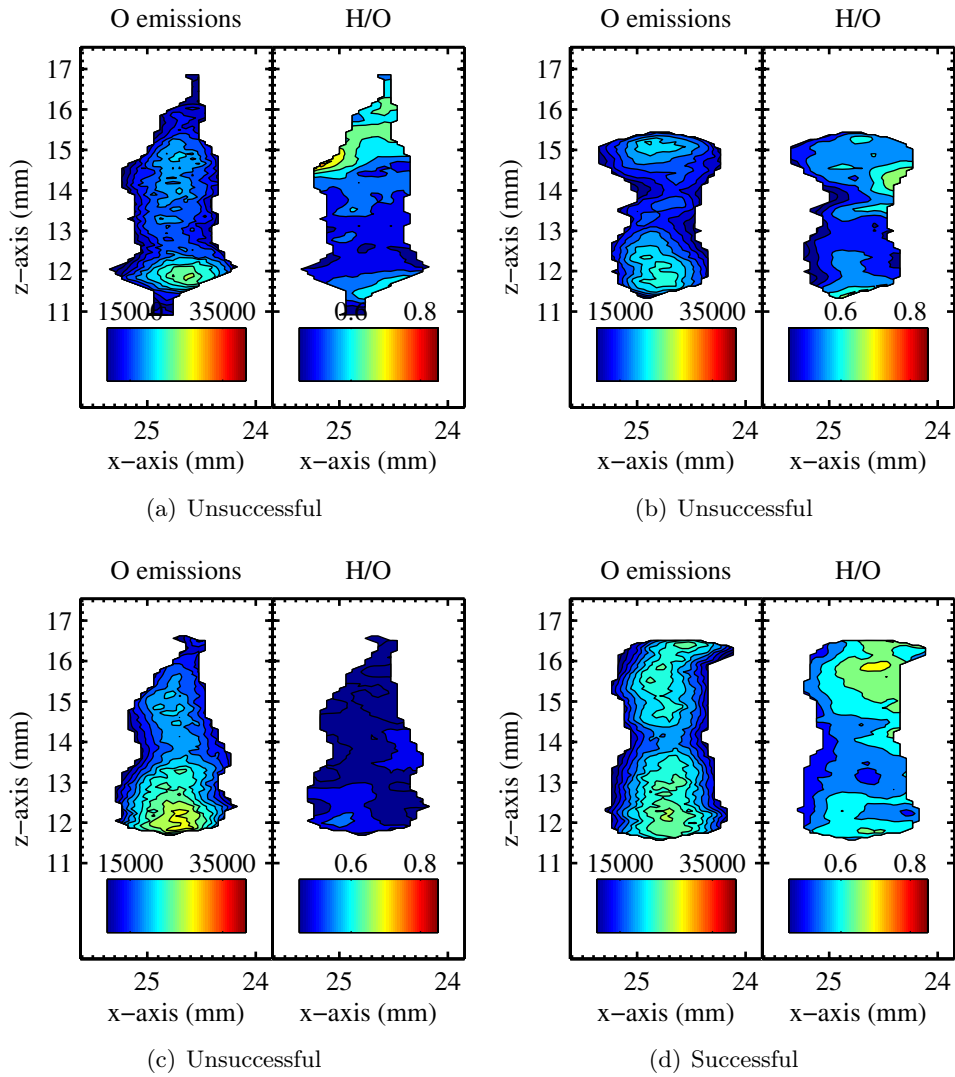


Figure D.25: Location *e*; Test#8, Analysis of 2D-LIPS experiments for (a) Spark#1, (b) Spark#2, and (c) Spark#3 which failed to ignite, and (d) Spark#4 which successfully ignited.

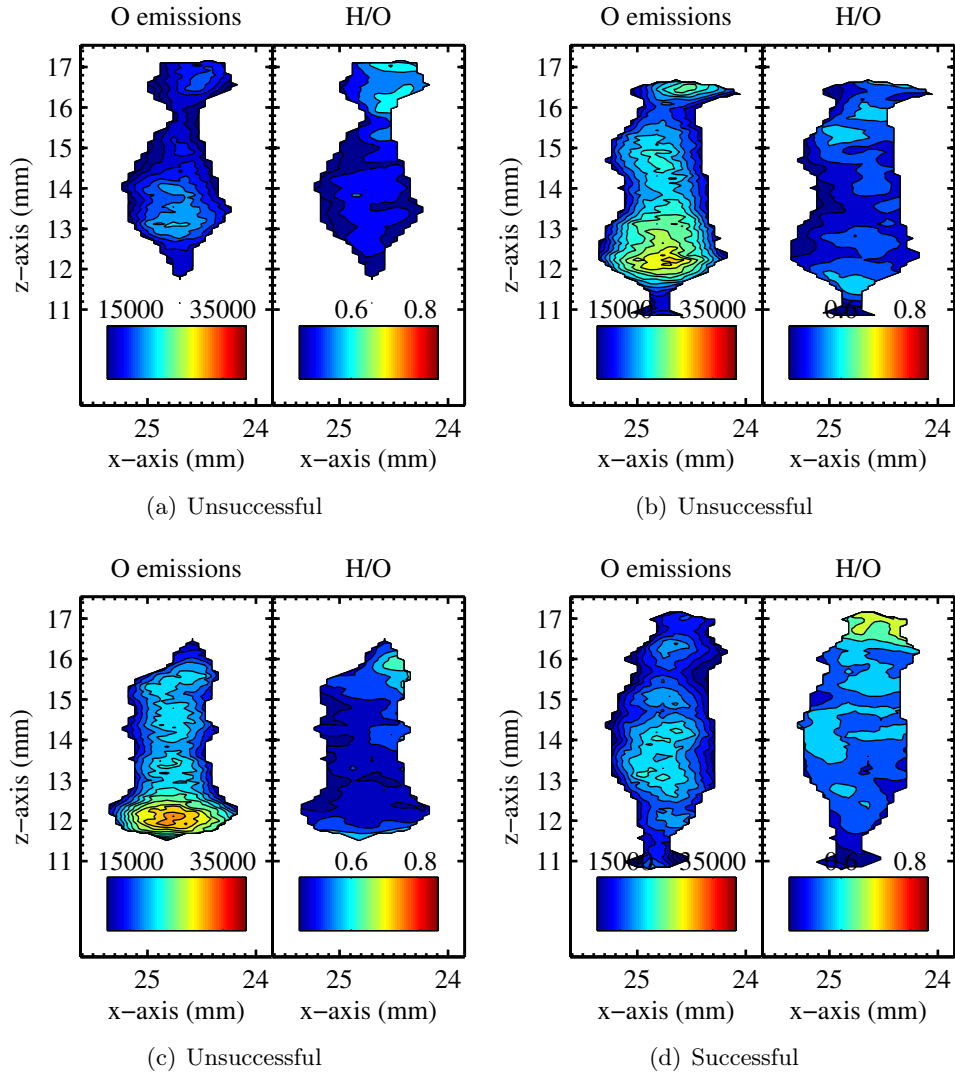


Figure D.26: Location *e*; Test#9, Analysis of 2D-LIPS experiments for (a) Spark#1, (b) Spark#2, and (c) Spark#3 which failed to ignite, and (d) Spark#4 which successfully ignited.

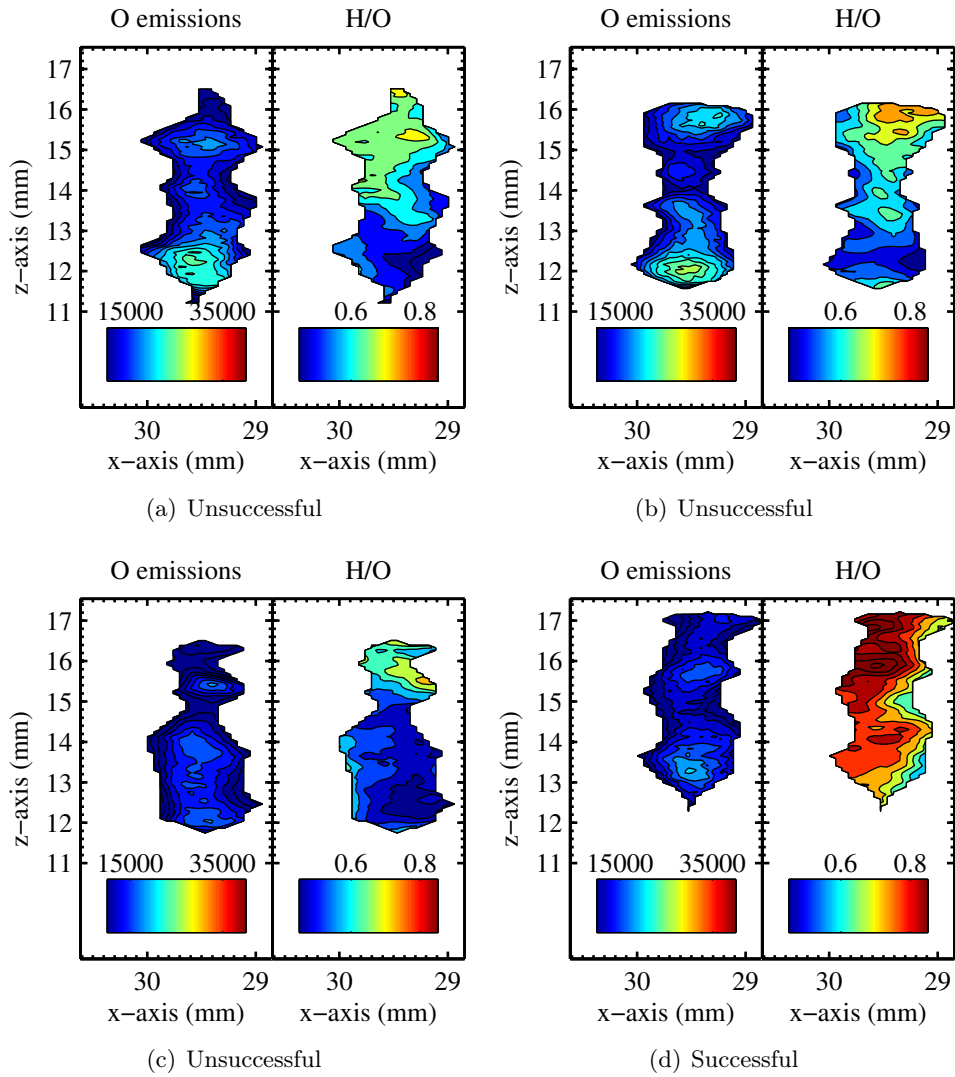


Figure D.27: Location *f*; Test#1, Analysis of 2D-LIPS experiments for (a) Spark#1, (b) Spark#2, and (c) Spark#3 which failed to ignite, and (d) Spark#4 which successfully ignited.

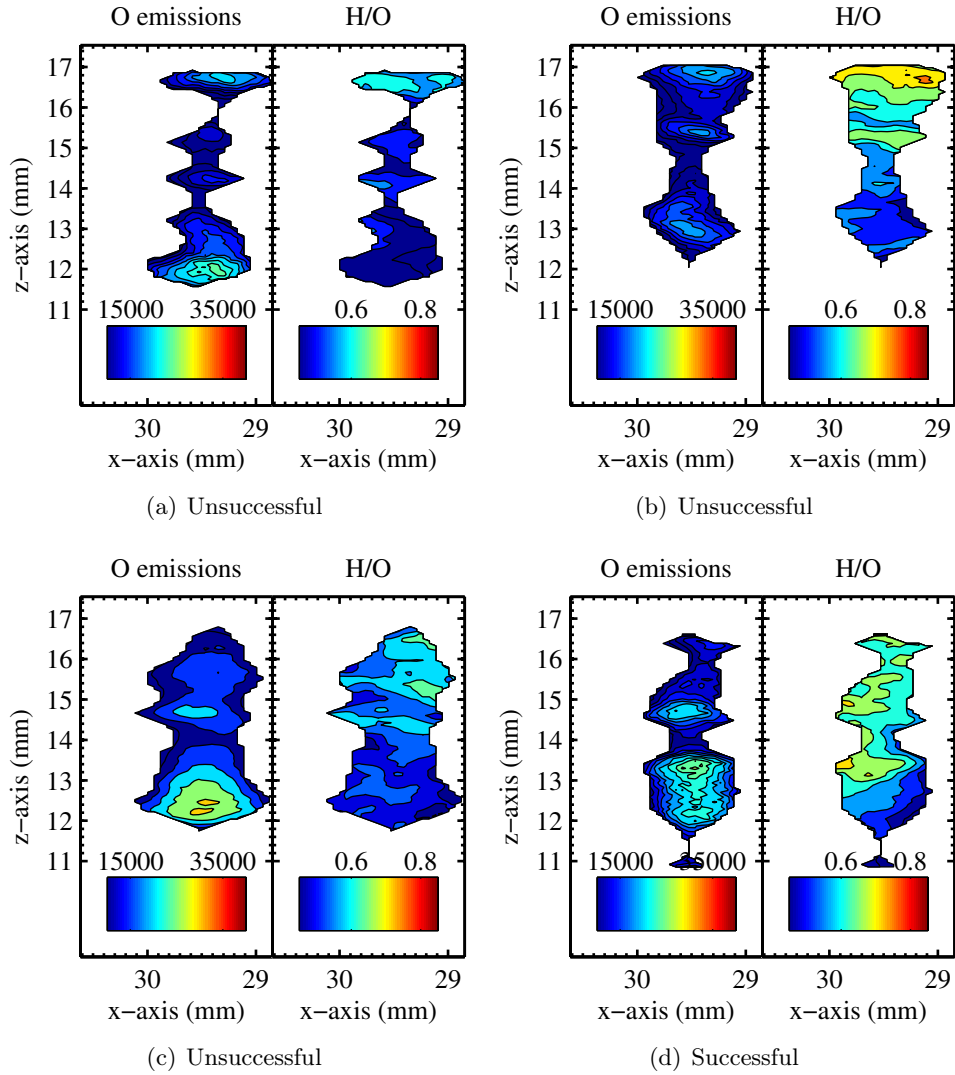


Figure D.28: Location *f*; Test#2, Analysis of 2D-LIPS experiments for (a) Spark#1, (b) Spark#2, and (c) Spark#3 which failed to ignite, and (d) Spark#4 which successfully ignited.

D.7 Location g

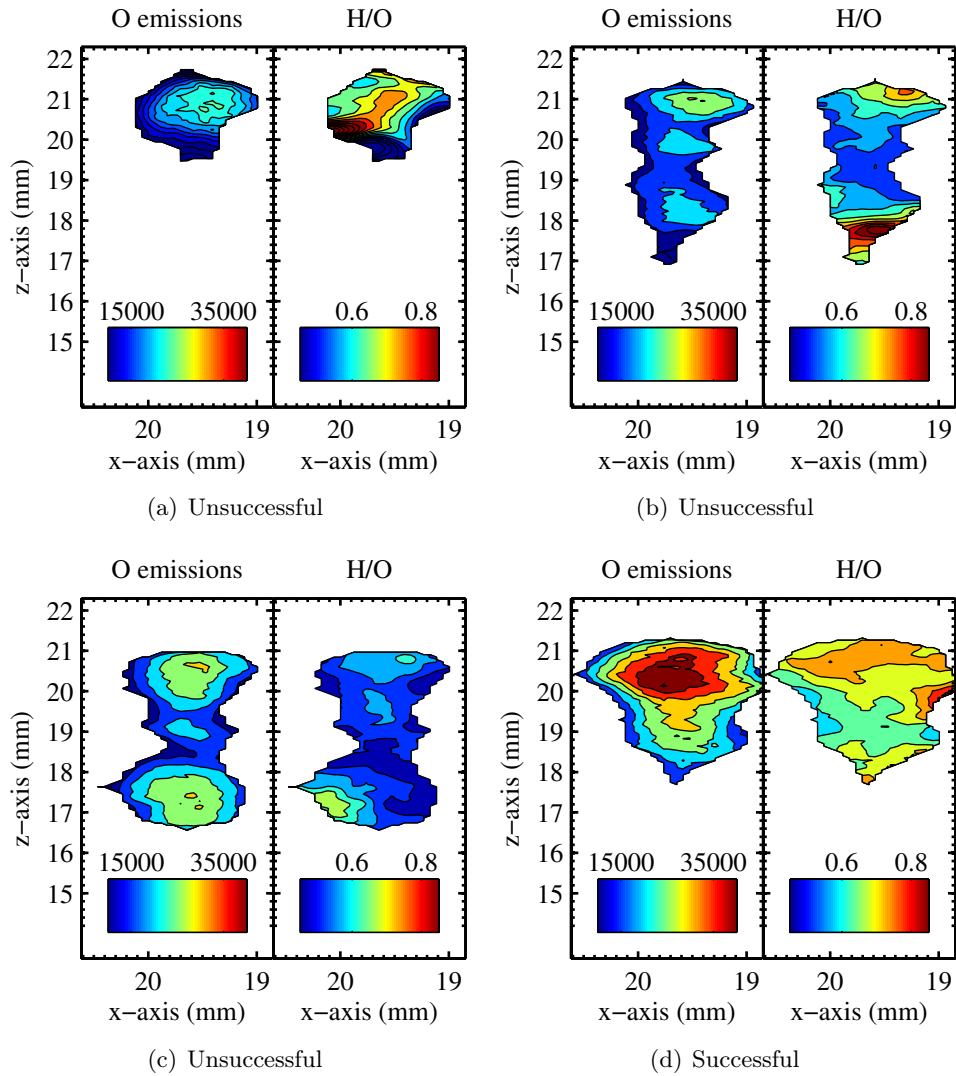


Figure D.29: Location g; Test#1, Analysis of 2D-LIPS experiments for (a) Spark#1, (b) Spark#2, and (c) Spark#3 which failed to ignite, and (d) Spark#4 which successfully ignited.

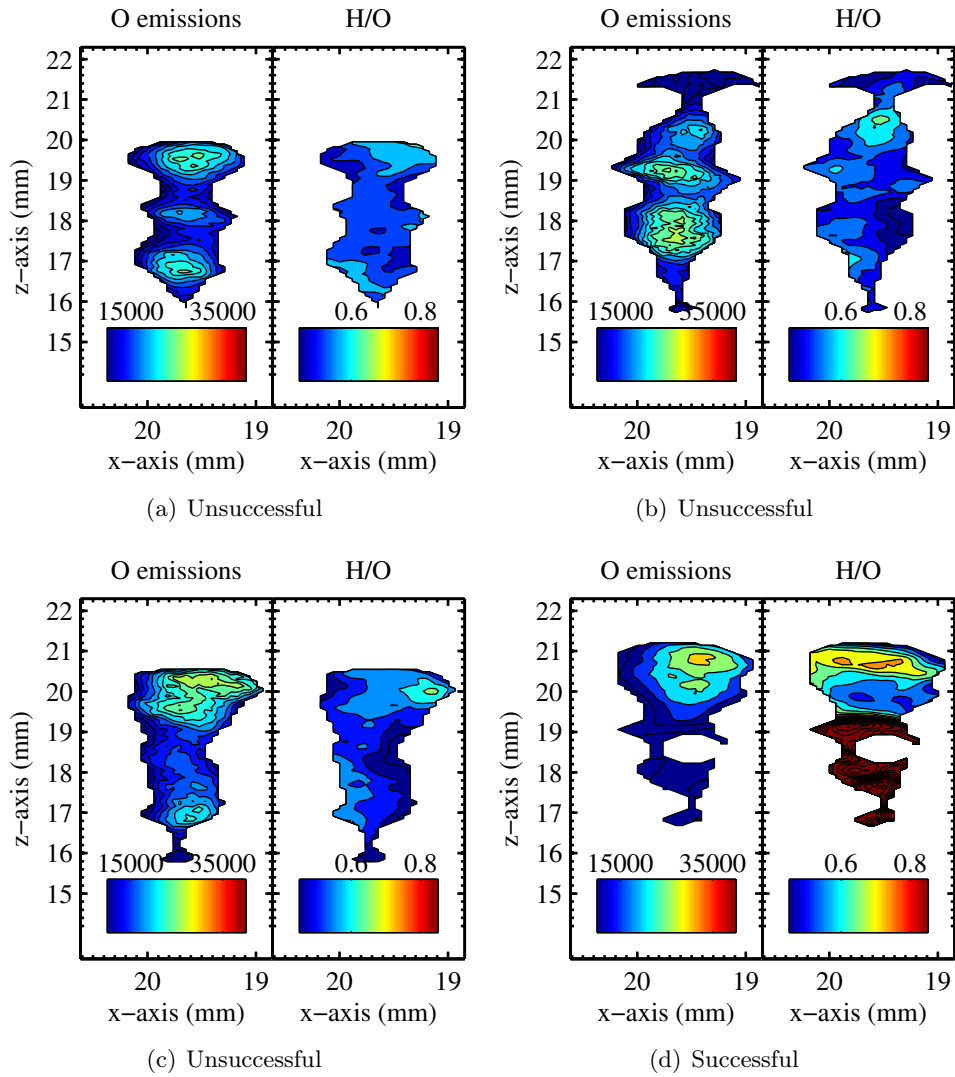


Figure D.30: Location *g*; Test#2, Analysis of 2D-LIPS experiments for (a) Spark#1, (b) Spark#2, and (c) Spark#3 which failed to ignite, and (d) Spark#4 which successfully ignited.

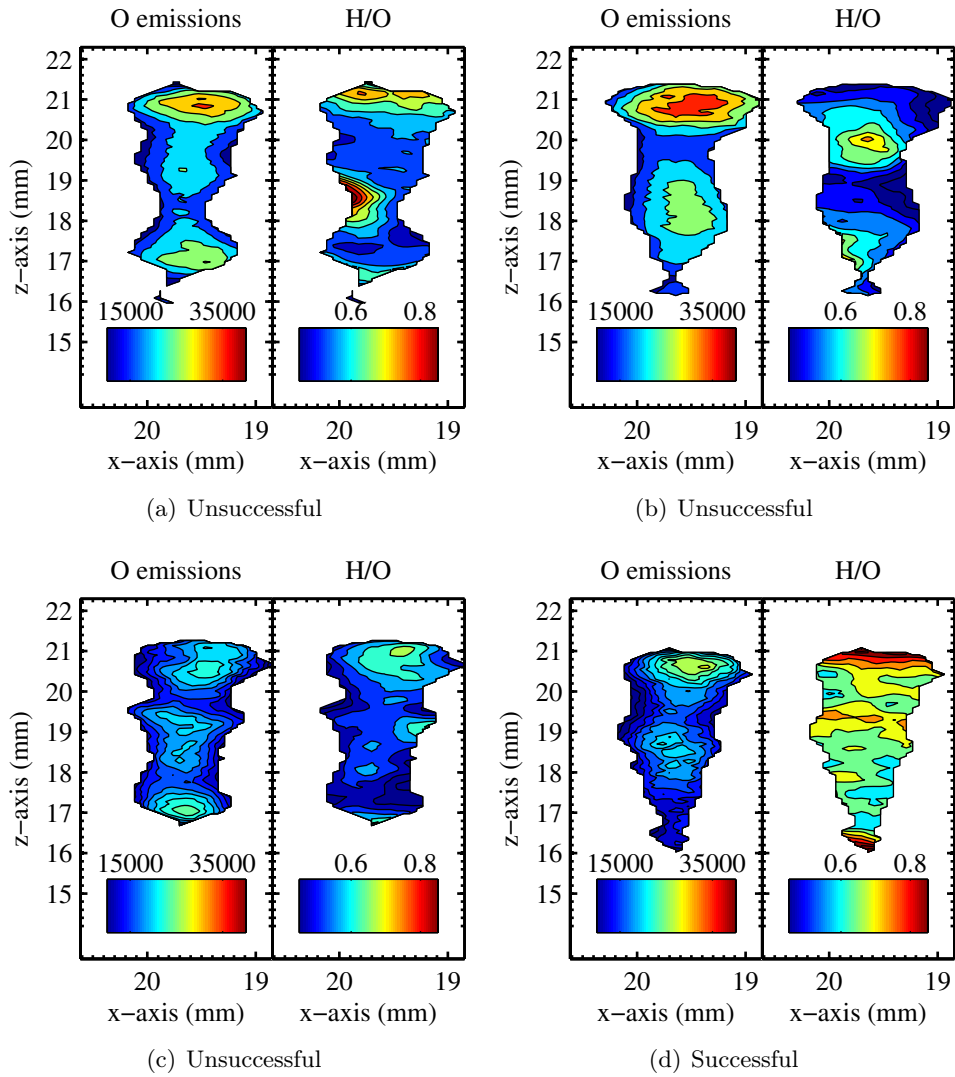


Figure D.31: Location *g*; Test#3, Analysis of 2D-LIPS experiments for (a) Spark#1, (b) Spark#2, and (c) Spark#3 which failed to ignite, and (d) Spark#4 which successfully ignited.

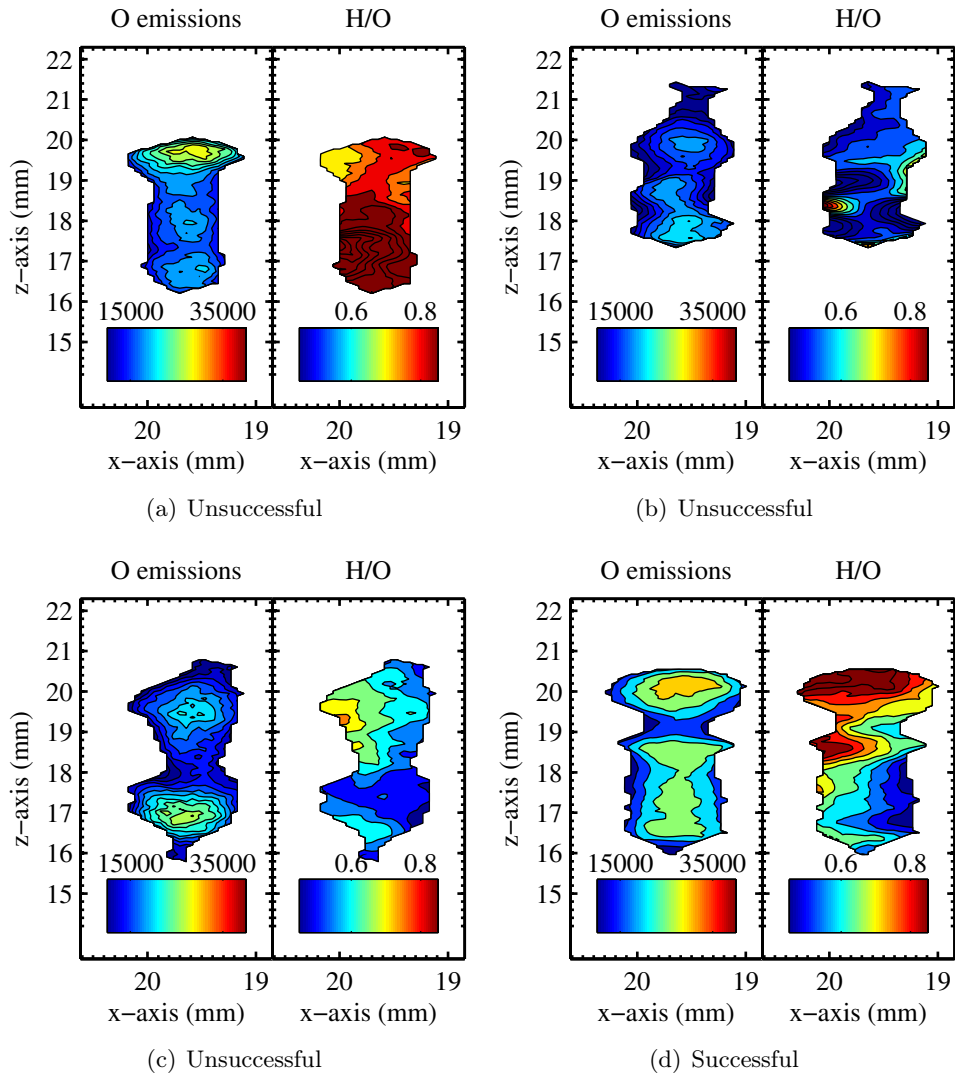


Figure D.32: Location *g*; Test#4, Analysis of 2D-LIPS experiments for (a) Spark#1, (b) Spark#2, and (c) Spark#3 which failed to ignite, and (d) Spark#4 which successfully ignited.

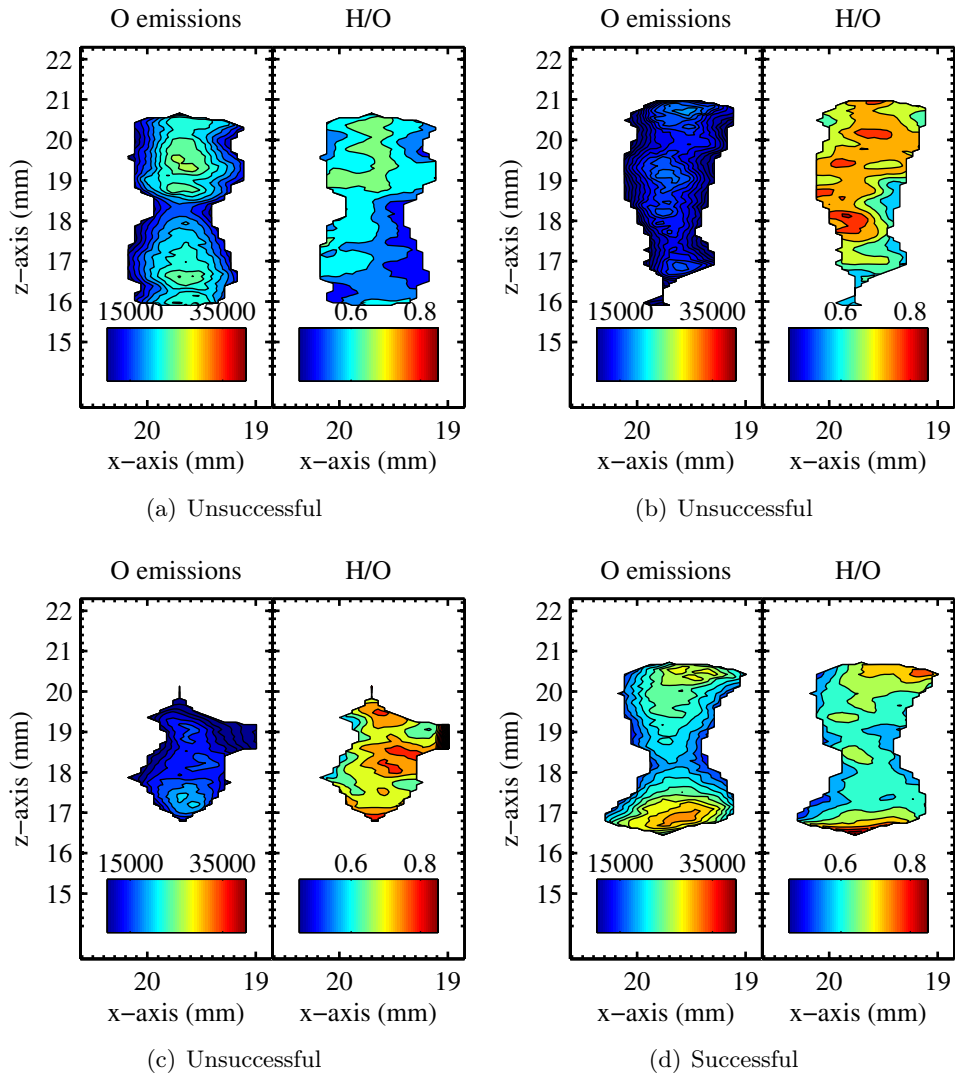


Figure D.33: Location *g*; Test#5, Analysis of 2D-LIPS experiments for (a) Spark#1, (b) Spark#2, and (c) Spark#3 which failed to ignite, and (d) Spark#4 which successfully ignited.

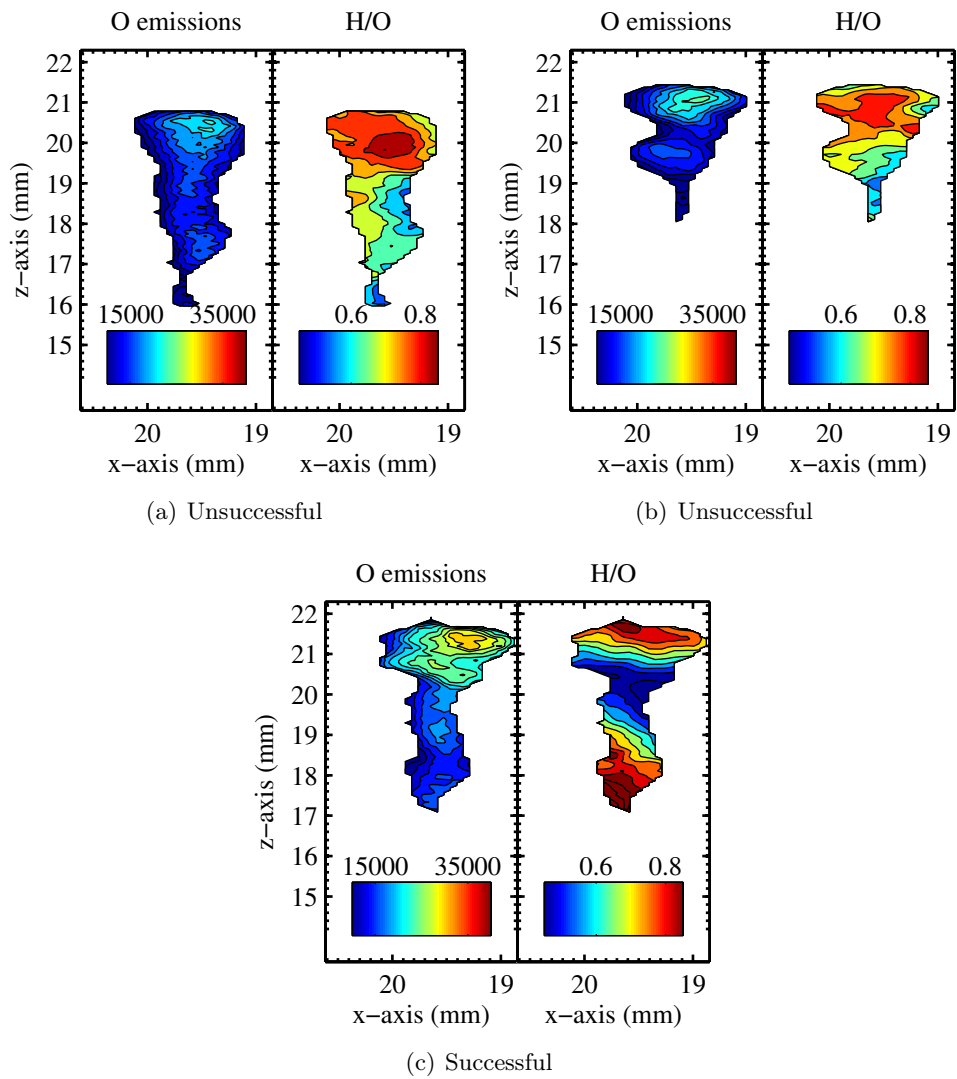


Figure D.34: Location *g*; Test#6, Analysis of 2D-LIPS experiments for (a) Spark#1, and (b) Spark#2 which failed to ignite, and (c) Spark#3 which successfully ignited.

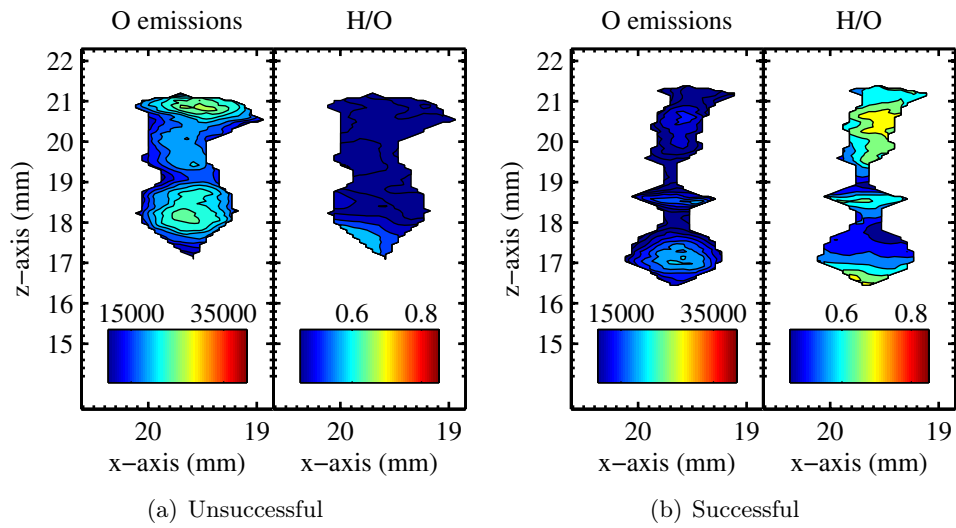


Figure D.35: Location *g*; Test#7, Analysis of 2D-LIPS experiments for (a) Spark#1 which failed to ignite, and (b) Spark#2 which successfully ignited.

References

- Agarwal, T., F. Richecoeur, and L. Zimmer (2010). Application of two dimensional laser induced plasma spectroscopy to the measurement of local composition in gaseous flows. In *15th International Symposium on application of laser techniques to fluid mechanics, July 5-8, Lisbon, Portugal*. (p. 10)
- Aggarwal, S. K. (1998). A review of spray ignition phenomena: Present status and future research. *Progress in Energy and Combustion Science* 24(6), 565–600. (p. 8)
- Aguilera, J., J. Bengoechea, and C. Aragon (2004). Spatial characterization of laser induced plasmas obtained in air and argon with different laser focusing distances. *Spectrochimica Acta Part B: Atomic Spectroscopy* 59(4), 461–469. (p. 86)
- Aguilera, J. A. and C. Aragon (2004). Characterization of a laser-induced plasma by spatially resolved spectroscopy of neutral atom and ion emissions: Comparison of local and spatially integrated measurements. *Spectrochimica Acta Part B: Atomic Spectroscopy* 59(12), 1861–1876. (p. 10, 86)
- Aguilera, J. A., C. Aragón, and J. Bengoechea (2003). Spatial characterization of laser-induced plasmas by deconvolution of spatially resolved spectra. *Appl. Opt.* 42(30), 5938–5946. (p. 86, 87)
- Ahmed, S., R. Balachandran, T. Marchione, and E. Mastorakos (2007). Spark ignition of turbulent nonpremixed bluff-body flames. *Combustion and Flame* 151(1-2), 366–385. (p. 7)
- Ahmed, S. and E. Mastorakos (2006). Spark ignition of lifted turbulent jet flames. *Combustion and Flame* 146(1-2), 215–231. (p. 7)
- Ahmed, S. F. and E. Mastorakos (2010). Correlation of spark ignition with the local instantaneous mixture fraction in a turbulent nonpremixed methane jet. *Combustion Science and Technology* 182(9), 1360–1368. (p. 9)
- Aragon, C. and J. Aguilera (2008). Characterization of laser induced plasmas by optical emission spectroscopy: A review of experiments and methods. *Spectrochimica Acta Part B: Atomic Spectroscopy* 63(9), 893 – 916. (p. 5, 86, 87)
- Asgill, M., H. Moon, N. Omenetto, and D. Hahn (2010). Investigation of

- polarization effects for nanosecond laser-induced breakdown spectroscopy. *Spectrochimica Acta Part B: Atomic Spectroscopy* 65(12), 1033 – 1040. (p. 159)
- Ballal, D. and A. Lefebvre (1978). Ignition of liquid fuel sprays at subatmospheric pressures. *Combustion and Flame* 31(0), 115 – 126. (p. 2)
- Ballal, D. R. and A. H. Lefebvre (1975). The influence of flow parameters on minimum ignition energy and quenching distance. *Symposium (International) on Combustion* 15(1), 1473 – 1481. (p. 2)
- Barbosa, S., P. Scoufflaire, and S. Ducruix (2009). Time resolved flowfield, flame structure and acoustic characterization of a staged multi-injection burner. *Proceedings of the combustion institute* 32, 2965–2972. (p. 18)
- Beduneau and J. (2003). Measurements of minimum ignition energy in premixed laminar methane/air flow by using laser induced spark. *Combustion and Flame* 132(4), 653–665. (p. 89)
- Beduneau, J. and Y. Ikeda (2004). Spatial characterization of laser-induced sparks in air. *Journal of Quantitative Spectroscopy and Radiative Transfer* 84(2), 123–139. (p. 86)
- Beduneau, J.-L., B. Kim, L. Zimmer, and Y. Ikeda (2003). Measurements of minimum ignition energy in premixed laminar methane/air flow by using laser induced spark. *Combustion and Flame* 132(4), 653 – 665. (p. 5, 6, 89)
- Berkooz, G., P. Holmes, and J. Lumley (1993). The proper orthogonal decomposition in the analysis of turbulent flows. *Annual Review of Fluid Mechanics* 25, 539–575. (p. 44)
- Boileau, M., G. Staffelbach, B. Cuenot, T. Poinsot, and C. Berat (2008). Les of an ignition sequence in a gas turbine engine. *Combustion and Flame* 154(1-2), 2–22. (p. 8)
- Bradley, D., C. Sheppard, I. Suardjaja, and R. Woolley (2004). Fundamentals of high-energy spark ignition with lasers. *Combustion and Flame* 138(1-2), 55–77. (p. 6)
- Chen, Y. L., J. W. L. Lewis, and C. Parigger (2000). Spatial and temporal profiles of pulsed laser-induced air plasma emissions. *Journal of Quantitative Spectroscopy and Radiative Transfer* 67(2), 91–103. (p. 86)
- Cowen, E. A. and S. G. Monismith (1997). A hybrid digital particle tracking velocimetry technique. *Experiments in Fluids* 22, 199–211. (p. 18)
- Cristoforetti, G., A. De Giacomo, M. Dell’Aglia, S. Legnaioli, E. Tognoni, V. Palleschi, and N. Omenetto (2010). Local thermodynamic equilibrium in laser-induced breakdown spectroscopy: Beyond the mcwhirter criterion. *Spectrochimica Acta Part B: Atomic Spectroscopy* 65(1), 86–95. (p. 86)
- Dahms, R. N., M. C. Drake, T. D. Fansler, T.-W. Kuo, and N. Peters (2011a). Understanding ignition processes in spray-guided gasoline engines using high-speed imaging and the extended spark-ignition model sparkcimm. part a: Spark channel processes and the turbulent flame front propaga-

- tion. *Combustion and Flame* 158(11), 2229 – 2244. (p. 8)
- Dahms, R. N., M. C. Drake, T. D. Fansler, T.-W. Kuo, and N. Peters (2011b). Understanding ignition processes in spray-guided gasoline engines using high-speed imaging and the extended spark-ignition model sparkcimm: Part b: Importance of molecular fuel properties in early flame front propagation. *Combustion and Flame* 158(11), 2245 – 2260. (p. 8)
- Darabiha, N., E. Esposito, F. Lacas, and D. Veynante (2010). *Third year course in combustion*. Ecole Centrale Paris. (p. 163)
- Dasch, C. J. (1992, Mar). One-dimensional tomography: a comparison of abel, onion-peeling, and filtered backprojection methods. *Appl. Opt.* 31(8), 1146–1152. (p. 39, 122)
- De Giacomo, A., R. Gaudiuso, M. Dell’Aglio, and A. Santagata (2010). The role of continuum radiation in laser induced plasma spectroscopy. *Spectrochimica Acta Part B: Atomic Spectroscopy* 65(5), 385–394. (p. 157)
- Egbert, R. B. (1942). *Ph.D. Thesis, Heat transmission by radiation from gases*. Ph. D. thesis, MIT. (p. 166)
- El-Rabii, H., G. Gaborel, J. P. Lapios, D. Thovenin, J. C. Rolon, and J. P. Martin (2005). Laser spark ignition of two-phase monodisperse mixtures. *Optics Communications* 256(4-6), 495–506. (p. 5)
- Ershovpavlov, E., K. Katsalap, K. Stepanov, and Y. Stankevich (2008). Time-space distribution of laser-induced plasma parameters and its influence on emission spectra of the laser plumes. *Spectrochimica Acta Part B: Atomic Spectroscopy* 63(10), 1024–1037. (p. 5, 85)
- Eyssartier, A., B. Cuenot, L. Gicquel, and T. Poinot (2013). Using les to predict ignition sequences and ignition probability of turbulent two-phase flames. *Combustion and flame (submitted)*. (p. 8, 128)
- Eyssartier, A., G. Hannebique, D. Barré, L. Gicquel, and B. Cuenot (2011). Ignition predictions from non-reacting LES: application and assessment on complex configurations. In *3ème colloque INCA*. (p. 128)
- Fansler, T., B. Stojkovic, M. Drake, and M. Rosalik (2002). Local fuel concentration measurements in internal combustion engines using spark-emission spectroscopy. *Applied Physics B: Lasers and Optics* 75, 577–590. 10.1007/s00340-002-0954-0. (p. 9)
- Feroli, F. and S. G. Buckley (2006). Measurements of hydrocarbons using laser-induced breakdown spectroscopy. *Combustion and Flame* 144(3), 435 – 447. (p. 9, 86, 87)
- Frigo, M. and S. G. Johnson (2005). The design and implementation of FFTW3. *Proceedings of the IEEE* 93(2), 216–231. Special issue on “Program Generation, Optimization, and Platform Adaptation”. (p. 41)
- Horn, B. and B. Schunck (1981). Determining optical flow. *Artificial intelligence* 17, 185–203. (p. 18)
- Itoh, S., M. Shinoda, K. Kitagawa, N. Arai, Y.-I. Lee, D. Zhao, and H. Yamashita (2001). Spatially resolved elemental analysis of a hydrogen-air diffusion flame by laser-induced plasma spectroscopy (lips). *Microchemi-*

- cal Journal* 70(2), 143–152. (p. 9, 85)
- Juddoo, M. and A. Masri (2011). High-speed oh-plif imaging of extinction and re-ignition in non-premixed flames with various levels of oxygenation. *Combustion and Flame* 158(5), 902 – 914. (p. 7)
- Kawahara, N., J. Beduneau, T. Nakayama, E. Tomita, and Y. Ikeda (2007). Spatially, temporally, and spectrally resolved measurement of laser-induced plasma in air. *Applied Physics B: Lasers and Optics* 86, 605–614. 10.1007/s00340-006-2531-4. (p. 86)
- Kiefer, J., J. Tröger, Z. Li, and M. Aldén (2011). Laser-induced plasma in methane and dimethyl ether for flame ignition and combustion diagnostics. *Applied Physics B: Lasers and Optics* 103, 229–236. 10.1007/s00340-010-4338-6. (p. 6)
- Kondo, S., A. Takahashi, and K. Tokuhashi (2003). Calculation of minimum ignition energy of premixed gases. *Journal of Hazardous Materials* 103(12), 11 – 23. (p. 6)
- Kramida, A. E., Y. Ralchenko, J. Reader, and N. Team (2012). NIST Atomic Spectra Database (version 5.0). (p. xi, 20, 21, 95)
- Kumar, K. and C.-J. Sung (2007). Laminar flame speeds and extinction limits of preheated ndecane/o₂/n₂ and n-dodecane/o₂/n₂ mixtures. *Combustion and Flame* 151, 209 – 224. (p. 167)
- Lacaze, G., B. Cuenot, T. Poinso, and M. Oschwald (2009). Large eddy simulation of laser ignition and compressible reacting flow in a rocket-like configuration. *Combustion and Flame* 156(6), 1166 – 1180. (p. 7)
- Lacaze, G., E. Richardson, and T. Poinso (2009). Large eddy simulation of spark ignition in a turbulent methane jet. *Combustion and Flame* 156(10), 1993 – 2009. (p. 7)
- Lee, W.-B., J. Wu, Y.-I. Lee, and J. Sneddon (2004). Recent applications of laser-induced breakdown spectrometry: A review of material approaches. *Applied Spectroscopy Reviews* 39(1), 27 – 97. (p. 85)
- Lefebvre, A. and D. Ballal (2010). *Gas turbine combustion Alternative fuels and emissions*. Taylor and Francis. (p. 1)
- Letty, C., A. Pastore, E. Mastorakos, R. Balachandran, and S. Couris (2010). Comparison of electrical and laser spark emission spectroscopy for fuel concentration measurements. *Experimental Thermal and Fluid Science* 34(3), 338 – 345. Sixth Mediterranean Combustion Symposium. (p. 10)
- Lewis, B. and G. von Elbe (1987). *Combustion, Flames and Explosions of Gases* (3 ed.). ACADEMIC PRESS INC. (p. 5)
- Lim, E., A. McIlroy, P. Ronney, and J. Syage (1996). *Detailed characterization of minimum ignition energies of combustible gases using laser ignition sources*. London: Taylor & Francis. (p. 5)
- Linassier, G., R. Lecourt, P. Villedieu, G. Lavergne, and H. Verdier (2011). Experimental database on high altitude turbojet ignition for numerical simulation validation. In *ILASS-Europe 2011, 24th European conference*

- on liquid atomization and spray systems, Estoril, Portugal, September 2011. (p. 8)
- Majd, A. E., A. Arabanian, and R. Massudi (2010). Polarization resolved laser induced breakdown spectroscopy by single shot nanosecond pulsed nd:yag laser. *Optics and Lasers in Engineering* 48(7-8), 750 – 753. (p. 157)
- Marchione, T., S. Ahmed, and E. Mastorakos (2009). Ignition of turbulent swirling n-heptane spray flames using single and multiple sparks. *Combustion and Flame* 156(1), 166–180. (p. 8)
- Mastorakos, E. (2009). ignition of turbulent non-premixed flames. *Progress in Energy and Combustion Science* 35, 57–97. (p. 7)
- Morgan, G. C. (1978). *Laser-induced electrical breakdown of gases*. Wiley series in plasma physics. John Wiley & Sons. (p. 4, 89)
- Morsy, M. H. (2012). Review and recent developments of laser ignition for internal combustion engines applications. *Renewable and Sustainable Energy Reviews* 16(7), 4849 – 4875. (p. 3)
- Mullett, J. D., G. Dearden, R. Dodd, A. T. Shenton, G. Triantos, and K. G. Watkins (2009). A comparative study of optical fibre types for application in a laser-induced ignition system. *Journal of Optics A: Pure and Applied Optics* 11(5), 054007. (p. 3)
- Neophytou, A., E. Mastorakos, and R. S. Cant (2012). The internal structure of igniting turbulent sprays as revealed by complex chemistry dns. *Combustion and Flame* 159(2), 641 – 664. (p. 9)
- Neophytou, A., E. Richardson, and E. Mastorakos (2012). Spark ignition of turbulent recirculating non-premixed gas and spray flames: A model for predicting ignition probability. *Combustion and Flame* 159(4), 1503 – 1522. (p. 9)
- Phuoc, T. (2000). single point versus multi point laser ignition. *Combustion and Flame* 122, 508–512. (p. 4)
- Phuoc, T. (2005). An experimental and numerical study of laser-induced spark in air. *Optics and Lasers in Engineering* 43(2), 113–129. (p. 4, 6)
- Phuoc, T. (2006a). Laser-induced spark for simultaneous ignition and fuel-to-air ratio measurements. *Optics and Lasers in Engineering* 44(6), 520–534. (p. 10, 86, 87)
- Phuoc, T. (2006b). Laser-induced spark ignition fundamental and applications. *Optics and Lasers in Engineering* 44(5), 351–397. (p. 85)
- Phuoc, T. X. (2004). An experimental and numerical study of laser induced spark in air. *Optics and lasers in engineering* 43, 113–129. (p. 4, 6, 165)
- Phuoc, T. X. (2006c). Laser-induced spark for simultaneous ignition and fuel-to-air ratio measurements. *Optics and Lasers in Engineering* 44(6), 520 – 534. (p. 6, 9)
- Phuoc, T. X. (2010). *Laser Ignition*. Wiley-VCH Verlag GmbH & Co. KGaA. (p. 5)
- Phuoc, T. X., C. White, and D. Mcneill (2001). Laser spark ignition of a jet

- diffusion flame. *Optics and lasers in engineering* 38, 217–232. (p. 6)
- Phuoc, T. X. and F. P. White (1999). Laser-induced spark ignition of ch₄/air mixtures. *Combustion and Flame* 119, 203–216. (p. 5)
- Phuoc, T. X. and F. P. White (2002a). Laser-induced spark for measurements of the fuel-to-air ratio of a combustible mixture. *Fuel* 81(13), 1761 – 1765. (p. 9, 10, 85, 86, 87)
- Phuoc, T. X. and F. P. White (2002b). An optical and spectroscopic study of laser-induced sparks to determine available ignition energy. *Proceedings of the Combustion Institute* 29, 1621–1628. (p. 19)
- Prasad, A. (2000). Stereoscopic particle image velocimetry. *Experiments in Fluids* 29, 103–116. (p. 18)
- Providakis, A. (2013). Phd thesis, etude de la dynamique de flamme swirle dans un injecteur diphasique multipoint etage. *PhD Thesis, Laboratoire EM2C*. (p. 32, 50, 71, 135)
- Providakis, A., L. Zimmer, P. Scouffaire, and S. Ducruix (2011). Effect of fuel distribution on spray dynamics in a two-staged multi-injection burner. *Proceedings of ASME Turbo Expo 2011: Power for Land, Sea and Air, GT 2011, June 6-10, 2011, Vancouver, Canada*. (p. 50)
- Providakis, A., L. Zimmer, P. Scouffaire, and S. Ducruix (2012). Acoustic response of droplets in a two-staged multi injection chamber. *Submitted to ASME Turbo Expo*. (p. 32)
- Richecoeur, F., L. Hakim, A. Renaud, and L. Zimmer (2012). Dmd algorithms for experimental data processing in combustion. *Center for Turbulence Research Proceedings of the Summer Program*. (p. 44)
- Schmid, P. J. (2010). Dynamic mode decomposition of numerical and experimental data. *Journal of Fluid Mechanics* 656, 5–28. (p. 44, 77)
- Schmieder, R. (1982). Combustion applications of laser-induced breakdown spectroscopy. Technical report, No. SAND81-8886, Sandia National Laboratories. (p. 85)
- Shringi, D., B. Shaw, and H. Dwyer (2009). Laser-induced fluorescence imaging of acetone inside evaporating and burning fuel droplets. *Optics and Lasers in Engineering* 47(1), 51 – 56. (p. 10)
- Shudo, T. and S. Oba (2009). Mixture distribution measurement using laser induced breakdown spectroscopy in hydrogen direct injection stratified charge. *International Journal of Hydrogen Energy* 34(5), 2488–2493. (p. 9, 86)
- Soufiani, A. and J. Taine (1997). High temperature gas radiative property parameters of statistical narrow-band model for h₂o, co₂ and co, and correlated-k model for h₂o and co₂. *International journal of heat and mass transfer* 40. (p. 166)
- Srivastava, D. K., K. Dharamshi, and A. K. Agarwal (2011). Flame kernel characterization of laser ignition of natural gas-air mixture in a constant volume combustion chamber. *Optics and Lasers in Engineering* 49(910), 1201 – 1209. (p. 7)

- Srivastava, D. K., M. Weinrotter, K. Iskra, A. K. Agarwal, and E. Wintner (2009). Characterisation of laser ignition in hydrogen-air mixtures in a combustion bomb. *International Journal of Hydrogen Energy* 34(5), 2475–2482. (p. 7)
- Srivastava, D. K., M. Weinrotter, H. Kofler, A. K. Agarwal, and E. Wintner (2009). Laser-assisted homogeneous charge ignition in a constant volume combustion chamber. *Optics and Lasers in Engineering* 47(6), 680 – 685. (p. 7)
- Stavropoulos, P., A. Michalakou, G. Skevis, and S. Couris (2005). Laser-induced breakdown spectroscopy as an analytical tool for equivalence ratio measurement in methane-air premixed flames. *Spectrochimica Acta Part B: Atomic Spectroscopy* 60(7-8), 1092 – 1097. Laser Induced Plasma Spectroscopy and Applications (LIBS 2004) Third International Conference - LIBS Malaga. (p. 9, 10, 86)
- Stöhr, M., I. Boxx, C. D. Carter, and W. Meier (2012). Experimental study of vortex-flame interaction in a gas turbine model combustor. *Combustion and Flame* 159, 2636–2649. (p. 44)
- Subramanian, V., P. Domingo, and L. Vervisch (2010). Large eddy simulation of forced ignition of an annular bluff-body burner. *Combustion and Flame* 157(3), 579 – 601. (p. 7)
- Syage, J. A., E. W. Fournier, R. Rianda, and R. B. Cohen (1988). Dynamics of flame propagation using laser-induced spark initiation: Ignition energy measurements. *Journal of Applied Physics* 64(3), 1499–1507. (p. 5)
- Taine, J. and J.-P. Petit (2010). *Heat Transfer*. (p. 165)
- Theunissen, R., F. Scarano, and M. Riethmuller (2010). Spatially adaptive piv interrogation based on data ensemble. *Experiments in Fluids* 48, 875–887. (p. 18)
- Trost, J., M. Laffler, L. Zigan, and A. Leipertz (2010). Simultaneous quantitative acetone-plif measurements for determination of temperature and gas composition fields in an ic-engine. *Physics Procedia* 5(Part 2), 689 – 696. Laser Assisted Net Shape Engineering 6, Proceedings of the LANE 2010, Part 2. (p. 10)
- Weinberg, F. J. and J. R. Wilson (1971). A preliminary investigation of the use of focused laser beams for minimum ignition energy studies. *Proceedings of the Royal Society of London. A. Mathematical and Physical Sciences* 321(1544), 41–52. (p. 3)
- Zhang, J. (2010). *Ph.D. Thesis*. Ph. D. thesis, Laboratoire EM2C, ECP. (p. 166)
- Zhao, Y., S. Singha, Y. Liu, and R. J. Gordon (2009). Polarization-resolved laser-induced breakdown spectroscopy. *Opt. Lett.* 34(4), 494–496. (p. 158)
- Zimmer, L., T. Agarwal, F. Richecoeur, and S. Yoshida (2010). Mesures de compositions locales par spectroscopie de plasma induit par laser. *Congres francophone de technique laser, September 14-17, 2010, Nancy, France*.

(p. 10)

- Zimmer, L., R. Domann, Y. Hardalupas, and Y. Ikeda (2003). Simultaneous laser-induced fluorescence and mie scattering for droplet cluster measurements. *AIAA Journal* 41, 2170–2178. (p. 18)
- Zimmer, L., K. Okai, and Y. Kurosawa (2007). Combined laser induced ignition and plasma spectroscopy: Fundamentals and application to a hydrogen-air combustor. *Spectrochimica Acta Part B: Atomic Spectroscopy* 62(12), 1484–1495. (p. 9, 10, 86, 87, 129)
- Zimmer, L. and S. Tachibana (2007a, March). Chemiluminescence sensor for active control of combustion. Research and Development Memorandum 06-016E, JAXA. (p. 39)
- Zimmer, L. and S. Tachibana (2007b). Laser induced plasma spectroscopy for local equivalence ratio measurement in an oscillating combustion environment. *Proceedings of the combustion institute* 31, 737–745. (p. 9, 10, 86, 87)
- Zimmer, L., S. Tachibana, and K. Suzuki (2005). Local equivalence ratio measurements using laser induced plasma spectroscopy. *AJCPP*. (p. 10)
- Zimmer, L. and S. Yoshida (2008). Measurement of mixture fraction with laser induced plasma spectroscopy. *Journal of combustion society of Japan* 50, 317–324. (p. 10, 86)
- Zimmer, L. and S. Yoshida (2011). Feasibility of laser-induced plasma spectroscopy for measurements of equivalence ratio in high-pressure conditions. *Experiments in Fluids*, 1–14. (p. 10, 86, 87)